UNIVERSITY OF SOUTHAMPTON

FACULTY OF NATURAL AND ENVIRONMENTAL SCIENCES

School of Chemistry

Mixed (ion and electron) Conducting Polymers, with Applications in Batteries

by

Suputtra Visetpotjanakit

Thesis for the degree of Doctor of Philosophy

October 2011

ABSTRACT

A new method to fabricate 3D batteries using mixed (ion and electron) conducting polymers as electrolytes has been developed. The majority of the work was done using the polymer Poly(1,11-Di(N-pyrryl)-3,6,9-trioxaundecane) (PP2O3) because it demonstrated mixed conducting properties. Methods are presented for synthesising the monomer then polymerising either electrochemically to give films or chemically to give bulk samples or powders. The conductivities of both polymers were determined by Electrochemical Impedance Spectroscopy (EIS). For polymer films prepared electrochemically on conducting substrates, the conductivities were determined as a function of the p-doping level, using a cell containing a liquid electrolyte and an applied bias potential. The results were fitted with a transmission line model and revealed an electronic conductivity varying from 4.20 $x10^{-10}$ to 1.69 $x10^{-5}$ S/cm dependent on the doping level, and a relatively constant ionic conductivity of 1.74 $x10^{-6}$ S/cm. Oxidative treatment by overdoping resulted in a reduction of electronic conductivity by a factor of about 50,000 times smaller at the potential of maximum conductivity, around 0.30 V with a small change in the ionic conductivity. Bulk samples of the chemically prepared polymer were examined between two blocking electrodes. The electronic conductivities of the as-prepared and chemically oxidized samples were both quite low, around 10^{-7} and 10^{-8} S/cm, whereas the ionic conductivity of both samples was around 10^{-5} and 10^{-6} S/cm. These values were slightly higher than those of the film samples due to a presence of PC plasticiser in bulk samples. Finally the polymers were tested as electrolyte/separators in lithium ion battery cells: the electrochemically treated film was found to be an effective separator between a 3D $LiFePO_4$ positive electrode and a liquid lithium amalgam negative, and the chemically prepared materials showed a capacity of around 150 mAh per gram $LiFePO_4$ in a conventional Li/$LiFePO_4$ cell,. These experiments demonstrate a proof of concept for the use of mixed conducting polymers as electrolytes in lithium battery systems.

Table of Contents

Chapter 1 Introduction

Chapter 2 Physical Characterisation Techniques

Chapter 5 Ionic and Electronic Conductivities of PP2O3

Appendices

Declaration of Authorship

I, Suputtra Visetpotjanakit, declare that the thesis entitled
"Mixed (ion and electron) Conducting Polymers, with Applications in Batteries"

and the work presented in the thesis are both my own, and have been generated by me as the results of my own original research.

- this work was done wholly or mainly while in candidature for a research degree at this University;
- where any part of this thesis has previously been submitted for a degree or any other qualification at this University or any other institution, this is always clearly attributed;
- where I have quote from the work of others, the source is always given. With the exception of such quotations, this thesis is entirely my own work;
- I have acknowledged all main sources of help;
- where the thesis is based on work done by myself jointly with others, I have made clear exactly what was done by others and what I have contributed myself;
- none of this work has been published before submission.

Signed:

Date:

Acknowledgements

I would like to thank Professor John Owen who has provided me with excellent guidance throughout my studies. Secondly Dr Gaber El-Enany guided me with great advice during my first year of studies. He really made my beginning in Electrochemistry research much easier than it might have been. Massive thanks goes to Dr Matthew Roberts. He always gave me both research and encouragement support. Not only he is a colleague, but also he is one of the great friends of mine. Without his support, my studies would have been very hard to succeed. I would also like to thank all the other members of the Owen group during my studies in Southampton, Dr Hannah Alcock, Phil Johns, Alex Madsen, Andrew Buck and Matthew Lacey and all the other members of floor 6 and 7 and as well as Dr. Martin Grossel and Dr. Francesco Cuda from the organic lab. All these people provided me with invaluable help at one time or another. I would like to thank the chemistry department support staffs who have assisted in issues at one point or another. Finally, I have special thanks to my family who have always closely supported me and continue to do so. I have always found there encouragement to be good source of inspiration.

List of symbols

A	Area	cm^2
C	Capacitance	F
E	Potential	V
E_a	Activation energy	kJ mol^{-1}
Δf	Frequency change	Hz
f_o	Natural frequency of quartz crystal microbalance	Hz
F	Faraday number (96487)	C mol^{-1}
G	Conductance	S
ΔG	Change in free energy	kJ mol^{-1}
I	Current	A
m	Number of mole of active material	
Δm	Mass change per unit surface	g cm^{-2}
n	Number of electrons	
p	Polymer weight	g
Q	Charge	C
R	Resistance	Ω
t_f	Film thickness	μm
t_{ion}	Ion transport number	
Z	Impedance	Ω
Z’	Real impedance	Ω
-Z”	Imaginary impedance	Ω
μ_Q	Shear modulus	N m^{-2}

μ_{Li}^{P}	Chemical potential of lithium in the cathode	kJ mol^{-1}
μ_{Li}^{N}	Chemical potential of lithium in the anode	kJ mol^{-1}
ρ_Q	Quartz density	g cm^{-3}
σ	Warburg coefficient	Ω $s^{-1/2}$
	OR	
	Conductivity	S cm^{-1}

List of Abbreviations

AB	Acetylene black
AC	Alternating Current
ACN	Acetonitrile
CPE	Constant Phase Element
CPE-P	Constant Phase Element Phase Angle
CV	Cyclic Voltammetry
DC	Direct Current
DI	De-ionised
DMC	Dimethyl carbonate
EC	Ethylene carbonate
EDOT	3,4-ethylenedioxythiophene
EQCM	Electrochemical Quartz Crystal Microbalance
FEG SEM	Field Emission Gun Scanning Electron Microscope
$Fe(OTs)_3$	Iron (III) p-toluenesulfonate
ITO	Indium tin oxide
$LiBF_4$	Lithium tetrafluoroborate
$LiCoO_2$	Lithium cobalt oxide
LiTFSI	Lithium bis(trifluoromethane) sulfonamide salt
Mw	Molecular Weight
NMR	Nuclear Magnetic Resonance
PC	Propylene carbonate
PEDOT	Poly(3,4-ethylenedioxythiophene)

PEO	Poly(ethylene oxide)
P2O3	1,11-Di(N-pyrryl)-3,6,9-trioxahendecane
PPO	Poly(propylene oxide)
PP2O3	Poly(1,11-Di(N-pyrryl)-3,6,9-trioxahendecane)
PTFE	Poly(tetrafluoro ethylene)
RVC	Reticulated vitreous carbon
SCE	Saturated calomel electrode
SDS	Sodium dodecylbenzenesulfonate
SEM	Scanning Electron Microscope
$TEABF_4$	Tetraethylammonium tetra-fluoroborate
TiO_2	Titanium dioxide
TSNa	Sodium p-toluene sulfonate

Chapter 1

Introduction

1.1 The Aim of this Work

Fabrication of a complete battery cell structure, i.e. an electrode-electrolyte-electrode sandwich, by electrodeposition is an attractive and novel concept that could be applied to the deposition of batteries on convoluted and even three dimensional sponge substrates. Although several electrode materials can be electrodeposited onto conducting substrates, a sequential electrodeposition of all three layers of the cell is a serious challenge, due to the fact that the electrolytic separator should be not only an ionic conductor but also an electronic insulator. In the strictest sense this means that it cannot sustain the electronic current required for its own electrodeposition, let alone pass a current for subsequent deposition of the final layer. A possible solution involves the deposition of a mixed, electronic plus ionic, precursor polymer with a tunable electronic conductivity that can be maximised during electrodeposition and then turned off completely for cell operation. The discovery and fabrication of such a polymer is the main aim of this work.

The following introductory material presents a general review of battery types, in particular lithium-ion batteries with polymer electrolytes which form the basis of the 3D microbatteries currently under study elsewhere. The construction method for a 3D battery is described and finally mixed conducting polymers are reviewed and presented as a solution to the problem of electrolyte deposition.

1.2 Batteries

1.2.1 Introduction

The first report of an electrochemical battery, the Voltaic pile, was introduced by Alexander Volta in 1800. Since then the field has continued to grow and develop. Nowadays, batteries play an important role in our everyday life as an electrical energy source. They are generally used to supply electrical energy to portable electronic devices such as laptops, mobile phones and digital cameras. There are also new battery sales such as electric vehicles, which will become progressively more important as petroleum reserves are depleted. A further application of batteries is to store electrical energy supplied from mains electricity this can then be delivered for short duration demand peaks or in conjunction with renewable energy sources, such as solar, wave or wind power[1].

The following section will introduce the concept of batteries focusing on lithium ion systems.

1.2.2 Concept of Lithium Ion Batteries

By definition, a battery or electrochemical power source is a device which enables the energy liberated in a chemical reaction to be converted directly into electricity. Batteries normally consist of three components as shown in Figure 1.1. These are;

- A cathode or positive electrode where electrons are taken from the circuit during discharge.
- An anode or negative electrode where electrons are supplied to the circuit during discharge.
- A separator with the properties of an electrolyte, electrically isolating the cathode and anode as well as providing a mechanism for charge to flow between the two electrodes in the form of ions.

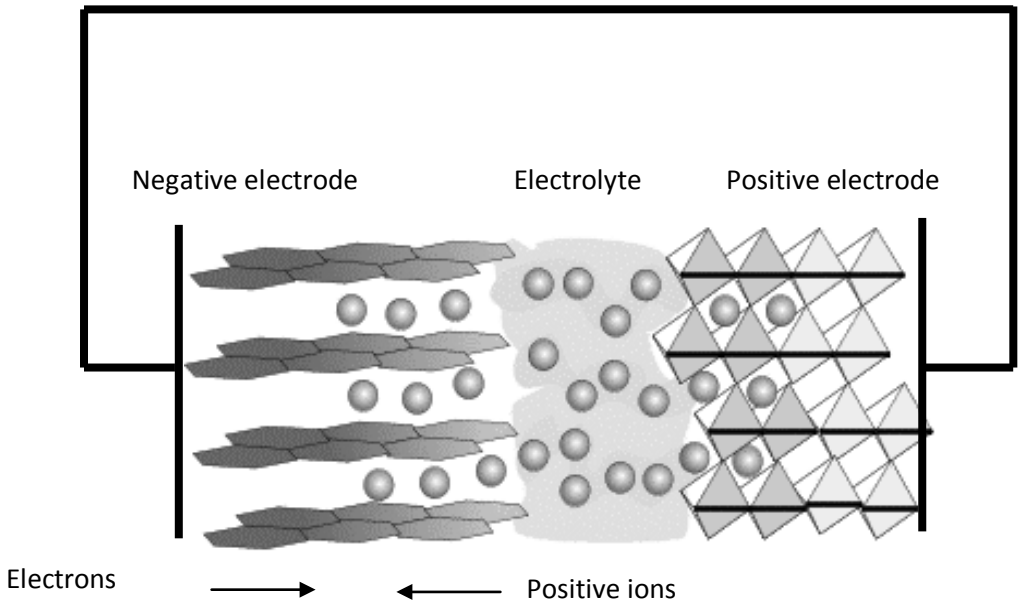

Figure 1.1 Schematic diagram of Lithium ion battery during charge[2].

The basic operation of a lithium ion battery is shown Figure 1.1. Lithium ion batteries are usually fabricated in the charged state. In this case an external current is applied to the cell which drives the removal of lithium ions from the cathode and the transport through the electrolyte and subsequent insertion into the negative electrode; shown in Figure 1.1. The transport of ions in an electric field is known as migration. However, this process does not always provide the ion fluxes required to compensate the electronic charge. Any mass imbalances due to the inability of the migration flows to provide the correct counter charge as required are made up by salt diffusion.

An example of a secondary, lithium ion battery can be seen from a series of equation below[3]. The cathode is $LiCoO_2$ and the anode is carbon, and the simple scheme assumes that one lithium is inserted per Co, rather than the practical case where the non-stoichiometric electrode, Li_xCoO_2 has a narrower range for reversible lithium insertion of $\Delta x \sim 0.5$

During discharge

At the anode: $LiC_6 \longrightarrow Li^+ + C_6 + e^-$ **Equation 1.1**

At the cathode: $CoO_2 + Li^+ + e^- \longrightarrow LiCoO_2$ **Equation 1.2**

During charge

At the anode: $Li^+ + C_6 + e^- \longrightarrow LiC_6$ **Equation 1.3**

At the cathode: $LiCoO_2 \longrightarrow CoO_2 + Li^+ + e^-$ **Equation 1.4**

Overall

$$LiC_6 + CoO_2 \underset{\text{charge}}{\overset{\text{discharge}}{\rightleftharpoons}} C_6 + LiCoO_2$$ **Equation 1.5**

During discharge the Li ions are extracted from the carbon and moved to CoO_2 as can be seen from Equation 1.1 and 1.2 respectively. On charge the process is reversed as shown in Equation 1.3 and 1.4. The overall reaction is shown in Equation 1.5.

1.2.3 Battery Parameters

1. Free Energy and Cell Voltage

When a battery is discharged, the free energy of the system is changed as the reactants are converted into products. The change in the molar free energy is directly related to the cell voltage[4-7] shown in Equation 1.6.

$$\Delta G = -nFE$$

Equation 1.6

Where ΔG is change in the molar free energy, n is number of electrons involved in the stoichiometric reaction, F is Faraday's constant (96487) and E is Potential (V).

In the case of a lithium ion cell n = 1, i.e. one electron passes in the circuit during the transfer of one lithium atom across the cell, and the free energy change can be expressed in terms of the chemical potential of lithium according to Equation 1.7

$$\partial G = (\mu_{Li}^{p} - \mu_{Li}^{N})\partial m$$

Equation 1.7

where ∂m is an infinitesimal number of moles of lithium transferred across the cell, μ_{Li}^{P} is the chemical potential of lithium in the cathode and μ_{Li}^{N} is chemical potential of lithium in the anode.

Equation 1.6 and 1.7 can then be combined to express the potential of a cell as a function of the chemical potential shown in Equation 1.8.

$$E = \frac{-(\mu_{Li}^{P} - \mu_{Li}^{N})}{F}$$

Equation 1.8

The voltage changes during discharge because the chemical potential changes with composition. For example in $Li_{1-x}CoO_2$ battery when x is in a range of 0-0.5, the composition varies continuously within a single phase and the discharge occurs at potentials between 4.3 and 3.6V[8]. This single phase behavior can be thought of as a gradual change in composition of the particles in the electrode. If we were to record the XRD pattern at various states of charge we would only see a single phase. A second behavior exists by which 2 phases co exist in the electrode the charged and the discharged. In this case if we were to record the XRD pattern at various states of charge we would see two phases. This results in a situation where the chemical potential of the lithium in the cathode does not change and therefore the potential during discharge does not change and the discharge plateau is flat.

2. Capacity

Capacity is one of the significant measurements used to characterise a battery material. Generally two specifications are quoted, theoretical and specific capacities, and each can be quoted as gravimetric and volumetric values. These terms again will be explained by using the example of the commercial battery material $LiCoO_2$.

Theoretical capacity

The theoretical capacity of a battery electrode can be calculated by considering the ideal charge reaction. The example of $LiCoO_2$, will now be used to demonstrate this; as shown in Equation 1.9.

Charge reaction $LiCoO_2$ $\quad LiCoO_2 \longrightarrow CoO_2 + Li^+ + e^-$

Equation 1.9

During charge, 1 mole of Li^+ is extracted from $LiCoO_2$ for every mole of electrons that flows around the external circuit. Therefore, the charge passed for an arbitrary number of moles of lithium extracted is equal to the number of moles of lithium, m multiplied by Faraday's constant according to Equation 1.10.

$$Q = mF$$

Equation 1.10

where Q is the theoretical charge passed during charge.

The gravimetric capacity can then be calculated by dividing the charge passed by the molar mass of the active material per mole of lithium according to Equation 1.11.

$$Q_M = \frac{mF}{M}$$

Equation 1.11

where Q_M is theoretical capacity per gram (C g^{-1}) and M is the molar mass of active material in (g) that exchanges one mole of lithium.

The above result in C g^{-1}, can be converted to the technical unit of mA h g^{-1} by dividing by 3.6 (the number of seconds in an hour divided by 1000). The molar mass of $LiCoO_2$ is 98. The calculated theoretical capacity of $LiCoO_2$ (based on the discharge state of CoO_2) is 273 mA h g^{-1}.

Specific capacity

The term specific capacity in this work will refer to the experimental value of the capacity on discharge. This is calculated by measuring the charge per gram of active material followed by conversion from C g^{-1} to the technical unit of mA h g^{-1}.

In the case of $LiCoO_2$ the reversible specific capacity from the measured charge is around 130 mA h g^{-1}. This is significantly different from the calculated theoretical capacity. This is normally explained as only around 0.5 moles of Li can be extracted reversibly from 1 mole of $LiCoO_2$[4, 9].

1.2.4 The Materials of Lithium Ion Batteries

Lithium ion batteries have already been introduced as a concept. The following section will examine some of the components that make up a lithium ion battery with particular focus on the polymer electrolytes as this will be the focus of the later chapters.

Anode materials

Originally lithium batteries consisted of a lithium foil negative electrode, electrolyte (formed by dissolving lithium salts in a non aqueous solvents) and a positive ion-insertion electrode material such as V_6O_{13} or TiS_2 which could undergo a reversible electrochemical reaction with lithium ions according to Equation 1.12[10].

$$xLi(s) + A_zB_y(s) \underset{\text{charge}}{\overset{\text{discharge}}{\rightleftharpoons}} Li_xA_zB_y(s)$$

Equation 1.12

However, there were safety issues with the use of lithium metal; on long term cycling due to dendrite formation sometimes caused short circuits, thermal runaway[11] or even explosions.

In the early 1980s these safety considerations led to the replacement of lithium metal with a lithium insertion electrode,[12, 13] which could still act as a lithium ion sink and source, accepting lithium ions during charge and releasing them during discharge. This was shown earlier in Figure 1.1. [14] Typically the materials used to replace the lithium were carbon[15] or metal oxides[14]. The new battery was termed a rocking chair battery or more generally a lithium ion battery. A general scheme for the reversible charge and discharge reaction of the rocking chair system is shown in Equation 1.13[14]. These systems removed the previous safety issues, however, did lead to a reduction in the available capacity.

$$Li_xC_nD_m(S) + A_zB_y(S) \underset{\text{charge}}{\overset{\text{discharge}}{\rightleftharpoons}} C_nD_m(S) + Li_xA_zB_y(S)$$

Equation 1.13

Cathode materials

Cathode materials have been made from a number of lithium metal oxides such as $LiCoO_2$, $LiNiO_2$, $LiCo_{0.5}Ni_{0.5}O_2$ and $LiMn_2O_4$ depending on the required cell voltage or

economics.[16] Two of the most relevant systems to consider are $LiCoO_2$ and $LiFePO_4$. $LiCoO_2$ is the most widely commercialised cathode material. It is highly crystalline and the capacity is relatively independent of the preparation method. It has a reasonable specific capacity of around 130 mA h g^{-1} and as long as the amount of lithium removed does not exceed 0.5 moles per mole of $LiCoO_2$ then the reversibility of the system is excellent. $LiFePO_4$ is one of the most promising cathode materials and will be used as a cathode in this project. This material operates with a 2 phase discharge and has a specific capacity of around 170 mA h g^{-1} which corresponds to the complete extraction of lithium from the structure during charge. This material is also highly attractive as it offers; low toxicity, low cost and high thermal stability. It also exhibits good cycling stability and high capacity at increased charge and discharge rates[17].

Non Aqueous Electrolytes

Lithium ion batteries typically use electrolytes which are composed of lithium salts dissolved in an organic solvent. These organic solvents operate well outside their potential stability window and should decompose[18]. However, this problem is resolved via the growth of a passivation layer known as the solid electrolyte interface (SEI)[19] on the surface of the negative electrode which protects against the decomposition, while, allowing ions to conduct through the electrolyte.

Some examples of salts used in lithium ion batteries are $LiPF_6$, LiTFSI and LiBOB. These salts are typically dissolved in various different organic solvents with ethylene carbonate (EC) and dimethyl carbonate mixtures (DMC) being the most widely used[20].

Polymer electrolytes

When a polymer electrolyte is used in a lithium ion battery the battery is often known as a lithium polymer battery, these have recently attracted much attention and this area has become one of expanding importance. Improved fabrication routes as a result of the elastic properties of polymeric electrolytes have led to an electrolytic phase which can be readily

formed with reduced thickness. The mechanical flexibility of the polymer enables solid-state cells to be designed with optimised electrode/electrolyte interface configurations. Moreover, it has low cost.

Since the initial report of polymer electrolyte lithium batteries in 1978[21, 22] they have been continuously developed and improved to overcome problems with the cathode and anode materials as well as a low ionic conductivity of polymer electrolyte itself.

Basically polymer electrolytes serve as electronic insulators between the anode and cathode and as good ionic conductors. In other words, they must function as both a separator and electrolyte in a solid-state battery. An essential feature for long-range cation transport is a process in which cations move between co-ordinating sites along the same molecule or between molecules. Polymer electrolytes have to meet a number of critical properties for their success. These are briefly listed as follows[23]:

Conductivity: the electrolyte must have sufficient ionic conductivity to allow a reasonable current density; $10^{-2} – 10^{-3}$ S cm^{-1} would be ideal at room temperature although a lower value may be acceptable i.e. 10^{-5} S cm^{-1} could be a minimum practical value[24]

Electronic conductivity: the polymer electrolyte must have low electronic conductivity like an insulator in order to prevent short circuit in batteries.

Electrochemical stability: the electrolyte should be electrochemically stable in a voltage window that is at least as wide as the voltage window defined by the electrode reactions. It should preferably be wider, to accommodate overcharge and discharge reactions.

Thermal stability: electrolyte must have good thermal stability, especially in contact with the negative electrode.

Availability: raw materials must be available and inexpensive. This is required so that their fabrication can be scaled up at a production level.

.

Examples of Polymer electrolytes

There are a number of ionic conductive polymers such as poly(ethylene oxide) (PEO)[25], polypropylene oxide (PPO)[26], Poly(ethylene glycol)[27] and other classes of conductive polymers like aliphatic polyesters[28], and polyamines. They have been prepared and their ionic conductivities optimised in order to meet electrolyte properties for their success. For example, PEO is frequently used as the polymer matrix because it is chemically inert and able to dissolve a number of inorganic salts to provide moderate ionic conductivity, a range of 10^{-8} to 10^{-4} S cm^{-1}. The polymer structure of PEO is shown in Figure 1.2.

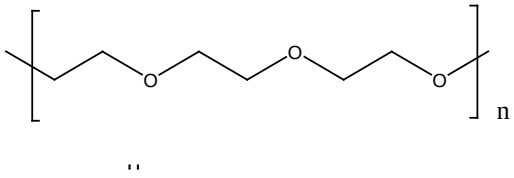

Figure 1.2 chemical structure of poly(ethylene oxide)[29]

The ionic motion of a lithium ion in a PEO-host is displayed in Figure 1.3[30]

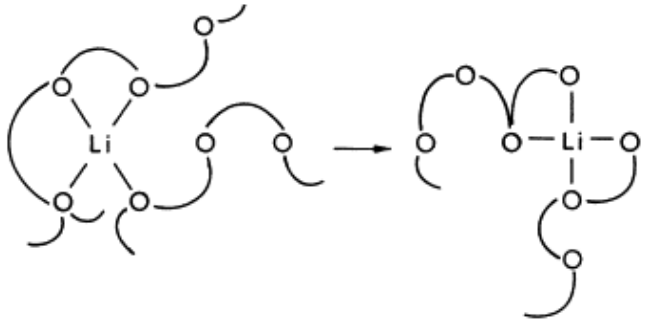

Figure 1.3 Cartoon of Lithium ion motion in a PEO host

So far we have introduced only conventional lithium batteries. The following section will introduce 3D microbatteries as a concept. One approach to develop these batteries will require an extremely specialized polymer electrolyte. This will be the focus of this thesis and will be discussed in much greater detail later.

1.3 3D Microbatteries

In recent years a need has been identified for microbatteries for small scale applications such as micro sensors, self powered integrated circuits or microelectromechanical system (MEMS). Such small devices need rechargeable batteries with a high storage density. The conventional 2D thin film batteries however are not able to provide a high energy density. Increasing electrode thickness will at some point lead to power limitations due to slow diffusion in the electrodes. This had led to the idea of novel 3D microbatteries. Cells comprise anodes and cathodes which have active surface areas exposed in three dimensions[31]. This leads to the concept of capacity per footprint area (μA h/cm^2) which is a key consideration for the construction of microbatteries. With 3D structures, making electrodes longer, rather than thicker results in increased cell capacity per footprint area and power.

Such structures require current collector architectures such as small arrays pillars and also three conformal coated layers on current corrector i.e. cathode, electrolyte and anode. The overall of 3D battery fabrication is shown in Figure 1.4.

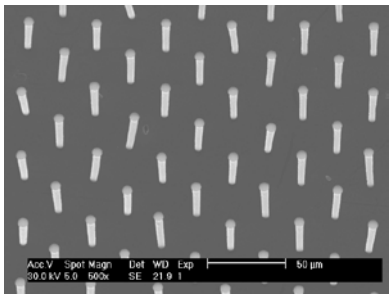

SEM image of carbon pillars
(an example of current collector)

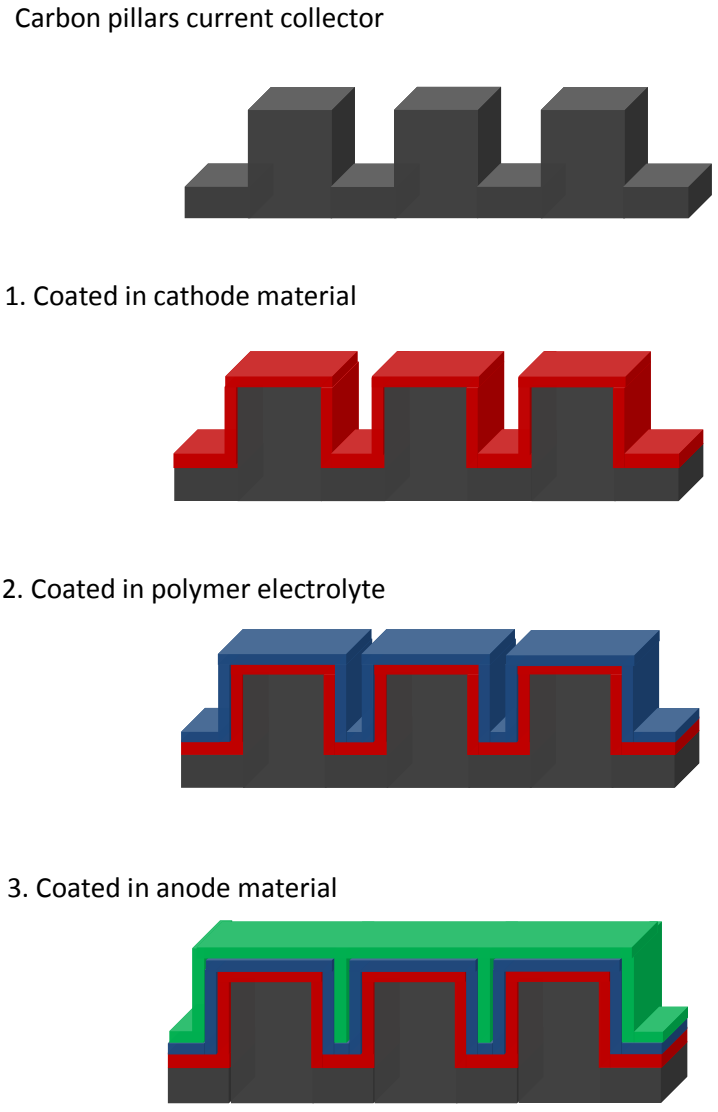

Figure 1.4 The left SEM image shows an array of carbon pillars which could be used as a substrate for 3D microbatteries. On the left a schematic of the 3D microbattery fabrication process is shown. In initially the dark grey substrate is coated in the red cathode material. This is then coated by the blue electrolyte and finally the green anode material. A second current collector could also be added but is not shown here.

Many researchers have tried to find a suitable techniques to fabricate complete 3D microbatteries[32-35]. Whilst many have been successful in the deposition of the first electrode on a 3D current collector[36-39] relatively few have been successful in the

fabrication of the full cell[40]. This is typically due to cracks and holes in battery layers, particularly the electrolyte.

The most successful full 3D microbattery was developed by Golodnitsky *et al.*[41] this focused on the deposition of conformal battery materials on silicon 'micro channel plates' (MCP, essentially silicon wafers perforated by a regular array of microchannels). The structure of the 3D microbattery was based on high aspect ratio channels onto which thin films of cathode and polymer electrolyte were deposited; the remaining volume in the channel was filled with a slurry containing the anode. Fabrication began by depositing a current collector onto the silicon substrate, in this case Ni, onto which an electrodeposited cathode (molybdenum sulphide) was plated. The polymer electrolyte was based on PVDF and was deposited onto the molybdenum sulphide through the depth of the microchannel using what was described as 'sequential spin-coating and vacuum pulling steps'. The anode was a slurry containing mesoporous microbeads (MCMB's), polymer binder and solvent (also deposited into the microchannel using sequential spin-coating and vacuum pulling steps). Once constructed the whole assembly was soaked in 1 M $LiPF_6$ 1EC:1DEC or 1 M $LiBF_4$ 1 EC : 9 DEC under vacuum for 10 hours. Lithium foil placed on top of the structure provided lithium intercalation into the anode. The 3D microchannel plate (molybdenum sulphide / polymer electrolyte / MCMB soaked in 1M LiPF6 1EC:1DEC or 1M $LiBF_4$ 1 EC : 9 DEC) and the equivalent 2D planar microbatteries were tested in parallel by galvanostatic cycling, between 2.2 and 1.3 V *vs.* lithium, in order to compare the available capacity (mA h/cm^2). The 3D system increased the capacity available per footprint by greater than 10 times that the 2D system. This gain corresponds to the increase in surface area achieved by the 3D structure.

Electrolyte Materials for 3D Microbatteries

This research focuses on preparation of polymer electrolyte for 3D batteries which is the most difficult step in the fabrication of any 3D microbattery. Coating the electrolyte layer between cathode and anode materials must be perfect. Cracks or holes will result in short circuits and associated problems. The following will detail several examples of systems examined in the literature.

A hybrid co-polymer vinylidene fluoride-hexafluoropropylene(PVDF-HFP) was prepared as an electrolyte for the nanostructured 3D electrode(Cu_2Sb)[39] by a spray-coating technique. The obtained film conformally coated onto the 3D nanostructured electrode arrays. However, the resulting structure did not leave sufficient space to insert a second electrode.

Poly(acrylonitrile) (PAN) films were fabricated as 3D microbattery electrolyte via electrodeposition onto MnO_2 on a glassy carbon electrode. Thereafter the layers were submerged into a Li-Hg amalgum to make a soft contact in order to observe the cell behaviour under galvanoststic intermittent titration technique. The cell had a stable open circuit potential and behaved normally. However, although this work demonstrated an operational electrolyte no 3D structures were developed.

Another proposed route for preparing an electrolyte for 3D microbatteries is oligomeric poly(ether amine) (PEA). The polymer was formed as ultra thin layers on $LiFePO_4$ cathode particles[42]. PEA with cross-linked PPO-diacrylate was also prepared. Batteries constructed *vs.* Li and then cycled. It showed only normal capacity at low cycling rates, probably due to high interfacial resistance. This approach also only demonstrated an operational electrolyte and no 3D structures were developed.

Fabrication of a separator between interlaced pores in a rigid Si substrate, which acted as micro-containers for the cathode and anode materials, were also studied[43]. The silicon separating the micro-containers was exposed to metal-assisted anisotropic wet-etching technique this resulted in the silicon being transformed into a nanoporous separator (membrane). The ionic conductivity of the liquid electrolyte trapped in the interlaced mesoporous membrane was in a range of 0.07 to 0.24 mS cm^{-1}. However, although the electrolyte has been developed no operational batteries have been investigated.

These examples show that the fabrication of full 3D microbatteries is not trivial. All materials must be compatible to each other without crack and holes. This project aims to develop a new route to these electrolytes.

Project Goal

This research focuses on a route to prepare electrolyte material using an electrodeposited polymer. The idea is to prepare conformal thin electrolyte film on a substrate by electropolymerisation of electronically conducting polymer. The polymer would then be treated to convert it to an electronic insulator with ionic conductivity to act as an electrolyte for lithium conduction. This will be explained in more detail later. The following section therefore reviews the kind of mixed ionic and electronic polymers that will be investigated.

1.4 Mixed Ionic and Electronic Conducting Polymers

1.4.1 Introduction

The work reported in this thesis focuses on mixed ionic and electronic conducting polymers which can be polymerised via an electroinitiation step and converted to an ionic conductor as a solid-state electrolyte for lithium batteries.

1.4.2 Electronic conducting polymers

Electronic conducting polymers or conjugated polymers act as electronic conductor as a result of delocalized valence π-electrons in a carbon-based macromolecule. This feature results in materials with directional conductivity, strongest along the axis of the chain. Some simple examples of conducting polymers are polyacetylene, aromatic and heterocyclic polymers as shown Figure 1.5.

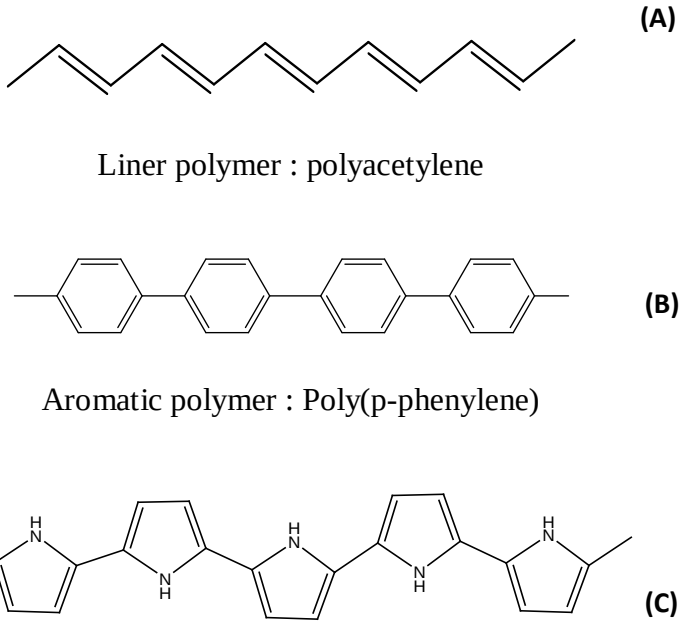

Figure 1.5 Conjugated polymer structure: (A) polyacetylene (B) Poly(p-phenylene) and (C) Polypyrrole.

The mechanism of conductivity in these polymers is based on the motion of charged defects within the conjugated framework. The charge carriers, either positive p-type (oxidation) or negative n-type (reduction), are the products of oxidizing or reducing the polymer respectively.

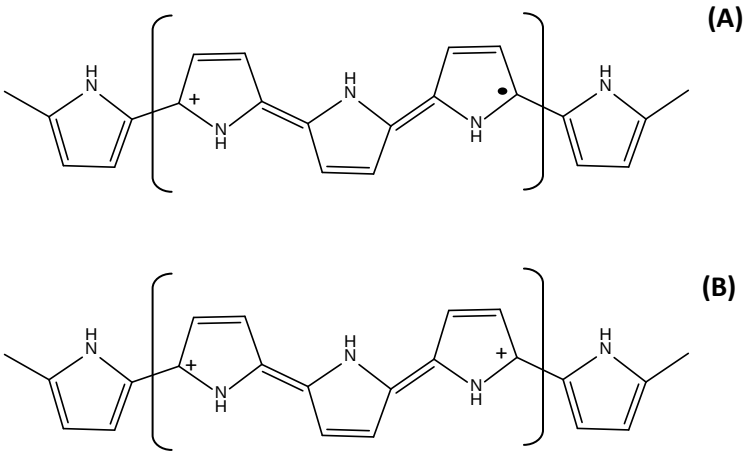

Figure 1.6 Proposed structure of polypyrrole for (A) polarons and (B) bipolarons

Oxidation of the polymer initially generates a radical cation with both spin and charge. This species is referred to as a polaron and is comprised of both the hole site and the structural distortion which accompanies it. An example of a positively charged defect on polypyrrole (polarons) is shown in Figure 1.6 (A). Theoretical treatments have demonstrated that two nearby polarons combine to form the lower energy bipolarron shown in Figure 1.6 (B). This charge carrier mobility leads to the high conductivity of these polymers. This examples is p-doping the polymer. It is generally also possible to reduce the polymer or n-dope it such that a similar mechanism of charge transport is possible.

Recent development

Many interesting conducting polymer have been developed over the past 25 years. Those based on polyanilines, polypyrroles, polythiophenes, polyphenylenes and poly(*p*-phenylene

vinylene)s[44]. The polyaniline family stands out for its ability to form processable conductive forms at relatively low cost[45]. Unfortunately, due to the possible presence of benzidine moieties in the polymer backbone, it might yield toxic (carcinogenic) products upon degradation and as a result many industrial and academic groups have limited their research in polyaniline chemistry. The (hetero)aromatic polypyrrole and polythiophene are also attractive due to their low toxicity and simple low cost synthesis, especially polythiophene derivative i.e. polyethylene dioxythiophene (PEDOT).

1.4.3 Mixed conducting polymers for this research

For a battery application we require ionic conductivity, and whilst for the specific goals of this project electronic conductivity also. This leads us to require a mixed electronic and ionic polymer. This will be termed a mixed conductive polymer. The following section will look at the candidates investigated in this thesis.

1.4.3.1 PEDOT

The first mixed conducting polymer to be investigated was polyethylene dioxythiophene (PEDOT). This polymer is one of the best electronic conductors as it is very stable in its doped state[46]. The conductivity of doped polymer is up to 200 S cm^{-1}[47] and it is stable up to 1000 h at 120 °C[48]. It also has a high degradation temperature of about 250 °C. Another advantage of this material is its low monomer oxidation potential[49] which makes it easy to deposit on a range of different substrates without significant corrosion problems. PEDOT structure is shown in Figure 1.7. PEDOT has been used in a wide range of applications such as an antistatic coating on different materials[50], a basic component for biosensors[49] and an electrode material in solid-state capacitors[51, 52].

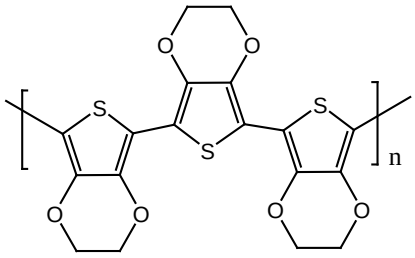

Figure 1.7 chemical structure of Polyethylene dioxythiophene[53]

For this polymer to be of interest for study in this thesis it must not only be electronically conductive but also ionically. The PEDOT structure is composed of oxygen atoms on the heterocyclic ring which may be possible to solvate lithium salts and/or encourage plasticisation by a liquid electrolyte (salt plus solvent). This makes this polymer a good candidate for initial study. The specifics of this polymers electrochemistry are now discussed.

Electrochemistry of PEDOT

PEDOT can be electropolymerised in both aqueous and non aqueous solutions. The polymerisation of the EDOT monomer is shown in Figure 1.8. The polymerisation reaction proceeds only when the potential is sufficiently high to oxidise the monomer. This undergoes oxidation via a two electron process.

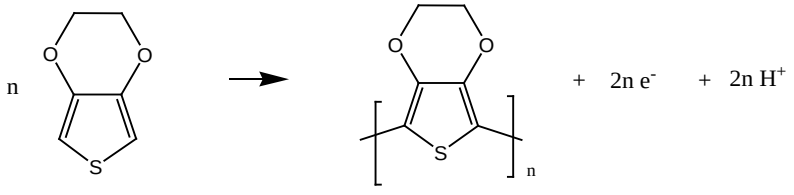

Figure 1.8 Polymerisation of EDOT

Doping/dedoping reaction of PEDOT is also shown in Figure 1.9. During the doping reaction dopant anions are inserted into the polymeric chain. This balanced by the removal of 2 electrons per three thiophene rings into the external circuit. This reaction is a reversible process and in the case of PEDOT has an electrochromic effect. The polymer colour switches from dark blue to transparent during the doping dedoping reaction. This doping

reaction also effects the conductivity of the polymer. The positive charges on the polymer backbone are the charge carriers for the electrical conduction. Increasing the doping level will increase the density of charge carriers and therefore the conductivity.

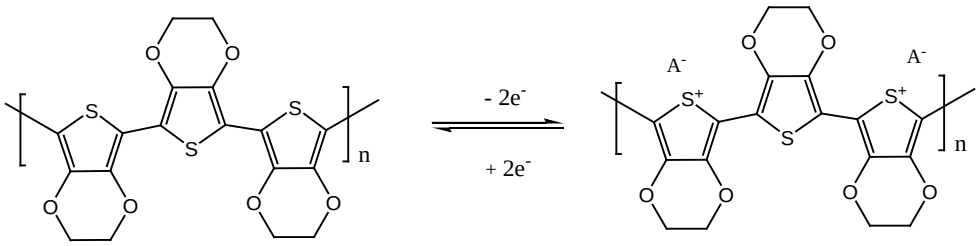

Figure 1.9 Doping and dedoping PEDOT[54]

Preparation Methods

PEDOT has a number of different preparative routes which are reviewed below. For the electrochemical synthesis in non aqueous solution there are several possible methods; Several authors[48] [55] have studied the electropolymerisation of EDOT in acetonitrile using various different electrolyte compositions. They found the oxidation potential of the monomer EDOT was in the range 1.1- 1.5 V *vs.* Ag/AgCl . Typically on the first scan a nucleation loop is seen with an increasing current with each cycle resulting from the formation of conducting polymer on the electrode. Although EDOT has low solubility in water, several authors[49][56] have attempted electropolymerisation in this medium. In these cases polymerisation occurred in the range 0.8 to 1.2 V *vs.* Ag/AgCl. Much the same electrochemical response was observed with a nucleation loop followed by increased currents on cycling. However, this route typically resulted in very thin polymer films of only around 0.20 μm.

1.4.3.2 PP2O3

Poly(1,11 Di (N-pyrryl)-3,6,9-trioxaundecane) (PP2O3) results from polymerisation of 1,11 Di (N-pyrryl)-3,6,9-trioxaundecane compound. It is a pyrrole derivative. The molecule structure is shown in Figure 1.10.

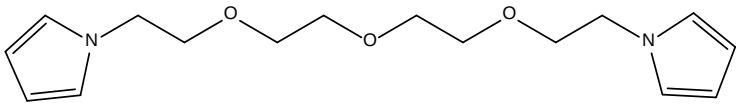

Figure 1.10 Chemical structure of 1,11 Di (N-pyrryl)-3,6,9-trioxaundecane (P2O3)[57]

The molecule structure consists of bipyrroles and triethyl ether chain link between the N sites. The pyrrole rings can be oxidised to form polymers and the oxygen coordination sites could be an ionic conduction. Due to these reasons, it was chosen to be a mixed ionic and electronic conducting polymer electrolyte for this research. Its polymer structure is shown in Figure 1.11.

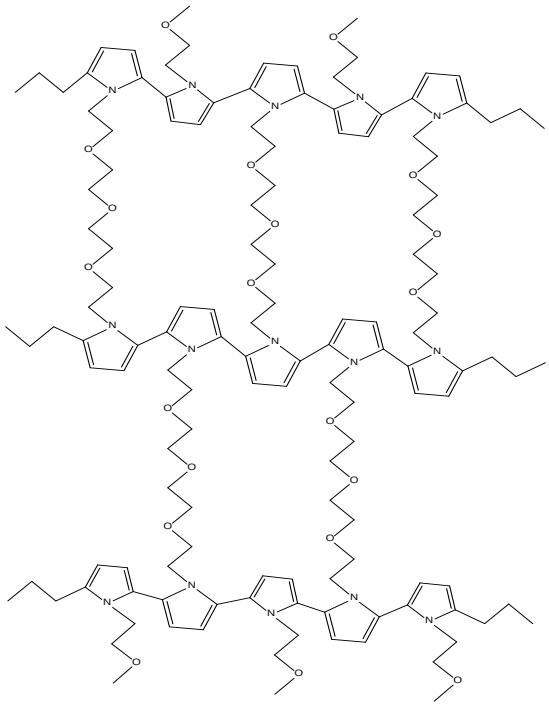

Figure 1.11 Molecular structure of PP2O3

P2O3 could be electropolymerised using similar condition as pyrrole. There are examples of electrochemical synthesis of polypyrrole in both aqueous and non aqueous solution. Cvetko *et al.*[58] studied electrochemical preparation of pyrrole in both aqueous and nonaqueous solutions. First the electropolymerisation of pyrrole in acidic solution, pyrrole + $K_3Fe(CN)_6$ dissolved in 1 M H_2SO_4 was studied. The deposition was carried out at 0.8 V

vs. SCE using platinum and titanium sheet electrodes. The film produced had powdery appearance and could be easily wiped off. The film was seen to be unstable in acidic solution, tending to polymerisation reaction without the application of voltage. This was due to acid-catalysed polymerisation reaction of pyrrole to saturated oligomers. In non aqueous system, the solution of PC containing 0.14 M pyrrole, 1% water and 0.05 M of various electrolyte, $K_3Fe(CN)_6$, sodium n-lauryl sulphate and tetra-ethyl ammonium p-toluene sulphonate, were used. The films were prepared at a constant potential of 1.0 V *vs.* SCE. The film from tetra-ethyl ammonium p-toluene sulphonate exhibited the best properties. All other electrolyte yielded films which either brittle or powdery and did not adhere well to the substrate. Beak *et al.*[59] prepared polypyrrole in non aqueous solution, 0.1 M pyrrole containing 0.05 M $NaBF_4$ in ACN. Polypyrrole was electrodeposited on platinum electrode at applied potential of 0.85 V *vs.* SCE. The film produced had very good adhesion on the substrate.

1.4.3.3 Breaking the electronic conductivity

There are several examples where the electronic conductivity has been broken in PEDOT and polypyrrole. Below is listed a few examples:

In non aqueous solutions there are a few examples of conductivity breaking in PEDOT; One route used by Kvarnstrom *et al.*[48] was to apply a high oxidation potential. They reported that the redox response of PEDOT vanished when potentials above 2.20 V *vs.* Ag/AgCl was applied indicating a breakdown in conductivity. Another report by Lapkowski *et al.*[60] found that when cycling the polythiophenes to dope and undope the polymer that a degradation in the polymer oxidation current was seen which was attributed to irreversible conductivity loss. Similar results were seen by Zykwinska *et al.*[61] when cycling the polymer above 1.60 V *vs.* Ag.

Only one example of conductivity damage of PEDOT in aqueous solution exists; Wang *et al.*[62] studied cyclic voltammogram of PEDOT/Pt electrode in 0.1 M $LiClO_4$ aqueous

solution using SCE as a reference electrode. They reported that the electroactivity of PEDOT film was lost at high potentials over 1.40 V.

There are two key examples of conductivity damage in polyprrrole electrodes in aqueous solutions; Fernandez *et al.*[63] cycled a polypyrrole film in 1 M KNO_3 in the potential range -1.0 to 1.5 V *vs.* SCE at 20 mV/s. They found reduction in magnitude of the oxidation peak current during cycling and concluded that the current decrease was caused by the loss of polypyrrole chain conjugation due to the overoxidation process. Yuan *et al.*[64] reported that cycling polypyrrole in a solution of 0.1 M NaCl above 0.7 V *vs.* SCE resulted in the loss of electrochemical activity and conductivity due to the overoxidation of the polymer. It is also possible to destroy conjugated bonds by reductive treatment, Ghanem *et al.*[65] converted polypyrrole to an insulator by cycling the film five times between -1.20 and 0.60 V *vs.* SCE at scan rate 10 mV/s in 0.1 M solution of sodium butane sulphonate.

Then pyrrole type polymers are cycled in a non aqueous system several authors have investigated conductivity damage. Novak *et al.*[66] reported that overoxidation of polypyrrole in PC containing 0.5 M $LiClO_4$ and 0.5M H_20 at potential range of 2-4 V *vs.* Li/Li^+ caused irreversible cyclic voltammograms due to destroyed conjugation of polypyrrole. They later[66] found that the overoxidation potential was 3.9 V *vs.* Li/Li^+. Ansari[67] reported that the overoxidation potential of polypyrrole was 1.0 V *vs.* Ag/AgCl in a non aqueous solution i.e. ACN. The overoxidation of the polymer resulted in irreversible loss of electrochemical activity, an interruption of conjugation and conductivity break down. This breakdown in conductivity is typically attributed to an interaction of trace water with the conjugated bonds, thus resulting in loss in its electronic activity In non aqueous systems reductive polymer degradation is also possible, Li[68] reported the overreduction of polypyrrole and thus reduced polypyrrole conductivity. Polypyrrole was cycled in PC containing 0.4 M $NaClO_4$ and 5% water. The film after cycling in the potential range from 0.28 to -1.0 V *vs.* SCE lost 43.1% of its conductivity.

1.5 Chapter 1 References

[1] C. A. Vincent and B. Scrosati, *Modern Batteries: An Introduction to Electrochemical Power Sources*, John Wiley & Sons, America, **1997**, p. 1.
[2] D. Linden and T. B. Reddy, *Handbook of Batteries*, McGraw-Hill, United States of America, **2002**, p. 1.7.
[3] P. Atkins, T. Overton, J. Rourke, M. Weller and F. Armstrong, *Inorganic Chemistry*, Oxford University Press, **2006**, p. 614.
[4] M. S. Whittingham, *Chemical Reviews* **2004**, *104*, 4271-4301.
[5] M. Winter and R. J. Brodd, *Chemical Reviews* **2004**, *104*, 4245-4269.
[6] J. R. Owen, *Chemical Society Reviews* **1997**, *26*, 259-267.
[7] D. Linden and T. B. Reddy, *Handbook of Batteries*, McGraw-Hill, United States of America, **2002**, p. 1.9.
[8] K. Mizushima, P. C. Jones, P. J. Wiseman and J. B. Goodenough, *Materials Research Bulletin* **1980**, *15*, 783-789.
[9] T. Ogasawara, A. Debart, M. Holzapfel, P. Novak and P. G. Bruce, *Journal of the American Chemical Society* **2006**, *128*, 1390-1393.
[10] C. A. Vincent and B. Scrosati, *Modern Batteries: An Introduction to Electrochemical Power Sources*, John Wiley & Sons, America, **1997**, p. 199.
[11] K. Xu, *Chemical Reviews* **2004**, *104*, 4303-4417.
[12] J. Morales, R. Trocoli, S. Franger and J. Santos-Pena, *Electrochimica Acta* **2010**, *55*, 3075-3082.
[13] M. Lazzari and B. Scrosati, *Journal of the Electrochemical Society* **1980**, *127*, 773-774.
[14] C. A. Vincent and B. Scrosati, *Modern Batteries: An Introduction to Electrochemical Power Sources*, John Wiley & Sons, America, **1997**, p. 200.
[15] C. A. Vincent and B. Scrosati, *Modern Batteries: An Introduction to Electrochemical Power Sources*, John Wiley & Sons, America, **1997**, p. 202.
[16] F. M. Gray, *Polymer electrolyte*, RSC Materials Monographs, United Kingdom, **1997**, p. 141-144.
[17] D. Zhang, R. Cai, Y. K. Zhou, Z. P. Shao, X. Z. Liao and Z. F. Ma, *Electrochimica Acta* **2010**, *55*, 2653-2661.
[18] K. Xu, *Chemical Reviews* **2004**, *104*, 4303-4418.
[19] E. Peled, *Journal of the electrochemical Society* **1979**, *126*, 2047-2051.
[20] D. Aurbach, Y. Talyosef, B. Markovsky, E. Markevich, E. Zinigrad, L. Asraf, J. S. Gnanaraj and H. J. Kim, *Electrochimica Acta* **2004**, *50*, 247-254.
[21] K. Murata, S. Izuchi and Y. Yoshihisa, *Electrochimica Acta* **2000**, *45*, 1501-1508.
[22] J. R. MacCallum and C. A. Vincent, *Polymer Electrolyte Reviews 2*, Elsevier Science, **1989**, p. 286.
[23] F. M. Gray, *Polymer Electrolytes*, RSC Materials Monographs, United Kingdom, **1997**, p. 31-32.
[24] M. B. Armand, J. M. Chabagno and N. J. Duclot, *Fast Ion Transport in Solids*
Elsevier Science, Amsterdam
1979, p. 131.
[25] J. Y. Song, Y. Y. Wang and C. C. Wan, *Journal of Power Sources* **1999**, *77*, 183-197.
[26] M. Kakihana, S. Schantz and L. M. Torell, *Journal of Chemical Physics* **1990**, *92*, 6271-6277.
[27] D. K. Cha and S. M. Park, *Polyethylene glycol as a solid polymer electrolyte*, **1997**, p. 249-253.
[28] D. W. Kim, J. S. Song and J. K. Park, *Electrochimica Acta* **1995**, *40*, 1697-1700.
[29] J. E. Mark, *Polymer Data Handbook*, Oxford University Press, United Kingdom, **1999**, p. 542.
[30] A. M. Stephan, *European Polymer Journal* **2006**, *42*, 21-42.

[31] R. W. Hart, H. S. White, B. Dunn and D. R. Rolison, *Electrochemistry Communications* **2003**, *5*, 120-123.
[32] L. Taberna, S. Mitra, P. Poizot, P. Simon and J. M. Tarascon, *Nature Materials* **2006**, *5*, 567-573.
[33] Y. Lei, B. Daffos, P. L. Taberna, P. Simon and F. Favier, *Electrochimica Acta* **2010**, *55*, 7454-7459.
[34] C. Lecoeur, J. M. Tarascon and C. Guery, *Electrochemical and Solid State Letters* **2011**, *14*, A6-A9.
[35] S. K. Cheah, E. Perre, M. Rooth, M. Fondell, A. Harsta, L. Nyholm, M. Boman, T. Gustafsson, J. Lu, P. Simon and K. Edstrom, *Nano Letters* **2009**, *9*, 3230-3233.
[36] M. M. Shaijumon, E. Perre, B. Daffos, P. L. Taberna, J. M. Tarascon and P. Simon, *Advanced Materials* **2010**, *22*, 4978-4981.
[37] H. Mazor, D. Golodnitsky, L. Burstein and E. Peled, *Electrochemical and Solid State Letters* **2009**, *12*, A232-A235.
[38] P. Johns, M. Roberts and J. Owen, *Journal of Materials Chemistry* **2011**, *21*, 10153-10159.
[39] E. Perre, P. L. Taberna, D. Mazouzi, P. Poizot, T. Gustafsson, K. Edstrom and P. Simon, *Journal of Materials Research* **2010**, *25*, 1485-1491.
[40] M. Nathan, D. Golodnitsky, V. Yufit, E. Strauss, T. Ripenbein, I. Shechtman, S. Menkin and E. Peled in *Recent advances in three dimensional thin film microbatteries*, *Vol. 835* Eds.: P. Knauth, C. Masquelier, E. Traversa and E. D. Wachsman), Materials Research Society, Warrendale, **2005**, pp. 367-372.
[41] D. Golodnitsky, M. Nathan, V. Yufit, E. Strauss, K. Freedman, L. Burstein, A. Gladkich and E. Peled, *Solid State Ionics* **2006**, *177*, 2811-2819.
[42] S. Tan, S. Walus, J. Hilborn, T. Gustafsson and D. Brandell, *Electrochemistry Communications* **2010**, *12*, 1498-1500.
[43] T. Ripenbein, D. Golodnitsky, M. Nathan and E. Peled, *Electrochimica Acta* **2010**, *56*, 37-41.
[44] B. L. Groenendaal, F. Jonas, D. Freitag, H. Pielartzik and J. R. Reynolds, *Advanced Materials* **2000**, *12*, 481-494.
[45] H. S. Nalwa, *Handbook of Organic Conductive Molecules and Polymers*
Wiley, Chichester, **1997**, p. 505-572.
[46] M. Dietrich, J. Heinze, G. Heywang and F. Jonas, *Journal of Electroanalytical Chemistry* **1994**, *369*, 87-92.
[47] Q. B. Pei, G. Zuccarello, M. Ahlskog and O. Inganas, *Polymer* **1994**, *35*, 1347-1351.
[48] C. Kvarnstrom, H. Neugebauer, S. Blomquist, H. J. Ahonen, J. Kankare and A. Ivaska, *Electrochimica Acta* **1999**, *44*, 2739-2750.
[49] S. S. Zhang, J. Hou, R. Zhang, J. K. Xu, G. M. Nie and S. Z. Pu, *European Polymer Journal* **2006**, *42*, 149-160.
[50] F. Jonas and J. T. Morrison, *Synthetic Metals* **1997**, *85*, 1397-1398.
[51] G. Heywang and F. Jonas, *Advanced Materials* **1992**, *4*, 116-118.
[52] A. M. White and R. C. T. Slade, *Electrochimica Acta* **2004**, *49*, 861-865.
[53] V. Noel, H. Randriamahazaka and C. Chevrot, *Journal of Electroanalytical Chemistry* **2003**, *558*, 41-48.
[54] M. C. Morvant and J. R. Reynolds, *Synthetic Metals* **1998**, *92*, 57-61.
[55] H. Randriamahazaka, V. Noel and C. Chevrot, *Journal of Electroanalytical Chemistry* **1999**, *472*, 103-111.
[56] L. Pigani, A. Heras, A. Colina, R. Seeber and J. Lopez-Palacios, *Electrochemistry Communications* **2004**, *6*, 1192-1198.

[57] M. G. Minett in *New composite insertion electrode materials for secondary lithium cells*, *Vol. PhD* University of Salford, **1989**, p. 22.
[58] B. F. Cvetko, M. P. Brungs, R. P. Burford and M. Skyllaskazacos, *Journal of Applied Electrochemistry* **1987**, *17*, 1198-1202.
[59] F. Beck, P. Braun and M. Oberst, *Berichte Der Bunsen-Gesellschaft-Physical Chemistry Chemical Physics* **1987**, *91*, 967-974.
[60] M. Lapkowski and A. Pron, *Synthetic Metals* **2000**, *110*, 79-83.
[61] A. Zykwinska, W. Domagala, B. Pilawa and A. Lapkowski, *Electrochimica Acta* **2005**, *50*, 1625-1633.
[62] X. Du and Z. Wang, *Electrochimica Acta* **2003**, *48*, 1713-1717.
[63] I. Fernandez, M. Trueba, C. A. Nunez and J. Rieumont, *Surface & Coatings Technology* **2005**, *191*, 134-139.
[64] Y. J. Yuan, S. B. Adeloju and G. G. Wallace, *European Polymer Journal* **1999**, *35*, 1761-1772.
[65] M. A. Ghanem, P. N. Bartlett, P. de Groot and A. Zhukov, *Electrochemistry Communications* **2004**, *6*, 447-453.
[66] P. Novak, B. Rasch and W. Vielstich, *Journal of the Electrochemical Society* **1991**, *138*, 3300-3304.
[67] R. Ansari, *E-Journal of chemistry* **2006**, *3*, 186-201.
[68] Y. F. Li, *Electrochimica Acta* **1997**, *42*, 203-210.

Chapter 2

Physical Characterisation Techniques

2.1 Introduction

In this work several techniques were used to determine deposition and characterise of the polymers. These include electropolymerisation techniques for preparing PEDOT and PP2O3 films. An electrochemical quartz crystal microbalance was used for measuring the mass change during electrochemical experiments. Electrochemical impedance spectroscopy (EIS) was used for determining polymer conductivities. The polymers were used as electrolytes in a battery and tested using galvanostatic cycling. All techniques will be explained briefly in this chapter.

2.2 Electropolymerisation Techniques

Chronoamperometry and Cyclic voltammetry are the most commonly used electrochemical techniques to prepare films of PEDOT and PP2O3 in this work. The cell composed of working, reference and counter electrodes as shown in Figure 2.1.

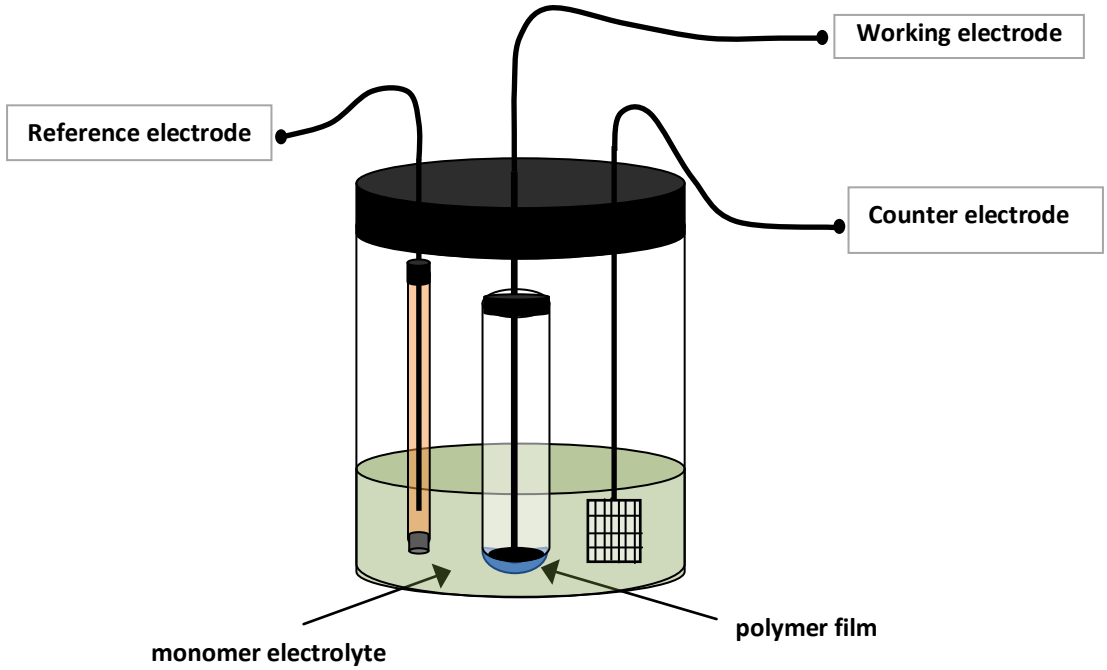

Figure 2.1 The cell construction for electropolymerisation of PEDOT and PP2O3 film.

Various monomer electrolytes both non aqueous and aqueous solutions were used. In the case of non aqueous solutions a Ag/10 mM $AgNO_3$ reference electrode was used in combination with a Pt gauze counter electrode and several different working electrodes. In the case of the aqueous solution an SCE reference electrode was used. The cell was connected to a potentiostat.

2.2.1 Chronoamperometry

Chronoamperometry is a technique where the current response to an applied potential step is measured as a function of time.

A constant potential for monomer oxidation (E_p) was applied to the working electrode in the setup described in Figure 2.1. The current-time response reflects the amount of charge used to calculate electrodeposited polymer on the substrate from the monomer oxidation (Q_p). By controlling the deposition charge the film thickness could be controlled. An example of the plots of applied potential *vs.* time and the current-time response can be seen from Figure 2.2.

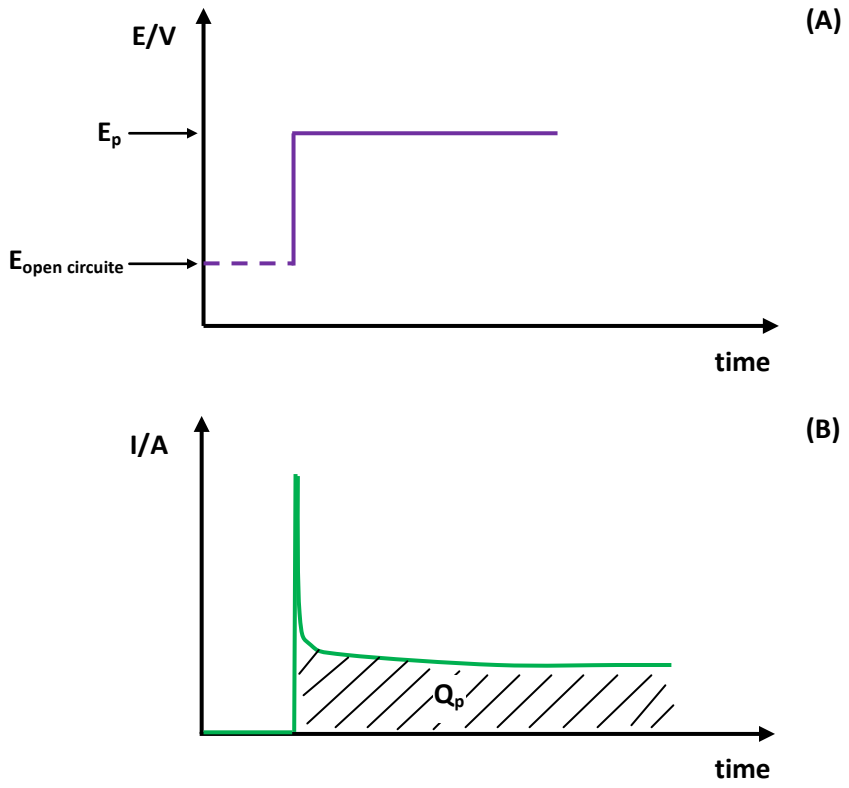

Figure 2.2 Chronoamperometry technique for electropolymerisation of PEDOT and PP2O3 film (A) the plots of applied potential *vs.* time and (B) the current-time response.

2.2.2 Cyclic Voltammetry

Cyclic voltammetry is the most widely used technique to investigate electrochemical reactions. This technique scans the potential of the working electrode linearly using a triangular potential waveform. The current response is then measured as a function of the applied potential[1].

In this work cyclic voltammetry was used to prepare the polymer films and also study the electrochemical film behavior. The potential of the cell was increased linearly in the potential range of doping/dedoping behavior (E_d) and polymerisation (E_p) of the polymer. An example CV of the electropolymerisation is shown in Figure 2.3.

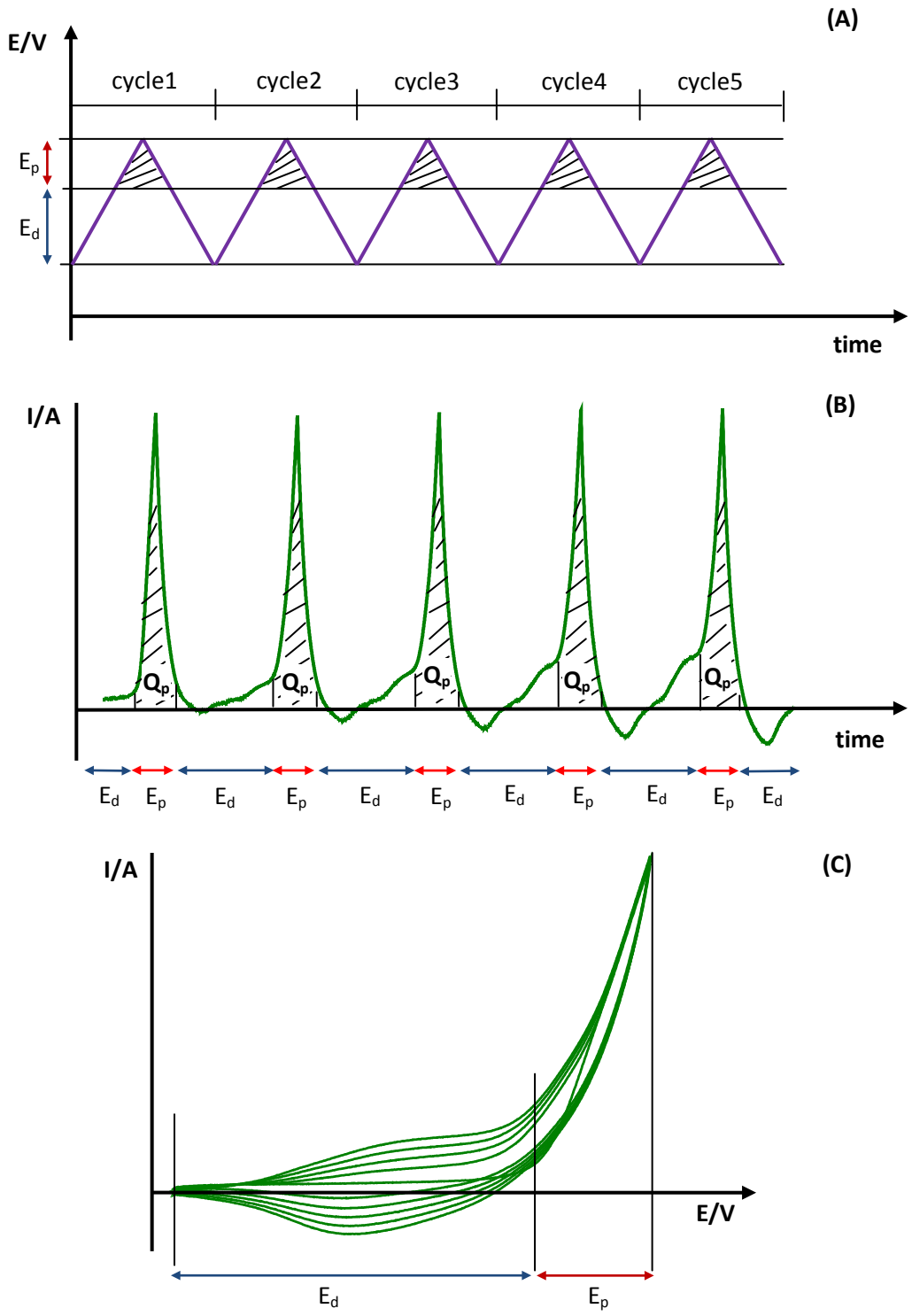

Figure 2.3 Cyclic voltammogram technique for electropolymerisation of PEDOT and PP2O3 film (A) applied potential, (B) respond current and (C) respond voltammograms.

The linear potential scan with a triangular waveform is show in Figure 2.3 (A). E_d is the doping/dedoping potential due to electrochemical activity of the polymer and E_p is the polymerisation potential. The current-time response is plotted as shown in Figure 2.3(B). In the doping/dedoping potential range the current-time reflects doping/dedoping behavior of conductive polymer whereas in the polymerisation potential range the response reflects the amount of charge due to electrodeposition of polymer on substrate (Q_p). In each cycle the polymerisation charge does not change, but the doping/dedoping charge increases due to deposition of more polymer. The film thickness can be controlled by cycle number. The typical cyclic voltammogram which is a plot of measuring the current during the potential scan can be seen from Figure 2.3(C). The doping/dedoping peaks can be seen in the doping/dedoping potential (E_d) and a steep rise of current is observed from the polymerisation potential (E_p).

2.2.3 Thickness calculation of PEDOT and PP2O3 films

The polymerisation charges were used to estimate the film thickness.

Faraday'Law[2] can be used to calculate the total charge passed between two electrodes *during the electrolysis* of the monomer to produce the polymer as follows,

$$Q = it = nmF$$

Equation 2.1

where Q is charge (C), i is current (A), t is time (s), n is number of electrons exchanged per mole of monomer in the redox reaction (n = 2 and 4 for polymerisation of EDOT and P2O3 respectively), m is number of moles deposited and F is Faraday constant (96485).

The moles of polymer can then be replaced by the polymer weight divided by the molecular weight of the monomer as shown in Equation 2.2.

$$Q = \frac{npF}{M}$$

Equation 2.2

where p is polymer weight (g) and M is molecular weight of monomer (142 for EDOT and 292 for P2O3)

The thickness then can be estimated from the charge according to Equation 2.3.

$$t_f = \frac{QM}{n\rho AF}$$

Equation 2.3

where ρ is density of polymer (1.46 g/cm^3 for PEDOT[3] and 1.50 g/cm^3 for PP2O3 [4]), A is area of working electrode (cm^2) and t_f is film thickness (cm).

In the above cases the value of n = 2 and 4 for PEDOT and PP2O3 assumes that:

- All the oxidised monomer is deposited on the electrode i.e. there is no oligomer that is dissolved into the solution.
- The measured charge does not include any side reactions, e.g. solvent decomposition.

Therefore application of Equation 2.3 to the polymerisation charge can *overestimate* the thickness.

The density of 1.46 and 1.50 g/cm^3 for PEDOT and PP2O3 assumes that:

- The polymers are not swollen by solvation of electrolyte.

Therefore the calculated polymerisation charge will *underestimate* the thickness.

In practice, both oligomer formation and side reactions occur. In this case the thickness estimate must involve a faradic efficiency factor, ε such that

$$t_f = \frac{\varepsilon Q M}{z \rho A F}$$

Equation 2.4

2.3 Electrochemical Quartz Crystal Microbalance

In the past decade the use of electrochemical quartz crystal microbalances (EQCM) has emerged as a powerful technique. It is able to detect small mass changes that accompany electrochemical process at electrode surfaces such as adsorption of species, multilayer deposition and dissolution and formation of polymer films. It is a simple and cost-effective technique that can give very useful information for the study of processes at electrode surface[5].

The EQCM equipment mainly comprises of a quartz crystal (typically pre coated in Au) used as an electrode for an electrochemical reaction. The resonance of the crystal is then monitored as a function of time. This resonance changes as a function of the mass deposited on the electrode. Standard electrochemical equipment is then used to effect electrochemical reactions on the quartz crystal substrate.

A quartz crystal microbalance consists of a thin quartz disk coated with a metallic film on both faces as can be seen from Figure 2.4 [6]. Quartz crystals coated with films of Au, Al, Ag, Co, Cr, Cu, Fe, Ni, Pt or Zn is produced commercially.

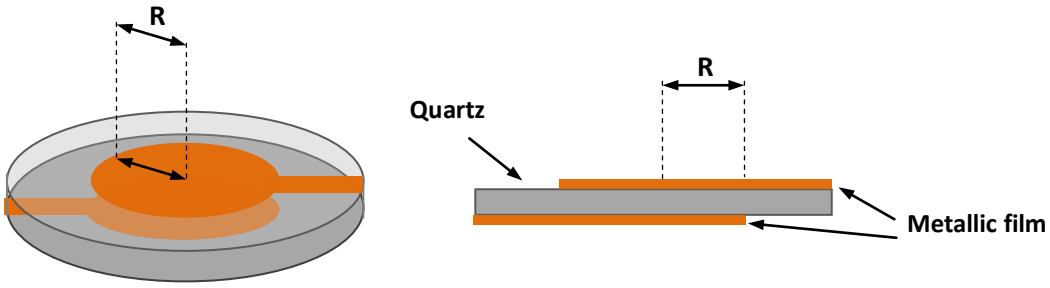

Figure 2.4 A typical quartz crystal resonator used for mass measurement: the left is top view and the right is cross section, R is the radius of the circular active electrode.

One face is exposed to the solution in the electrochemical cell, while the other is exposed to the frequency sensor. The face exposed to the solution serves as the working electrode of the electrochemical cell, and thus the electrochemical perturbation of this electrode can be

used to simultaneously measure the electrochemical response and change in frequency or mass at the electrode surface [7]. The relation between the frequency change and mass is well established by Sauerbrey[8] as shown in the Equation 2.5.

$$\Delta f = \frac{-2f_0^2}{A\sqrt{\rho_q \mu_q}} \Delta m$$

Equation 2.5

where f_o is in the natural frequency of the quartz (5 MHz), ρ_q is the quartz density (2.649 g cm^{-3}), and μ_q is the shear modulus (2.947×10^{11} g s^{-2} cm^{-1})
Therefore,

$$\Delta f = -C * \Delta m$$

Equation 2.6

where C = 56.6 Hz $\mu g^{-1} cm^2$

For a quartz crystal with a typical resonance frequency of 5 MHz, EQCM has a theoretical sensitivity of 56.6 Hz $\mu g^{-1} cm^2$ as can be seen from Equation 2.6. It can typically be operated with a noise level of < 1 Hz; under these conditions the minimum detectable mass is approximately 10 ng cm^{-2}[9]. Higher sensitivities can be achieved by using quartz crystals that operate with natural frequencies greater than 5 MHz, where the sensitivities increases with the square of the natural frequency, f_0^2.

In electrochemistry experiments, commonly used format for the analysis of EQCM data are plots of mass change and their corresponding voltammograms *vs.* E. From this plot it is possible to observe more electrode surface behavior such as differentiation between mass change due to Faradic and non Faradic processes (e.g. adsorption of species from solution).
In this work EQCM was used for an overoxidation treatment of PP2O3 to measure the mass change of the sample due to overoxidation behavior of PP2O3 (assuming PP2O3 film is rigid, no significant effects of viscoelastic property on frequency change). The film was electrodeposited on quartz crystal resonator and then it was cycled in an electrolyte solution at an overoxidation potential range. The experimental detail will be explained in Chapter 4.

2.4 Impedance

In the early 20th century impedance spectroscopy was initially discovered as a novel technique for measuring the electrical properties of materials.[10]

The principle of AC impedance with potentiostatic control is that a small sinusoidal voltage is applied to the cell. This voltage amplitude should be sufficiently small to yield a linear current-potential relationship.

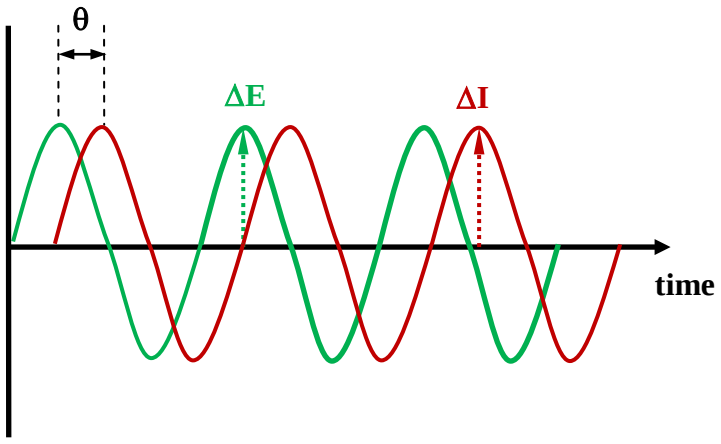

Figure 2.5 Sinusoidal voltage and phase-shifted current[11].

A typical single frequency behavior is shown in Figure 2.5. This I-E relationship is recorded at various frequencies.

The sinusoidal signals of the perturbation and cell response can be defined as by Equation 2.7 and 2.8.

$$E = \Delta E \sin \omega t$$

Equation 2.7

where E is the perturbation value, $\boldsymbol{\Delta E}$ is the amplitude of perturbation and ω is the angular frequency ($2\pi f$) and f is the frequency of the perturbation (Hz).

$$I = \Delta I \sin(\omega t + \theta)$$

Equation 2.8

where I is the response value, $\boldsymbol{\Delta I}$ is the amplitude of response and ω is the angular frequency ($2\pi f$), f is the frequency of the perturbation (Hz). θ is the phase different between response and perturbation.

Using Equation 2.7 and 2.8, an impedance, Z, can be defined analogously to the resistance of the DC measurement. The magnitude of the impedance is defined according to Equation 2.9.

$$|Z| = \frac{|\Delta E|}{|\Delta I|} = |Z(\omega)| = \frac{|\Delta E(\omega)|}{|\Delta I(\omega)|}$$

Equation 2.9

The impedance response of the sample can be defined as a vector quantity, because it has both magnitude and phase. A representation of such a vector diagram can be seen in Figure 2.6 which is commonly referred to as a complex plane or Nyquist plot.

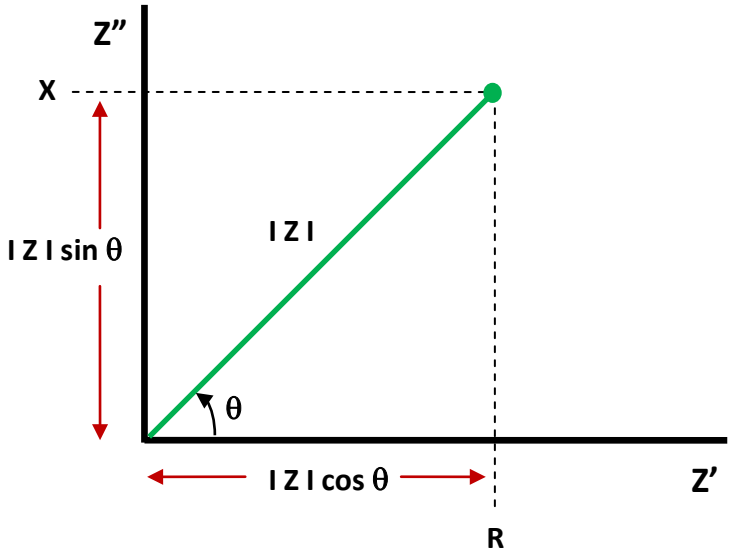

Figure 2.6 The impedance Z plotted as a planar vector using rectangular and polar coordinates.

The real part of the impedance, Z', may be defined as the resistance, R, where there is no phase shift between the current and the voltage. The imaginary part of the impedance can be defined as the reactance, X, which induces a phase shift -π/2 between the voltage and current. The complex impedance of a sample, Z^*, is therefore the sum of both the real and imaginary parts with the complex number operator, j, which has the value of √-1 according to Equation 2.10.

$$Z^* = Z' + jZ''$$

Equation 2.10

To determine the impedance of a sample, circuit models based on equivalent physical components are used. Resistors (R), capacitors (C) and constant phase element (CPE) are commonly used. An example of resistors and capacitors appear in the Nyquist plots in Figure 2.7 and Figure 2.8.

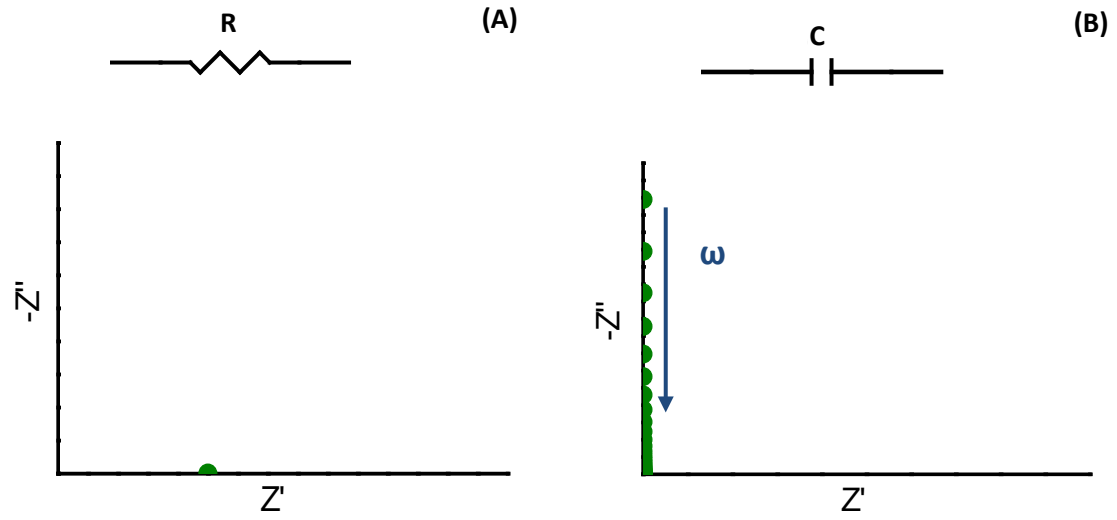

Figure 2.7 Representation of a resistor, R (A) and a capacitor, C (B) in a Nyquist plot.

The impedance of a resistor where there is no phase shift between the current and the voltage is therefore independent of frequency. Only a single value of the resistance appears on the real axis for all applied frequencies as can be seen from Figure 2.7 (A). The magnitude of the impedance is given by Equation 2.11

$$Z_R^* = R$$

Equation 2.11

For a capacitor, C, the impedance is purely reactive. The voltage leads the current by 90^O. A series of points appears on the imaginary axis with the high frequency points being nearest the origin as shown in Figure 2.7 (B). The magnitude of the impedance is frequency dependent, and is defined by Equation 2.12

$$Z_C^* = -\frac{j}{\omega C}$$

Equation 2.12

Also an example of resistors and capacitors in both series and parallel can be seen from Figure 2.8.

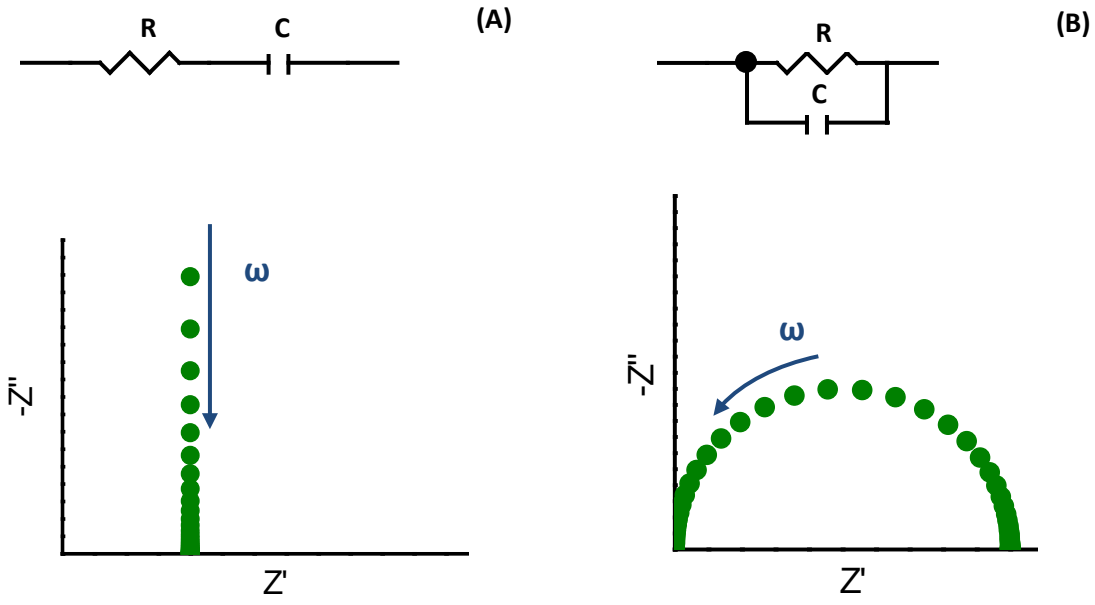

Figure 2.8 Representation of a resistor and a capacitor in series (A) and a resistor and a capacitor in parallel (B) in a Nyquist plot.

The impedance of a resistor and capacitor in series can be seen in Figure 2.8 (A). The vertical spur of the capacitive component is shifted away from the origin by the value of the resistance. The complex impedance for a series combination of a resistor and capacitor is defined by Equation 2.13

$$Z^*_{total} = R - \frac{j}{\omega C}$$

Equation 2.13

When a resistor and capacitor is in parallel a semi-circle is visible as can be seen from Figure 2.8 (B). The high frequency points are seen to intercept the real axis at the origin, while the low frequency points intercept the real axis at the value of the resistor. The complex impedance of such a parallel combination can be defined by Equation 2.14

$$Z^*_{total} = \frac{1}{\left(\frac{1}{R} + j\omega C\right)}$$

Equation 2.14

An electrochemical reaction is usually represented by the Randles equivalent circuit depicted in Figure 2.9 (A). This represents the series resistance of the electrolyte and a charge transfer resistance, R_{ct} to represent the electrode kinetics in terms of the linear I/E part of the Tafel expression. A parallel capacitance C_{dl} represents the double layer and a new component, the Warburg impedance, Z_w is used to represent reactant and product diffusion through a Warburg coefficient, σ and the impedance expression of Equation 2.15.

$$Z_w = \sigma\omega^{-1/2} - j\sigma\omega^{-1/2}$$

Equation 2.15

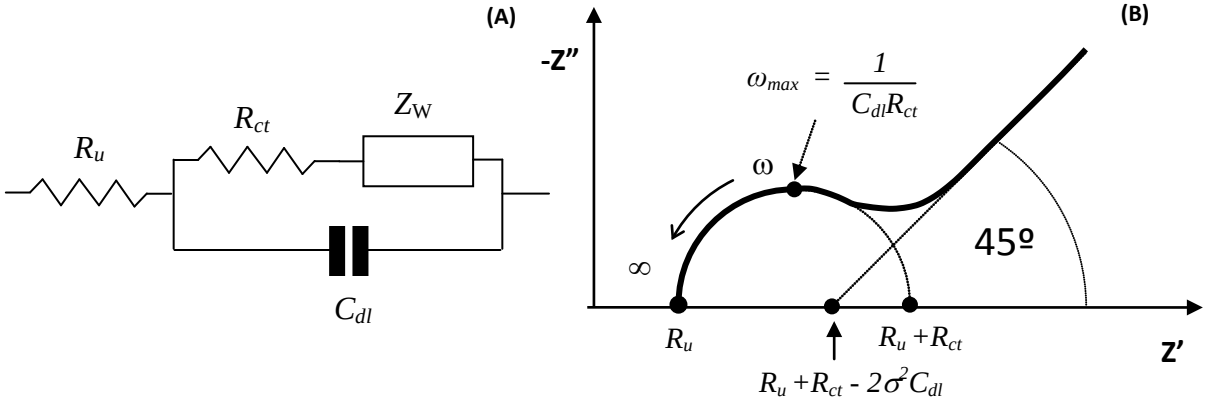

Figure 2.9 (A) The Randles circuit, used to represent an electrochemical reaction with both kinetic and mass transfer control and (B) A simulated Nyquist plot.

Another equivalent circuit is given in Figure 2.10 to give further insight into the meaning of the Warburg impedance. This represents the same combination of series resistance, charge transfer resistance, double layer capacitance and the coupled diffusion of ions and electrons as a transmission line. The transmission line expresses diffusion as a combination of a

distributed ionic resistance, R_i, due to the electrolyte paths within the electrode, and a distributed charge storage capacitance, C_s. Further analysis will be presented in Chapter 5.

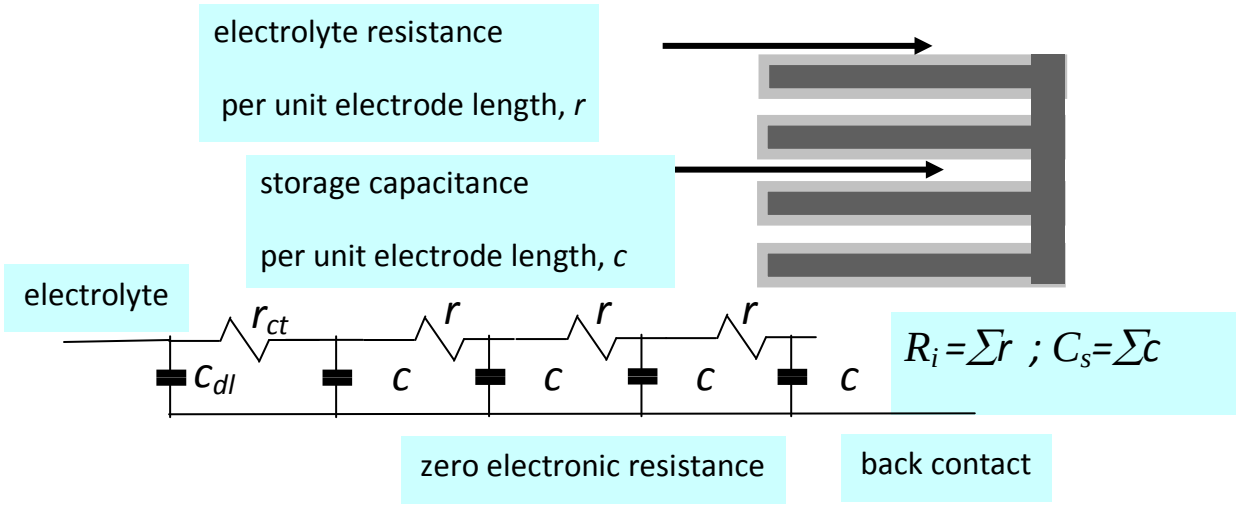

Figure 2.10 A transmission line representation of the Randles Circuit.

2.5 Battery Tests

2.5.1 Self-discharge test

Self-discharge measurement is one of the most important battery tests. A battery at full or partial initial state of charge will naturally lose its charge capacity when kept for a period of time. This phenomenon is referred to as battery self-discharge, in which the kinetics will vary depending on the battery chemistry, electrode composition and design, electrolyte formulation and impurities, and the storage temperature[12]. An example of major factors contributed to the battery self-discharge is listed as follows.

- Internal electron leakage coming from the electrolyte partial electronic conductivity, or other internal shorts.
- External electron leakage resulting from the poor isolating properties of the battery seals or gasket.
- Electrode/electrolyte reaction such as anode corrosion or cathode reduction by the electrolyte or impurities.
- Partial dissolution of the electrodes active material.
- Electrode passivation by decomposition products.

In this work a sample cell was fabricated and then charged. The open circuit potential was then measured a function of time. The self-discharge behavior could be explained by a simply equivalent circuit as shown in Figure 2.11.

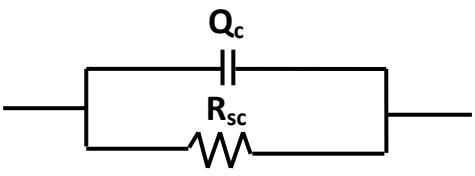

Figure 2.11 The equivalent circuit of a cell for self-discharge test

$$Q_c = \int_0^t I_{sc} dt$$

Equation 2.16

where Q_c, is charge capacity (C), I_{sc} is short circuit current (A) and t is time (s).

The charge capacity is obtained from initial charge capacity before self discharge measurement. The short circuit current is then expressed by Equation 2.17.

At a self-discharge potential

$$I_{sc} = \frac{E(t)}{R_{sc}}$$

Equation 2.17

where R_{sc} is short circuit resistance (Ω), E is discharge potential (V) (potential of delithation of lithium from anode material i.e. $Li_xTi_5O_{12}$ anode occurs at about 1.85V *vs.* $LiFePO_4$)

Therefore

$$R_{sc} = \frac{1}{Q_c} \int_0^t E(t) dt$$

Equation 2.18

At a self-discharge potential short circuit resistances of the sample cell would be determine according to Equation 2.18.

In this work, the chemically prepared samples, untreated and treated, would be prepared as an electrolyte. The self-discharge test was used to determine the internal electron leakage resulting from the partial electronic conductivities of the polymer. The experimental details would be explained in Chapter 6.

2.5.2 Galvanostatic test

Galvanostatic testing is an electrochemical measuring mode for electrochemical analysis or for the determination of the kinetics and mechanism of electrode reactions and also related to ion transportation along the electrolyte based on the control of the current flowing through the system. A constant current was applied to the cells within an appropriate potential range depending on electrode active materials. An operating diagram of a galvanostat is shown in Figure 2.12.

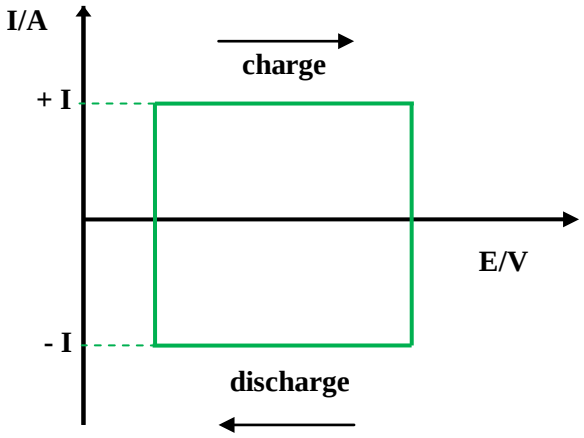

Figure 2.12 Operating diagram of galvanostat.

From galvanostatic testing specific capacity could be determined. Also there are a number of other important battery parameters which could be investigated as listed below.

Cyclability

Cyclability refers to how well a battery can maintain its capacity during cycling. This is observed by plotting a graph of specific capacity *vs.* cycle number and qualitatively observing the performance. Also its percentage capacity retention per cycle can be determined by Equation 2.19[13].

$$\%CRP = 100 - \frac{100(Q_{SI} - Q_{SF})}{(Q_{SI} \times C)}$$

Equation 2.19

where $\%CRP$ is percentage capacity retention per cycle, Q_{SI} is initial specific capacity (mA h g^{-1}), Q_{SF} is final specific capacity (mA h g^{-1}) and C is number of cycles.

Rate

C-rate

C-rate is a term which refers to how fast or slow a battery is charged or discharged, based on the theoretical capacity of limited active material in a battery. The capacity of the active material under test is calculated as in Equation 2.20

$$\boldsymbol{Q_p = m_p \times Q_T}$$

Equation 2.20

where Q_p is capacity of active material pellet (A h), Q_T is theoretical capacity of a material (A h g^{-1}) and m_p is mass of active material pellet (g).

From this value the C-rate can be calculated using Equation 2.21

$$f = \frac{I}{Q_P}$$

Equation 2.21

where f is C-rate and I is current (A).

This is a rate which is the inverse of the time it takes to discharge the battery. For instance, a C-rate of 0.2 (1/5) means that the full capacity of active material pellet will be completely discharged in 5 h.

Rate capability

Rate capability is determined by how well a material retains its specific capacity at various rates of discharge. This is reported by plotting graphs of specific capacity *vs.* C-rate or current.

In this work sample cells will be fabricated. The cells were tested to determine their specific capacities and cyclability. The specific capacity and cyclability of sample cells would be related to ability of electrode reaction to store charge and also the electrolyte resistance to prevent electrodes from giving up storage charge between each other. The experimental detail is explained in Chapter 6.

2.6 Chapter 2 References

[1] P. T. Kissinger, *Journal of Chemical Education* **1983**, *60*, 702-706.
[2] P. Atkins, *Physical Chemistry: Equilibrium electrochemistry: ions and electrode*, Oxford University, Great Britain **1978**, p. 329.
[3] D. M. DeLongchamp, B. D. Vogt, C. M. Brooks, K. Kano, J. Obrzut, C. A. Richter, O. A. Kirillov and E. K. Lin, *Langmuir* **2005**, *21*, 11480-11483.
[4] J. Tietje-Girault, C. Ponce de Leon and F. C. Walsh, *Surface & Coatings Technology* **2007**, *201*, 6025-6034.
[5] G. Trejo, Y. Meas, R. Ortega and E. Bahena, *New Develpoment in Electrochemistry Research* Nova Science, **2005**, p. 86-111.
[6] C. Gabrielli, M. Keddam and R. Torresi, *Journal of the Electrochemical Society* **1991**, *138*, 2657-2660.
[7] B. L. Wu, H. W. Lei and C. S. Cha, *Journal of Electroanalytical Chemistry* **1994**, *374*, 97-99.
[8] G. Sauerbrey, *Physics* **1959**, *155*, 206.
[9] M. D. Ward, *Physical Electrochemistry : Principles, Methodes and Applications*, Marcel Dekker, New York, **1995**, p. 293-338.
[10] J. R. Macdonald and E. Barsoukov, *Impedance Spectroscopy : Theory, Experiment, and Applications*
John Wiley & Sons, Canada, **2005**, p. 1.
[11] C. G. Zoski, *Handbook of Electrochemistry*, Elsevier, Netherlands, **2007**, p. 454.
[12] R. Yazami and Y. F. Reynier, *Electrochimica Acta* **2002**, *47*, 1217-1223.
[13] K. M. Shaju and P. G. Bruce, *Advanced Materials* **2006**, *18*, 2330-2334.

Chapter 3

Synthesis and Characterisation of Poly(ethylene dioxythiophene) (PEDOT)

3.1 Introduction

In this chapter initial experiments to deposit PEDOT films will be carried out. As stated in the introduction these films have well known electronic conductivity and good potential for ionic conductivity as a result of potential lithium coordination with the oxygen electron lone pairs. The deposition of the films will first be investigated before degradation of the electronic conductivity and characterisation of the effectiveness of this process.

3.2 Electropolymerisation of EDOT

The method of **e**lectropolymerisation of EDOT has important effects on the properties of the PEDOT films. The many important factors include solubility of EDOT in the electrolyte systems, polymerisation potential, electrolyte, working electrode (substrate) and the electropolymerisation method applied[1].

3.2.1 Initial Studies

EDOT has a low solubility in water. Many studies on the electropolymerisation of EDOT have been carried out from organic electrolytes[2-5], however, several examples exist of depositions from aqueous solution[6-8]. This research seeks to compare the differences between electropolymerisation of EDOT in non aqueous and aqueous systems.

3.2.1.1 Chemicals, Materials and Equipment

EDOT, Lithium bis(trifluoromethane) sulfonamide salt (LiTFSI), Tetraethylammonium tetra-fluoroborate ($TEABF_4$), Sodium dodecylbenzenesulfate (SDS) and Sodium p- toluene sulfonate (TSNa) were received from Sigma Aldrich and acetonitrile (ACN) was obtained from Fisher. Aqueous solutions were prepared with de-ionized water (DI) from a Whatman Still and RO 50 water purification system. Two different non aqueous electrolyte solutions were prepared: 10 mM EDOT containing 50 mM LiTFSI (LiTFSI elecrtrolyte) in ACN and 10mM EDOT containing 50 mM $TEABF_4$ ($TEABF_4$ elecrtrolyte) in ACN. Two different

aqueous solutions were also prepared 10 mM EDOT containing 50 mM SDS (SDS electrolyte) in DI water and the second a 10 mM EDOT containing 10 mM TSNa (TSNa electrolyte) and 5% of isopropanol in DI.

For both aqueous and non aqueous deposition a standard three electrode setup was used. A glassy carbon sealed in glass was used as working electrode (radius : 0.15 cm and surface area : 0.07 cm^2). Pt gauze counter electrode and SCE (saturated calomel electrode) reference electrode for aqueous solution and Ag/10 mM $AgNO_3$ reference electrode for nonaqueous solution were used. The cell was connected to a potentiostat (VMP2 from Bio Logic instruments).

3.2.1.2 Non aqueous electrolyte solution

The effect of the two different supporting electrolytes in non aqueous solution on the electropolymerisation efficiency and quality of polymer films will be investigated. The cyclic voltammogram recorded for the deposition of PEDOT in a LiTFSI electrolyte is shown in Figure 3.1.

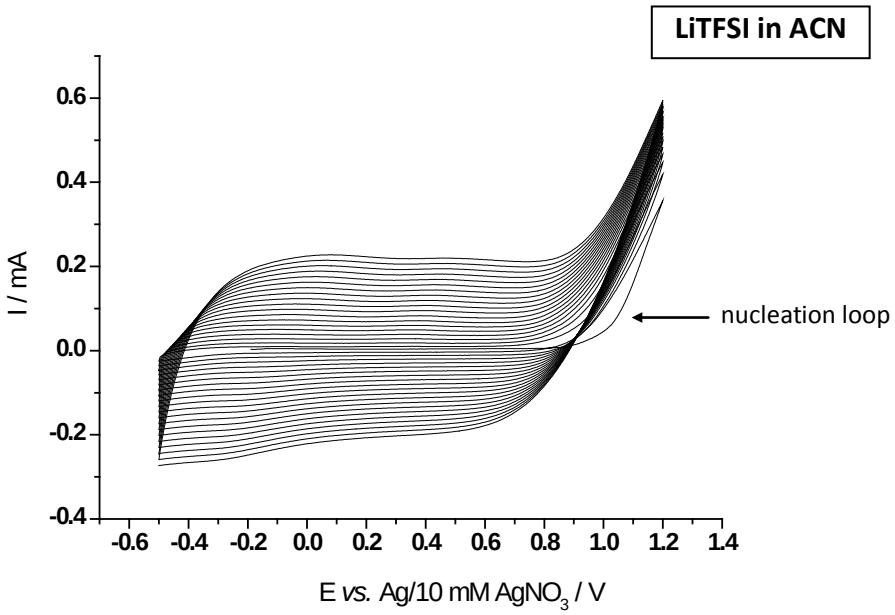

Figure 3.1 Cyclic voltammograms for the deposition of PEDOT film recorded between -0.5 and +1.2 V at 100 mV/s. The PEDOT film, which was electrosynthesised in ACN containing 10 mM EDOT and 50 mM LiTFSI was deposited on 0.07 cm^2 of a glassy carbon electrode.

The voltammograms shown in Figure 3.1 for the deposition of PEDOT from LiTFSI electrolyte showed an increase of current from cycle to cycle. The first scan showed a large characteristic nucleation loop[9] at 0.9 V *vs.* Ag/Ag^+. This indicated the initiation of the nucleation process of the polymer film. After the first cycle a steep increase in current above 0.9 V *vs.* Ag/Ag^+ indicates a continuation of the polymerisation. The increasing current plateaus between 0.0 and 0.8 V *vs.* Ag/Ag^+ indicate the capacitance is increasing as a result of an increasing amount of the polymer. This indicates successive deposition of more polymer on each cycle. The total polymerisation charge was 0.468 C/cm^2 which corresponded to approximately 2.29 μm (based on the assumption of PEDOT density and method of calculation introduced in Chapter 2) of PEDOT film (summarised later in Table 3.1). The cyclic voltammogram recorded for the deposition of PEDOT in a $TEABF_4$ electrolyte is shown in Figure 3.2.

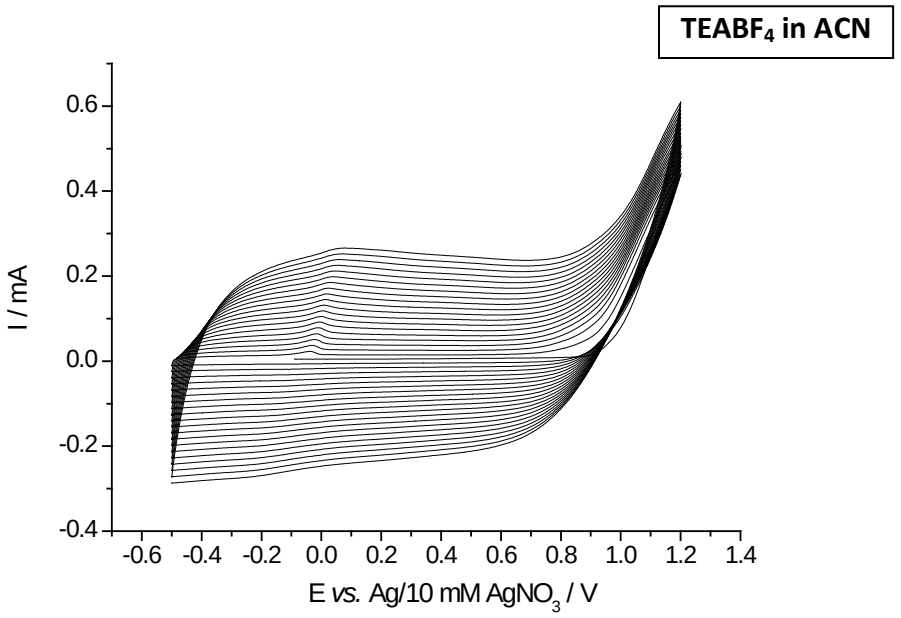

Figure 3.2 Cyclic voltammograms for the deposition of a PEDOT film recorded between -0.5 and +1.2 V at 100 mV/s. The PEDOT film, which was electrosynthesised in ACN containing 10 mM EDOT and 50 mM $TEABF_4$ was deposited on 0.07 cm^2 of a glassy carbon electrode.

The voltammograms in Figure 3.2 of the PEDOT deposition from $TEABF_4$ electrolyte were quite similar to those recorded from the preparation in LiTFSI electrolyte. On the first cycle there was a smaller nucleation loop[9] above 0.9 V which was the initiation of the nucleation process of the polymer film. The voltammograms again showed an increase of current from cycle to cycle. The total polymerisation charge was 0.459 C/cm^2, and the film thickness was calculated as before to correspond to 2.25 μm (shown in Table 3.1). The PEDOT films from both supporting electrolytes had similar thicknesses according to the thickness calculation. This indicated that a successive polymerisation process in the nonaqueous systems was taking place due to the good solubility of EDOT in ACN and the low oxidation potential of EDOT in the systems.

3.2.1.3 Aqueous electrolyte solution

The deposition of PEDOT from aqueous solutions was also investigated. This approach has several advantages; using water allows for easier processing. Although EDOT has a very low solubility in water, there are several possible ways to increase this; by adding surfactant molecules and low amounts of polar organic solvent. Two experiments were performed SDS electrolyte and TSNa to investigate the effect of surfactant and polar organic solvent on electropolymerisation efficiency and quality of the polymer films. The cyclic voltammogram recorded for the deposition of PEDOT in an SDS electrolyte is shown in Figure 3.3.

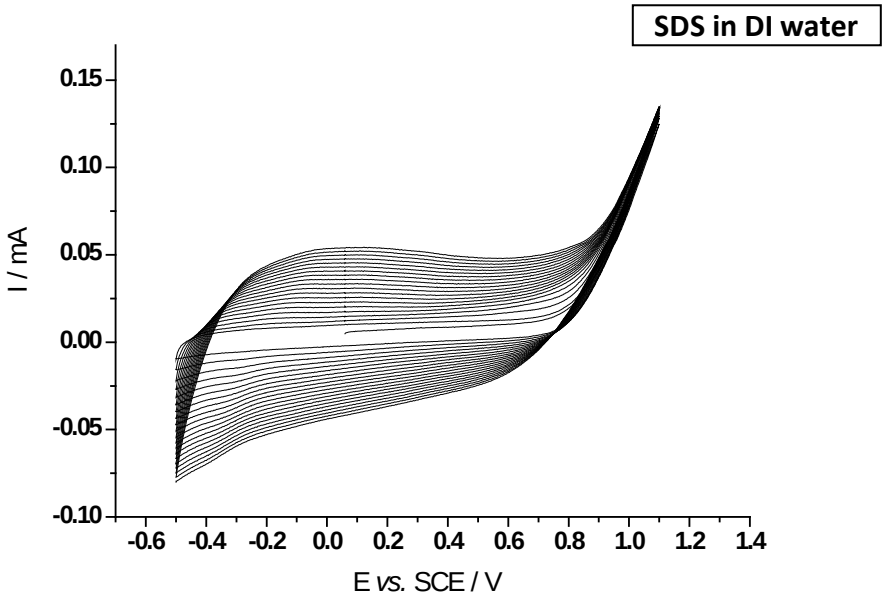

Figure 3.3 Cyclic voltammograms for the deposition of a PEDOT film recorded between -0.5 and +1.1 V at 100 mV/s. The PEDOT film, which was electrosynthesised in aqueous solution containing 10 mM EDOT and 10 mM SDS was deposited on 0.07 cm^2 of a glassy carbon electrode.

The current response in the cyclic voltammograms shown in Figure 3.3 increased from cycle to cycle. Again during the first cycle there was a very small nucleation loop compared with those from nonaqueous solution. There was a steep increase of current above 0.8 V *vs.* SCE indicating polymerisation and an increase of plateau current between -0.2 and 0.6 V *vs.* SCE due to increased capacitance of a result of an increased amount of PEDOT. Finally

the polymerisation charge was 0.115 C/cm^2 which was corresponded to a 0.564 μm PEDOT film (based on the previous stated assumptions) (summarised in Table 3.1). The reduced deposition charge and therefore lower thickness compared with the nonaqueous electrolyte system.

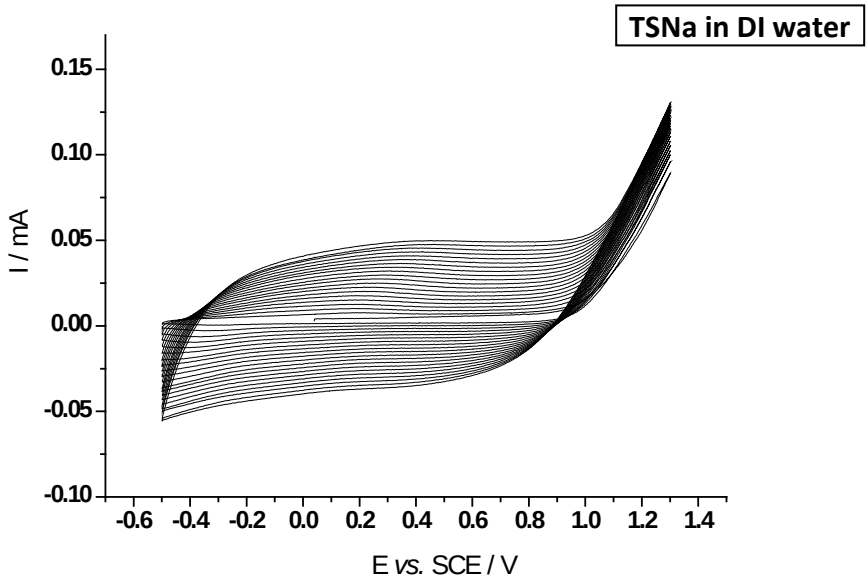

Figure 3.4 Cyclic voltammograms for the deposition of a PEDOT film recorded between -0.5 and +1.3 V at 100 mV/s. The PEDOT film, which was electrosynthesised in aqueous solution containing 10 mM EDOT, 10 mM TSNa and 5% of isopropanol was deposited on 0.07 cm^2 of a glassy carbon electrode.

The voltammograms of EDOT from TSNa were quite similar to the one from SDS. The onset of polymerisation potential however was slightly higher 0.9 V *vs.* SCE than those of EDOT from SDS 0.8 V *vs.* SCE. This result reproduces the previous finding which concluded that SDS facilitated polymerisation of EDOT by lowering the oxidation potential[10]. The total polymerisation charge was 0.123 C/cm^2, which corresponds to an estimated film thickness of 0.603 μm as shown in Table 3.1. This thickness was quite close to that from the SDS system. Both films were quite thin when compared with the films from nonaqueous solution.

Table 3.1 PEDOT film thicknesses from polymerisation charge calculation with different electrolytes from aqueous and non aqueous solutions.

Polymerisation system	Polymerisation charge (C/cm^2)	Film thickness* (μm)
Non aqueous : PEDOT+ LiTFSI	0.468	2.293
Non aqueous : PEDOT+ $TEABF_4$	0.459	2.253
Aqueous : PEDOT+ SDS	0.115	0.564
Aqueous : PEDOT+ TSNa	0.123	0.603

* assuming number of e^- exchanged per mole of monomer = 2 and ρ = 1.46 g/cm^3

In summery PEDOT films with the different supporting electrolytes in non aqueous system had similar thicknesses. The two supporting electrolytes did not have a significant effect on polymerisation process. Similarly, both PEDOT films from aqueous system had similar thicknesses. However, PEDOT films from aqueous system were much thinner than those of PEDOT films from nonaqueous system. The PEDOT film prepared from aqueous solution was studied in more detail looking at the effect of deposition time on thickness and the effect of substrate; these results are included as Appendix 1 and 2 as supplementary information.

To investigate the deposition of PEDOT over a the type of 3D substrates required for the formation of a 3D battery layers were electrodeposited on 3D reticulated vitreous carbon substrates (RVC) with nonaqueous and aqueous electrolyte systems with different supporting electrolytes. The film surfaces were visualized by SEM (Philips XL 30 ESEM) as shown in Figure 3.5.

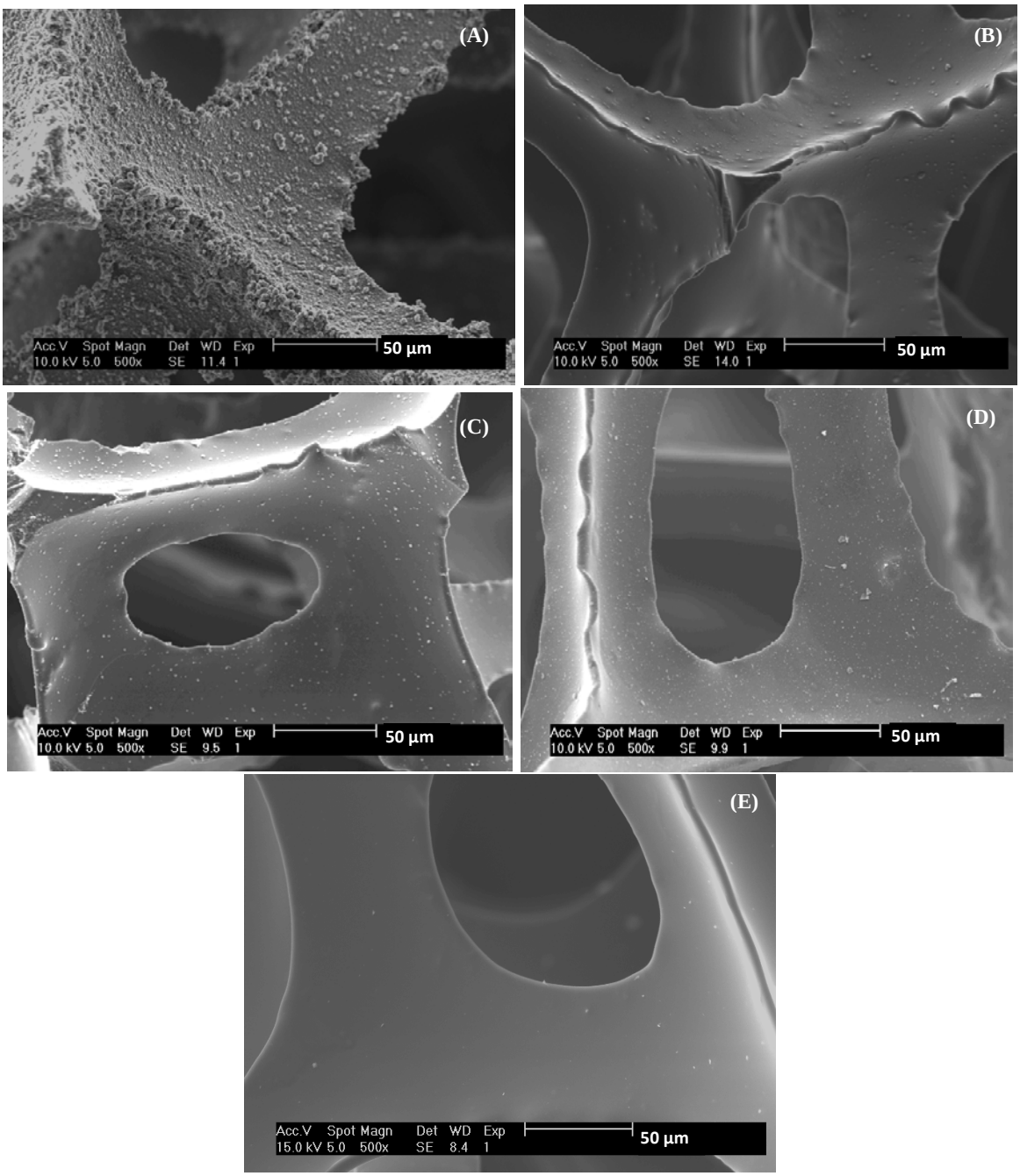

Figure 3.5 SEM images of electrodeposited PEDOT films on 3D RVC by chronoamperometry technique at 1.0 V *vs.* SCE for aqueous solution and 10 mM Ag/Ag^{+} for non aqueous solution for 10 minutes with different electrolytes (A) 10 mM EDOT containing 50 mM LiTFSI in ACN (B) 10 mM EDOT containing 50 mM $TEABF_4$ in ACN (C) 10 mM EDOT in a solution of 10 mM SDS, (D) 10 mM EDOT in a solution of 10 mM TSNa and 5% of isopropanol and (E) bare 3D RVC. The scale bar corresponds to 50 µm in all cases.

The SEM images in Figure 3.5 show that a film has been evenly deposited in all cases. The presence of the film can be seen as the rather smooth edges of the bare RVC appear bumpy. Another feature is small imperfections in the PEDOT films on all substrates these are seen as small particulate deposits on the surface. These deposits are most obvious in the case of the film with LiTFSI electrolyte (Figure (A)), here the uniform film was partly covered with small globules, probably due to dendritic growth of thick polymer islands.

These initial experiments have led to the following conclusions:

- PEDOT films could be grown successfully in all the electrolyte compositions
- Thick (>1 μm) PEDOT films could be grown much quicker in non aqueous electrolytes.
- When non aqueous electrolytes are much smoother films could be obtained when using a $TEABF_4$ supporting electrolyte.

The next section addresses the destruction of the electronic conductivity in the deposited PEDOT films. The non aqueous electrolyte will be selected for these experiments as this route allows thicker films to be easily prepared with a smooth morphology which provides more consistent conformal layers which are less likely to form pinholes which may create short circuits when a second electrode is filled into the 3D structure.

3.3 Electrochemical treatment

The following studies of electrochemical behavior of PEDOT were carried out in order to investigate a technique to destroy its electronic conductivity for films to be used in polymer electrolyte application. To complete a comprehensive study the effects of using both overoxidation[3, 11] and overreduction treatments on the polymer films was studied[12].

3.3.1 Chemicals, Materials and Equipment

EDOT was obtained from Sigma. $TEABF_4$ was received from Aldrich and ACN was obtained from Fisher.

Pt disc working electrode, Pt gauze counter electrode and Ag/10 mM $AgNO_3$ reference electrode were used. The cell was connected to a potentiostat (VMP2 from Bio Logic science instruments)

3.3.2 Overoxidation treatment

PEDOT was cycled in a monomer free electrolyte at an overoxidation potential (>0.9 V *vs.* Ag/Ag^+). This experiment was composed of four steps as follows.

1) Preparing the PEDOT film on the Pt working electrode by chronoamperometry at 0.95 V *vs.* Ag/ 10 mM $AgNO_3$ for 6 minutes (estimated film thickness : 2 µm)

2) Cycling PEDOT in a normal potential range of 0.9 to 1.2 V *vs.* Ag/10 mM $AgNO_3$ to observe redox behaviour of PEDOT

3) Cycling PEDOT at overoxidation potential window of 0.2 to1.9 V *vs.* Ag/10 mM $AgNO_3$ to destroy its electronic conductivity

4) Cycling PEDOT at the normal potential range again to observe changes in its redox behaviour after the treatment.

Figure 3.6, 3.7 and 3.8 shows the cyclic voltammetry recorded during the overoxidation treatment, the comparison of the before and after treatment and the background signal provided by a blank platinum substrate respectively.

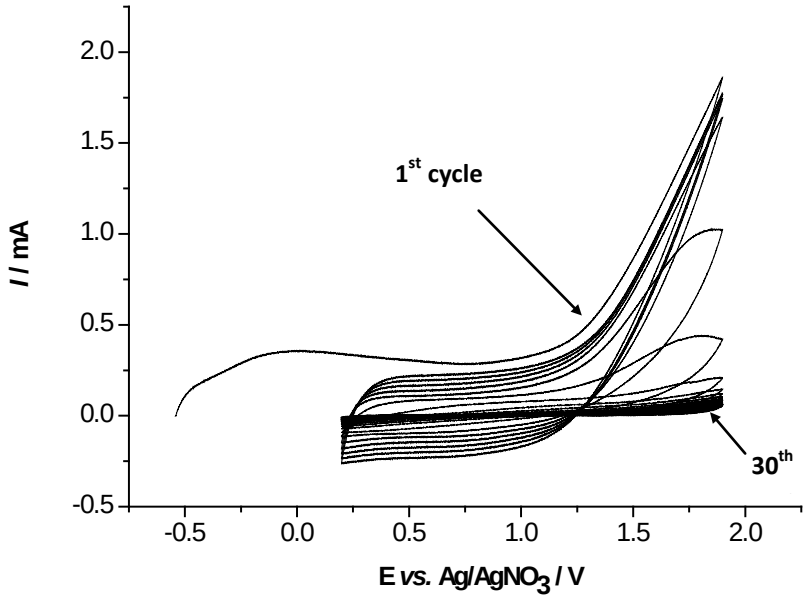

Figure 3.6 Cyclic voltammograms for cycling PEDOT film at the overoxidation potential range between +0.2 and +1.9 V in 50 mM $TEABF_4$ in ACN at 100 mV/s for 30 cycles

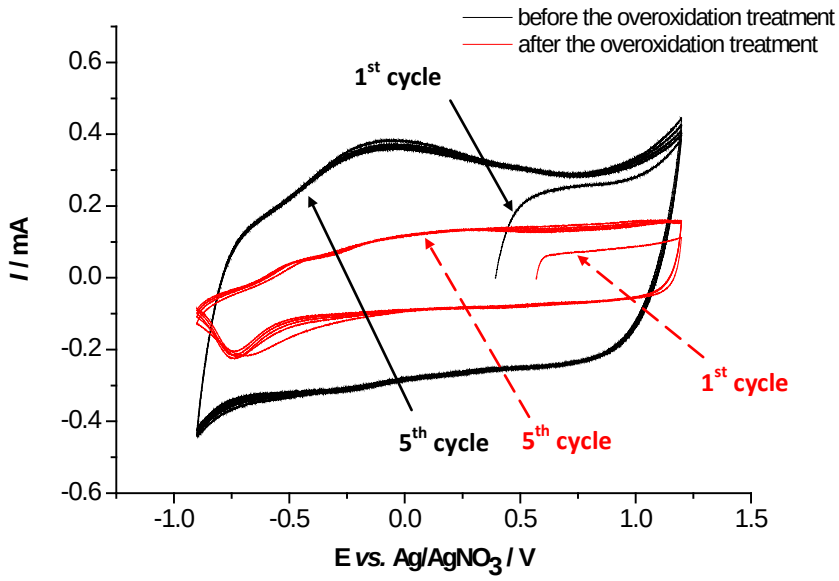

Figure 3.7 Cyclic voltammograms for cycling PEDOT film at the normal potential range between -0.9 and +1.2 V in 50 mM $TEABF_4$ in ACN at 100 mV/s for 5 cycles for a comparison between the CV before and after overoxidation treatment

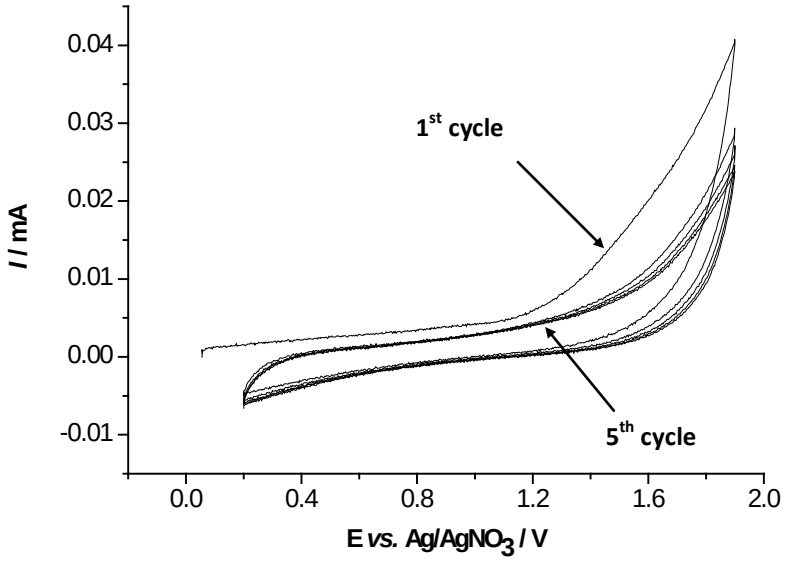

Figure 3.8 Cyclic voltammograms for cycling Pt disc in 50 mM $TEABF_4$ in ACN (blank)

The two micron film was cycled in 50 mM $TEABF_4$ in ACN in the range -0.9 to 1.2 V *vs.* Ag/Ag^+ (this is referred to as the normal potential range) as shown in Figure 3.7. The CV of the untreated film was very stable. It was then cycled in the overoxidation potential range between +0.2 and +1.9 V as shown in Figure 3.6. The steep current above +1.3 V decreased continuously over 30 cycles. The film was still present on electrode and the physical condition remained unchanged. During this experiment the film turned from dark to light blue. The film was cycled again at the normal potential range in order to compare redox behavior to the untreated film this is shown in Figure 3.7 (black line for the untreated film (before treatment) and red for the treated film (after treatment)). The CVs recorded for the treated film was still stable but when compared with the CV of the untreated sample the doping peak current at 0.0 V decreased. This result agrees well with the work of Zykwinska *et al.*[11]. They reported that the oxidation boundary of stability in PEDOT was found to be located around +1.6 V *vs.* Ag wire (1.9 V *vs.* Ag/10 mM $AgNO_3$) and that the overoxidised polymer still retained some residual electroactivity.

In order to distinguish current due to polymer redox reaction from those due to electrolyte instability CVs were carried out on the Pt disc in 50 mM $TEABF_4$ in ACN without polymer (blank). It is notable that the anodic currents are most significant in the same potential range as that which caused polymer overoxidation shown in Figure 3.8. Therefore we may conclude that overoxidation process may be caused by a catalytic reaction product (e.g. $OH^{\bullet}$, OH^- or H_2O_2) of the oxidation with trace amounts of water in the electrolyte.

It is clear that overdoping PEDOT in 50 mM $TEABF_4$ in ACN did decrease the doping peak current at 0.0 V from 0.38 mA to 0.12 mA (a 42 % decrease) without physical decomposition of film as can be seen from Figure 3.7 i.e. black and red CVs respectively. However, some residual activity remains suggesting that the polymer conductivity is still present and therefore significant electronic conductivity remains. This result suggests that this method will not be suitable to form a polymer electrolyte which must behave as an electronic insulator.

3.3.3 Overreduction treatment

It is also possible to damage the conductivity of the polymer by cycling the film down to lower potentials (<-0.9 V *vs.* Ag/Ag^+) than the normal used under stable cycling. This is referred to as an over reduction treatment.

The overreduction treatment was done as follows.

1) Preparing the PEDOT film on the Pt working electrode by chronoamperometry at 0.95 V *vs.* Ag/10 mM $AgNO_3$ for 6 minutes (estimated film thickness : 2 μm)

2) Cycling the PEDOT at a normal potential range of -0.9 to 1.2 V *vs.* Ag/10 mM $AgNO_3$ to observe redox behaviour of PEDOT

3) Cycling the PEDOT at an overreduction potential window of -2.1 to 0.6 V *vs.* Ag/10 mM $AgNO_3$ to destroy its electronic conductivity

4) Cycling the PEDOT at the normal potential range again to observe changes in its redox behaviour after the treatment.

Figure 3.9, 3.10 and 3.11 shows the cyclic voltammograms recorded during the overreduction treatment, the comparison of the before and after treatment and the background signal provided by a blank platinum substrate respectively.

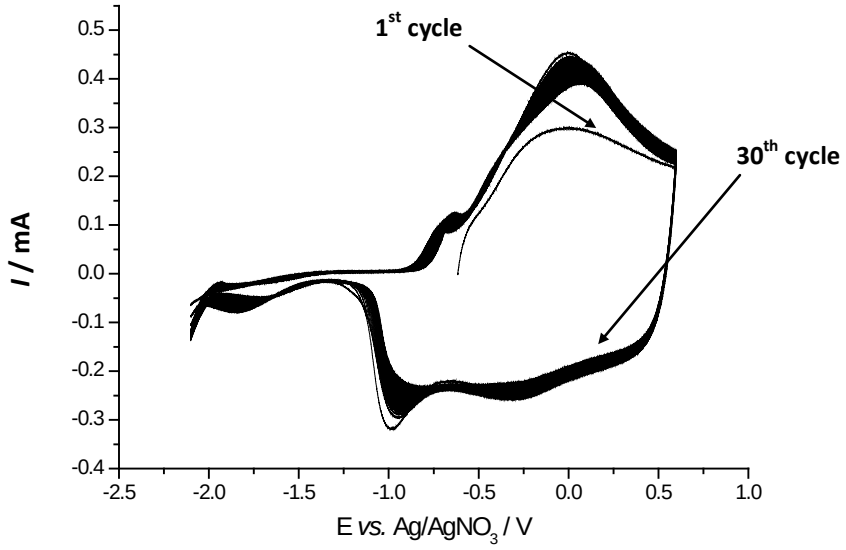

Figure 3.9 Cyclic voltammograms for the PEDOT film at the overreduction potential range between -2.1 and +0.6 V in 50 mM $TEABF_4$ in ACN at 100 mV/s for 30 cycles

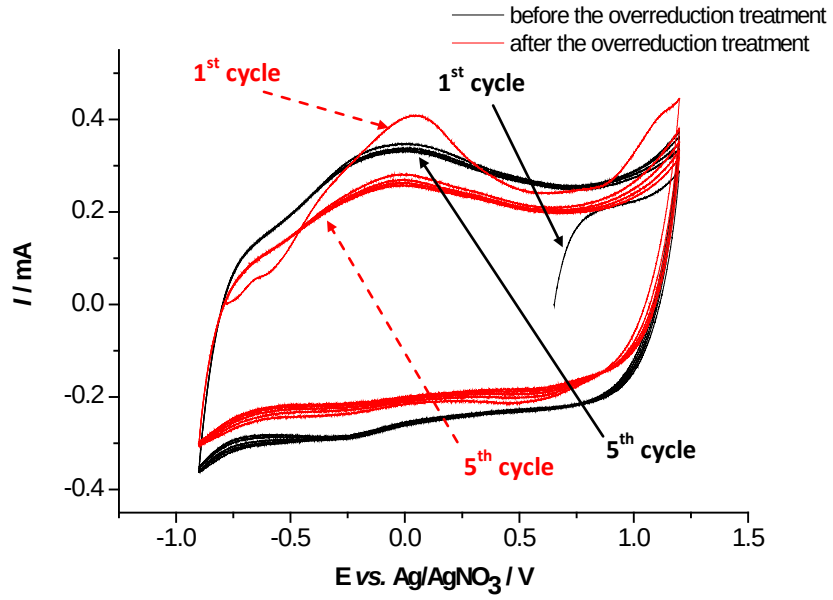

Figure 3.10 Cyclic voltammograms for cycling PEDOT film at the normal potential range between -0.9 and +1.2 V in 50 mM $TEABF_4$ in ACN at 100 mV/s for 5 cycles for a comparison between the CV before and after overreduction treatment

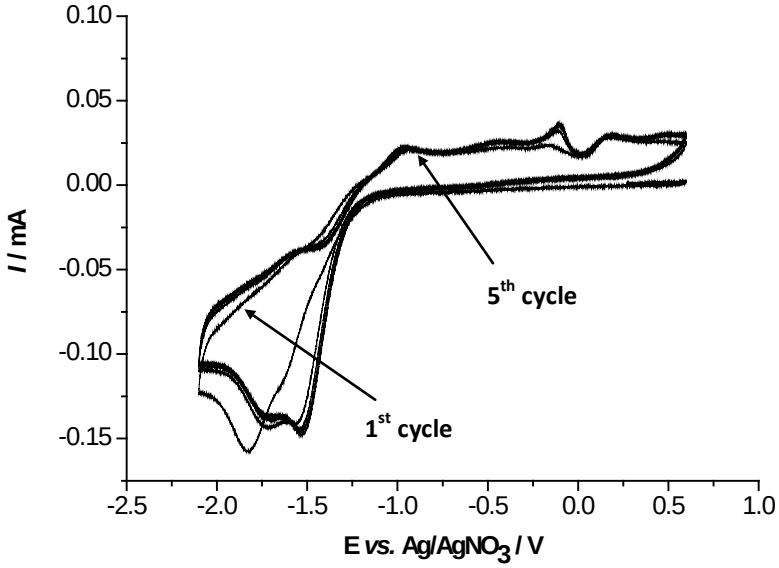

Figure 3.11 Cyclic voltammograms for cycling Pt disc in 50 mM $TEABF_4$ in ACN (blank)

The two micron film was cycled in 50 mM $TEABF_4$ in ACN at the normal potential range as can be seen from Figure 3.10 (the black CVs). The CVs of the untreated film were stable as seen previously. The film was then cycled at in overreduction potential range between -2.1 and +0.6 V as shown in Figure 3.9. The peak current at 0.0 V decreased slightly during the 30 cycles. The film was still present on electrode and still dark blue. The film was cycled again at the normal potential range in order to compare redox behavior of film before and after the overreduction treatment this is shown in Figure 3.10 (black for the untreated film (before treatment) and red for the treated film (after treatment)). The CVs of treated PEDOT film were quite stable, however, the doping peak current at 0.0 V decreased slightly when compared with the untreated sample. This indicated that the treated film lost some electronic conductivity, however, when compared with the degradation observed in the overoxidised sample this degradation was only very small.

In addition, the CVs for cycling the Pt disc in 50 mM $TEABF_4$ in ACN (blank) are shown in Figure 3.11 these showed a peak in the potential range -1.3 and -2.1 V that was similar to the peak attributed to overreduction of PEDOT as shown in Figure 3.9. This is again likely to be reduction of trace amounts of water. This indicates that these observed current

increases at -1.3 and -2.1 V were probably not due to PEDOT but electrolyte decomposition. However, unlike in the oxidation limit this did not cause polymer overreduction and breakdown of the electronic conductivity. The overreduction treatment only slightly decreased the PEDOT electronic activity. This is indicated by the doping peak current at 0.0 V decreasing from 0.34 mA to 0.26 mA (23 %) as can be seen from Figure 3.10 in the black and red CVs respectively.

To study the effect of the over reductive and over oxidative treatment on the surface morphology of the PEDOT samples, SEM images were recorded of the as prepared, over oxidised and over reduced films, these images are shown below in Figure 3.12.

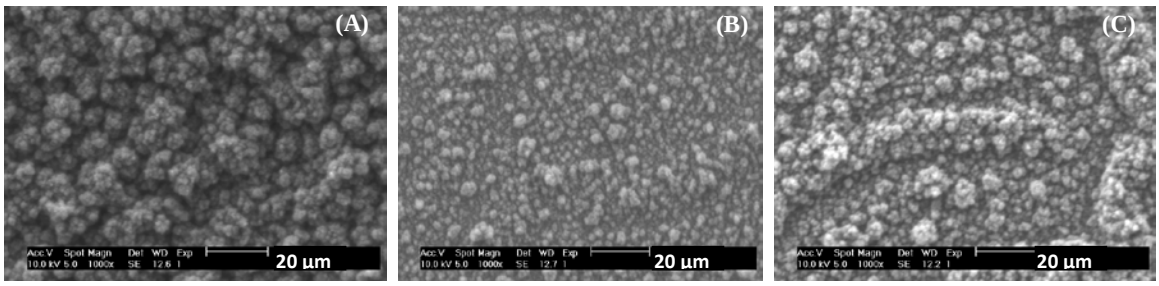

Figure 3.12 Scanning electron micrographs of PEDOT films:
(A) as prepared (B) as overoxidative tretaed and (C) as overreductive treated

Figure 3.12 shows that the PEDOT films of the polymer in the three states were not significantly different. The film surface appeared as many globules.

From all these results, it was quite clear to conclude that the overoxidation treatment was more beneficial for reducing conductivity than overreduction.

3.4 Chapter 3 Conclusions

Appropriate methods for electropolymerisation of PEDOT were investigated. PEDOT films were electrodeposited from both aqueous and non-aqueous electrolyte solutions. The films from the non aqueous solution were thicker than those of films from the aqueous solution.

To destroy the electronic conductivity of the PEDOT samples to allow their use as a polymer electrolyte two techniques that comprised of overoxidation and overreduction treatments of PEDOT were studied. The overoxidation treatment was able to decrease the electronic activity 42 % without physical film damaging whereas the overreduction treatment was capable of decreasing the electronic activity only 23 % without breakage of film. The overoxidation treatment was therefore more benefit. However, PEDOT seems to be an electrochemically stable material. Polymer electrolytes must be electronic insulating (electronic conductivity is less than 1 % of the total conductivity). Therefore it is suggested that it may not be possible to investigate a successful inactivation of PEDOT electronic conductivity.

Poly(1,11-Di(N-pyrryl)-3,6,9-trioxaundecane) (PP2O3) which is a conjugated polymer with polar side chains could be a better option. It was therefore chosen for further work in the subsequent chapters.

3.5 Chapter 3 References

[1] X. Du and Z. Wang, *Electrochimica Acta* **2003**, *48*, 1713-1717.
[2] C. Kvarnstrom, H. Neugebauer, S. Blomquist, H. J. Ahonen, J. Kankare and A. Ivaska, *Electrochimica Acta* **1999**, *44*, 2739-2750.
[3] M. Lapkowski and A. Pron, *Synthetic Metals* **2000**, *110*, 79-83.
[4] V. Noel, H. Randriamahazaka and C. Chevrot, *Journal of Electroanalytical Chemistry* **2003**, *558*, 41-48.
[5] H. Gustafsson, C. Kvarnstrom and A. Ivaska, *Thin Solid Films* **2008**, *517*, 474-478.
[6] L. Pigani, A. Heras, A. Colina, R. Seeber and J. Lopez-Palacios, *Electrochemistry Communications* **2004**, *6*, 1192-1198.
[7] S. S. Zhang, J. Hou, R. Zhang, J. K. Xu, G. M. Nie and S. Z. Pu, *European Polymer Journal* **2006**, *42*, 149-160.
[8] J. Bobacka, A. Lewenstam and A. Ivaska, *Journal of Electroanalytical Chemistry* **2000**, *489*, 17-27.
[9] S. C. Luo, E. M. Ali, N. C. Tansil, H. H. Yu, S. Gao, E. A. B. Kantchev and J. Y. Ying, *Langmuir* **2008**, *24*, 8071-8077.
[10] N. Sakmeche, S. Aeiyach, J. J. Aaron, M. Jouini, J. C. Lacroix and P. C. Lacaze, *Langmuir* **1999**, *15*, 2566-2574.
[11] A. Zykwinska, W. Domagala, B. Pilawa and A. Lapkowski, *Electrochimica Acta* **2005**, *50*, 1625-1633.
[12] M. X. Chen, *Proceedings of the Ieee* **2005**, *93*, 1339-1347.

Chapter 4

Synthesis and Characterisation of Poly(1,11-Di (N-pyrryl)-3,6,9-trioxaundecane) (PP2O3)

4.1 Introduction

In this chapter a new polymer (Poly(1,11-Di (N-pyrryl)-3,6,9-trioxaundecane) will be synthesised. This polymer is specially designed to have a switchable electronic conductivity and permanent ionic conductivity. The preparation of the monomer will be reported. This will be followed by the use of an electrochemical quartz crystal microbalance to study the deposition, doping undoping and conductivity degradation of this polymer. Also presented in parallel is a chemical preparation route of bulk powders of the same polymer. The electronic conductivity of this bulk powder will also be broken using a chemical oxidation.

4.2 1,11-Di(N-pyrryl)-3,6,9-trioxaundecane (P2O3)

The monomer design for this work is 1,11-Di(N-pyrryl)-3,6,9-trioxaundecane (P2O3) it is an oligoether-substituted pyrrole composed of an oligoether group linked between two pyrroles as shown in Figure 4.1. It was designed to be a precursor monomer for the oxidative polymerisation to give a polymer with mixed conducting properties, i.e. both ionic and electronic conduction. The latter is expected from the knowledge that polypyrroles are electronic conductors. Ionic conductivity is expected to be induced by addition of a salt whose cation can be solvated by the oligoether groups. Alternatively, an electrolyte (salt plus solvent) may be introduced as a plasticiser, made compatible by the polar nature of the oligoether groups.

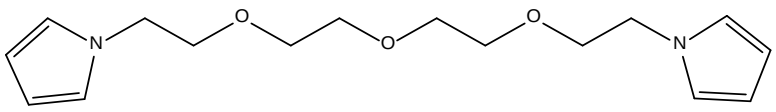

Figure 4.1 Chemical structure of 1,11-Di(N-pyrryl)-3,6,9-trioxaundecane (P2O3)

The monomer was synthesised from a reaction of nucleophilic displacement with a pyrrole potassium salt as detailed later.

4.2.1 Synthesis of P2O3

4.2.1.1 Chemicals and Materials

Pyrrole (>99 %) was obtained from Aldrich. Bis[2-(2-chloroethoxy) ethyl] ether (>99 %) was used as received from Fluka. THF was purchased from Aldrich and was purified by distillation and stored in nitrogen atmosphere. Potassium metal (>99.95 %, ingot), DMSO (>99.9 %, anhydrous), Na_2SO_4 (>99 %, anhydrous, granular), ether (>99 %) and hexane (>99 %) were obtained from Sigma. Ethyl acetate (>99 %) was received from Fluka.

4.2.1.2 Equipment

The P2O3 synthesis was performed in a round bottomed flask attached to a reflux column. Column chromatography was used to purify the compound. The reflux and chromatography columns are shown in Figure 4.2.

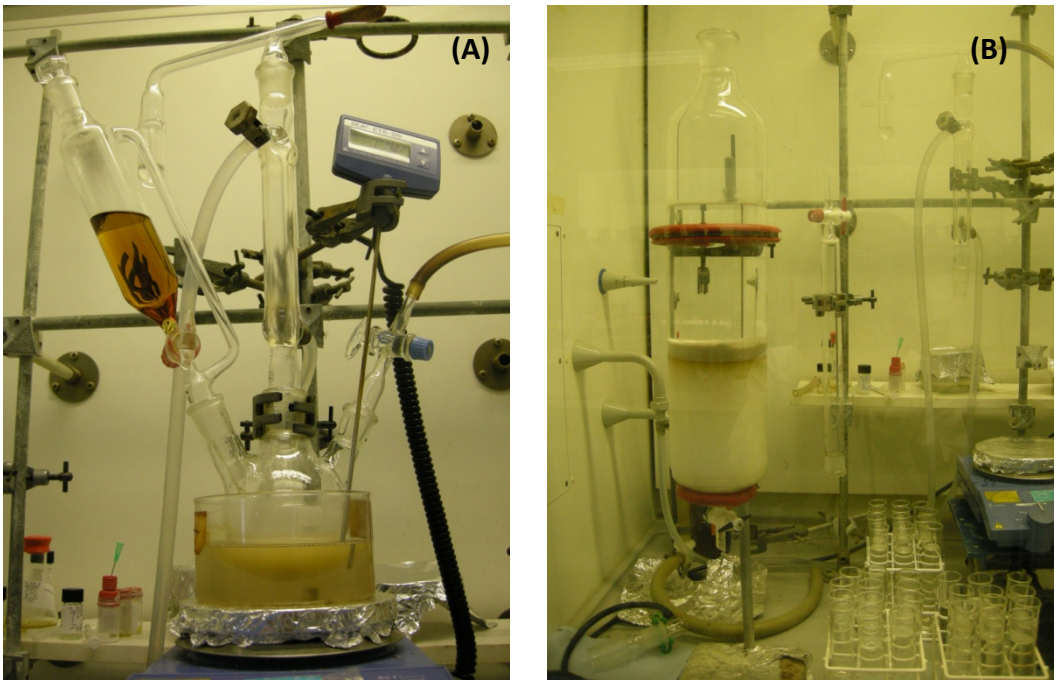

Figure 4.2 Equipment for P2O3 compound synthesise (A) reflux column and (B) chromatography column

4.2.1.3 Procedure[1]

The P2O3 formation from the corresponding commercially available glycolic dihalides was achieved by nucleophilic displacement with pyrrole potassium salt according to the equation in Figure 4.3.

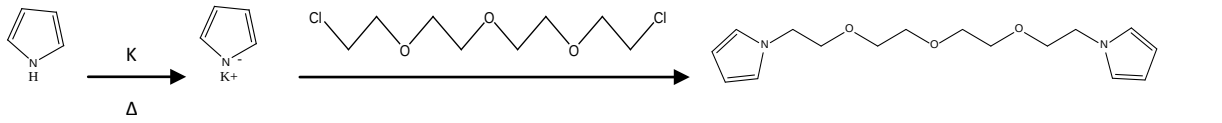

1,11-Di(N-pyrryl)-3,6,9-trioxaundecane (P2O3)

Figure 4.3 Synthesis of 1,11-Di(N-pyrryl)-3,6,9-trioxaundecane (P2O3)

Preparation of the potassium pyrrole salt was carried out using the reflux set shown previously. Dry THF (90 ml) was added into the round bottom flask. Small pieces of fresh potassium metal (6.7 g) were slowly added to the THF, with vigorous stirring. The suspension was then heated at 70^{o}C while maintaining stirring, until small beads of molten potassium were formed. Pyrrole (12 ml) was added dropwise to the heated suspension until the potassium was completely consumed. The mixture was then cooled down to room temperature. DMSO (10 ml) was then added dropwise into the mixture. A solution containing bis[2-(2-chloroethoxy) ethyl] ether in 20 ml of THF was then added. The mixture was left stirring at room temperature over night. THF was evaporated off using a Buchi rotary evaporator, with a temperature setting of 30 ^{o}C under a vacuum of 10 mbar. DI water was added and the mixture was treated with ether. The organic phase was washed with DI water several times, dried over Na_2SO_4 and the solvent was evaporated. A yellowish oily impure compound was obtained. It was purified by column chromatography on silica gel with hexane:ethyl acetate (2:1) as the eluent. Finally the pure light yellow oily compound was obtained as can be seen from Figure 4.4.

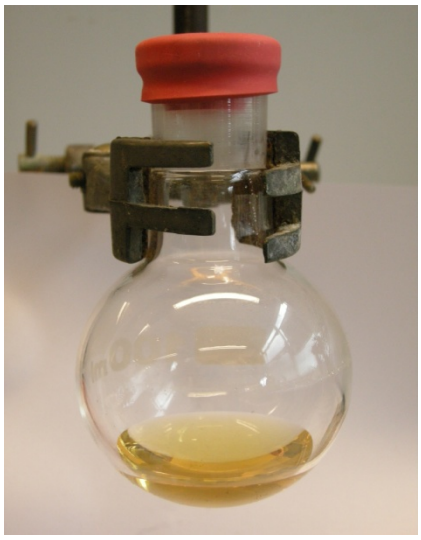

Figure 4.4 Photo of 1,11-Di(N-pyrryl)-3,6,9-trioxaundecane (P2O3)

The compound weight was 12.30 g which was a yield of 75.12 %. The loss of the compound was probably a result of incomplete coupling of the pyrrole with the glycol dihalide and also the loss of some compound during the purification processes. The compound was characterised by NMR spectroscopy, Mass spectrometry and IR spectroscopy as shown in Figure 4.5, 4.6 and 4.7 respectively.

4.2.2 Characterisations of P2O3

4.2.2.1 NMR spectrum of P2O3

NMR spectrum of P2O3 was shown in Figure 4.5

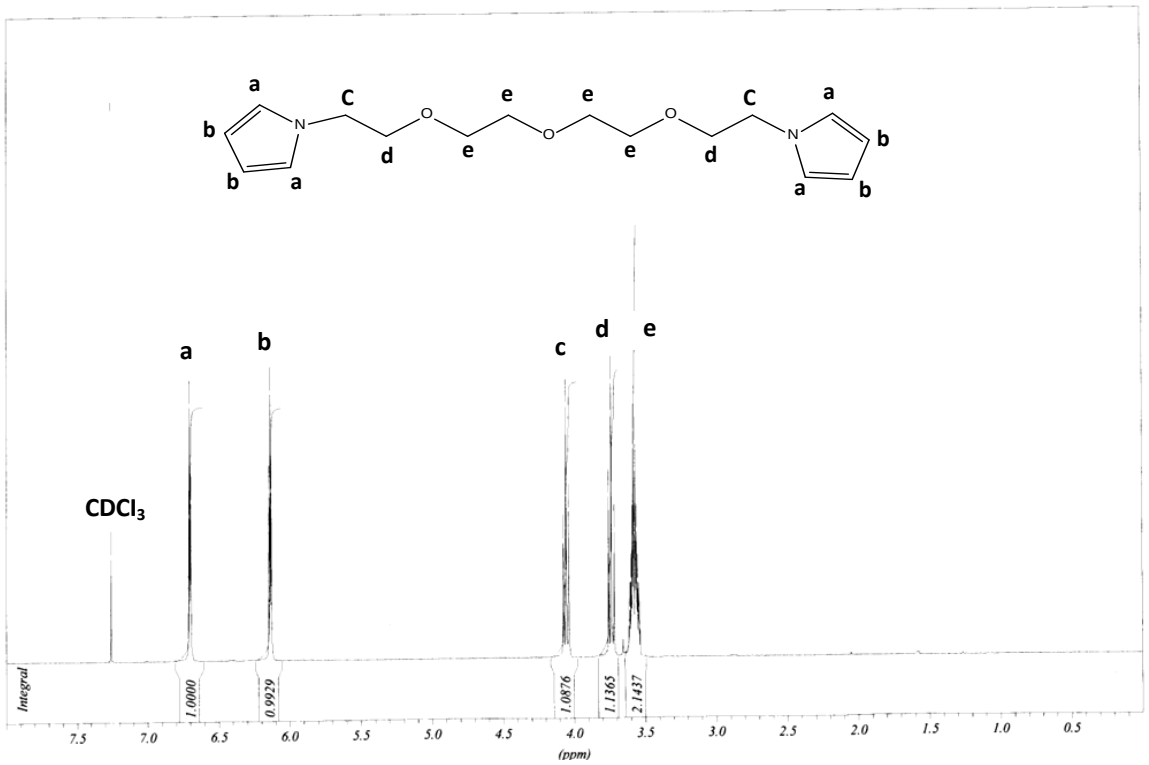

Figure 4.5 NMR spectrum of P2O3

^{1}H-NMR(300 MHz, $CDCl_3$) δ/ppm: 6.70 (t,4H, pyrryl-H (2,5), J=2.19 Hz, integrated area = 1.00), 6.14 (t,4H, pyrryl-H (3,4), J= 2.19 Hz, integrated area = 0.99), 4.06 (t,4H, CH_2 J= 5.67 Hz, integrated area = 1.09), 3.74 (t,4H, CH_2O J= 5.67 Hz, integrated area = 1.14), 3.59 (m,8H, CH_2O integrated area = 2.14)

The compound spectrum is composed of five main peaks as can be seen from Figure 4.5 and the NMR characterisation includes integrated peak areas as stated above. The integrated peak area ratio is proportional to the relative number of protons causing the peaks which were at 1.00:0.99:1.09:1.14:2.14 at 6.70, 6.14, 4.06, 3.74 and 3.59 ppm

respectively. These ratios match the theoretical rating 1:1:1:1:2 expected within an error margin of 14 %. The protons were labeled with the respect to the chemical equivalence and environment in P2O3 structure as shown in Figure 4.5.

4.2.2.2 Mass spectrum of P2O3

The mass spectrum of P2O3 compound is shown in Figure 4.6.

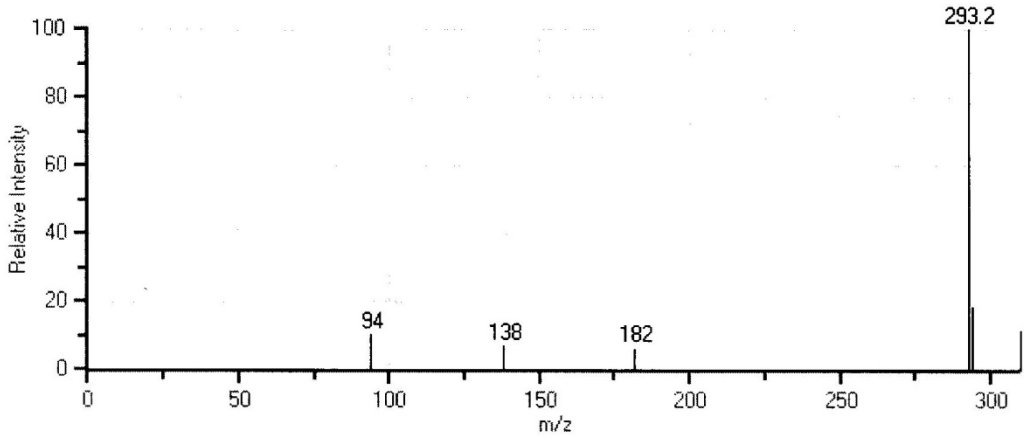

Figure 4.6 Mass spectrum of P2O3 compound (Fast CI-MS non-polar)

The peak in Figure 4.6 at 293.2 corresponds to the P2O3 molecular ion mass. The three other peaks i.e. 94, 138 and 182 correspond to fragment ion of P2O3 compound as can be seen from Figure 4.7.

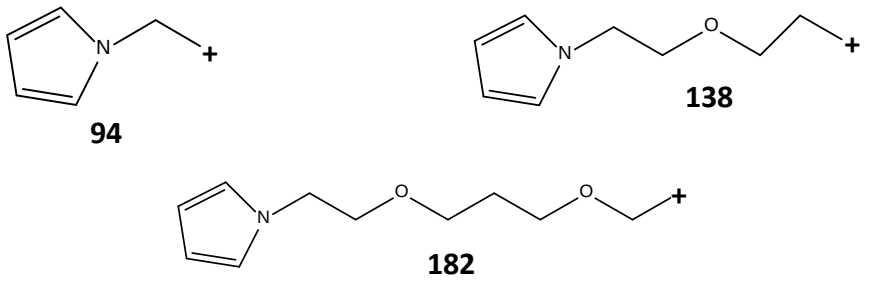

Figure 4.7 Fragment ions of P2O3.

4.2.2.3 IR spectrum of P2O3

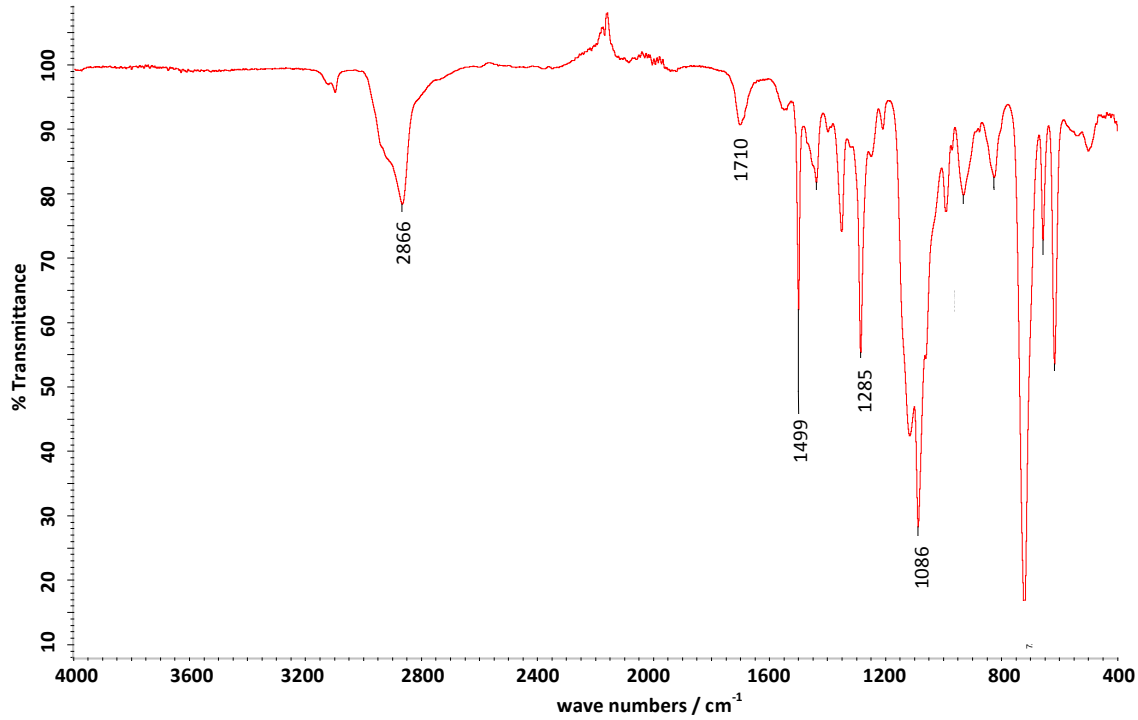

Figure 4.8 IR spectrum of P2O3

IR spectra of P2O3 was recorded in Thermo Electron Coporation (Nicolet 380 FT-IR) IR spectrometer at room temperature in the region 4000–400 cm^{-1}. The IR spectrum had five main peaks as shown in Figure 4.8. These were in a band of C-H stretch at about 2866 cm^{-1}, C=C stretch at about 1710 cm^{-1}, C-N ring stretching band of pyrrole ring at 1499 cm^{-1}, C-H plane deformation of the pyrrole at 1285 cm^{-1} and C-O stretch at about 1086 cm^{-1}. The C=C peak was very small probably due to a small proportion of C=C bonds when compared with others in the compound molecule.

4.3 Polymerisation of P2O3

This section will address two methods for the preparation of poly(1,11-Di (N-pyrryl)-3,6,9-trioxaundecane (PP2O3) from the monomer synthesised as described in section 4.2. The first is an electrochemical route which will allow for the preparation of thin film layers of PP2O3 on both planar and 3D substrates. The second method produces bulk amounts of the powdered sample which will be used to study conductivities and the practical application of this polymer in battery systems.

4.3.1 Electrodeposition of PP2O3

Using the P2O3 monomer polymer films can be prepared by electrodeposition. Poly(1,11-Di (N-pyrryl)-3,6,9-trioxaundecane (PP2O3) film properties are significantly affected by the electropolymerisation conditions. These involve several factors such as solubility of P2O3 in the electrolyte solution, oxidation potentials of P2O3 with electrolytes, working electrode (substrate) and the electropolymerisation technique.

P2O3 has a large molecular structure and has a low water solubility. However electropolymerisation from both aqueous and nonaqueous solutions have been attempted, with different supporting electrolytes. Initially comparisons of the CVs recorded during deposition from the various electrolytes are made. This is followed by deposition from all routes on 3D substrates to compare the quality of the deposits using SEM.

4.3.1.1 Non aqueous electrolyte solutions

4.3.1.1.1 Chemicals, Materials and Equipment

P2O3 was synthesised as explained in section 4.2. LiTFSI and $TEABF_4$ were received from Aldrich and ACN was obtained from Fisher. Two electrolytes were prepared: 10 mM P2O3

containing 50 mM LiTFSI in ACN (LiTFSI electrolyte) and 10 mM P2O3 containing $TEABF_4$ in ACN ($TEABF_4$ electrolyte).

Glassy carbon sealed in glass (radius : 0.15 cm and surface area : 0.07 cm^2) and reticulated vitreous carbon foams (a pressure contact was made to the foam with Ti foil) working electrodes were used. Pt gauze counter electrode and Ag/10mM $AgNO_3$ reference electrode were used. The cell was connected to a potentiostat (VMP2 from Bio Logic science instruments).

4.3.1.1.2 Results and Discussion

Figures 4.9 and 4.10 show the CV response recorded in the LiTFSI and $TEABF_4$ electrolytes. This will highlight the effect of the two supporting electrolytes on the electropolymerisation efficiency and quality of polymer films.

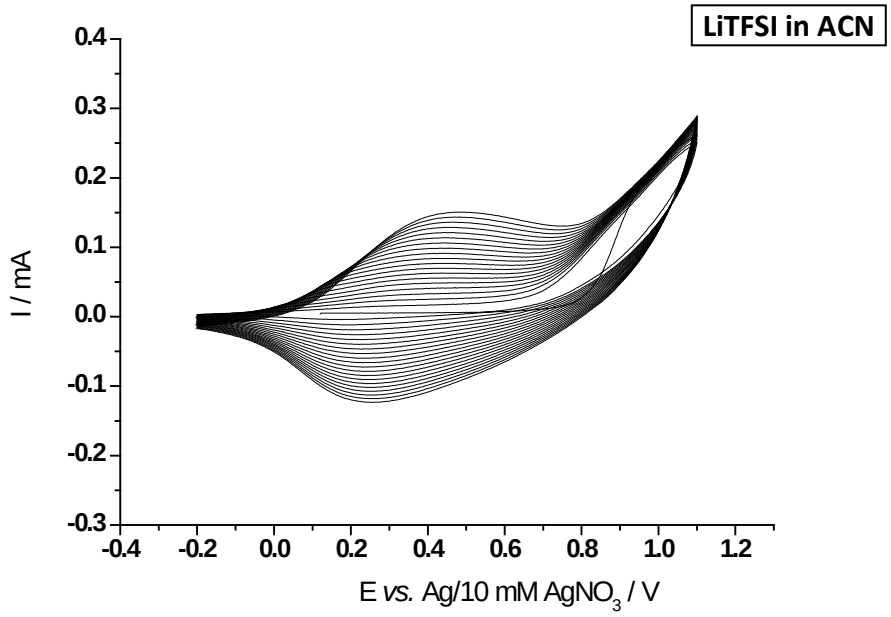

Figure 4.9 Cyclic voltammograms for the deposition of PP2O3 film recorded between -0.2 and +1.1 V at 100 mV/s. The PP2O3 film, which was electrosynthesised in ACN containing 10 mM P2O3and 50 mM LiTFSI was deposited on a glassy carbon electrode.

The voltammograms in Figure 4.9 showed an increase of currents from cycle to cycle. The first scan show a characteristic nucleation loop[2] above 0.9 V *vs.* Ag/Ag^+. With each cycle an increase of current above 0.9 V *vs.* Ag/Ag^+ was seen this indicated continued polymerisation. The broad anodic peak at 0.5 V *vs.* Ag/Ag^+ and cathodic peak at 0.3 V *vs.* Ag/Ag^+ are the doping and dedoping of the conducting polymer. The increase in these peak currents on each cycle indicated an increasing amount of deposited polymers. The total polymerisation charge was 0.280 C/cm^2, and the film thickness was approximated to be 1.141 μm as described earlier (summarised in Table 4.1).

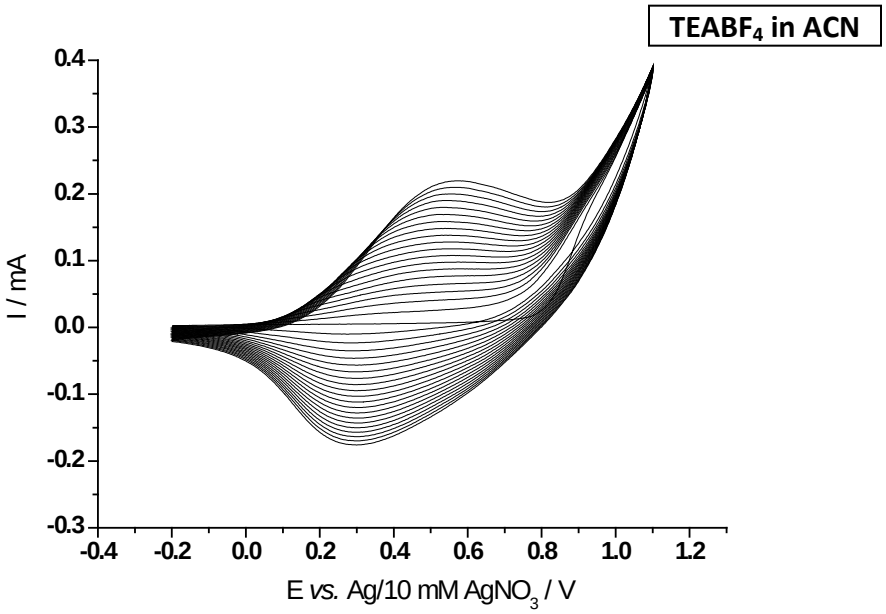

Figure 4.10 Cyclic voltammograms for the deposition of PP2O3 film recorded between -0.2 and +1.1 V at 100 mV/s. The PP2O3 film, which was electrosynthesised in ACN containing 10 mM P2O3 and 50 mM $TEABF_4$ was deposited on a glassy carbon electrode.

When depositing a PP2O3 film from the $TEABF_4$ electrolyte, the voltammograms showed increased currents from cycle to cycle as shown in Figure 4.10 similar to that seen in Figure 4.9. Again the broad anodic peak at +0.5 V *vs.* Ag/Ag^+ and cathodic peak at +0.3 V *vs.* Ag/Ag^+ indicated the doping and dedoping states of the conducting polymer respectively. The increase in these peak currents on each cycle indicated deposition of more polymer.

The total polymerisation charge was 0.377 C/cm^2 which corresponded to 1.906 μm film of PP2O3 film as shown in Table 4.1.

The film from $TEABF_4$ was slightly thicker than the films prepared from the LiTFSI electrolyte, and both reactions were considered to be satisfactory for electropolymerisation.

As an alternative preparation route two aqueous electrolytes are examined in the next section.

4.3.1.2 Aqueous electrolyte solutions

4.3.1.2.1 Chemicals, Materials and Equipment

P2O3 was synthesised as explained in the previous section. SDS and TSNa were received from Aldrich.

Glassy carbon sealed in glass (radius : 0.15 cm and surface area : 0.07 cm^2) and RVC substrate (a pressure contact was made to the foam with Ti foil) working electrodes were used with Pt gauze counter electrode and SCE reference electrode were used. The cell was connected to a potentiostat (VMP2 from Bio Logic science instruments). Two aqueous electrolyte solutions were prepared: 10 mM P2O3, 50 mM SDS in DI water (SDS electrolyte) and 10 mM P2O3, 10 mM TSNa (TSNa electrolyte) and 5 % of isopropanol in DI water

4.3.1.2.2 Results and Discussion

Although P2O3 has a very low solubility in water, it is possible to improve the water solubility of P2O3 by adding surfactant molecules and/or low polar organic solvent into the P2O3 electrolyte solution. The polymer films were deposited from the SDS and TSNa electrolyte to investigate the effect of the two supporting electrolytes on electropolymerisation efficiency and quality of the polymer films.

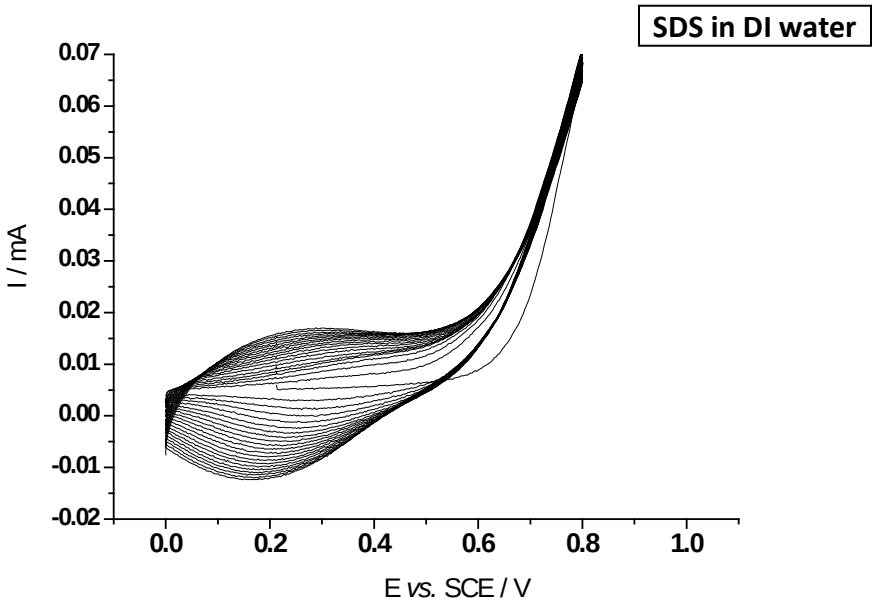

Figure 4.11 Cyclic voltammograms for the deposition of PP2O3 film recorded between 0.0 and +0.8 V at 100 mV/s. The PP2O3 film, which was electrosynthesised in aqueous solution containing 10 mM P2O3 and 10 mM SDS was deposited on a glassy carbon electrode.

Unlike PP2O3 films from non aqueous solutions, the voltammograms show only a slight increase of current from cycle to cycle as can be seen from Figure 4.11. There was little change in the polymerisation current above 0.6 V *vs.* SCE with increasing cycle number. This indicated a slow rate of polymerisation. The broad anodic peak at 0.3 V *vs.* SCE and anodic peak at 0.2 V *vs.* SCE indicated the doping and dedoping states of the conductive polymer. The slight increase in these peak currents on each cycle indicated a small gain of deposited polymer. The polymerisation charge was 0.050 C/cm^2. The film thickness was 0.253 μm as shown in Table 4.1.

The CV recorded for the film deposition from a TSNa electrolyte is shown below in Figure 4.12.

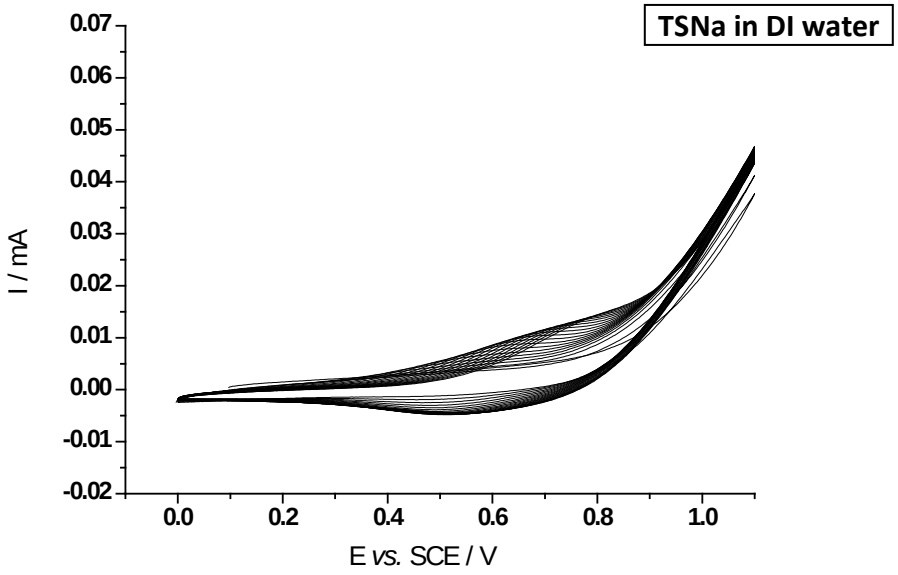

Figure 4.12 Cyclic voltammograms for the deposition of PP2O3 film recorded between 0.0 and +1.1 V at 100 mV/s. The PP2O3 film, which was electrosynthesised in aqueous solution containing 10 mM P2O3, 10 mM TSNa and 5% of isopropanol was deposited on a glassy carbon electrode.

The voltammograms in Figure 4.12 showed a very low ratio of the doping charge to the polymerisation charge. The broad cathodic and anodic peaks at 0.6 V indicated the doping and dedoping states of conductive polymer. The slight increase in these peak currents on each cycle indicated that the deposition of polymer occurred very slowly. Moreover it is important to notice that the onset of polymerisation potential was higher than those of P2O3 from SDS i.e. 0.6 and 0.9 V *vs.* SCE for SDS and TSNa solutions respectively. SDS lowered the oxidation potential of the monomer, this has been reported by other authors[3-5]. The polymerisation charge was 0.033 C/cm^2 which corresponded to a film thickness of 0.165 μm as shown in Table 4.1. This was very thin when compared with the films from non aqueous solution and also with the films from SDS solution.

Table 4.1 Film thicknesses of PP2O3 with different electrolytes in aqueous and non aqueous solutions.

Polymerisation system	Polymerisation charge (C/cm^2)	Film thickness* (µm)
Non aqueous : PP2O3+ LiTFSI	0.280	1.414
Non aqueous : PP2O3+ $TEABF_4$	0.377	1.906
Aqueous : PP2O3+ SDS	0.050	0.253
Aqueous : PP2O3+ TSNa	0.033	0.165

* assuming number of e^- exchanged per mole of monomer = 4 and ρ = 1.50 g/cm^3

The two films from non aqueous solution had a similar thickness. The electrolyte composition did not significantly affect the polymerisation reaction. On the other hand, the films from aqueous solution had different thicknesses. The film from SDS surfactant solution was thicker than those of the film from TSNa solution. When the films from aqueous and non aqueous solutions are compared, the films from aqueous solution were much thinner than those of films from non aqueous solution. This indicates higher rates of deposition in non aqueous solutions than aqueous solutions. In other words thicker films could be deposited faster.

To investigate the deposition of the PP2O3 films over the 3D type substrates required for the formation of a 3D battery layers were electrodeposited on 3D RVC with nonaqueous and aqueous electrolyte systems with different supporting electrolytes. The film surfaces were visualized by SEM (Philips XL 30 ESEM) as shown in Figure 4.13.

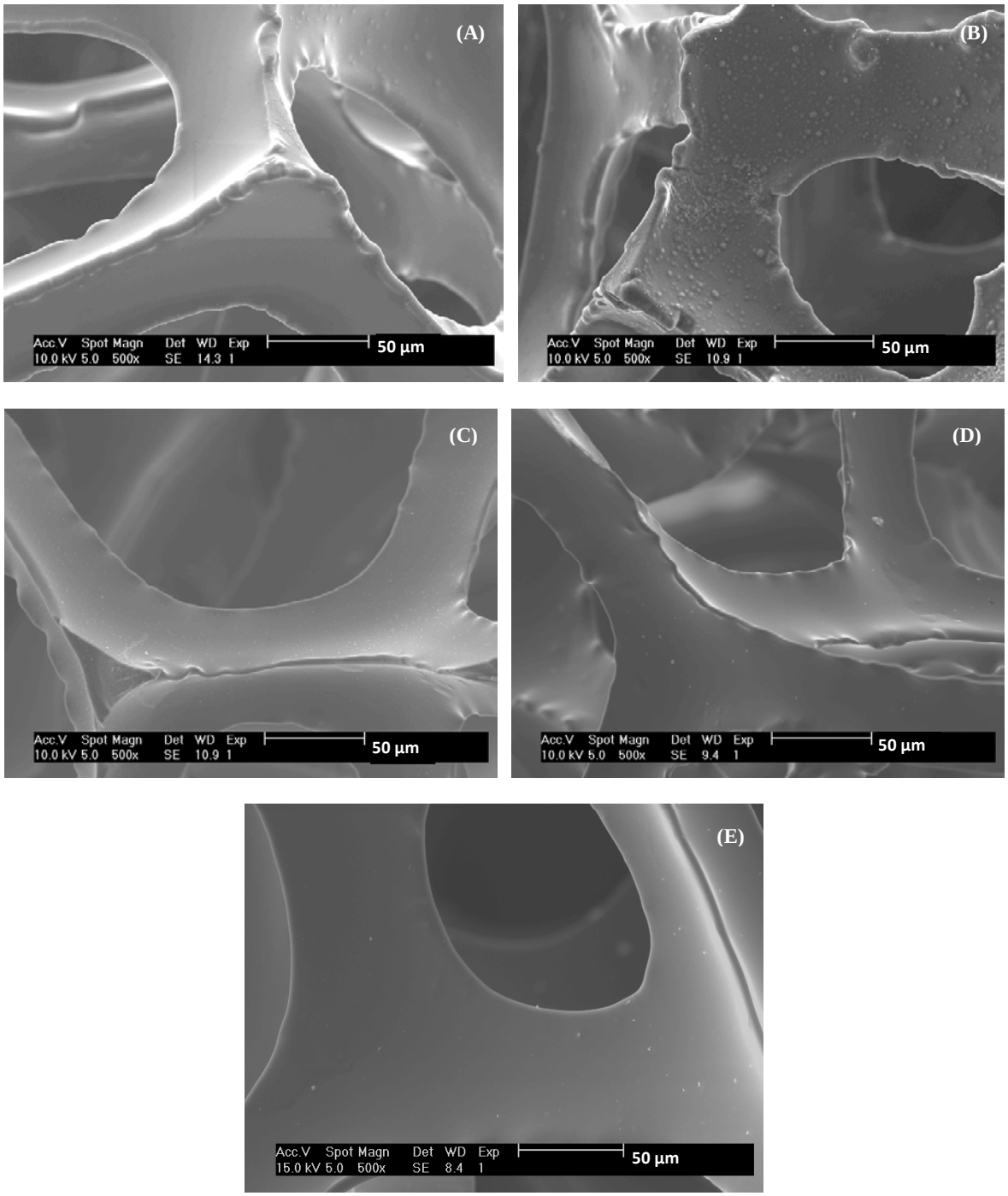

Figure 4.13 SEM images of electrodeposited PP2O3 films on 3D RVC by chronoamperometry technique at 1.0 V *vs.* SCE for aqueous solution and 10 mM Ag/Ag^{+} for non aqueous solution for 10 minutes with different electrolytes (A) 10 mM P2O3 containing 50mM LiTFSI in ACN (B) 10 mM P2O3 containing 50 mM $TEABF_4$ in ACN (C) 10 mM P2O3 in a solution of 10 mM SDS (D) 10 mM P2O3 in a solution of 10 mM TSNa and 5 % of isopropanol and (E) bared 3D RVC.

.

Figure 4.13 indicates that all films were conformal. The films can be obviously seen, with the key feature being the smoothing of edges, normally sharp on the RVC foam. By observation through the foam it can be observed to some extent that the polymer is conformally coating the struts within the foam and not just the edges nearest the bulk electrolyte. The films from the LiTFSI and $TEABF_4$ electrolyes were the thickest, and still had very smooth surfaces as can be seen from Figure 4.13 (A) and (B). The film prepared from the $TEABF_4$ electrolyte has some globular deposits on the surface possibly resulting from dendrite growth. The films prepared from aqueous solutions (shown in Figure 4.13 (C) and (D)) were also smooth, but the films were thinner than those prepared from non aqueous solution.

From these depositions we can draw the following conclusions:

- Conformal films could be deposited from all routes.
- The rate of deposition was much larger in non aqueous systems.
- In non aqueous systems the LiTFSI salt produced films with the smoothest deposit.

These conclusions led to the use of non aqueous depositions with the LiTFSI electrolyte for all further electrodeposited films.

This polymer can also be prepared using a chemical route. This preparative route is now discussed.

4.3.2 Chemical polymerisation of P2O3

PP2O3 was also polymerised by chemical technique using Iron(III) p-toluenesulfonate oxidant[6]. The reaction is shown in Figure 4.14.

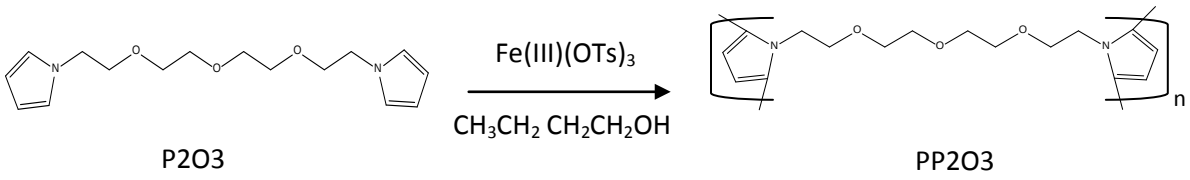

Figure 4.14 Chemical polymerisation of P2O3 with Iron(III) p-toluenesulfonate

4.3.2.1 Chemicals, Materials, Equipment and Procedure

Iron(III) p-toluenesulfonate and butanol were obtained from Sigma.

Iron(III) p-toluenesulfonate (8.80 g) was dissolved in butanol (22 ml) in a 50 ml beaker with vigorous stirring at room temperature. P2O3 (0.5 g) was added to the solution, which turned black within a few minutes. It was left stirring over night. The black PP2O3 precipitate was obtained and then filtered and washed with DI water and isopropanol for several times. The PP2O3 precipitate was dried out at 80 ^{o}C for 3 hours.

4.3.2.2 Results and Discussion

The polymerisation of P2O3 using Iron(III) p-toluenesulfonate oxidant was successful. Fine dark gray PP2O3 powder was obtained as can be seen from Figure 4.26 (A) and its IR spectrum is shown in Figure 4.28 (A) (These Figures are reported at the end of this chapter where more details are given and comparisons between the polymers formed with chemical and electrochemical drawn). The yield% was around 83.83 %. A loss of polymer was probably because of uncompleted polymerisation reaction and also loss of some sample during washing and filtering processes.

4.4 Breaking the Electronic Conductivity in PP2O3

Methods for breaking the electronic conductivity in PP2O3 polymers are presented in this section. Initially an electrochemical overoxidation will be applied to the electrodeposited PP2O3. This will attempt to break the conductivity in a similar approach as described earlier for the PEDOT films. Then a chemical route will be used to break the conductivity in the bulk powders prepared by chemical polymerisation.

4.4.1 Electrochemical treatment for preparing non electronic conductive PP2O3 by EQCM technique

Published literature reported that cycling conjugated polymers in non aqueous electrolytes can be used to decrease the electronic conductivities of the polymers[7, 8]. They suggested that trace water in ACN interacted with the conjugated bonds at high potentials which lead to the formation of a substitution product (hydroxylation). This resulted in interrupted π electron delocalization thus decreased electronic conductivity.

EQCM is a useful tool for detecting small mass changes that accompany electrochemical processes on the electrode surfaces. It was therefore used to record mass changes in the polymer during the entire overoxidation experiment. This will provide significant evidence of the mass changes due to the substitution product during the overoxidation treatment. EQCM principle is explained in Chapter 2.

.

4.4.1.1 Materials and Equipment

P2O3 was synthesised as explained in section 4.2. LiTFSI (99.9 %) was obtained from Aldrich. ACN (99.9 %) and H_2SO_4 were obtained from Fisher Scientific. H_2PtCl_6 was obtained from Aldrich. A gold coated quartz crystal resonator (EQCM) (surface area of electrode : 1.37 cm^2), Pt and 10 mM $Ag/AgNO_3$ were used as a working, counter and reference electrodes respectively.

4.4.1.2 Procedure

The electrochemical behavior of PP2O3 sample was studied with in-situ mass determination by EQCM, in four steps as follows.

1) Pt was electrodeposited on a gold quartz crystal resonator to prepare an adhesive surface for the PP2O3 film. A 10 mM H_2PtCl_6 and 0.5 M H_2SO_4 electrolyte solution was used.

2) PP2O3 was deposited by cyclic voltammetry from a potential range of -0.3 to 1.1 V *vs.* Ag/10 mM $AgNO_3$ at 100 mV/s for 20 cycles, using the solution of 10mM P2O3 + 50 mM LiTFSI in ACN.

3) The polymer film was cycled in the monomer free electrolyte in the normal potential window from -0.3 to 0.3V *vs.* Ag/10 mM $AgNO_3$ at 100 mV/s for 5 cycles to observe mass changes during doping/dedoping behaviour of polymer.

4) The film was cycled in the electrolyte again, but this time at the overoxidation potential range from -0.3 to 1.9V *vs.* Ag/10mM $AgNO_3$ at 100 mV/s for 25 cycles to destroy its conjugated bonds.

4.4.1.3 Pt deposition

Pt was deposited electrochemically using a potential step method on a gold quartz crystal resonator in order to improve surface adhesion of PP2O3 film on the gold quartz crystal resonator. The information recorded during the EQCM deposition is shown in Figure 4.15.

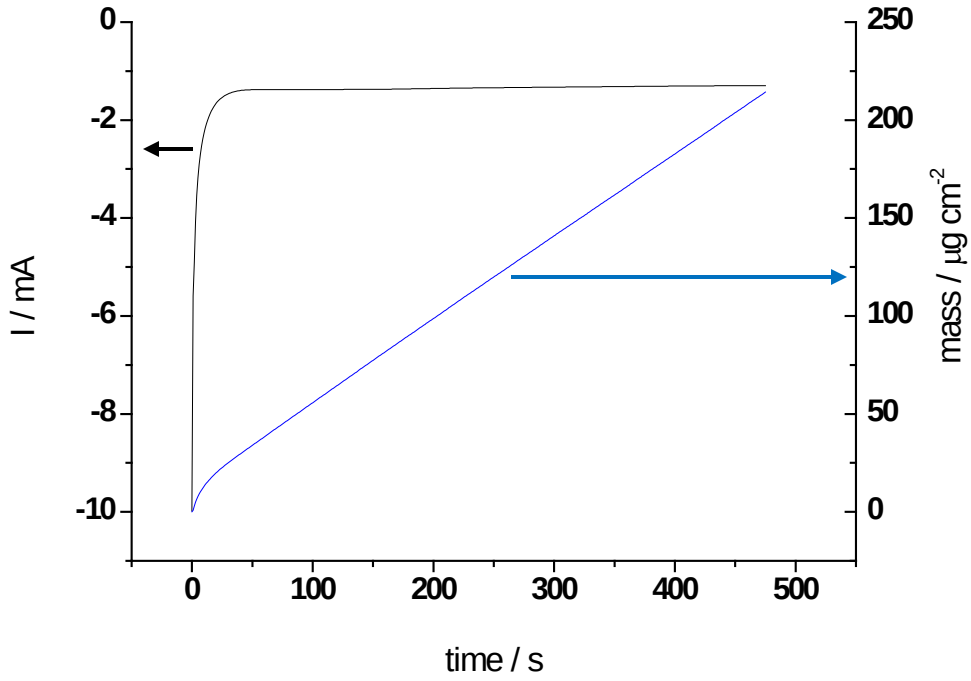

Figure 4.15 Electrodeposition of Pt on a gold quartz crystal resonator from the solution of 10 mM H_2PtCl_6 in 0.5 M H_2SO_4 by chronoamperometry at an applied potential of -0.15 V *vs.* SCE for 8 minutes

Pt was electrodeposited on a gold quartz crystal resonator using a method described in the literature[9]. The deposition of Pt was successful and the mass increased continuously as a function of time as can be seen from Figure 4.15. For 8 minutes 214 µg/cm^2 of Pt was obtained. Pt density is 21.45 g/cm^3[10]. This suggests an estimated Pt thickness of 0.1 µm.

4.4.1.4 PP2O3 deposition

PP2O3 was electrodeposited by cyclic voltammetry to observe mass change during polymerisation. The information recorded during the EQCM deposition is shown in Figure 4.16.

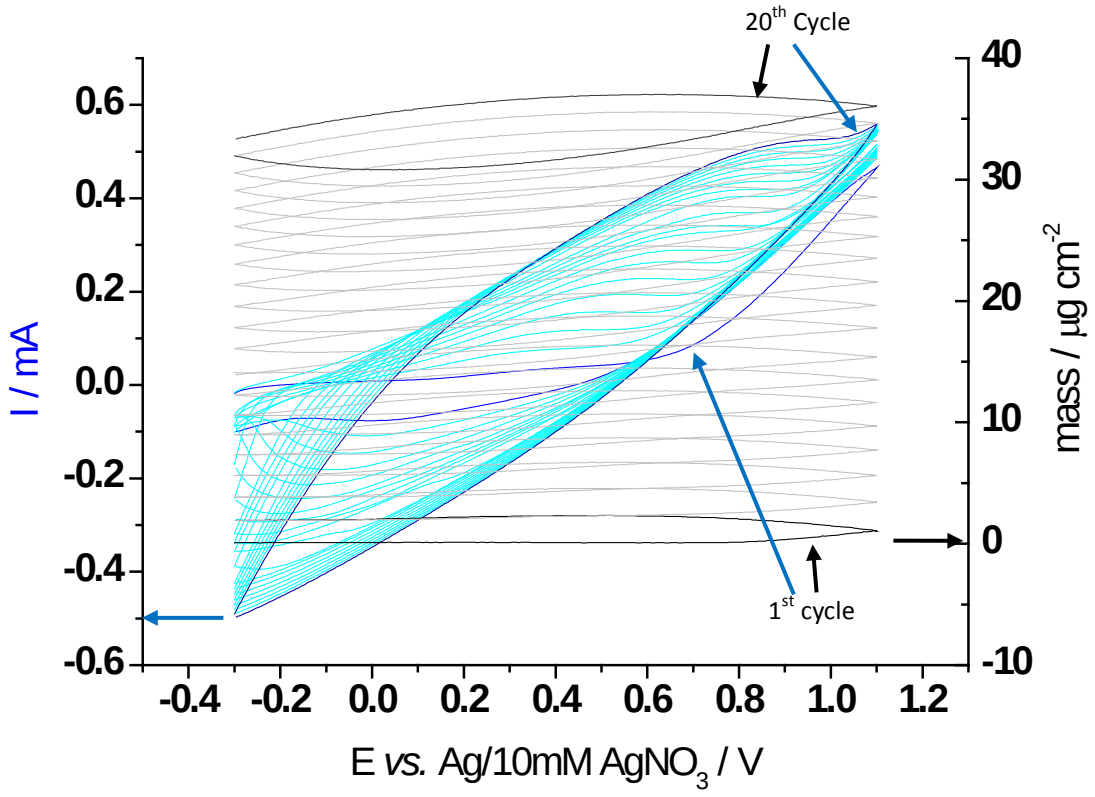

Figure 4.16 Electrodeposition of PP2O3 on the quartz crystal resonator from the solution of 10 mM P2O3 + 50 mM LiTFSI in ACN at scan rate of 100 mV/s, potential window from -0.3 to 1.1 V for 20 cycles.

Figure 4.16 shows the voltammogram (blue (1st and 20th cycle) and light blue (subsequent cycles) curves) of PP2O3 electrodeposition on the quartz crystal resonator, the response is similar to that reported earlier on a planar carbon electrode. It can be noted that there is a continuous increase of currents from cycle to cycle. The first scan shows the characteristic nucleation loop[2] above 0.6 V *vs.* Ag/Ag^+. After the first cycle an increase of current above 0.9 V *vs.* Ag/Ag^+ indicated the continuous state of polymerisation. Also the mass changes (black and gray curves) showed a gradual increase of deposition mass of polymer.

The cyclic voltammogram in Figure 4.16 was replotted as voltage, current and mass *vs.* time profiles in order to observe the film growth behavior clearly. The plots of these profiles can be seen form Figure 4.17.

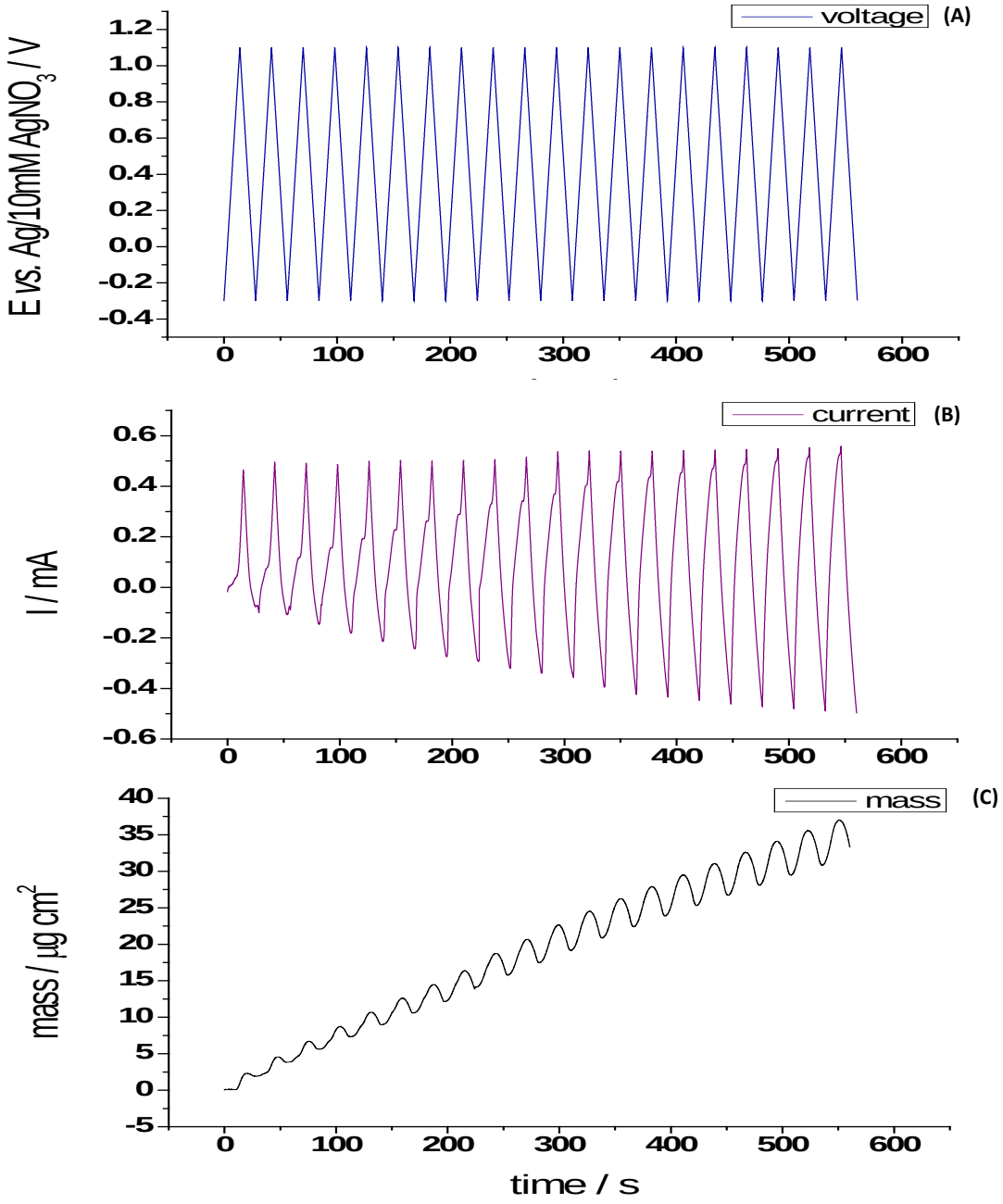

Figure 4.17 Electrodeposition of PP2O3 on the quartz crystal resonator from the solution of 10 mM P2O3 + 50 mM LiTFSI in ACN at scan rate of 100 mV/s, potential window from -0.3 to 1.1 V for 20 cycles; plot of (A) voltage *vs.* time (B) current *vs.* time and (C) mass *vs.* time.

The PP2O3 film was electrodeposited on the quartz crystal resonator well, its mass increased from cycle to cycle at a constant rate around 1.849 μg/cycle cm^2 as can be seen from Figure 4.17 (C). The overall linear mass change indicated a continuous electropolymerisation of PP2O3 on Pt adhesive surface. Although there is an overall linear mass change there is an obvious second effect. There is an oscillation on the linear increase from cycle to cycle. This is a result of the doping and undoping of the polymer film. When doped the polymer sample has a greater mass. The sample mass at the end of deposition was 36.04 μg/cm^2. The PP2O3 thickness was estimated as 0.240 μm using the EQCM measured mass (assuming the film density of 1.50 g/cm^3 approximated from polypyrrole density[11]). The film thickness calculated from the electrodeposition charge gave the remarkably similar value of 0.243 μm. This estimated mass of deposit based on the charge is extremely accurate suggesting a high deposition efficiency. The SEM image also revealed the film thickness was around 0.27 μm as can be seen from Figure 4.18.

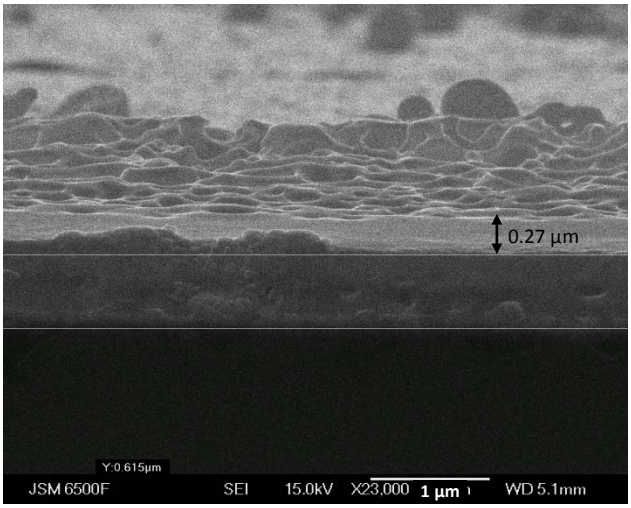

Figure 4.18 FEG SEM photograph of electrodeposited PP2O3 on the quartz crystal resonator

The calculated thickness was slightly underestimated probably because the porous PP2O3 film trapped solvent in the polymer structure.

4.4.1.5 Cycling PP2O3 film

EQCM measurements were then used to confirm the reversibility of the doping and undoping reaction. The film was cycled in the monomer free electrolyte within a reduced potential window to observe mass changes during the doping/dedoping of the polymer. This range is much smaller than normally used as the electronic conductivity of the film was to be completely preserved so that the degradation reaction could be studied later. The information recorded during the EQCM deposition is shown in Figure 4.16.

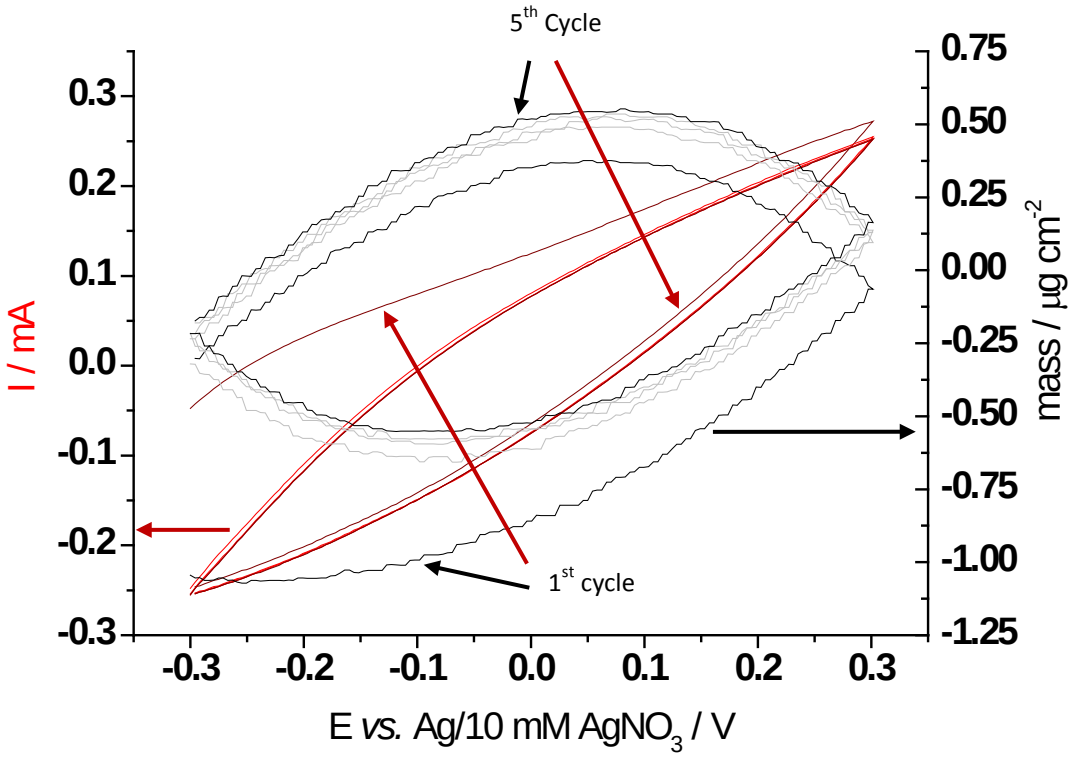

Figure 4.19 Cyclic voltammograms of PP2O3 film from 50 mM LiTFSI in ACN at scan rate of 100 mV/s, a potential window from -0.3 to 0.3 V for 5 cycles.

The mass change curve shown in Figure 4.19 (black and gray curve) started with a negative mass. This was probably due to some trapped P2O3 in the polymer film which diffused away to the monomer free electrolyte. After the second cycle the CVs were very stable and also the mass changes were quite stable. Polymer gained weight and lost almost the same

weight during the doping and dedoping processes respectively. This indicated a reversible reaction between the polymer sample and the ions which exchange in the polymer network. No irreversible chemical changes or degradation occurred during the doping/dedoping processes.

4.4.1.6 Overoxidation treatment of PP2O3 film

The polymer film was cycled again, but at an overoxidation potential range from -0.3 to 1.9V *vs.* Ag/10mM $AgNO_3$ for 25 cycles to destroy its conjugated bonds. The mass changes due to a substitution product were monitored again using an EQCM. The information recorded during the EQCM deposition is shown in Figure 4.16.

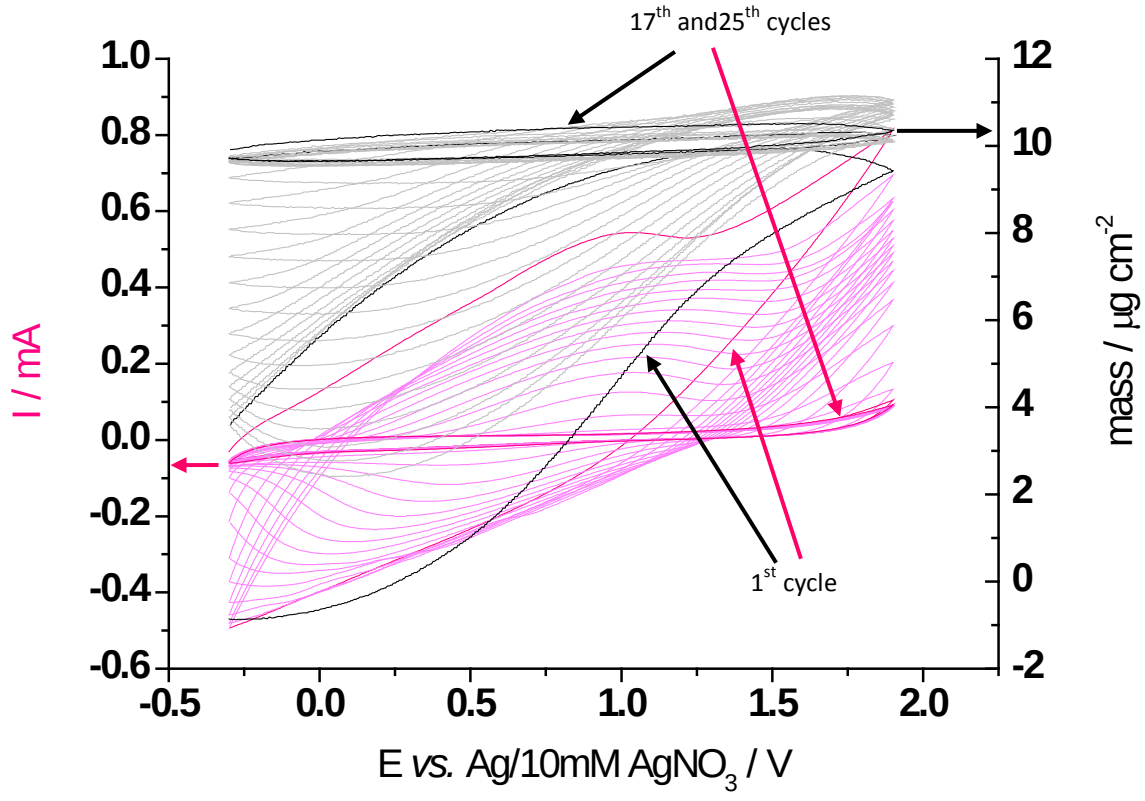

Figure 4.20 Cyclic voltammograms of PP2O3 film from 50 mM LiTFSI in ACN at scan rate of 100 mV/s, potential window from -0.3 to 1.9 V for 25 cycles.

The CV currents shown in Figure 4.20 decreased from cycle to cycle (pink and light pink curves). After 17 cycles only double layer capacitance with small currents and no doping/dedoping behavior was seen. This indicated that the polymer had become unreactive due to interrupted π electron delocalisation from formation of the water substitution product. A suggested mechanism for the overoxidation reaction following a previous report[12] on conductivity loss in unsubstituted polypyrrole which leads to irreversible loss of the electrochemical activity is shown in Figure 4.21. The loss of conjugation clearly breaks the continuity of the electronic conduction path. In this case it is because electrons cannot branch into adjacent aromatic chains. Another key observation is that after degradation of the conductivity in this way the films remained well adhered to the substrate and were mechanically strong. This can be explained by the network formed by the oligoether linkages which maintain this excellent mechanical stability.

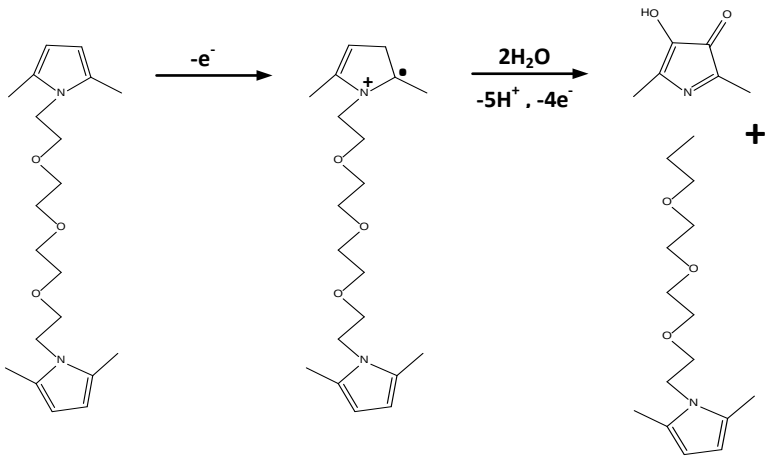

Figure 4.21 Proposed mechanism for overoxidation of PP2O3

From the cyclic voltammograms in Figure 4.20 the data was replotted as voltage, current and mass *vs.* time profiles in order to observe the conductivity degradation behavior more clearly. The plots of these profiles can be seen from Figure 4.22.

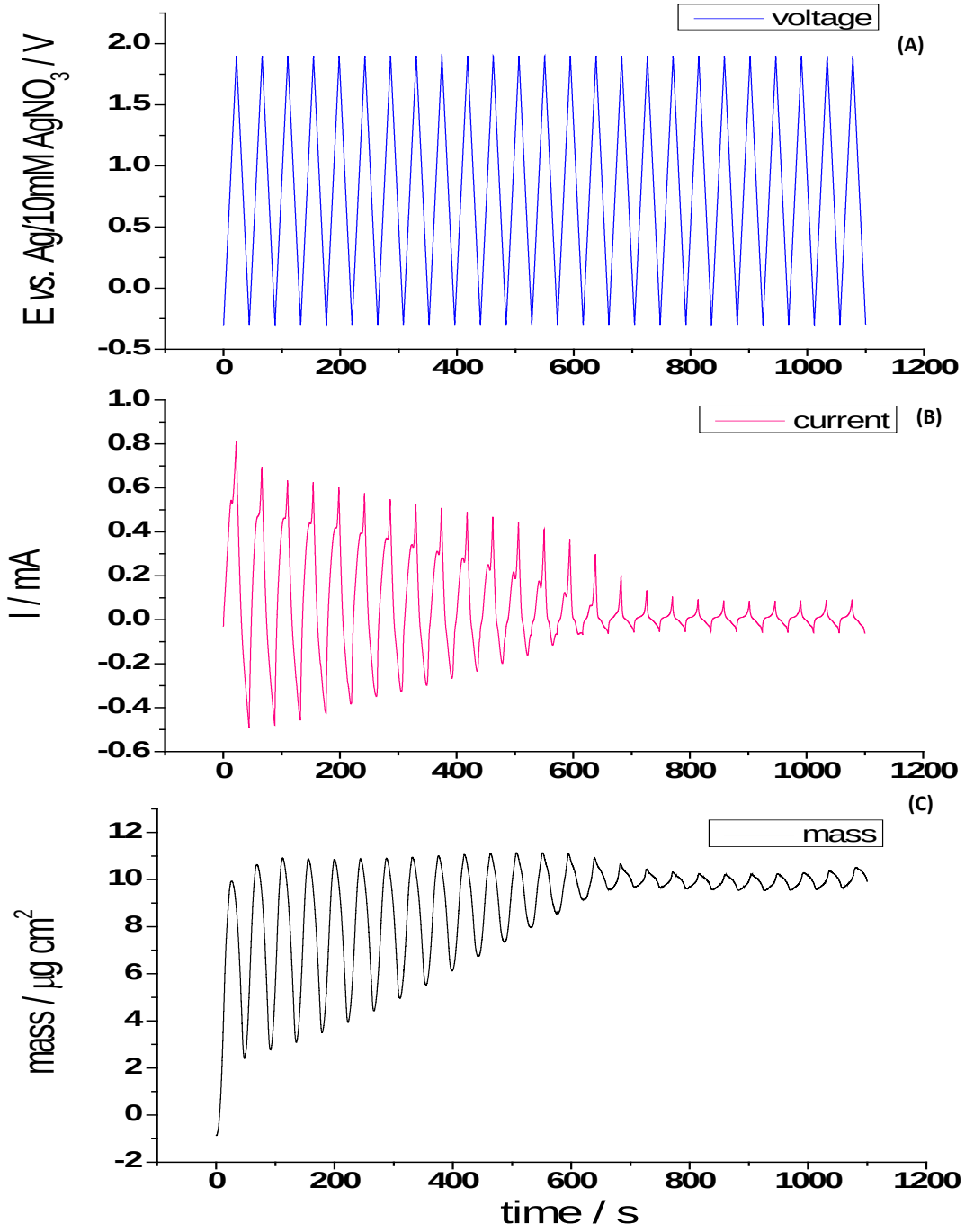

Figure 4.22 plot of (A) votage *vs.* time (B) current *vs.* time and (C) mass *vs.* time of the PP2O3 overoxidation treatment.

From Figure 4.22(C) it can be seen that at +1.9 V *vs.* Ag/Ag^+ the mass was constant in all the cycles. However, at -0.3 V *vs.* Ag/Ag^+ there was a trend of increasing mass from cycle to cycle. These can be explained by gradually increasing amounts of trapped $TFSI^-$ in the polymer network. This occurs as when sections of the polymer become electronically disconnected during the oxidative treatment the TFSI anion cannot be removed. This means that the $TFSI^-$ anion is trapped and the overall film weight is irreversibly increased. With increasing cycle number more and more of the $TFSI^-$ anions were trapped in the polymer network until all the possible electronic conductivity damage by hydroysis is complete i.e. 17 cycles. After cycle 17 the mass changes in each cycle were small over the whole potential window. This agreed well with the flat low current CVs seen after cycle 17 indicating that this substitution is responsible for the breakdown in electrochemical activity.

At the end of cycling the polymer had gained 10.35 $\mu g/cm^2$ (from the original polymer weight itself of 36.04 $\mu g/cm^2$) due to trapped $TFSI^-$ in the polymer network and also the functional group of the substitution product i.e. -OH and =O. Molecular weight of P2O3 and $TFSI^-$ are similar i.e. 292.38 and 280.149 respectively. If we approximate that P2O3 and $TFSI^-$ have the same molecular weight and ignore the small masses gained from the hydrolysis product from -OH or =O substitutions, it could be concluded that the ratio of P2O3 and trapped $TFSI^-$ was approximately 4:1. This proposed structure is shown in Figure 4.23 (B).

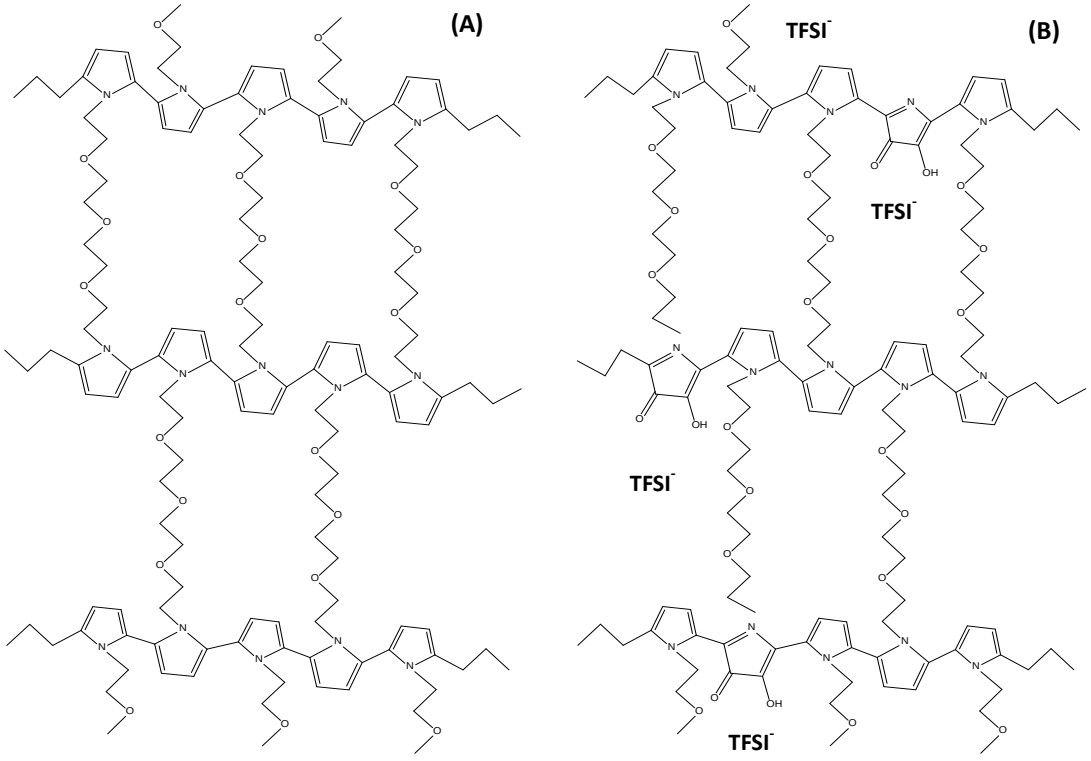

Figure 4.23 Molecular structure of PP2O3 samples (A) untreated and (B) treated (possible -OH and =O substituted PP2O3)

It is important to notice that the treated PP2O3 network lost some oligoether chain linkages between the two pyrrole rings. This also could have an effect on the ionic conductivity of polymer sample.

4.4.2 Chemical treatment for preparing non electronic conductive PP2O3

The method for breaking the conductivity of the chemically prepared PP2O3 samples will now be investigated. The oxidation of alkenes using $KMnO_4$ solution under alkaline condition was used as the technique to destroy the conductivity.

4.4.2.1 Chemicals, Materials, Equipment and Procedure

PP2O3 was prepared as explained in section 4.3.2. $KMnO_4$ and $NaCO_3$ were obtained from Sigma.

PP2O3 (0.2 g) was added into a 200 ml solution of 0.04 M $KMnO_4$ + 0.04 M $NaCO_3$. The mixture was stirred for 3 hrs at 5 °C in order to prevent a further reaction forming MnO_2. The treated PP2O3 product was filtrated and washed with DI water several times[13, 14].

4.4.2.2 Results and Discussion

The proposed untreated and treated polymer networks formed using the chemical preparation technique are shown in Figure 4.24.

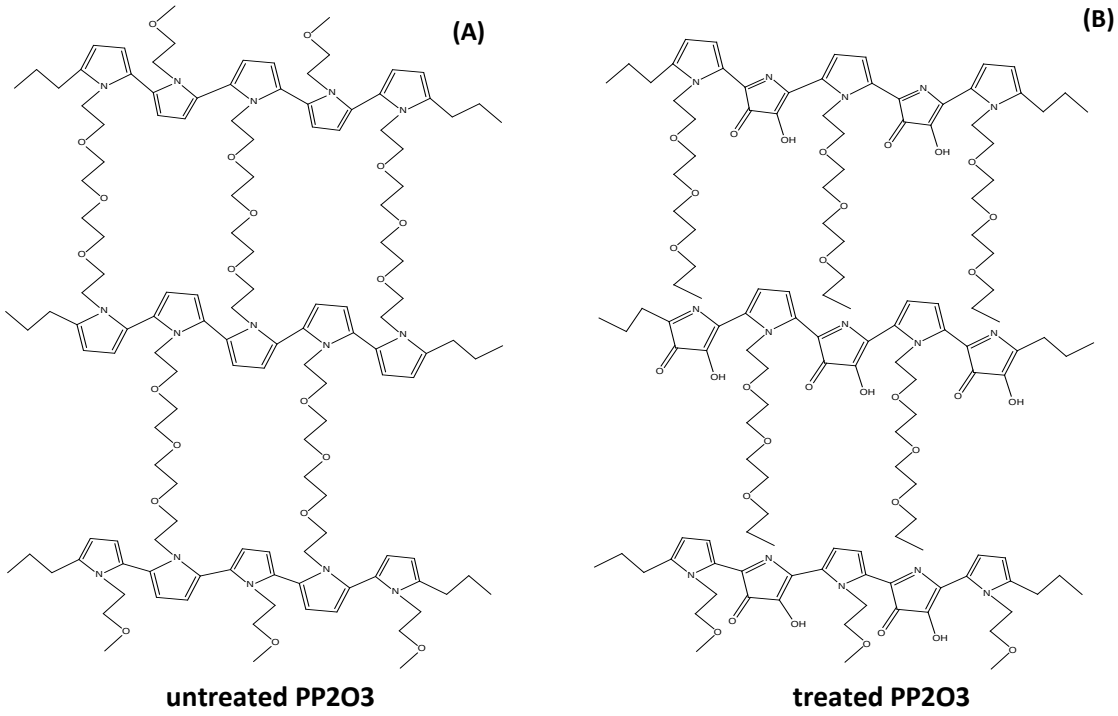

Figure 4.24 Molecular structure of PP2O3 samples (A) untreated and (B) treated

The treated sample has a higher molecular mass than those of untreated one due to a number of substituted OH- and O= groups. It is important to notice that the chemically treated PP2O3 network also lost some oligoether linkage between the two pyrrole rings in the same way as the electrochemically treated one. This could affect the ionic conductivity of polymer sample.

The treated sample was powdery black as can be seen from Figure 4.26 (B). Its IR spectrum is shown in Figure 4.28 (B). The yield wt % was around 106.21 %. The excess mass was probably due to some amount of the by product MnO_2.

4.5 Images and IR spectrums of PP2O3 samples

The visual and IR spectrum characterisation of the PP2O3 samples from all routes will now be compared.

4.5.1 Images of PP2O3 films by electrochemical technique

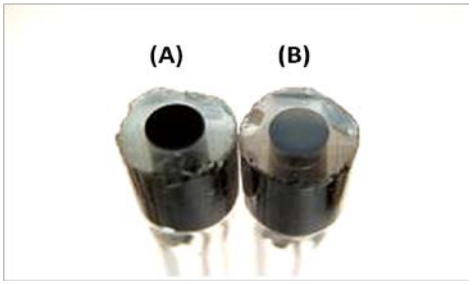

Figure 4.25 Electrochemical synthesised PP2O3 films on glassy carbon electrodes (A) untreated and (B) treated

The untreated and treated films are shown in Figure 4.25 (A) and (B) respectively. The untreated sample was a dark black conformal film. This film was well adhered to the surface and appeared to be mechanically strong. The treated sample had turned to a lighter gray, indicating a loss of electronic conductivity. However, the film was still well adhered to the substrate and appeared to have maintained its mechanical strength.

4.5.2 Images of PP2O3 samples by chemical technique

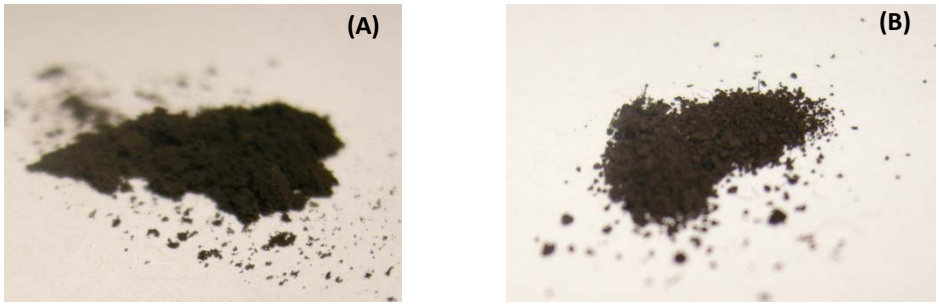

Figure 4.26 Chemically synthesised PP2O3 samples (A) untreated and (B) treated

The chemically prepared untreated and treated samples are shown in Figure 4.26 (A) and (B) respectively. They both looked like similar dark grey fine powders.

4.5.3 IR spectrum of PP2O3 film by electrochemical technique

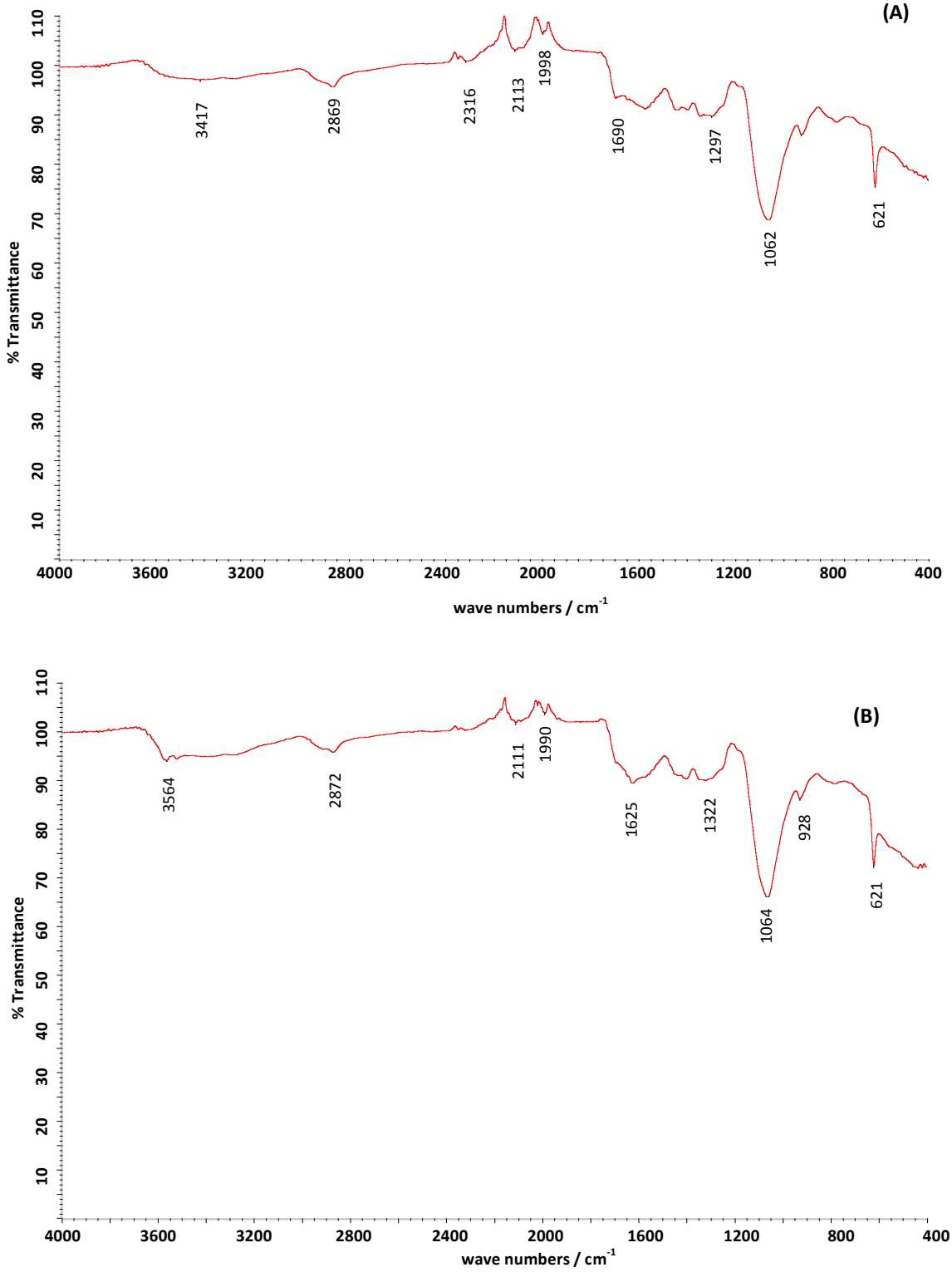

Figure 4.27 IR spectrum of PP2O3 samples by electrochemical technique (A) untreated and (B) treated

Figure 4.27 shows the treated and untreated samples prepared by electrochemical technique; both spectra appear similar. A C-H stretch at about 2870 cm^{-1}, C=C stretch at about 1690 cm^{-1} and C-O stretch at about 1060 cm^{-1} can be seen. In case of treated sample there was a broad peak about 3500 cm^{-1}. This was probably an O-H stretch peak due to substituted OH groups on pyrrole rings as can be seen from Figure 4.23(B). Unexpectedly at 1690 cm^{-1} the two samples had a similar intensity. In the case of the treated sample this is possibly because the C=C and C=O s (C=O substitution on pyrrole rings) peaks overlapped. The treated sample contained less C=C when compared with untreated sample but included C=O, thus there was no obvious difference in this band between the two samples. Also this was possibly due to a small intensity of the C=C. We could only see a small increase in the O-H stretches from the electrochemical treatment. This is similar to what is expected from the EQCM results where the mass increase predicted only a small change to the polymer structure.

4.5.4 IR spectrum of PP2O3 sample by chemical technique

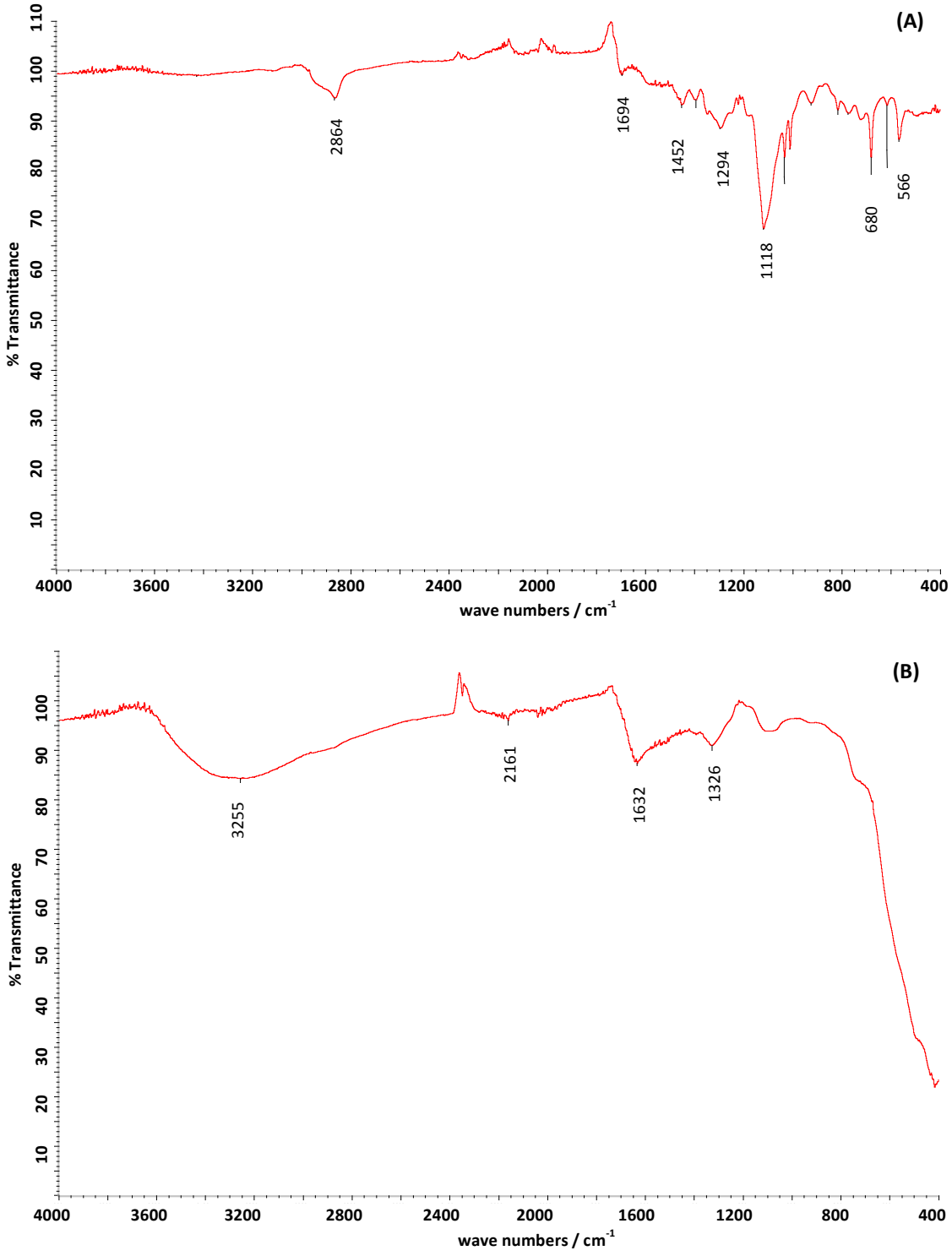

Figure 4.28 IR spectrum of PP2O3 samples by chemical technique (A) untreated and (B) treated

The IR spectrums of the untreated and treated samples prepared by the chemical technique were obviously different as shown in Figure 4.28. In the case of the untreated sample, there was a C-H stretch at about 2864 cm^{-1}. IR spectrum of the treated sample composed of a broad band O-H stretch at about 3255 cm^{-1}. This is consitent with the large increase in hydroxyl groups predicted by the scheme presented in Figure 4.24. The region below 1500 cm^{-1} generally consisted of a large number of absorptions due to C-C, C-O and C-N single-bond vibration that are unique for each organic molecule known as fingerprint region[15]. However, IR spectrums of untreated and treated samples in this region were not similar because the treated sample was probably contaminated by the by-product MnO_2. The IR spectrum of pure MnO_2 is shown for information in Figure 4.29. The IR spectrum of MnO_2 consisted of a very broad shoulder at this region and a slope above 600 cm^{-1}. This possibly explains the IR spectrum in the fingerprint region of the treated sample that composed of broad peaks and a slope above 600 cm^{-1} as a combination of major treated sample and small amount of MnO_2 by product.

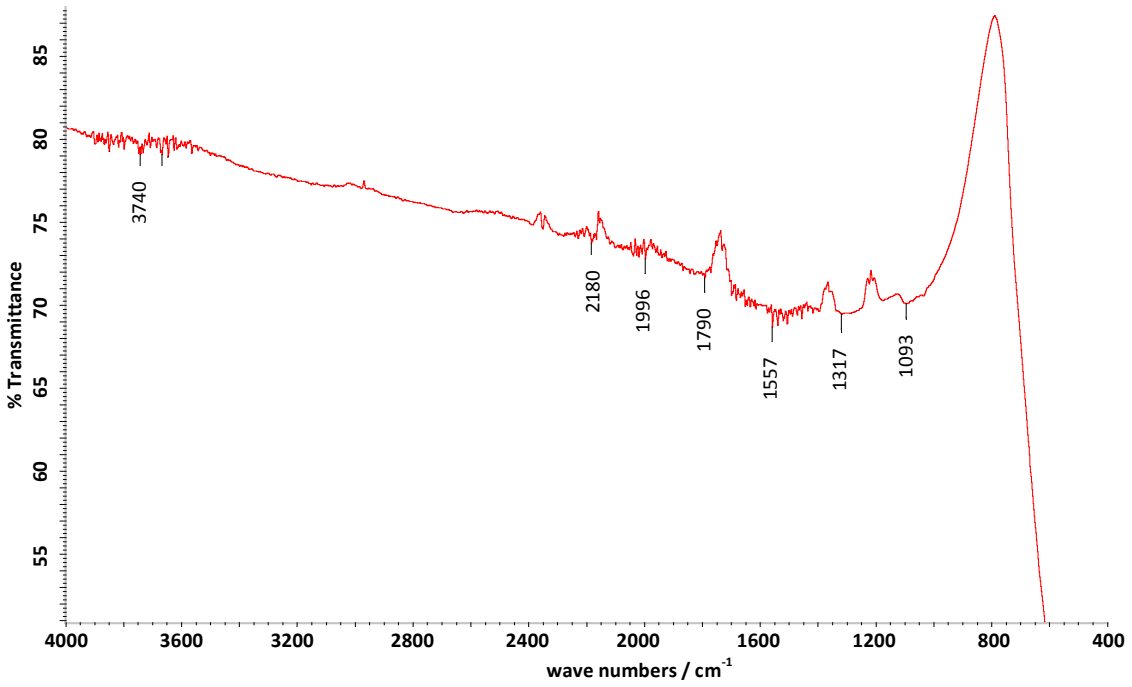

Figure 4.29 IR spectrum of pure MnO_2

4.6 Chapter 4 Conclusion

The results from the electrochemical deposition show that it is possible to prepare films of PP2O3 in both aqueous and non aqueous solutions. It was also found that the film from TSNa solution was thinner than those of the film from SDS solution. This was probably because SDS surfactant facilitated electrodeposition of PP2O3 by lowering the oxidation potential. In case of non aqueous solution the films from LiTFSI and $TEABF_4$ were much thicker than those of the film from aqueous solution.

The electrochemical treatment to convert PP2O3 to an electronically insulating material was successful. EQCM was used as a technique to monitor the mass changes due to the electrochemical behavior of the polymer sample during the entire overoxidation treatment. A continuously increasing mass due to trapped $TFSI^-$ anions in the non electrochemically active sites of polymer network during the treatment was seen. Finally the treated PP2O3 was converted to non electronically conductive with the rough ratio of P2O3 and trapped $TFSI^-$ of 4:1.

Both chemical polymerisation and treatment of PP2O3 were successful with high yield% i.e. 83.83 % and 106.21 % respectively. The latter was overweight due to addition of substituted OH- and O= groups on pyrrole rings and probably small amounts of the by-product MnO_2.

Untreated and treated PP2O3 samples were successfully prepared by both chemical and electrochemical techniques.

In the next chapters chemically and electrochemically synthesised untreated and treated PP2O3 are characterised to investigate their conductive properties. PP2O3 samples were then tested in real battery applications.

4.7 Chapter 4 References

[1] M. G. Minett in *New composite insertion electrode materials for secondary lithium cells*, *Vol. PhD* University of Salford, **1989**, p. 22.
[2] S. C. Luo, E. M. Ali, N. C. Tansil, H. H. Yu, S. Gao, E. A. B. Kantchev and J. Y. Ying, *Langmuir* **2008**, *24*, 8071-8077.
[3] X. Du and Z. Wang, *Electrochimica Acta* **2003**, *48*, 1713-1717.
[4] N. Sakmeche, J. J. Aaron, M. Fall, S. Aeiyach, M. Jouini, J. C. Lacroix and P. C. Lacaze, *Chemical Communications* **1996**, 2723-2724.
[5] N. Sakmeche, S. Aeiyach, J. J. Aaron, M. Jouini, J. C. Lacroix and P. C. Lacaze, *Langmuir* **1999**, *15*, 2566-2574.
[6] D. O. Kim, P. C. Lee, S. J. Kang, K. Jang, J. H. Lee, M. H. Cho and J. D. Nam, *Thin Solid Films* **2009**, *517*, 4156-4160.
[7] I. Fernandez, M. Trueba, C. A. Nunez and J. Rieumont, *Surface & Coatings Technology* **2005**, *191*, 134-139.
[8] P. Novak, B. Rasch and W. Vielstich, *Journal of the Electrochemical Society* **1991**, *138*, 3300-3304.
[9] J. L. Zubimendi, L. Vazquez, P. Ocon, J. M. Vara, W. E. Triaca, R. C. Salvarezza and A. J. Arvia, *Journal of Physical Chemistry* **1993**, *97*, 5095-5102.
[10] Z. Decoste, *Introductory Chemistry*, Charles Hartford, Boston, **2008**, p. 42.
[11] J. Tietje-Girault, C. Ponce de Leon and F. C. Walsh, *Surface & Coatings Technology* **2007**, *201*, 6025-6034.
[12] R. Ansari, *E-Journal of chemistry* **2006**, *3*, 8.
[13] P. Darpan, *Competition Science Vision* **1999**, *2*, 136.
[14] S. Wolfe, C. F. Ingold and R. U. Lemieux, *Journal of the American Chemical Society* **1981**, *103*, 938-939.
[15] J. McMurry, *Fundamentals of organic chemistry 4th*, International Thomson Publishing Europe, London, **1998**, p. 413-414.

Chapter 5

Ionic and Electronic Conductivities of PP2O3

5.1 Introduction

Ionic and electronic conductivity are the most significant properties of polymer electrolytes. An ionic conductivity of 10^{-2} – 10^{-3} S cm^{-1} would be ideal at room temperature, however, a lower value, not less than 10^{-5} S cm^{-1}, may also be acceptable[1]. The films must act as an electronic insulator as even small levels of electronic conductivity lead to self discharge of the battery. In this work, ionic and electronic conductivities of electrodeposited PP2O3 films were measured by Electrochemical Impedance Spectroscopy (EIS) and interpreted using the simple Randles circuit shown in Chapter 2 and its transmission line equivalent, modified to show the effect of introducing increasing levels of electronic resistance as the electronic conductivity decreases.

The electronic and ionic conductivities of PP2O3 were measured for both bulk powders produced by chemical polymerisation and thin films prepared on glassy carbon electrode acting as a support and electrical contact. In the latter case, the conductivities were determined as a function of the applied doping potential after equilibration in a lithium ion electrolyte. The electronic conductivities of the samples were then reduced by overoxidation treatments, using cyclic voltammetry in the case of supported films, and chemical treatment for the powders as reported in Chapter 4. Finally the conductivities were measured again to evaluate the effects of the treatments.

As explained below, a mixed conductor can be represented by a two-channel transmission line, one channel for the electronic conducting network structure and another one for the interpenetrating network of ionic conducting regions filling the pores. Thus the standard two-channel transmission line shown in Figure 5.1(A) can represent both types of polymer sample used in this work with the notation R_1, R_2, C_1 represents the total ionic resistance, the electronic resistance and the interfacial capacitance of the pore. The two types of *measurement*, for the bulk and thin film samples respectively, are differentiated in the two submodels by the nature of the electrical contacts made to the measuring circuit as also shown in Figure 5.1(B). For the bulk sample, both contacts (X) and (Y) are metallic, i.e. electronically conducting and blocking to ions. This is simulated by the Short Warburg, W_S in the Scribner Z-view fitting software, also known as the Finite Length Warburg (FLW) in

the literature. For the film sample, one contact, (Y), is electronically conducting carbon, and the other (Z) is the ionic conducting electrolyte. A similar model was described many years ago by Albery *et al.*[2] It is called an Open Warburg (W_o) in Z-view and a Finite Space Warburg (FSW) in the literature.

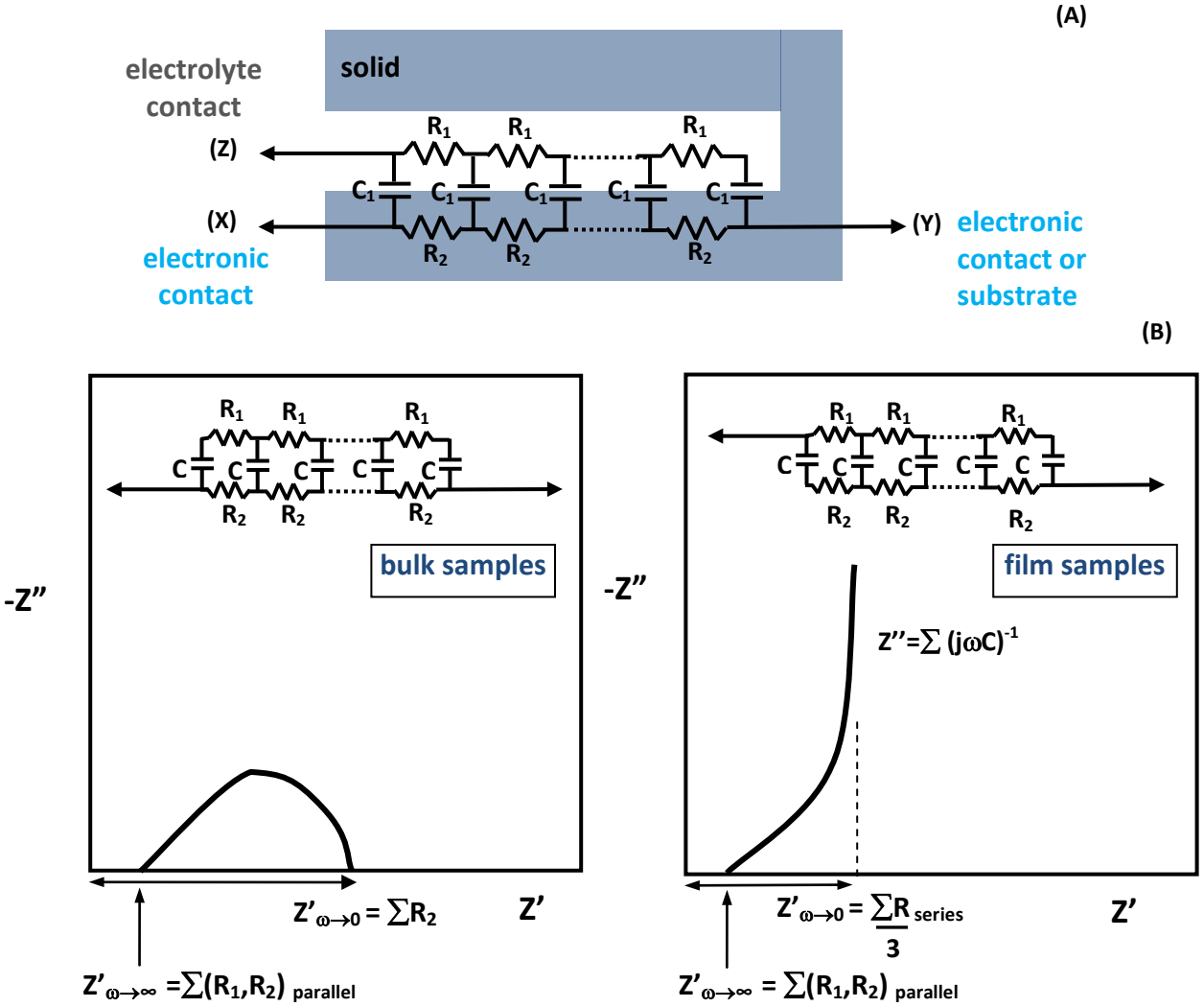

Figure 5.1 Equivalent circuits and Nyquist plot impedance of mixed ionic and electronic conducting porous polymer in electrolyte. R_1: ionic resistance, R_2 : electronic resistance and C_1 : solid/liquid interface capacitance[3]. The arc-like shape of the Shorted or Finite Length Warburg Impedance is obtained for the symmetrical electronic contacts and the λ-shape of the Open or Finite Space Warburg is obtained for a sample placed between an electronic contact and an electrolyte. The Warburg impedance components used in fitting programs such as Z-view usually approximate the resistance of one channel to zero. We therefore must account for the additional resistance at high frequency by adding the parallel resistance of the two lines to the normal Warburg expression.

Two schematic results of the model are shown in Figure 5.1(B) with regions near the origin representing the high frequency limit where the capacitors are effectively short circuits. Here the impedance equals the parallel resistance combination of both channels regardless of whether the contacts are between (X) and (Y) or (Z) and (Y). Commonly the resistances of the ionic and electronic channels are very different, in which case the parallel resistance is simply the smaller of the two. Conversely, if they are equal, the parallel resistance is half that of each channel. In general, the parallel resistance will lie somewhere between the smaller of the two resistances and half that value. N.B. The Warburg impedance components used in fitting programs such as Z-view usually approximate the resistance of one channel to zero. We therefore must account for the additional resistance at high frequency by adding the parallel resistance of the two lines in series with the normal Warburg expression.

Towards the low frequency, high impedance end here follows a Warburg impedance region, with a 45^{o} slope (or less in the case of CPE behaviour) up to the frequency where the two submodels diverge towards different low frequency limits.

The impedance at the low frequency limit depends on the submodel. In the case of the two electronic contacts (X) and (Y) we have simply the total resistance in the electronic line. For alternate contacts (Y) and (Z) we have the total capacitance of the ionic/electronic conductor interface, represented by an upward straight line (90^{o} or less for a CPE). In the general case, the real part is limited to one third of the combined series resistance due to *both* lines. When one resistance dominates e.g. the ionic resistance, this reduces to the standard De Levie impedance[4] where the real part becomes a third of the dominant resistance. The low frequency limit in this case can therefore be interpreted in terms of the electronic or the ionic conductivity, whichever is believed to be the higher[3].

Finally, we can anticipate the *approach* to the low frequency conductivity limit in the two submodels by considering equivalent circuits that represent the transmission line in the finite boundary condition. These are shown in Figure 5.2.

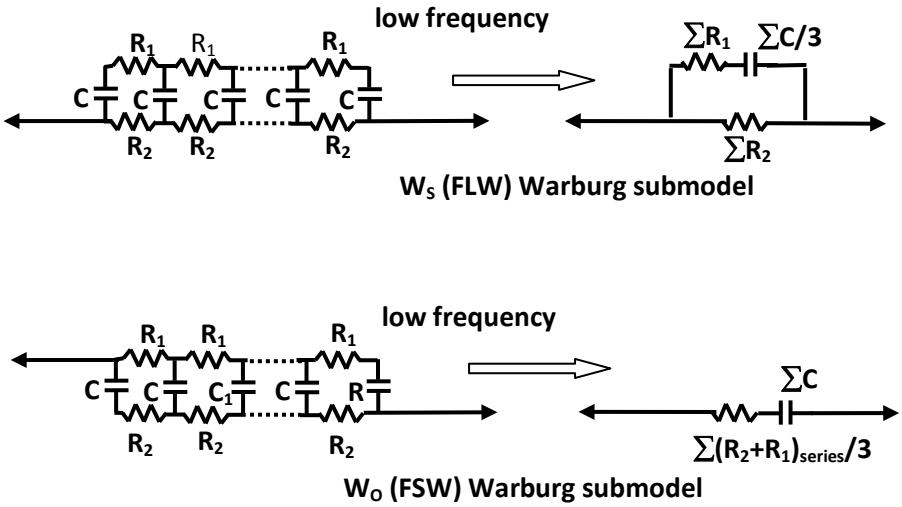

Figure 5.2 Approximations of equivalent circuits for the finite boundary condition at low frequency. Top is for the (X)(Y) contacts and bottom for the (X)(Z) contacts.

5.2 Conductivity Measurements for Bulk Powder Samples

5.2.1 Chemicals and Materials

Untreated and treated PP2O3 samples were chemically synthesised as explained in Chapter 4, LiTFSI and PTFE were purchased from Sigma and carbon loaded gasket (C5-9134 carbon loaded conductive silicone) was obtained from RS.

A pellet contained PP2O3 sample, LiTFSI (lithium salt), PC (plasticiser) and PTFE (binder). PP2O3, LiTFSI ([O]/[Li] = 10) and PC59 %wt total content were mixed together by adding ACN 7 ml. The mixtures were stirred and left overnight. To eliminate ACN the mixture was heated up at 80 ^{o}C for 1 hr and then it was ground with PTFE (2.5 %wt of PP2O3) to form polymer film. The film was rolled to give a thickness of 200 μm. The polymer film was cut into pellets of diameter 1.1 cm^2. Pellets were dried under vacuum overnight to eliminate ACN and moisture before impedance measurement in a glove box.

5.2.2 Equipment and Procedure

The polymer pellets were sandwiched between two ionically blocking carbon electrodes and connected to a potentiostat (Ivium Plus module: for the CompactStat) as shown in Figure 5.3. This was used for ionic and electronic conductivity measurements by EIS at frequency range from 500 KHz to 0.01 Hz with 10 mV amplitude at 20, 30, 40 and 50 ^{o}C.

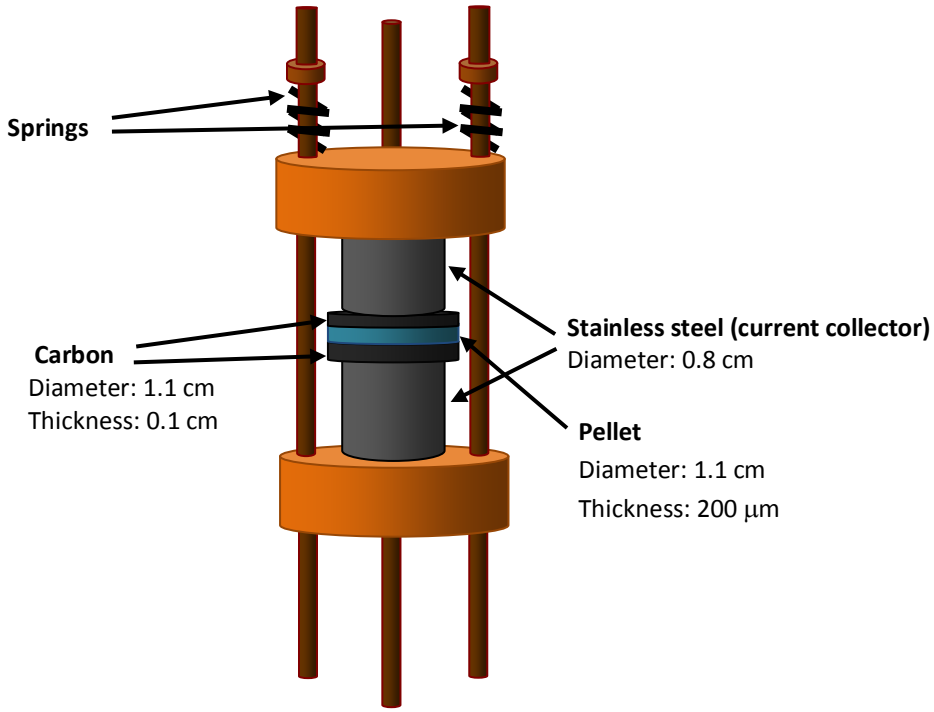

Figure 5.3 The two ionic blocking electrode cell configuration for measuring ionic and electronic conductivity of PP2O3 samples by impedance technique

5.2.3 Results and Discussion

Untreated Samples

Nyquist plots for untreated samples are shown in Figure 5.5 and Bode plots are shown in Fig 5.6. The real part at the highest frequency is interpreted as the parallel, ionic electronic combination, which simplifies to the ionic resistance in this case since this is much less than the electronic resistance. An initial (depressed) semicircle, spans from R_{ionic} due to R_{ct} - C_{dl} combinations, possibly at both electrode/polymer interfaces. This is followed by a line of 45^o slope suggesting a Warburg impedance and indicating a diffusion process or transmission line of finite length as in the normal Randles circuit. A slight curvature is seen at the low frequency end of the Nyquist plot is interpreted as a surprisingly small electronic conductivity. A Finite Length Warburg, or Short Warburg, W_s submodel is used to include the effect of a finite electronic conductivity all the way across the sample. The Bode plot in Figure 5.6 shows an accurate fit, using the modified Randles equivalent circuit of figure 5.4 to fit the final curvature.

The circuit parameters defining W_s are given in Table 5.1 and their significance is explained below.

W_R (Ω) – the resistance at zero frequency, e.g. the electronic resistance.

W_T (sec).– the charge storage time constant, L^2/D or W_R x $\sum C$ /3.

W_P – a parameter representing the slope of the Nyquist plot as a fraction of 90^o

R_{ct} is the charge transfer resistance encountered by electrons entering the transmission line. C_{dl} is the double layer capacitance is shown as being in parallel with R_{ct}.

R_{ionic} is the ionic resistance, appearing as the high frequency resistance.

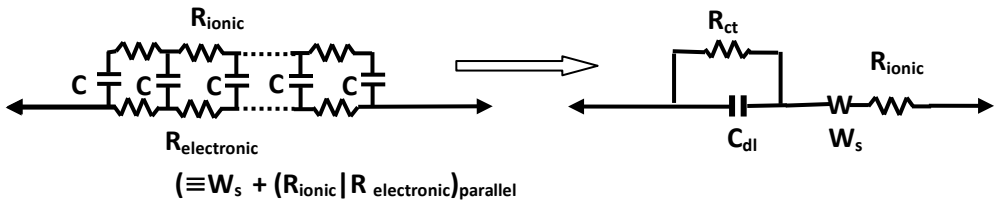

Figure 5.4 The equivalent circuit of the untreated sample, expressed as a modified Randles circuit in which the Warburg impedance is terminated in a short circuit and represented by W_S.

The zero frequency resistance W_R becomes equal to $R_{electronic}$ because the ionic channel is blocked. The low frequency limit only shows a hint that it will eventually curve over and progress to intercept the real axis because this feature was not accessible within the frequency range of measurement. At the high frequency limit we observe a parallel combination of ionic and electronic resistances in series with R_{ct} forming an arc with C_{dl}.

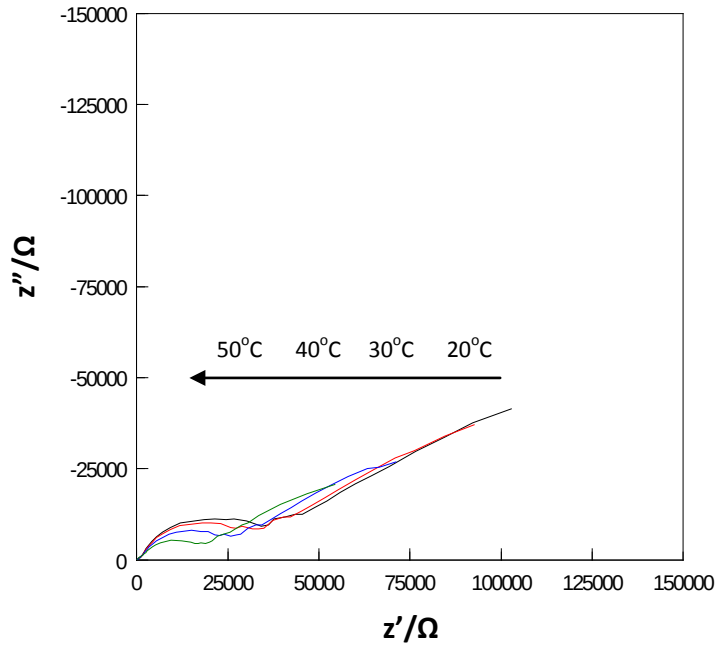

Figure 5.5 Resulting impedance of untreated samples from 500 KHz to 0.01 Hz at various temperatures i.e. black:20 °C, red 30 °C, blue:40 °C and green:50 °C

An example of the fitting impedance of untreated samples at 20 ^{o}C is shown in Figure 5.6 and fits at other temperatures are shown in Appendix 3.

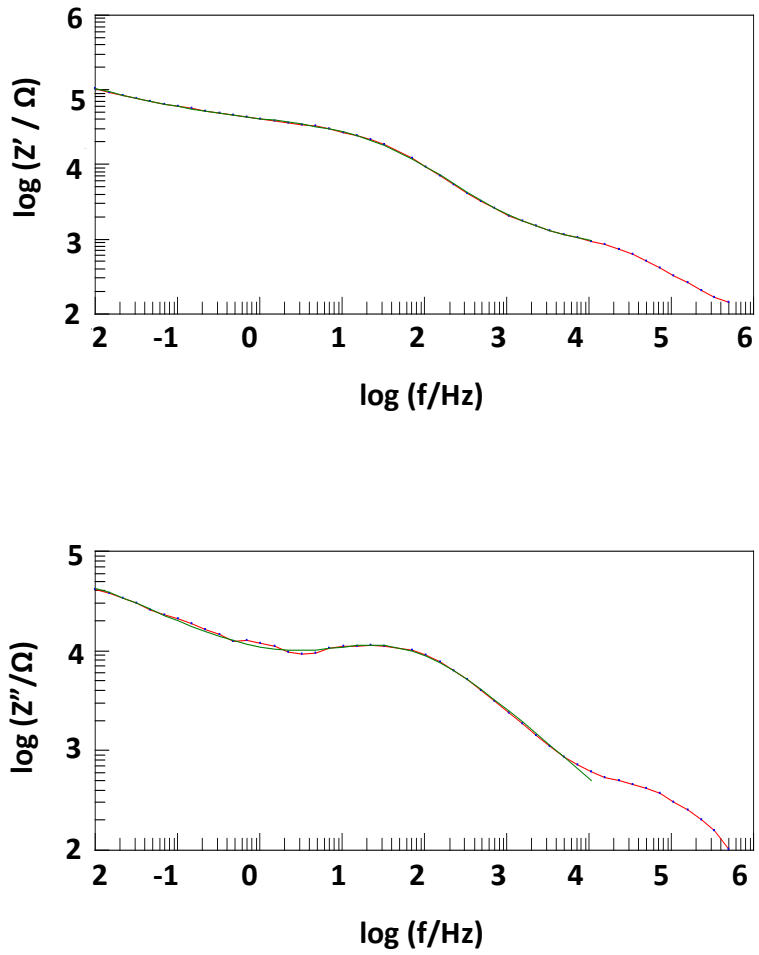

Figure 5.6 Fitting the equivalent circuits to impedance of the untreated sample at 20 ^{o}C (A) log Z' vs logf and (B) log Z" vs logf

Treated samples

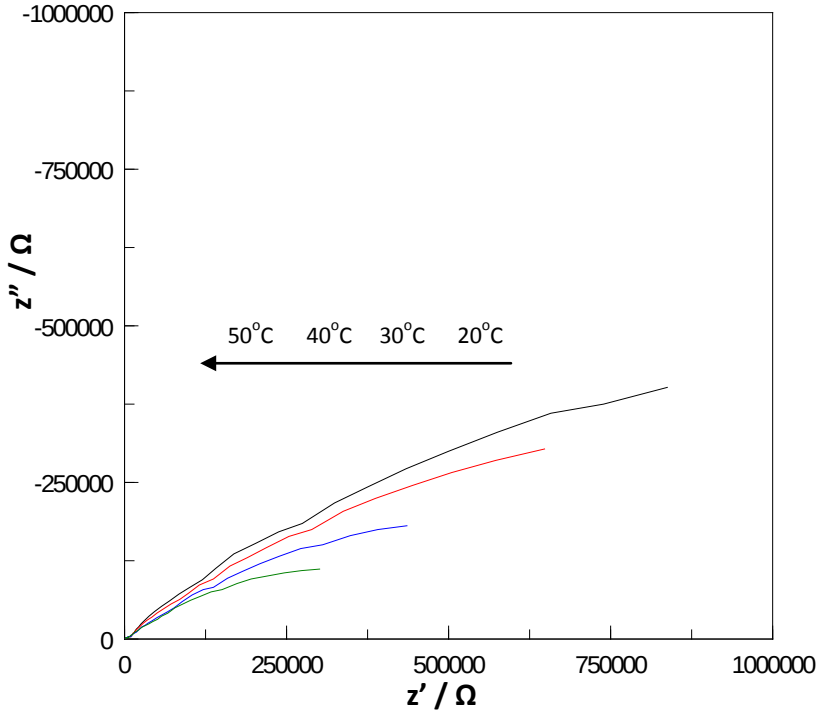

Figure 5.7 Nyquist plots of treated samples from 500 KHz to 0.01 Hz at various temperatures i.e. black:20 °C, red 30 °C, blue:40 °C and green:50 °C

The Nyquist plots are shown in Figure 5.7 and Bode plots in Figure 5.9. These could not be fitted directly to the anticipated form of a Short (Finite Length) Warburg as used for the untreated material. However, the equivalent circuit of Figure 5.8 gave very good fits, using a CPE and a parallel resistor to represent the well-formed semicirular arcs characteristic of the data. The circuit can be rationalised according to a CPE to represent an *infinite* Warburg (i.e. one with a W_T value far above the cycle period at the lowest frequency used). The CPE –T values, representing the amount of charge stored in the doping reaction, were found to be an order of magnitude lower than the treated samples, characteristic of the destruction of redox activity due to the treatment. The independent electronic short, $R_{electronic}$ is taken to indicate that the short circuit does not represent electronic conductivity in the bulk material, but a leakage curent from some filaments of residual conducting material percolating through an otherwise electronically insulating bulk material. Finally, a series resistance,

representing the high frequency limiting impedance is added, improving the fit at high frequency.

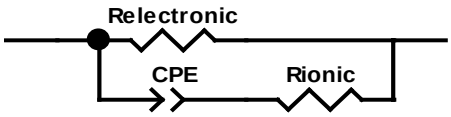

Figure 5.8 The equivalent circuit used to fit the treated samples.

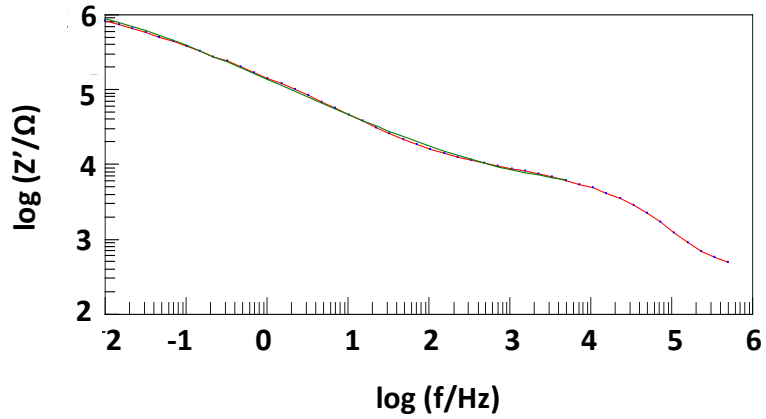

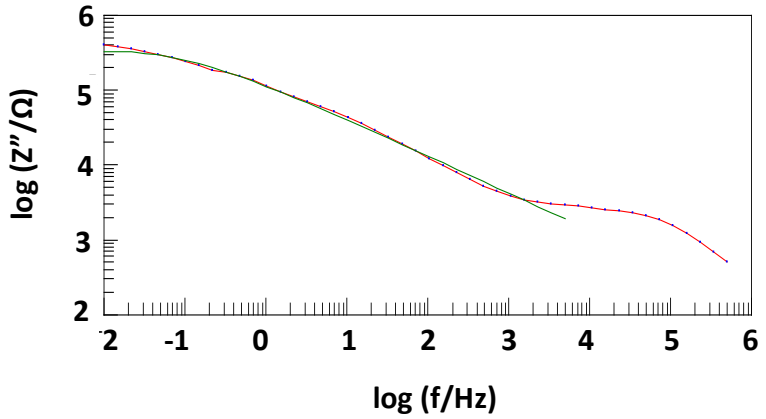

Figure 5.9 Fitting the equivalent circuits to impedance of the treated at 20 ^{o}C (A) log Z' vs logf and (B) log Z" vs logf

Discussion

The values of electronic conductivity were lower than expected for the untreated samples. Several factors may be responsible for poor intra-chain conductivity, e.g. dilution of the electron path by the polyether co-polymer, poor linearity of the conjugated chains, a low doping level. Large charge transfer resistances between chains could also give a low inter-chain conductivity. The electronic conductivities of the treated samples were lower still and, as mentioned above, represented occasional conducting paths within an otherwise uniformly insulating material.

The activation energy is evaluated for each polymer type in the Arrhenius plots of Figure 5.10, 5.11, 5.12 and 5.13 with the associated errors. The activation energy values are tabulated in Table 5.3. The temperature dependence is therefore interpreted according to the standard model of electron (or polaron) hopping along the polymer chain. The raw data show clearly that the treatment resulted in a substantial loss of electronic conductivity and the activation energies show that the average hopping distances were much larger in the treated material.

The ionic conductivity values are typical of non-aqueous plasticised polymer electrolytes, e.g. in the range of 2.9-5.5 x 10^{-5} and 4.8-9.3 x 10^{-6} S/cm for untreated and treated respectively.

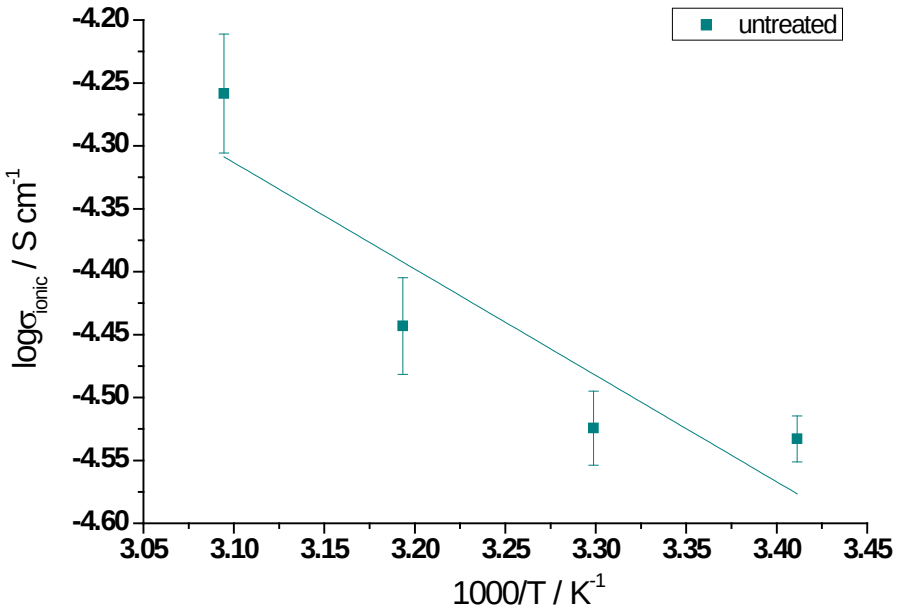

Figure 5.10 The plot of log σ_{ionic} *vs.* temperatures (1000 K^{-1}) of the untreated sample

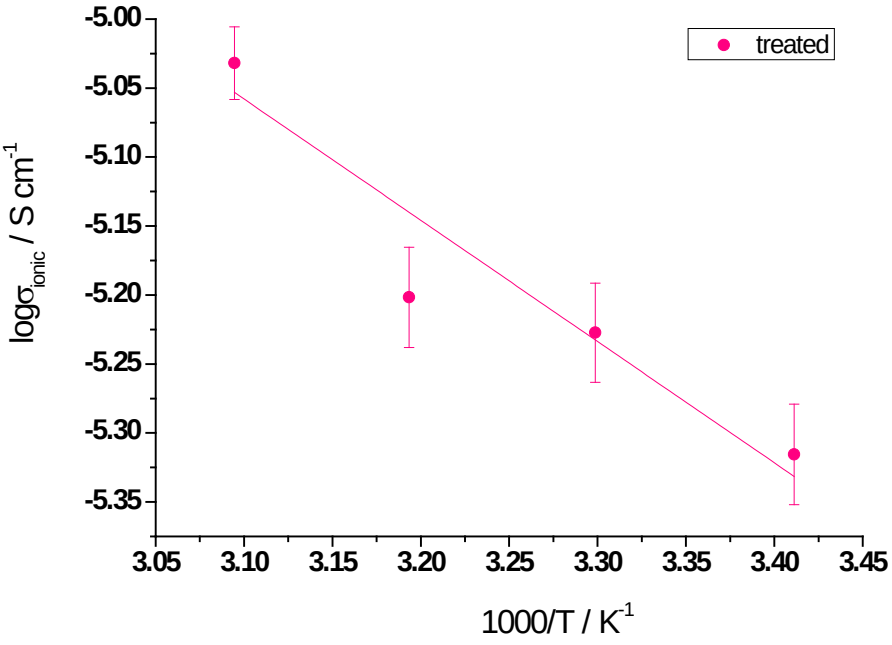

Figure 5.11 The plot of log σ_{ionic} *vs.* temperatures (1000 K^{-1}) of the treated sample

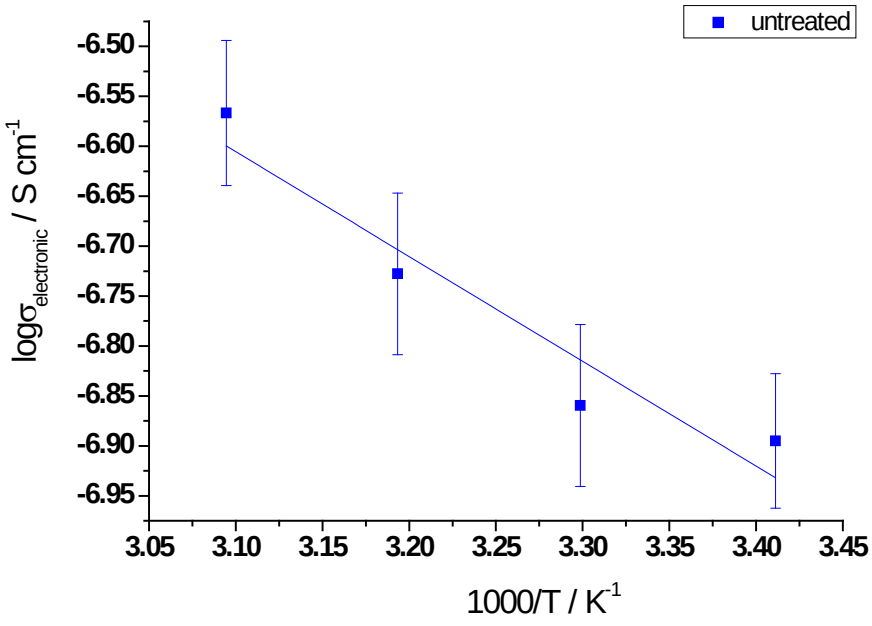

Figure 5.12 The plot of log $\sigma_{electronic}$ *vs.* temperatures (1000 K^{-1}) of the untreated sample

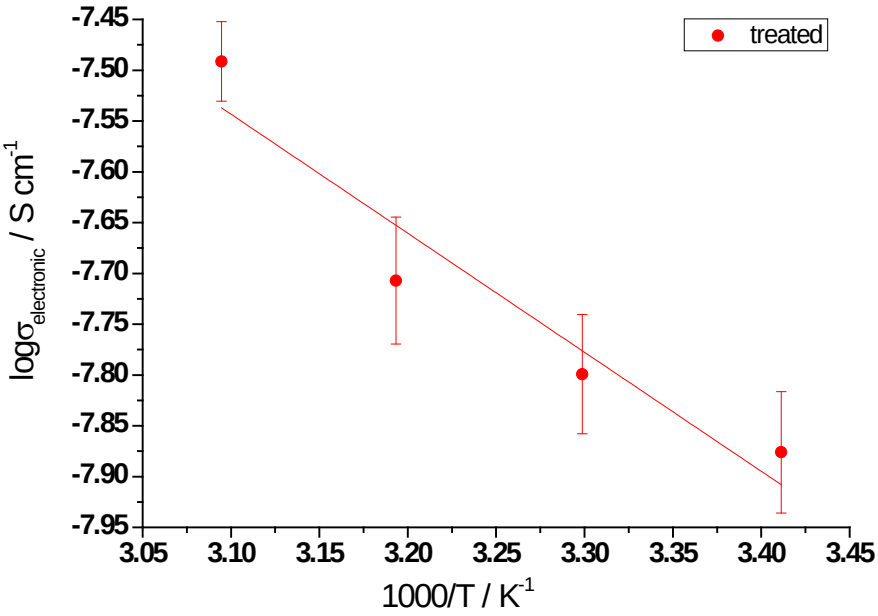

Figure 5.13 The plot of log $\sigma_{electronic}$ *vs.* temperatures (1000 K^{-1}) of the treated sample

Table 5.1 The parameters obtained from fitting the impedance of the untreated samples to the equivalent circuit of Figure 5.4. R_{ionic} was estimated from the high frequency limiting resistance. W-R represents the electronic resistance, W-T the diffusion time constant. R_{ct} is an interfacial charge transfer resistance, C is the redox storage capacitance, estimated from W_T/W_R, D is the diffusion coefficient (L^2/W-T) and CPE-T approximates the double layer capacitance, using a constant phase element to express nonideality.

Temp. (^oC)	R_{ionic}[a] (Ω)	(W-R)[b] (Ω)	W-T[c] (s)	W-P[d]	R_{ct}[e] (Ω)	$C_{storage}$ (F)	D ($cm^2\ s^{-1}$)	CPE-T[f] (F)	CPE-P[g]
20	718	$1.65x10^5$	112	0.36	30360	$6.77x10^{-4}$	$3.57x10^{-6}$	$5.71x10^{-7}$	0.73
30	704	$1.52x10^5$	115	0.36	28531	$7.53\ x10^{-4}$	$3.48x10^{-6}$	$6.96x10^{-7}$	0.70
40	584	$1.13x10^5$	96	0.36	23580	$8.54\ x10^{-4}$	$4.16x10^{-6}$	$9.79x10^{-7}$	0.65
50	382	$7.77x10^4$	74	0.36	17641	$9.47\ x10^{-4}$	$5.44x10^{-6}$	$1.55x10^{-7}$	0.60

a 2-12%error from fitting the impedance to equivalent circuit
b 9-15%error from fitting the impedance to equivalent circuit
c 31-29%error from fitting the impedance to equivalent circuit
d 2-5%error from fitting the impedance to equivalent circuit
e 2-6%error from fitting the impedance to equivalent circuit
f 1-2%error from fitting the impedance to equivalent circuit
g 1-2%error from fitting the impedance to equivalent circuit

Table 5.2 The parameters from the fitting impedance of the treated samples. R_{ionic} and $R_{electronic}$ were obtained by fitting to the circuit of Figure 5.8. The CPE represents a double layer capacitance which is non-ideal due to some microstructure at the electronic / ionic interface.

Temp.(^oC)	R_{ionic}[a] (Ω)	(W-R)[b] (Ω)	CPE-T[c] (F)	CPE-P[d]
20	4355	$1.58x10^6$	$2.12x10^{-6}$	0.50
30	3554	$1.33x10^6$	$2.78x10^{-6}$	0.47
40	3350	$1.07x10^6$	$4.12x10^{-6}$	0.42
50	2266	$6.53x10^6$	$5.46x10^{-6}$	0.41

a 3-5%error from fitting the impedance to equivalent circuit
b 3-7% error from fitting the impedance to equivalent circuit
c 1-2%error from fitting the impedance to equivalent circuit
d 0.6-1% error from fitting the impedance to equivalent circuit

Table 5.3 Effective Activation energies E_a for the ionic and electronic conductivities of the untreated and treated samples as obtained from the Arhhenius plots of Figure 5.10 to 5.13.

Sample	**E_a (kJ/mol)**	
	σ_i	σ_e
untreated	16.18	20.09
treated	15.80	22.43

5.3 Preparation of Thin Film Samples

5.3.1 Chemicals, Materials and Equipment

P2O3 was synthesised as explained in Chapter 4. ACN and LiTFSI were obtained from Aldrich.

The cell for the transmission line model impedance measurement of the film samples is shown in Figure 5.14. A glassy carbon (radius : 0.15 cm and surface area : 0.07 cm^2), Ag/10 mM $AgNO_3$ and Pt gauze were used as working, reference and counter electrodes respectively. The cell was fabricated and sealed in a glove box. The cell was then connected to a potentiostat (VMP2 from Bio Logic science instruments) for impedance measurement.

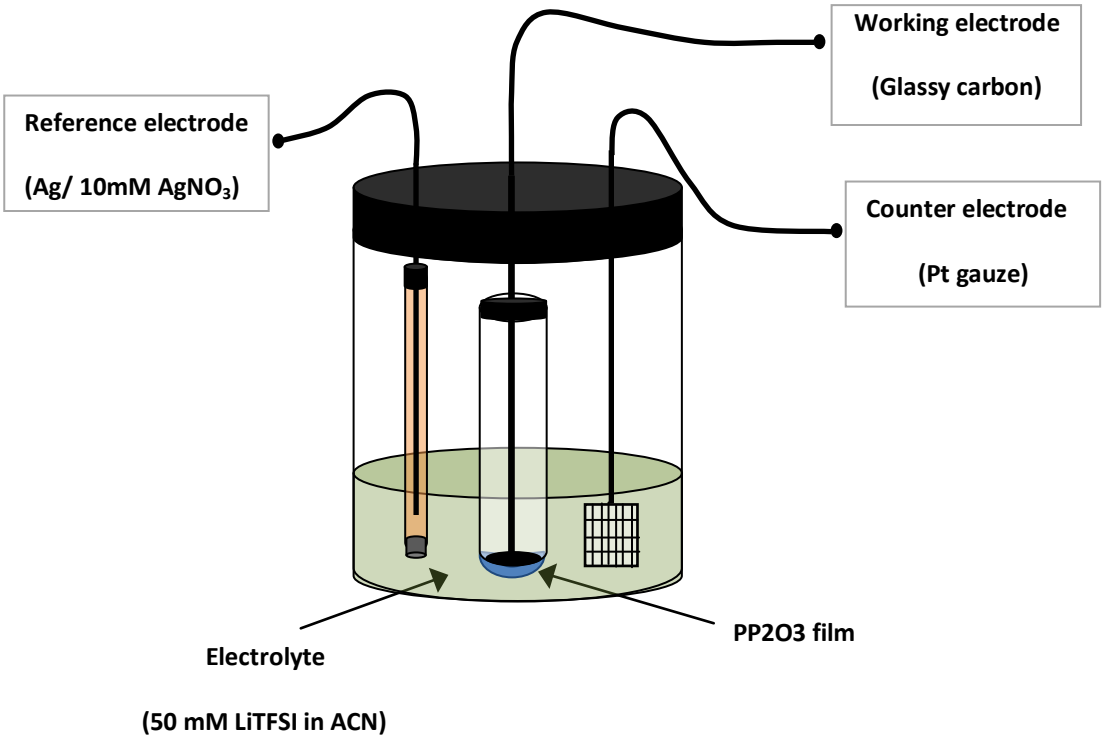

Figure 5.14 The cell construction for determining ionic and electronic conductivities of PP2O3 by transmission line model impedance measurement.

5.3.2 Film deposition and cycling procedures

A PP2O3 film was prepared electrochemically by cyclic voltammetry as described in Chapter 4, using the glassy carbon electrode as the substrate.

An example CV for film deposition is shown in Figure 5.15

The films were then cycled in the electrolyte, 50 mM LiTFSI in ACN, to observe their doping/dedoping behavior as prepared samples. An example is shown in Figure 5.17.

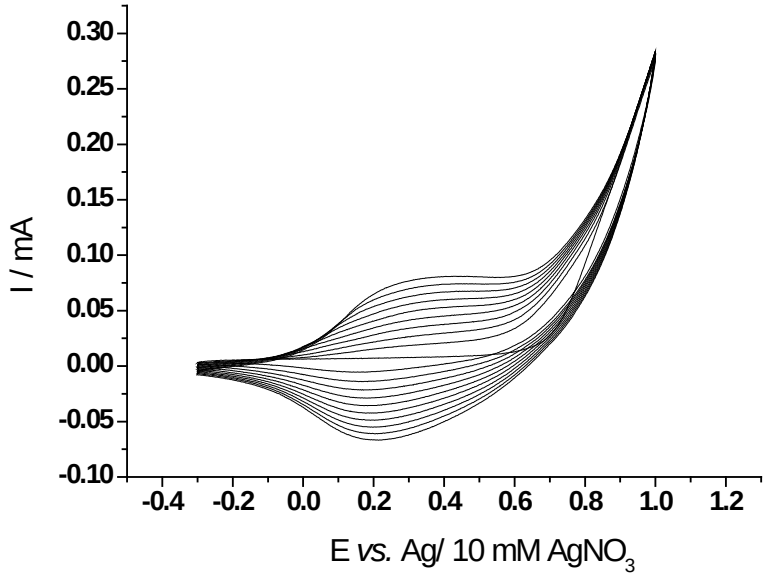

Figure 5.15 Cyclic voltammograms for the deposition of PP2O3 film recorded between -0.3 and +1.0 V at 100 mV/s. The PP2O3 film, which was electrosynthesised in ACN containing 10 mM P2O3 and 50 mM LiTFSI was deposited on a glassy carbon electrode.

Figure 5.15 shows that the current increases from cycle to cycle i.e. current of the broad anodic peak at 0.4 V and cathodic peak at 0.2 V. This indicates a continuous increase in polymer layer thickness from cycle to cycle. It is important to notice that the broad cathodic and anodic peaks showed the doping and dedoping states of the conductive polymer. The polymerisation charge totally was 0.12 C/cm^2, thus the film thickness was 0.61 μm.

5.4 Determination of Ionic and Electronic Conductivities of untreated PP2O3 film as a function of doping level

5.4.1 Procedure

The electrochemical behavior of the PP2O3 sample depends on its doping state which can be varied by altering the potential. To determine the ionic and electronic conductivities of the PP2O3 the sample was examined at various doping states formed by stepping and holding the potential for 10 minutes at each value before the impedance measurement and applying the same potential as a bias during the EIS measurement Impedance measurements were made over a frequency range from 200 kHz to 10 mHz and with a 50 mV amplitude. The potential scan was made in 0.05 V steps for 10 min from -0.3 to 0.8 V *vs.* Ag/Ag^+ and back as can be seen from Figure 5.16.

The sample was cycled again at the end of the series of impedance measurements to determine whether, and to what extent, the properties of the sample had been changed due to the measurement itself. The interpretation of the following series of impedance measurements depends on any sample degradation being negligible. The CVs recorded before and after the impedance cycling are shown in Figure 5.17. Their similarity is reassuring, although a small shift in the potentials of both peaks should be noted.

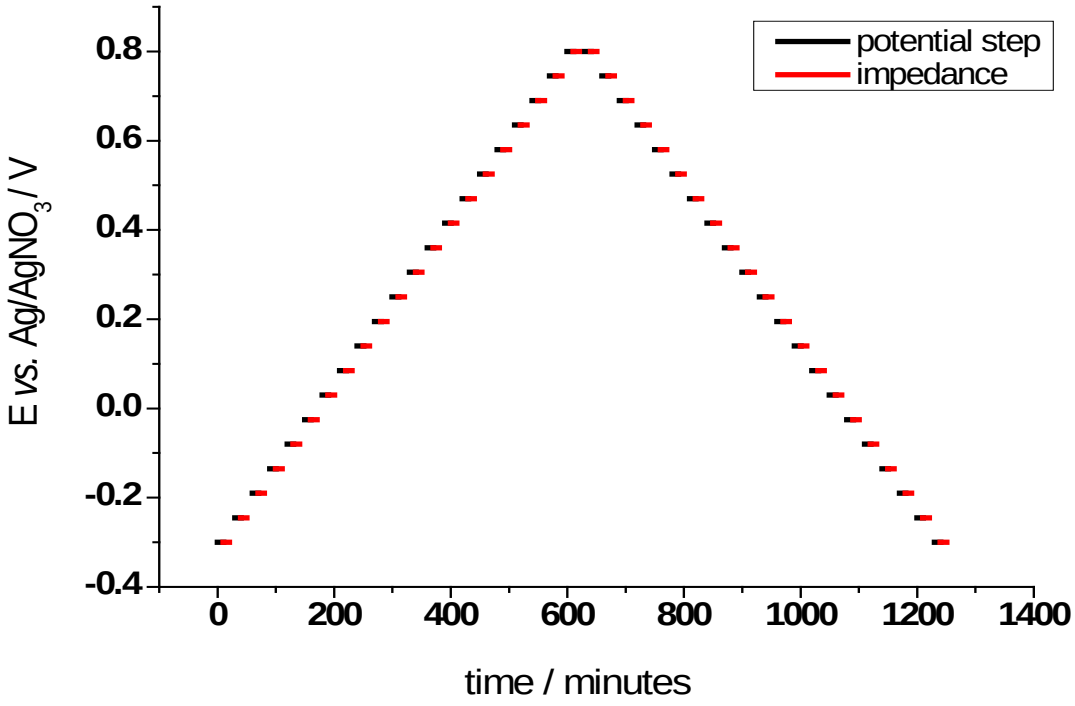

Figure 5.16 Potential steps for doping PP2O3 for transmission line model impedance measurement; PP2O3 sample was doped by holding the step potential of 0.05 V for 10 minutes started from a potential of -0.3 V to 0.8 V then reversed and measuring impedance in each step afterward

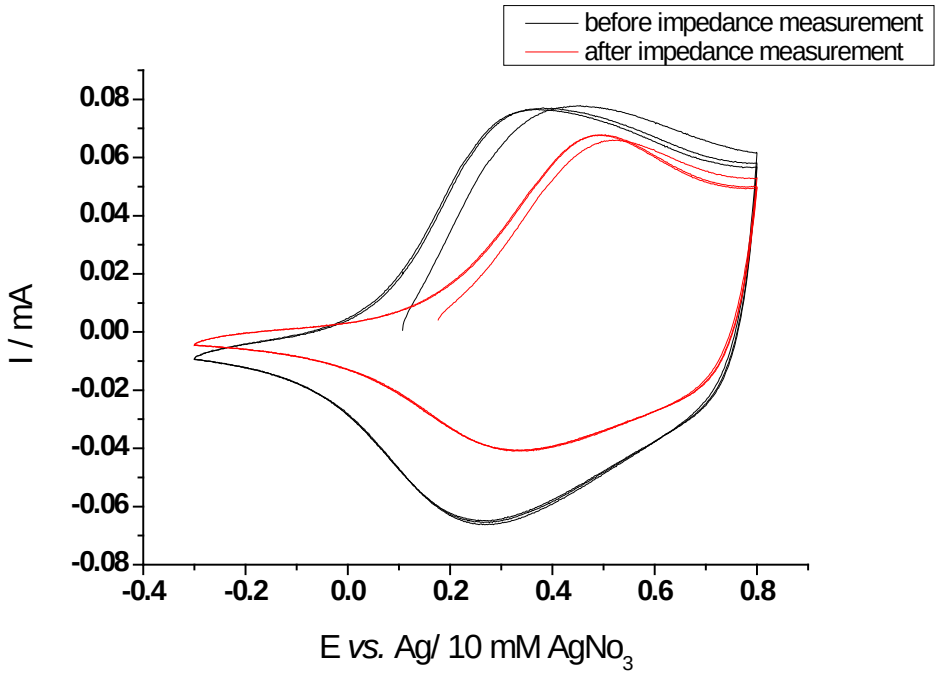

Figure 5.17 Cycling untreated PP3O2 sample in the electrolyte i.e. 50 mM LiTFSI in ACN at a potential range of -0.3 to 0.8 V with 100 mV/s scan rate: the black CVs; before impedance measurement and the red CV; after impedance measurement.

5.4.2 Results for untreated samples

The sequence of EIS results is presented as Nyquist plots in Table 5.4 and Bode (effective series resistance, capacitance) plots in Figure 5.18. With increasing potential, the Nyquist plots show progressions from large to small depressed semicircles, then the λ shaped plots as anticipated in Figure 5.1. According to Figure 5.1 the real parts at high frequency and low frequency should represent the parallel resistance and a third of the series resistance respectively. Although the model does not resolve the ionic and electronic parts, it is easy to see from the plots that the low frequency impedance is dominated by a low ***electronic*** conductivity, since it would not be reasonable for the ionic conductivity to vary by more than two orders of magnitude as it does in the plots. The Bode plots show a rise, then fall in the electronic conductivity as a function of the applied potential as will be discussed later.

Assuming that the above analysis is correct, a low series resistance at high frequency indicates that the impedance is dominated by the ionic conductivity. This is shown clearly in the Bode plot of Figure 5.18, from which we can deduce a relatively constant ionic resistance of around 500 Ω, corresponding to a conductivity of 1.74×10^{-6} S/cm

Looking at the capacitance, we can follow the doping reaction by the increase on moving from low to high potential. The capacitance also varies by two orders of magnitude, primarily because electronic conductivity is required to access the capacitance. Other features may be seen, for example the saturation of the capacitance to its maximum value at 10 mHz, typical of a redox storage capacitance of the doped state at low frequency where it is not limited by the series resistance. At high frequency the capacitance is increasingly limited by the ionic resistance which becomes the dominant part of the impedance.

Table 5.4 Resulting impedance of untreated samples at various doping states, Running the experiment in the order as labled on the right conner in each cell, On the left : forward scan measurement from -0.300 V to 0.800 V and the right : backward scan measurement from 0.800 to -0.300 V

Forward scan	Backward scan
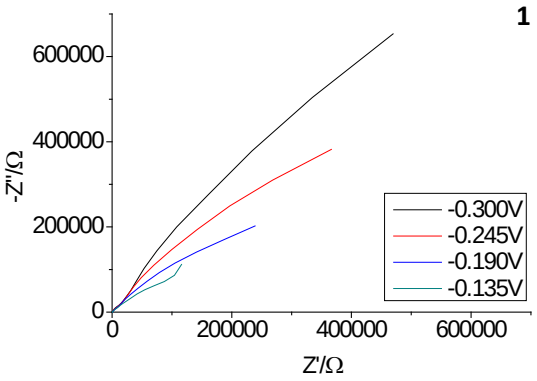	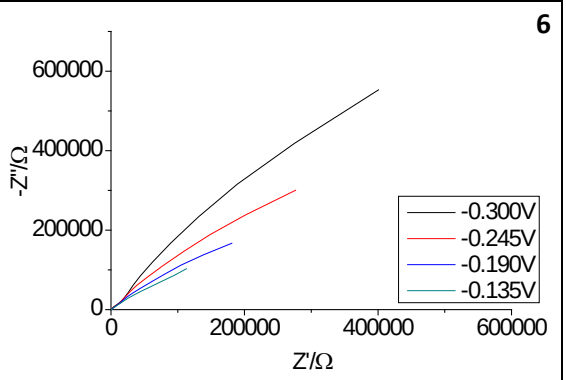
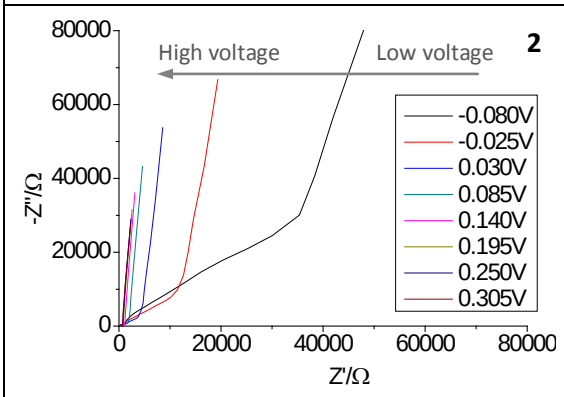	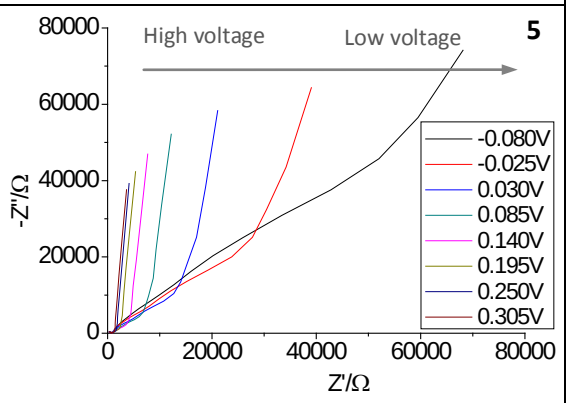
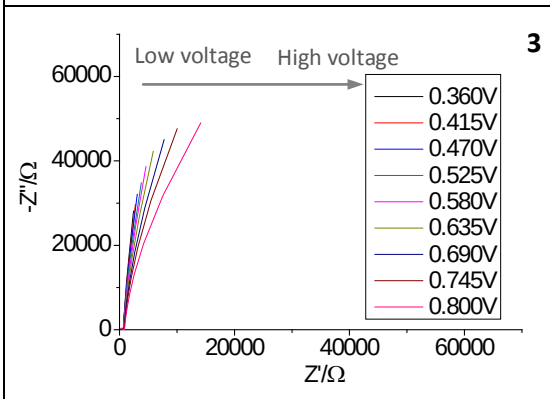	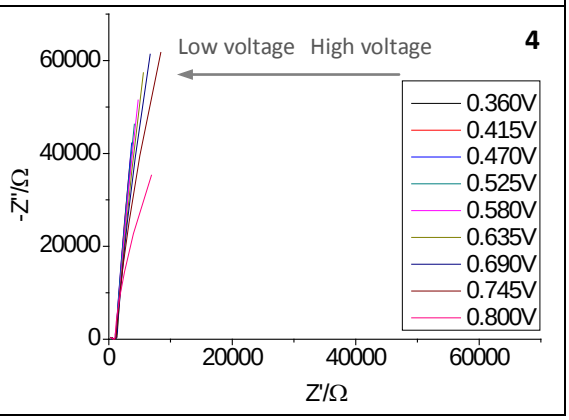

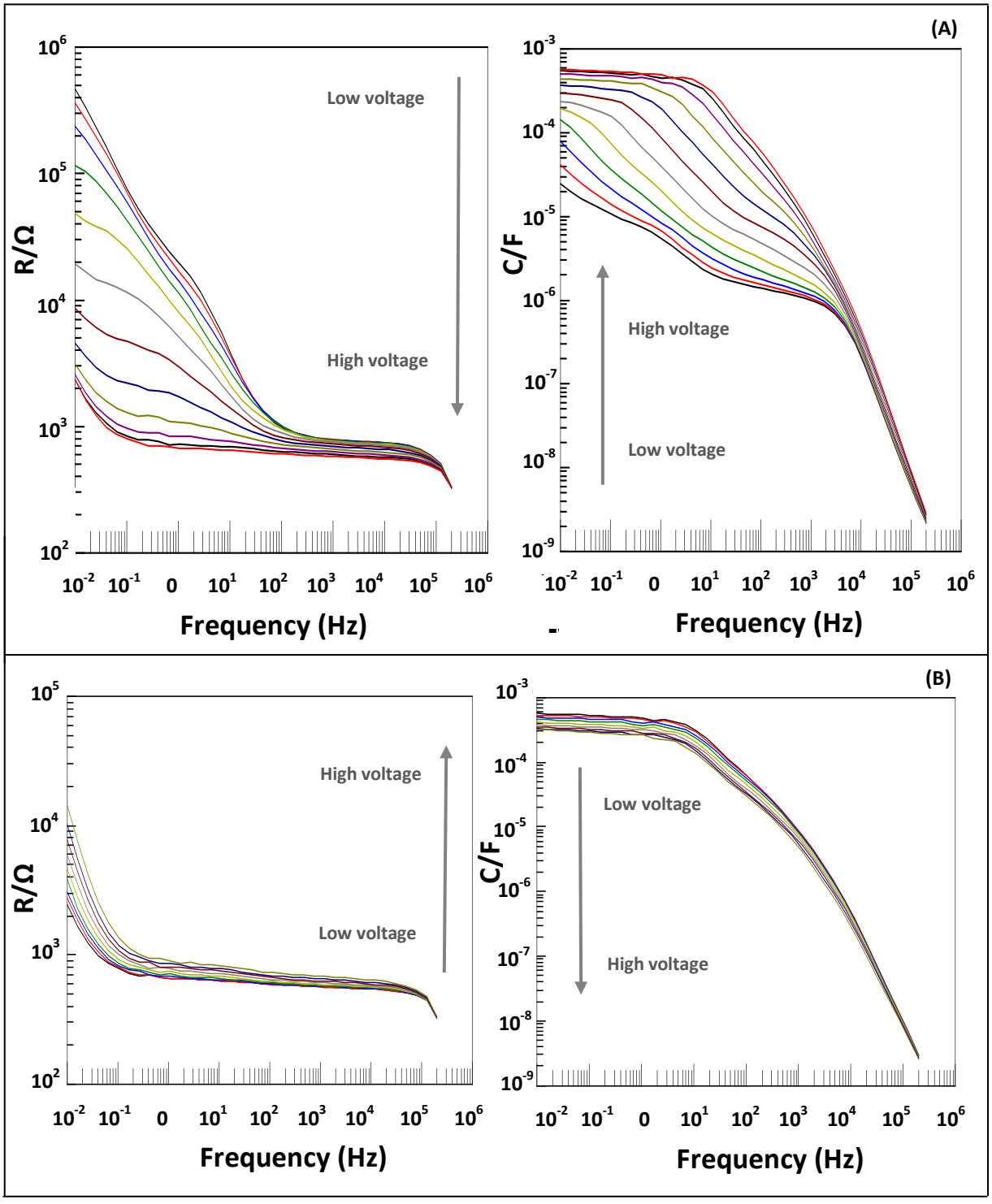

Figure 5.18 Resistance and capacitance of untreated PP2O3 film at various doping states on forward scan measurement of a potential range of -0.300 V to 0.800 V (A) -0.300 V, -0.245 V, -0.190 V, -0.135 V, -0.080 V, -0.025 V, 0.030 V, 0.085 V, 0.140 V, 0.195 V, 0.250 V and 0.305 V and (B) 0.360 V, 0.415 V, 0.470 V, 0.525 V, 0.580 V, 0.635 V, 0.690 V, 0.745 V and 0.800 V respectively.

In Figure 5.19 a simulation of a battery electrode in electrolyte is shown this is based on a model proposed by Jamnik[5]. In such an electrode both ionic and electronic conductivity pathways are present, this can be considered similar to the system under study here. The similarity of the Nyquist data plots to the simulation results shown in Figure 5.19[5] for the Open Warburg (W_O) (FSW) transmission line model in Figure 5.1 (B) is extremely good. This suggests that a model proposed by Jamnik *et al.* should form the basis of a physically realistic equivalent circuit for these data according to the impedance expression[5]. This model is proposed for these data according to the impedance expression.

$$Z_{trm} = \frac{R_{Li^+}R_{e^-}}{R_{Li^+} + R_{e^-}} + \frac{R_{Li^+}^{\perp}}{1 + j\omega R_{Li^+}^{\perp} C^{\perp}} + \frac{1}{4}\frac{(R_{Li^+} - R_{e^-})^2}{R_{Li^+} + R_{e^-}}\frac{tanh\sqrt{j\omega\tau^{\delta}}}{\sqrt{j\omega\tau^{\delta}}} + \frac{1}{4}(R_{Li^+} + R_{e^-})\frac{coth\sqrt{j\omega\tau^{\delta}}}{\sqrt{j\omega\tau^{\delta}}}$$

Equation 5.1

where $R_{Li^+}$is ionic resistance, R_{e^-} is electronic resistance, $R_{Li^+}^{\perp}$ is charge transfer resistance, $C^{\perp}$ is interfacial capacitance and τ^{δ} is the diffusion relaxation time

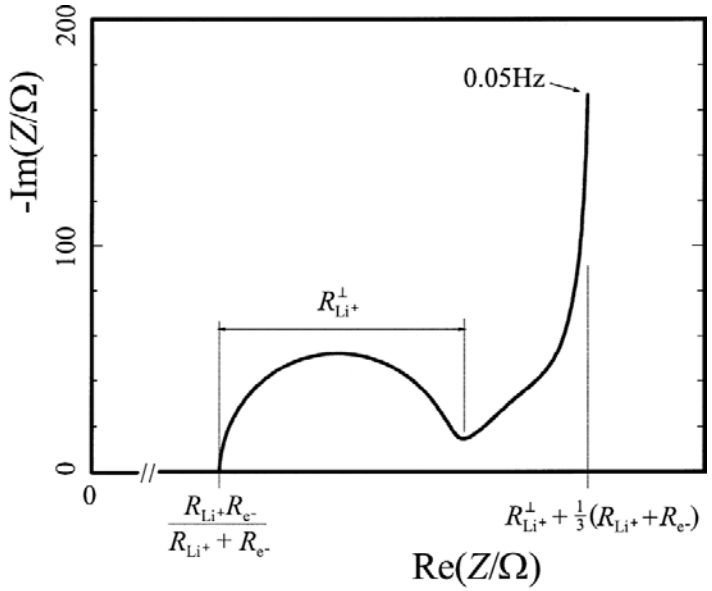

Figure 5.19 Impedance simulation of the mixed ionic and electronic sample according to Equation 5.1. The following parameters were used in the calculation: $R_{Li^+} = 400\ \Omega$, $R_{e^-} = 200\ \Omega$, $R^{\perp}_{Li^+} = 100\ \Omega$, $C^{\perp} = 10\ \mu F$ and $C^{\delta} = 20\ \mu F$.

In Equation 5.1 the first term is the parallel combination of ionic and electronic resistances. The next represents a possible Rct.Cdl semicircle that did not generally appear in our data. The third term is a Finite Length Warburg and the last term is a Finite Space Warburg.

At low frequency the impedance can be approximated by

$$Z(\omega \ll 1/\tau^{\delta}) \approx R^{\perp}_{Li^+} + \frac{1}{3}(R_{Li^+} + R_{e^-}) + \frac{1}{j\omega C^{\delta}}$$

Equation 5.2

where C^{δ} is chemical capacitance

The high frequency impedance can be considered to be a parallel combination of the ionic and electronic resistance added to an uncompensated resistance of the electrolyte. The real part of the low frequency impedance can then be considered as one third of the series combination of the ionic and electronic resistance. The equivalent circuit parameters of untreated samples obtained by fitting the equivalent circuits to the impedance data are

shown in Table 5.5. Electronic conductivities are given in the table on the assumption of a constant ionic resistance of 200 Ω (based on the lowest high frequency values obtained, where the electronic resistance was assumed to be much smaller). Results of both forward and backward potential scans show the the same trend, showing reversibility, albeit with some hysteresis as shown in Figure 5.20. The capacitance behaves in a similar way in Figure 5.21. A clear trend is seen where the logarithm of the conductivity almost follows the capacitance with a rise to a peak at around 0.3 V and a subsequent fall at high dopant levels. The decreases in both the electronic condutivity at the end and after the forward scan measurement suggests a decrese in its electronic activity due to holding positive potentials for a long periods of time (> 20 hours).

Comparison of the CV's in of PP2O3 before and after the series of impedane measurements in Figure 5.17 adds evidence to this explanation, and introduces the concept of suppression of electronic conductivity by overdoping, as discussed later.

Table 5.5 The parameters from the fitting impedance of the untreated samples

	Forward						backward					
E (V)	Wo-R (Ω)	R_1 (Ω)	Wo-P	Wo-T (s)	D ($cm^2 s^{-1}$)	σ_e (S cm^{-1})	Wo-R (Ω)	R_1 (Ω)	Wo-P	Wo-T (s)	D ($cm^2 s^{-1}$)	σ_e (S cm^{-1})
-0.03	2.07E+06	624	0.69	57.89	4.09E-10	4.20E-10	1.80E+06	788	0.69	64.75	3.65E-10	4.83E-10
-0.245	1.33E+06	621	0.67	50.43	4.69E-10	6.55E-10	1.02E+06	761	0.66	54.74	4.32E-10	8.54E-10
-0.19	8.06E+05	606	0.63	50.15	4.72E-10	1.08E-09	6.17E+05	732	0.62	54.56	4.34E-10	1.41E-09
-0.135	4.06E+05	587	0.59	44.18	5.36E-10	2.14E-09	3.81E+05	710	0.58	52.69	4.49E-10	2.28E-09
-0.08	1.54E+05	578	0.54	27.93	8.47E-10	5.65E-09	2.27E+05	695	0.55	45.26	5.23E-10	3.82E-09
-0.025	41403	588	0.49	9.45	2.50E-09	2.11E-08	1.18E+05	695	0.53	29.10	8.13E-10	7.37E-09
0.03	11185	623	0.46	2.97	7.96E-09	7.91E-08	50953	700	0.50	13.85	1.71E-09	1.71E-08
0.085	3765	663	0.47	1.23	1.93E-08	2.44E-07	21613	711	0.48	6.26	3.78E-09	4.06E-08
0.14	1382	656	0.48	0.54	4.37E-08	7.35E-07	10094	739	0.47	3.11	7.62E-09	8.78E-08
0.195	596	626	0.48	0.27	8.89E-08	2.19E-06	5149	767	0.47	1.73	1.37E-08	1.76E-07
0.25	332	598	0.49	0.16	1.48E-07	6.60E-06	2816	775	0.48	1.02	2.32E-08	3.32E-07
0.305	251	576	0.49	0.12	1.90E-07	1.69E-05	1727	773	0.48	0.65	3.65E-08	5.69E-07
0.36	234	563	0.48	0.11	2.07E-07	2.52E-05	1215	772	0.48	0.45	5.24E-08	8.56E-07
0.415	244	560	0.48	0.11	2.12E-07	1.99E-05	992	779	0.48	0.35	6.72E-08	1.10E-06
0.47	268	565	0.48	0.11	2.10E-07	1.28E-05	925	792	0.48	0.30	7.77E-08	1.20E-06
0.525	297	571	0.48	0.11	2.08E-07	8.98E-06	964	812	0.48	0.29	8.25E-08	1.14E-06
0.58	352	584	0.48	0.12	1.95E-07	5.73E-06	1097	844	0.48	0.29	8.08E-08	9.68E-07
0.635	404	601	0.48	0.13	1.87E-07	4.27E-06	1257	884	0.48	0.30	7.87E-08	8.22E-07
0.69	445	617	0.48	0.13	1.87E-07	3.55E-06	1197	890	0.48	0.26	9.02E-08	8.71E-07
0.745	479	639	0.47	0.13	1.89E-07	3.11E-06	889	861	0.48	0.19	1.26E-07	1.26E-06
0.8	497	669	0.47	0.12	1.99E-07	2.92E-06	556	753	0.47	0.12	1.94E-07	2.44E-06

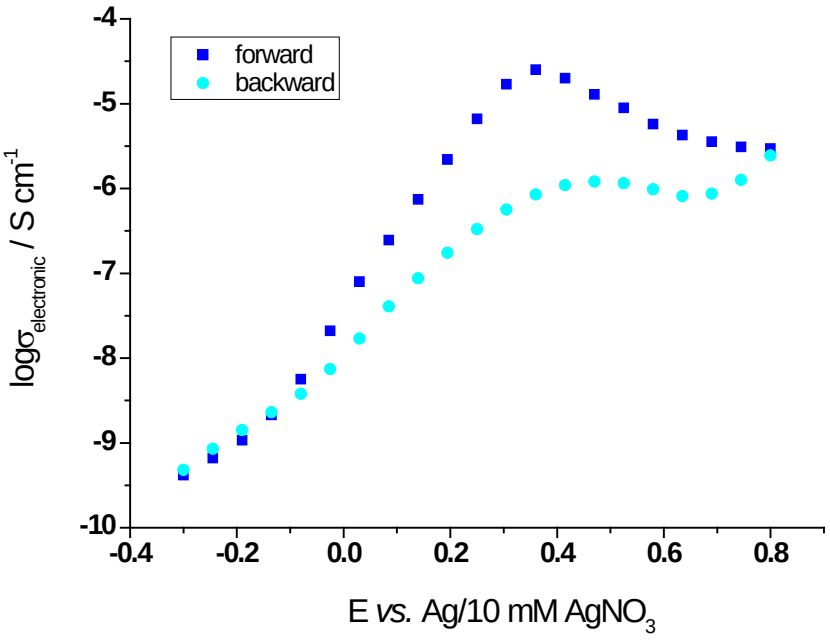

Figure 5.20 Electronic conductivity of untreated PP2O3 sample at various doping states by transmission line impedance model

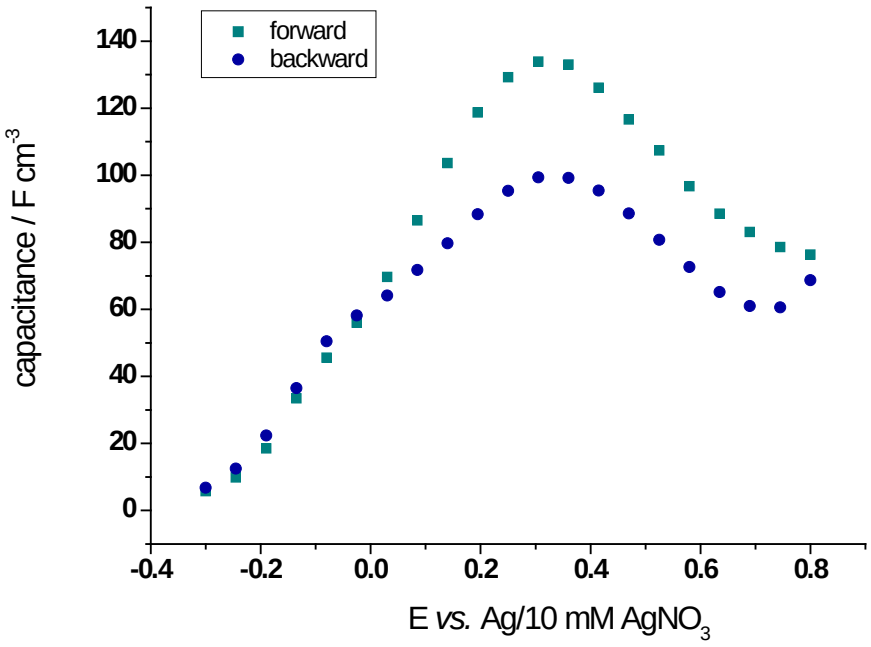

Figure 5.21 Capacitance at low frequency of untreated PP2O3sample at various doping states by transmission line impedance model

5.5 Preparation of treated films

Treated PP2O3 sample was prepared by the overoxidation treatment, cycling the polymer in the electrolyte at an overoxidation potential range as can be seen from Figure 5.22.

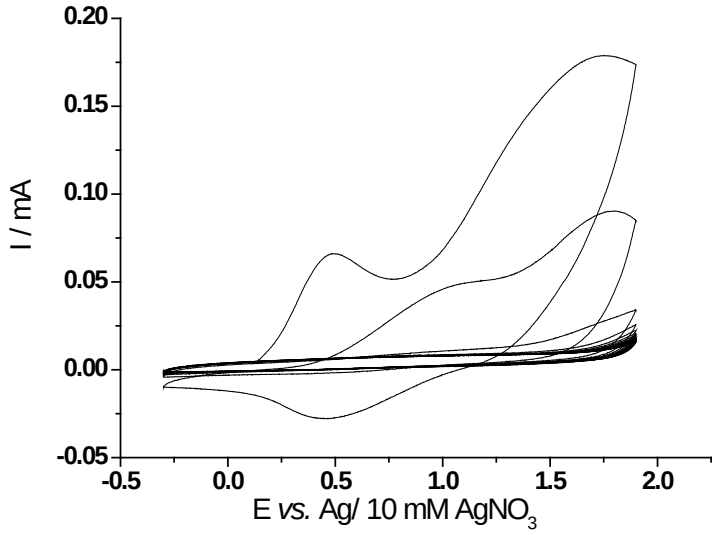

Figure 5.22 Cyclic voltammograms of cycling PP2O3 sample in the electrolyte i.e. 50 mM LiTFSI in ACN at the overoxidation potential range of -0.3 to 1.9 V with 100 mV/s scan rate.

The currents measured in the cyclic voltammograms decreased from cycle to cycle. This suggested the electronic conductivity was damaged by cycling the polymer in the electrolyte at the overoxidation potential range due to formation of water substitution product, OH- and O= groups on pyrrole rings as explained in Chapter 4, section 4.4. The polymer was transformed into an insulating material in five cycles by observation of the currents.

5.6 Doping/dedoping and Impedance Measurement of Treated PP2O3 Films

Like the untreated film, the treated film was doped at various potentials before impedance measurement to determine the effects of its doping state on the ionic and electronic conductivities. The resulting impedance can be seen from Table 5.6.

Table 5.6 Resulting impedance of treated samples at various doping states, Runing the experiment in the order as labled on the right conner in each cell, On the left : forward scan measurement from -0.300 V to 0.800 V and on the right : backward scan measurement from 0.800 to -0.300 V

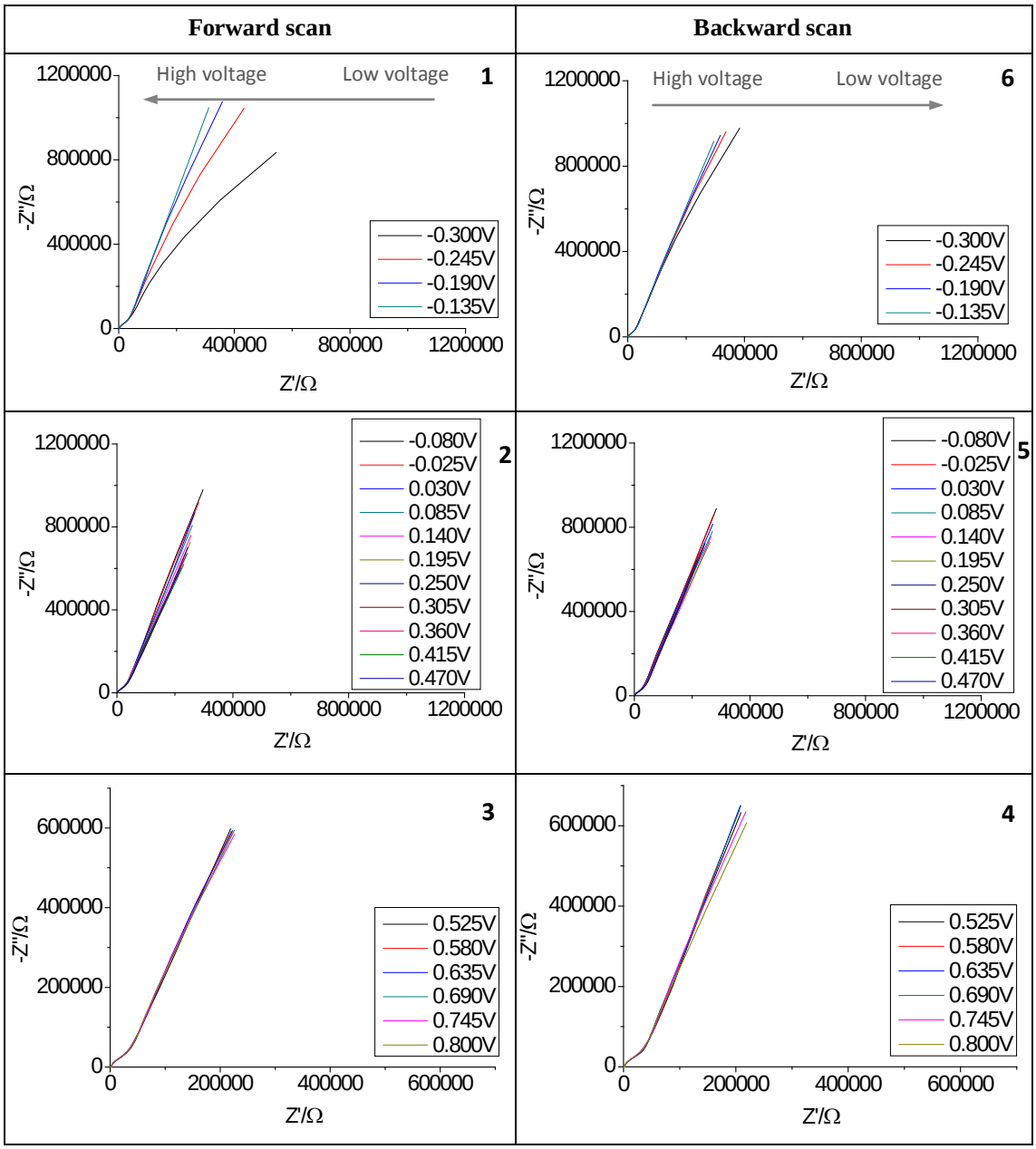

Unlike the results for untreated samples, the impedances shown in Table 5.6 did not show much change with the holding potentials in both the forward and backward scan measurements. All resulting impedance looked almost the same. This suggests that irreversible loss of the electrochemical activity from the overoxidation treatment was successful, thus no doping could be achieved. These results agreed well with the plots of resistance and capacitance *vs.* frequency as can be seen from Figure 5.23.

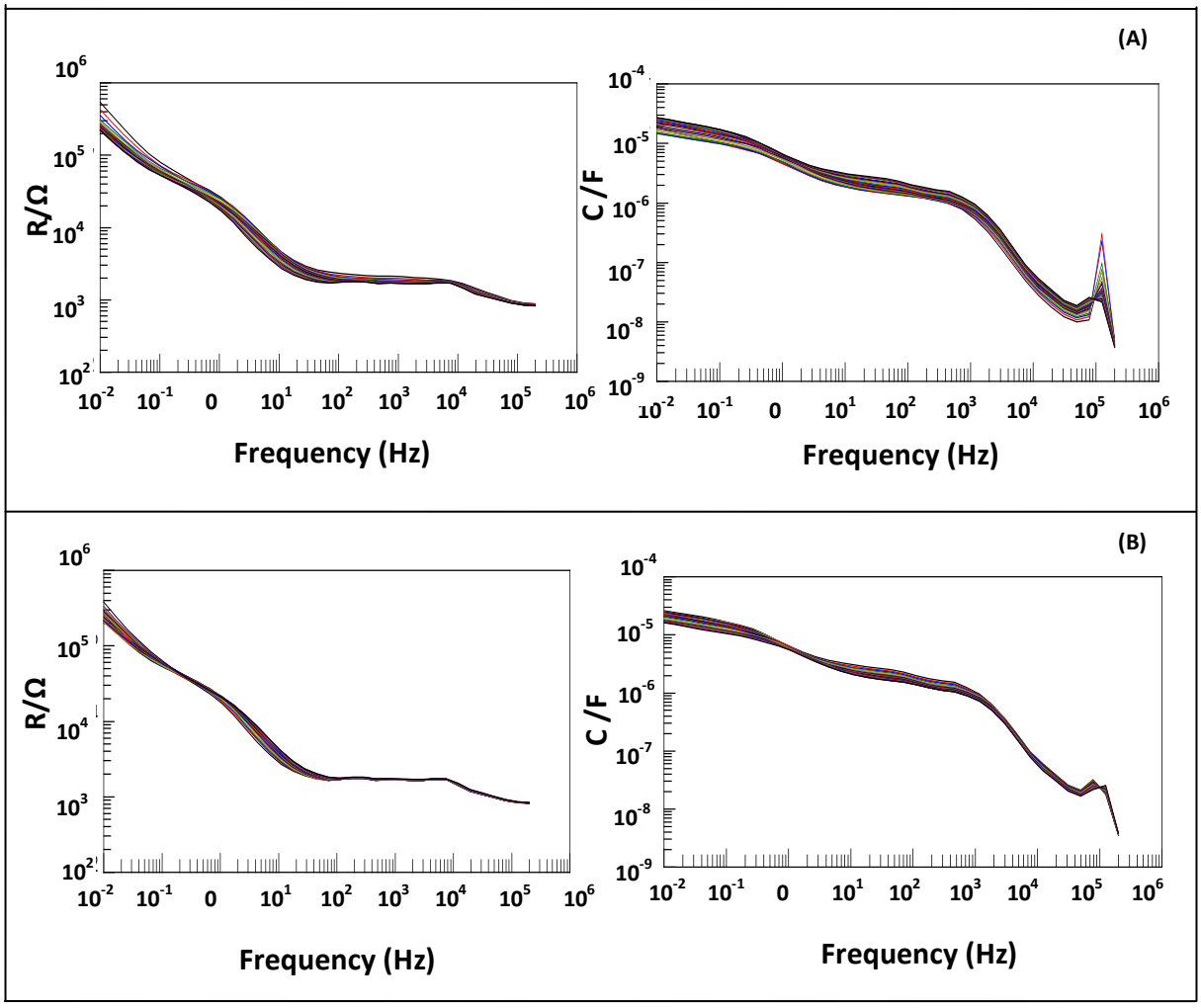

Figure 5.23 Resistance and capacitance of treated PP2O3 at various doping states of a potential range of -0.30V to 0.80V (A) on forward scan and (B) backward scan : -0.300 V, -0.245 V, -0.190 V, -0.135 V, -0.080 V, -0.025 V, 0.030 V, 0.085 V, 0.140 V, 0.195 V, 0.250 V, 0.305 V, 0.360 V, 0.415 V, 0.470 V, 0.525 V, 0.580 V, 0.635 V, 0.690 V, 0.745 V and 0.800 V respectively.

Figure 5.23 shows the resistance, obtained from the real part, and the effective series capacitance. The observation that these parameters did not change substantially with the potentials confirms a loss of electrochemical activity in the treated sample as expected. (The rise in resistance at low frequency is an effect of a frequency-dependent capacitance, represented by a CPE which as a substantial resistive component at low frequency.)

From the transmission line impedance model in Figure 5.1 and Equation 5.2 according to Jamnik the ionic and electronic resistances as well as the capacitance at low frequency of treated PP2O3 sample could be determined and shown in Table 5.7. The plots of ionic and electronic conductivities and also capacitance can be seen from Figure 5.24, 5.25 and 5.26 respectively.

Table 5.7 The parameters from the fitting impedance of the treated samples

	forward							backward						
E (V)	**Wo-R (Ω)**	**R_1 (Ω)**	**Wo-P**	**Wo-T (s)**	**D ($cm^2 s^{-1}$)**	**σ_e (S cm^{-1})**	**σ_i (S cm^{-1})**	**Wo-R (Ω)**	**R_1 (Ω)**	**Wo-P**	**Wo-T (s)**	**D ($cm^2 s^{-1}$)**	**σ_e (S cm^{-1})**	**σ_i (S cm^{-1})**
-0.3	2.77E+06	1721	0.68	82	2.89E-10	3.14E-10	5.04E-07	3.36E+06	1432	0.71	99	2.39E-10	2.59E-10	6.06E-07
-0.245	3.68E+06	1639	0.70	102	2.31E-10	2.36E-10	5.30E-07	3.34E+06	1422	0.71	103	2.30E-10	2.60E-10	6.11E-07
-0.19	3.76E+06	1581	0.70	105	2.25E-10	2.31E-10	5.49E-07	3.25E+06	1409	0.70	104	2.27E-10	2.67E-10	6.16E-07
-0.135	3.68E+06	1545	0.70	107	2.21E-10	2.36E-10	5.62E-07	3.20E+06	1396	0.70	107	2.22E-10	2.72E-10	6.22E-07
-0.08	3.47E+06	1518	0.70	109	2.17E-10	2.51E-10	5.72E-07	3.11E+06	1382	0.69	109	2.18E-10	2.79E-10	6.28E-07
-0.025	3.26E+06	1500	0.69	110	2.15E-10	2.67E-10	5.79E-07	3.04E+06	1371	0.69	111	2.13E-10	2.86E-10	6.33E-07
0.03	3.08E+06	1483	0.69	112	2.12E-10	2.82E-10	5.85E-07	2.95E+06	1361	0.69	113	2.09E-10	2.94E-10	6.38E-07
0.085	2.92E+06	1466	0.68	115	2.07E-10	2.98E-10	5.92E-07	2.87E+06	1349	0.68	115	2.06E-10	3.03E-10	6.44E-07
0.14	2.78E+06	1450	0.68	117	2.03E-10	3.13E-10	5.99E-07	2.80E+06	1338	0.68	117	2.02E-10	3.10E-10	6.49E-07
0.195	2.66E+06	1435	0.68	118	2.01E-10	3.27E-10	6.05E-07	2.75E+06	1330	0.68	119	2.00E-10	3.16E-10	6.53E-07
0.25	2.60E+06	1424	0.67	120	1.98E-10	3.34E-10	6.10E-07	2.73E+06	1326	0.68	120	1.97E-10	3.18E-10	6.55E-07
0.305	2.53E+06	1413	0.67	121	1.96E-10	3.43E-10	6.14E-07	2.67E+06	1320	0.68	121	1.95E-10	3.25E-10	6.58E-07
0.36	2.49E+06	1402	0.67	124	1.91E-10	3.50E-10	6.19E-07	2.61E+06	1312	0.67	123	1.92E-10	3.32E-10	6.62E-07
0.415	2.40E+06	1390	0.67	124	1.90E-10	3.62E-10	6.25E-07	2.54E+06	1308	0.67	125	1.90E-10	3.42E-10	6.64E-07
0.47	2.38E+06	1382	0.67	126	1.88E-10	3.66E-10	6.28E-07	2.48E+06	1307	0.67	125	1.89E-10	3.50E-10	6.64E-07
0.525	2.36E+06	1382	0.67	125	1.90E-10	3.69E-10	6.28E-07	2.48E+06	1314	0.67	125	1.89E-10	3.50E-10	6.61E-07
0.58	2.35E+06	1385	0.68	123	1.92E-10	3.69E-10	6.27E-07	2.50E+06	1325	0.68	123	1.93E-10	3.48E-10	6.55E-07
0.635	2.35E+06	1390	0.68	121	1.95E-10	3.69E-10	6.25E-07	2.51E+06	1339	0.68	120	1.98E-10	3.47E-10	6.48E-07
0.69	2.34E+06	1392	0.68	119	1.98E-10	3.71E-10	6.24E-07	2.53E+06	1357	0.69	119	1.99E-10	3.44E-10	6.40E-07
0.745	2.34E+06	1390	0.69	119	1.99E-10	3.71E-10	6.25E-07	2.49E+06	1372	0.69	118	2.01E-10	3.49E-10	6.33E-07
0.8	2.36E+06	1394	0.69	119	2.00E-10	3.69E-10	6.23E-07	2.42E+06	1387	0.69	118	2.00E-10	3.58E-10	6.26E-07

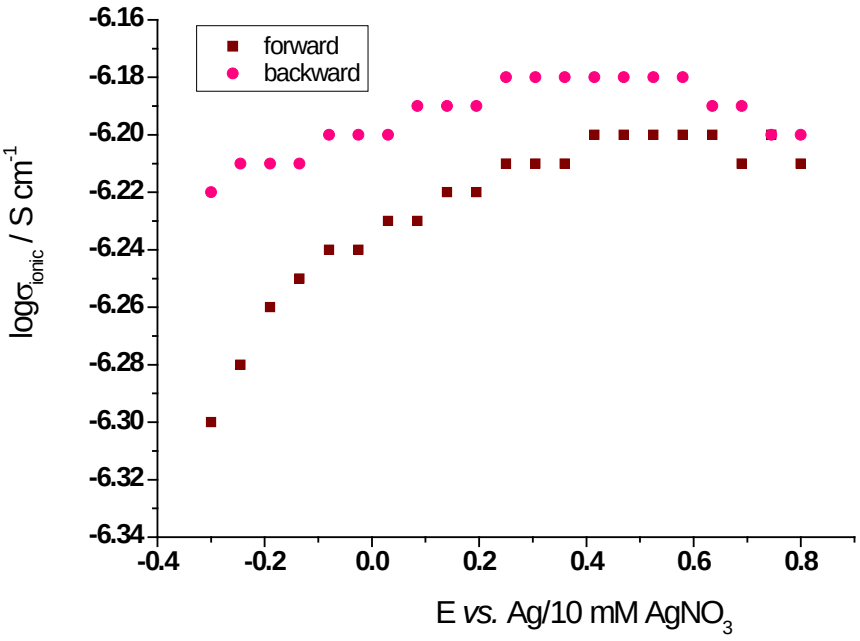

Figure 5.24 Ionic conductivity of treated PP2O3 sample at various doping states by transmission line impedance model

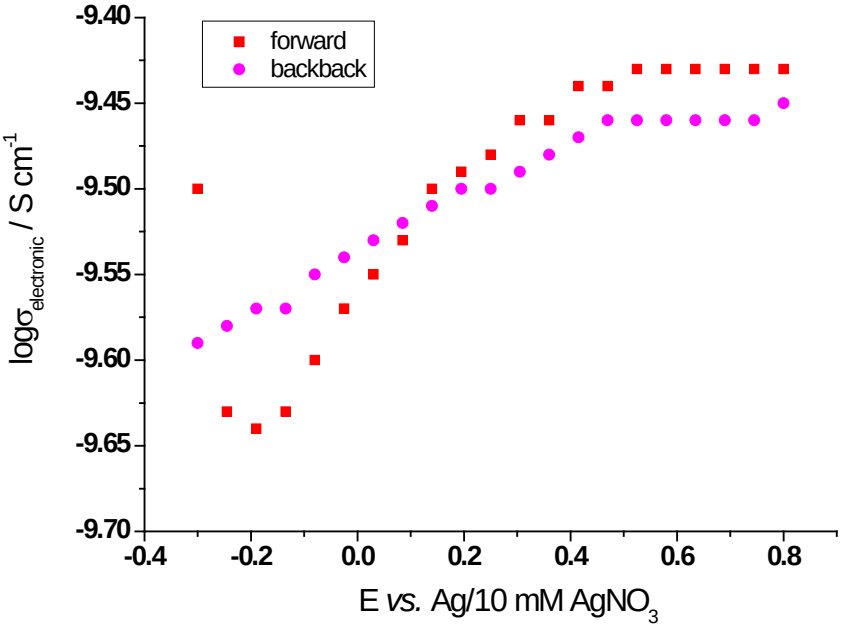

Figure 5.25 Electronic conductivity of treated PP2O3 sample at various doping states by transmission line impedance model

Figure 5.24 and 5.25 showed both ionic and electronic conductivities were quite stable. The ionic conductivity was around $6.2x10^{-7}$ S/cm. Clearly electronic conductivity of treated sample was very low when compared with those of the untreated sample due to loss of electrochemical activity i.e. $3.43x10^{-10}$ and $1.69x10^{-5}$ S/cm at 0.305 V for treated and untreated samples respectively. Its electronic conductivity was decreased by the overoxidation treatment around 50,000 times. Now its electronic conductivity was 0.06 % of total conductivity at 0.305 V. Also the plot of capacitance can be seen from Figure 5.26.

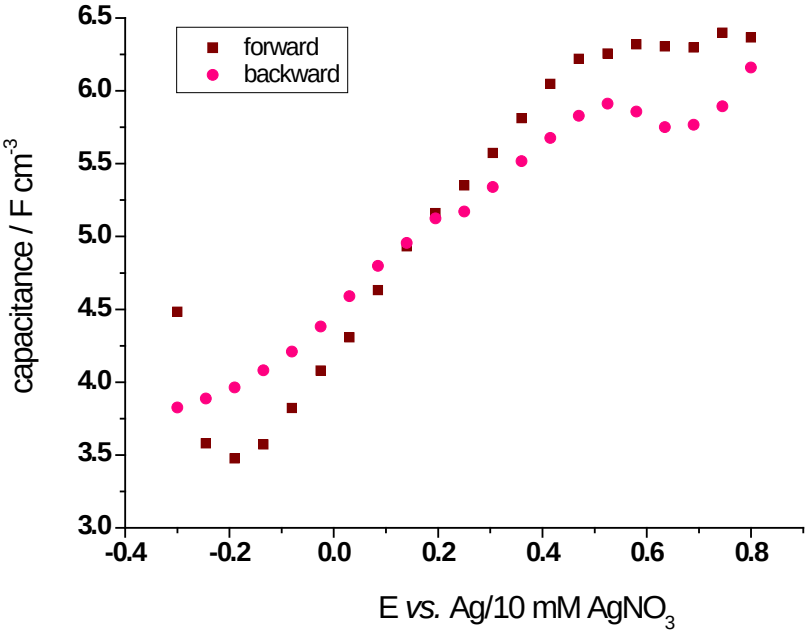

Figure 5.26 Capacitance of treated PP2O3 sample at various doping states by transmission line impedance model

The capacitance of the treated sample was hardly changed with the holding potentials because of the lack of electrochemical activity. This agreed well with electronic conductivity of treated sample.

The comparison of the cyclic votammograms before and after the measurment shown Figure 5.27 indicates that the sample did not change significantly during the measurement. The low currents also show a very low level of redox activity.

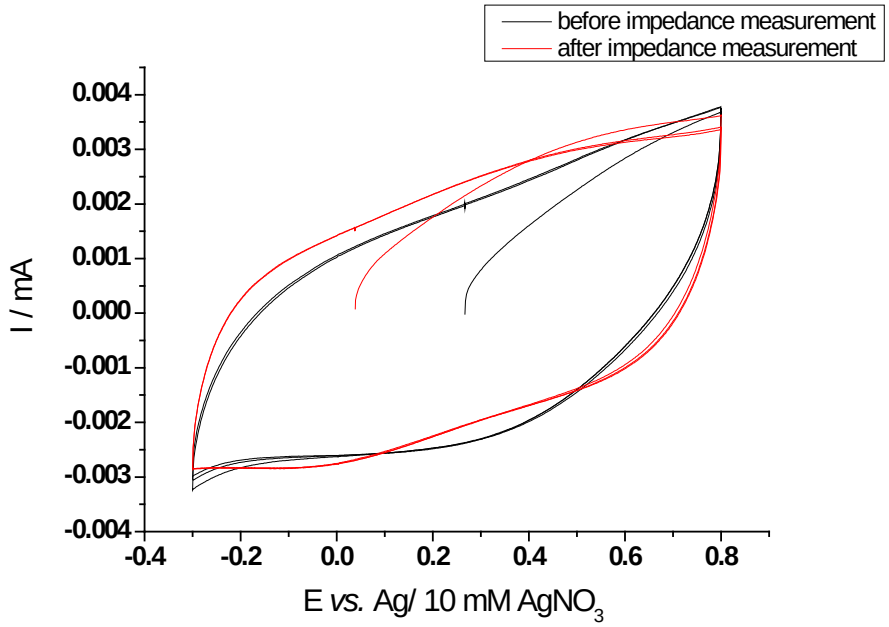

Figure 5.27 Cycling treated PP3O2 sample in the electrolyte i.e. 50 mM LiTFSI in ACN at a potential range of -0.3 to 0.8 V with 100 mV/s scan rate: the black CVs; before impedance measurement and the red CV; after impedance measurement.

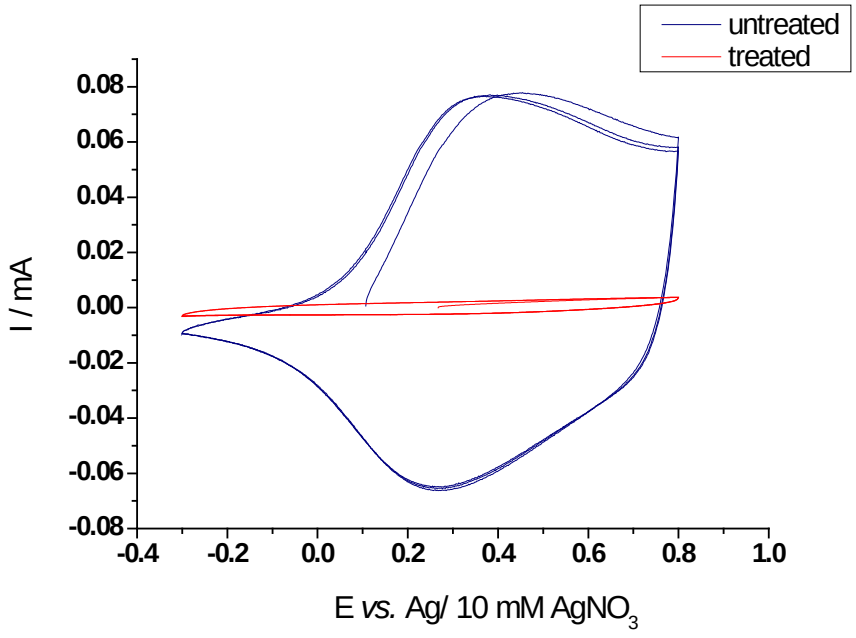

Figure 5.28 Cyclic voltammograms of untreated and treated PP3O2 samples in the electrolyte i.e. 50 mM LiTFSI in acetonitrile at a potential range of -0.3 to 0.8 V *vs.* Ag/Ag^+ with 100 mV/s scan rate; the blue : untreated and the red : treated.

Figure 5.28 shows an obvious change between the untreated and treated samples. The cyclic voltammogram of the untreated sample showed doping/dedoping beheviour of electronical active polymer as can be seen from Figure 5.28, blue CVs. By contrast, the treated sample had irreveribly lost its electrochemical activity. The cyclic votammogram showed only double layer charge with very low current as shown in Figure 5.28, red CVs. The CVs also confirms that the overoxidation treatment destroyed electronic conductivity of the PP2O3 sample. The ionic and electronic conductivities of both untreated and treated samples at 0.305 V *vs.* Ag/Ag^+ are shown in Table 5.8. This potential is where the highest conductivities were seen in the untreated sample.

.

Table 5.8 Some parameters measured for the untreated and treated sample at 0.305 V

	untreated	**treated**
$\sigma_{electronic,}$ **S cm^{-1}**	1.69×10^{-5}	3.43×10^{-10}
$\sigma_{ionic,}$ **S cm^{-1}**	1.74×10^{-6}	6.14×10^{-7}
% electronic conductivity	79.55	0.06

The overoxidation treatment destroyed PP2O3 electronic conductivity by 50,000 times approximately, reducing the electronic conductivity to 0.06 % of total conductivity as shown in Table 5.8. In the other words the electronic transference number – i.e. the ratio of electronic conductivity to total conductivity in the treated sample was only 5×10^{-4}. The treated sample was transformed into an electronic insulator. The ionic conductivity was slightly decreased by the overoxidation treatment.

The treated sample is therefore suitable as an electrolyte for 3D batteries at least in principle. Chapter 6 will describe the use of the treated PP2O3 sample in the fabrication and testing of both 2D and 3D batteries.

5.7 Chapter 5 Conclusions

For the bulk samples the ionic conductivities of the untreated and treated samples were in both cases promising i.e. in the range of 2.9-5.5 x 10^{-5} and 4.8-9.3 x 10^{-6} S/cm for untreated and treated respectively. It is also noted that the treated sample had a slightly lower ionic conductivity than those of the untreated one.

In the case of electronic conductivity the untreated sample had higher values than those of treated sample as expected. However, the untreated sample still had quite a low electronic conductivity i.e. around 1 x 10^{-7} S/cm. This was attributed to a low doping level as well as the effect of the plasticiser disrupting the percolation of the electron conducting paths.

For the untreated film samples the ionic conductivity was found to be a constant at around 1.74x10^{-6} S/cm. Its electronic conductivity and capacitance varied by two orders of magnitude on doping. Both electronic conductivity and capacitance increased with increasing the holding potential from -0.300 V to 0.305 V then decreased gradually until the end of measurement, at 0.800 V and afterwards. This decrease was tentatively attributed to sample degradation at high potential.

Electronic conductivities as well as capacitance of treated samples did not significantly depend on the holding potentials. Moreover electronic conductivity and capacitance were much smaller than those of untreated one. These results were expected because the overoxidation treatment destroyed its electronic conductivity and electrochemical activity. Consequently its electronic conductivity and capacitance were small and independent of potential.

Comparing untreated and treated film samples, it could be concluded that the overoxidation treatment decreased electronic conductivity by approximately 50,000 times. The ionic conductivity of the treated sample was slightly lower than that of the untreated one. The electronic transference number was only 5 x 10^{-4} and thus fulfilled the condition for a good separator membrane in a battery.

Comparing the bulk and film samples, the low electronic conductivity of bulk samples was explained as a combination of a low doping level and percolation of the electronic conductivity between conjugated chains in the polymer. Bulk samples showed higher ionic conductivities than the film samples (around 10^{-5} and 10^{-6} S/cm for the bulk and film samples respectively). This was possibly due to an enhancement in the ionic conductivity with the presence of plasticising PC in the bulk sample.

The bulk and film sample were used in battery applications as described in the next Chapter. The bulk samples were used in ordinary battery fabrication (2D batteries) whereas the film samples were constructed in 3D batteries.

5.8 Chapter 5 References

[1] M. B. Armand, J. M. Chabagno and N. J. Duclot, *Fast Ion Transport in Solids*
Elsevier Science, Amsterdam
1979, p. 131.
[2] W. J. Albery, C. M. Elliott and A. R. Mount, *Journal of Electroanalytical Chemistry* **1990**, *288*, 15-34.
[3] J. M. Elliott and J. R. Owen, *Physical Chemistry Chemical Physics* **2000**, *2*, 5653-5659.
[4] R. D. Levie, *Adv. Electrochem. Electrochem. Eng*
1967, *6*, 329.
[5] J. Jamnik, *Solid State Ionics* **2003**, *157*, 19-28.

Chapter 6

Battery Application of Chemically and Electrochemically Prepared PP2O3

6.1 Introduction

In the previous chapter ionic and electronic conductivities of the PP2O3 samples, both powder and electrodeposited film, were determined. In this chapter both samples were to build real battery systems. The powder samples were constructed into a standard 2D battery whereas the film samples were fabricated in novel 3D batteries.

6.2 2D Batteries using chemically prepared PP2O3 electrolyte

Initially the polymer was synthesised using a chemical route. Some of this polymer was then treated chemically to break the conductivity. The treated and untreated samples were then prepared into pellets as described in the previous chapter and sandwiched between a cathode and anode to make a complete battery. The self-discharge resistance of the cell was then determined and specific capacity of the cell as a function cycle number was also examined in order to investigate the practical use of this polymer as an electrolyte.

6.2.1 Materials, Equipment and Sample Preparation

$LiFePO_4$ and PTFE were obtained from Aldrich and $Li_4Ti_5O_{12}$ was received from Sud-chemie. 1 M $LiPF_6$ in EC:DMC was received from Novolyte technologies. Untreated and treated PP2O3 were synthesised using the chemical synthesis described in Chapter 4. Stainless steel small cells were used to characterise the electrolyte. The cell construction was built in house and is shown below in Figure 6.1. The cell was made by sandwiching the electrolyte pellet with anode and cathode material. This stack is then sealed using a stainless steel base and lid which also act as current collectors electronically isolated by a compressed viton ring. A spring and a stainless steel disc are included in the design to apply a stack pressure between electrodes and electrolyte. This cell can then be connected to a potentiostat for electrochemical evaluation.

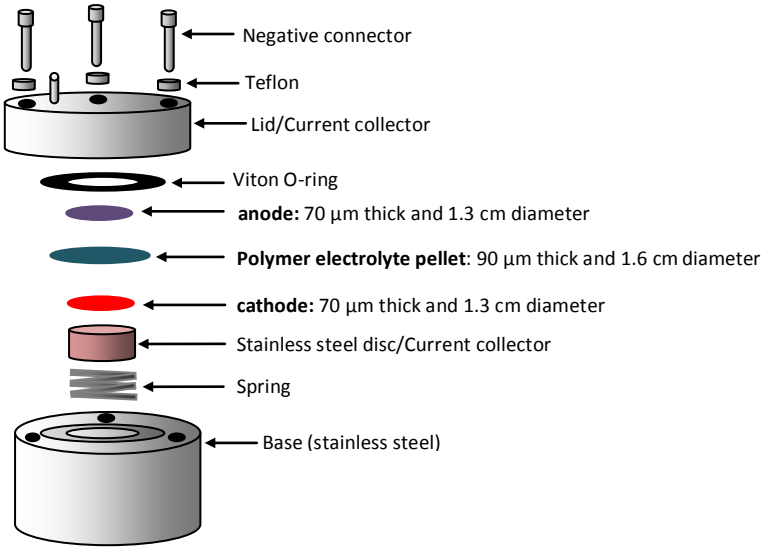

Figure 6.1 Cell construction of self-discharge and galvanostatic tests.

The three active parts of the electrode are the cathode, anode and electrolyte. The specifics of these components are discussed below:

1) Cathode

The cathode pellets were made from a mixture of $LiFePO_4$ active material, AB and PTFE powder in the ratio 75:20:5 by weight. $LiFePO_4$ was chosen as a cathode material. It is two phase material with 170 mAh/g specific capacity. The insertion/removal of Li in $LiFePO_4$ occurs at potential around 3.4 V *vs.* lithium[1]. It was however chosen mainly due to its inert chemical properties when in contact with the organic polymer. It performs the two-phase reaction as follows.

$$LiFePO_4 \longrightarrow FePO_4 + Li^+ + e^-$$

Equation 6.1

2) Anode

An anode pellet was made from a mixture of $Li_4Ti_5O_{12}$ active material, AB and PTFE powder in the ratio 75:20:5 by weight. $Li_4Ti_5O_{12}$ is a two phase material. It has a specific

capacity of 175 mA h/g. The insertion/removal of Li into/from $Li_4Ti_5O_{12}$ occurs at potential around 1.55 V *vs.* lithium with no volume change on lithaition/delithaition[2, 3]. The reaction can be summarised as follows[4].

$$Li_4Ti_5O_{12} + 3Li^+ + 3e^- \longrightarrow Li_7Ti_5O_{12}$$

Equation 6.2

3) Separator

The prepared PP2O3 composite pellets were used as the separator/electrolyte a mixture of PP2O3 : PC : LiTFSI : PTFE =30:59:10:1 wt % (this composite exhibits good ionic conductivity). The untreated and treated PP2O3 samples were synthesised using the chemical synthesis as explained in Chapter 4. The composite pellets containing the untreated or treated polymer will be referred to as the treated or untreated pellet.

These three parts were fabricated into a battery as shown in Figure 6.1. A small fraction (5 µl of 1 M $LiPF_6$ in EC:DMC(1:1)) of liquid electrolyte was added to the cathode and anode pellets. This was to provide ionic conduction through the composite electrodes. The self-discharge and galvanostatic cycling performance of the completed cell was then examined. The details of these electrochemical tests are detailed below.

6.2.2 Procedure

6.2.2.1 Self-discharge test

The self-discharge test was used to calculate the internal electron leakage resulting from partial electronic conductivities of polymer samples as explained in Chapter 2.

The cell was fabricated as shown in Figure 6.1. The cell was charged at 50 µA (A slow charging rate to ensure complete charging) from the open circuit potential up to 2.5 V. The open circuit potential was measured as a function of time. The short circuit resistance of the cell could then be determined according to Equation 2.18.

6.2.2.2 Galvanostatic test

The same cell as shown in Figure 6.1 was used with fresh electrodes for analysis using galvanostatic cycling. The cells of untreated and treated samples were tested at different C-rates i.e C/5 and 2C. Specific capacity and capacity retention on continued charging and discharge (cyclability) would be determined.

6.2.3 Results and Discussion

The following section details the results obtained from the experiments described above.

6.2.3.1 Self-discharge test

The cells were charged at a current of 50 µA from open circuit potential up to 2.5 V and then the open circuit potential was measured as a function of time the result of which is shown in Figure 6.2.

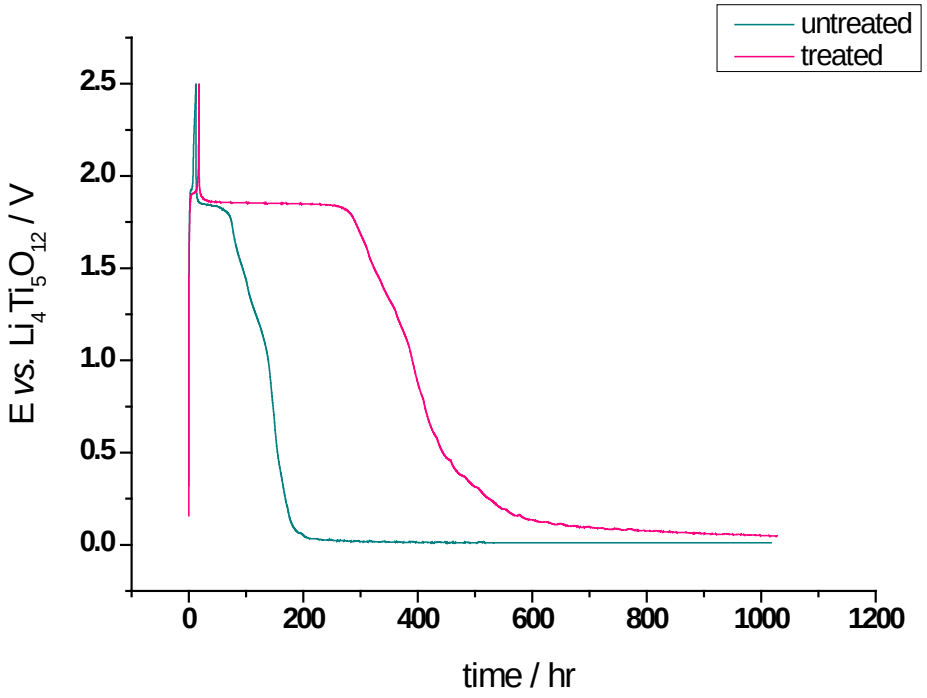

Figure 6.2 Self-discharge voltage profile of the cell of untreated and treated samples

During the open circuit measurement in both cases there was a potential plateau at about 1.85 V. This corresponds to the discharge potential of $Li_xTi_5O_{12}$/$LiFePO_4$ battery. This is a good indication that a slow discharge is occurring as a result of an internal short. Using Equation 2.18 the charge capacities and self-discharge time were used to calculate the short circuit resistances as shown in the Table 6.1.

Table 6.1 Short circuit resistances of untreated and treated samples of the cells from the self discharge test

sample	charge capacity (mA h)	discharge time (h)	short circuit resistance (k Ω)
untreated	1.36	237.71	322.38
treated	1.65	982.30	1101.81

The self-discharge time of the treated sample was nearly 4 times longer than that of the untreated one. This corresponds to a much higher short circuit resistance in the treated sample. This indicates that the treated sample was a better electronic insulator as expected whereas the untreated sample had a short circuit due to partial electronic conduction in the untreated polymer. However, the short circuit resistance indicates that the treated sample still has some electronic conductivity which is causing some self discharge. This is not ideal and requires further work to develop methods to improve the method of conductivity destruction.

6.2.3.2 Galvanostatic test

Initially the cells were continually charged and discharged between 3.0 V and 0.5 V at a rate of C/5 to investigate the slow rate cyclability. The same experiment was conducted at rate of 2C in order to observe the effect increased rate on cyclability.

6.2.3.2.2 Galvanostatic test at C-rate of C/5

Figure 6.3 shows the charge/discharge curves for 1st, 10th and 40th cycles of the untreated and treated cells.

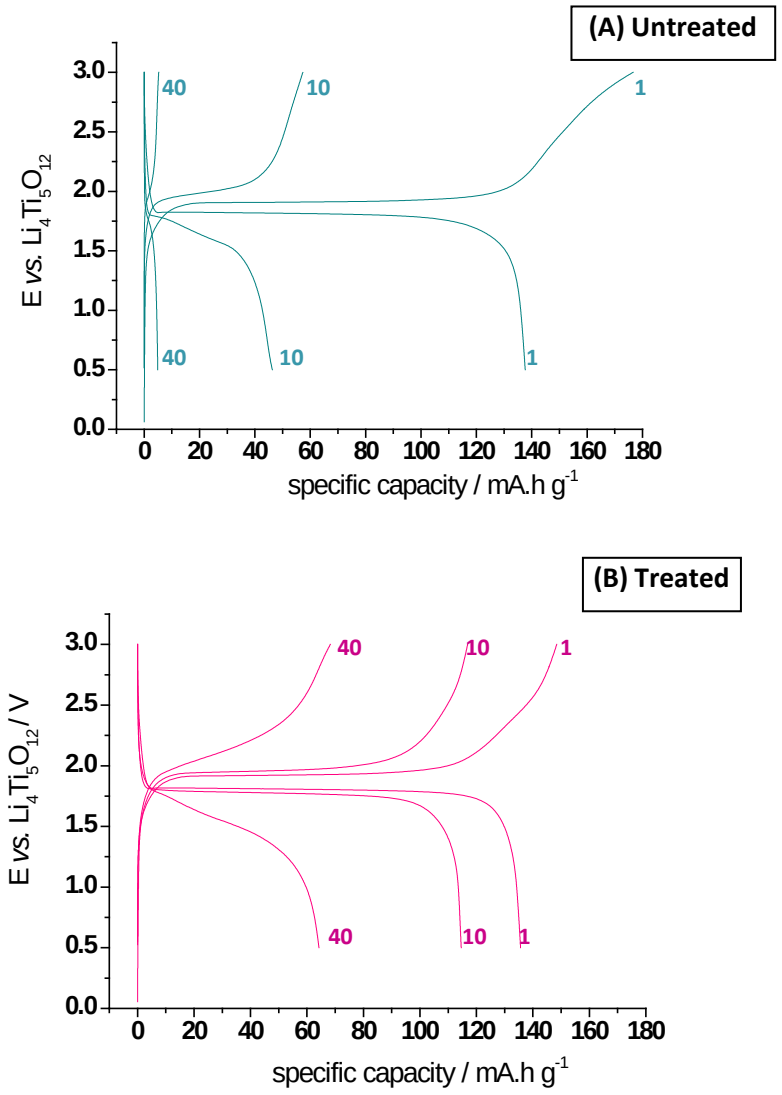

Figure 6.3 Charge/discharge voltage profile of $Li_4T_5O_{12}$/$LiFePO_4$ with the two separator samples (A) untreated and (B) treated at C-rate of C/5 for 40 cycles.

Figure 6.3 shows that the first cycle of both cells has a flat voltage plateau at around 2.0 V. This potential is characteristic of that expected for a $Li_4T_5O_{12}$/$LiFePO_4$, and the flat plateau is characteristic of the two phase nature of both materials. A significant charge discharge imbalance can be seen in both cases. This is highlighted in Table 6.2 below.

Table 6.2 Table showing the charge and discharge capacity at first, tenth and fortieth cycles of the battery shown in Figure 6.3. Also indicated is the discharge capacity as a percentage of the charge capacity.

Untreated			
Cycle Number	Charge Capacity (mA h g^{-1})	Discharge Capacity (mA h g^{-1})	Discharge Percentage of Charge (%)
1	176.59	137.63	77.94
10	57.30	45.29	79.04
40	-	-	-
Treated			
Cycle Number	Charge Capacity (mA h g^{-1})	Discharge Capacity (mA h g^{-1})	Discharge Percentage of Charge (%)
1	148.44	135.62	91.36
10	116.88	114.61	98.06
40	63.55	56.18	88.42

Table 6.2 indicates that there is a significant imbalance in the capacity of charge and discharge in all cases. However, this is much more significant in the case of the untreated sample. The reason for this imbalance is explained by the internal short circuit. As the battery is charged a fraction of the current is consumed in the short circuit therefore a greater amount of charge is required to fully charge the battery; this is highlighted by the charge capacity of the untreated sample during the first cycle which is greater than the theoretical capacity of $LiFePO_4$. During discharge a smaller amount of charge will be required as a fraction of the discharge current will occur through the internal short.

Another feature of the data shown in Figure 6.3 is the decrease in capacity loss with increased cycling. To clarify this capacity *vs.* cycle number behavior has been plotted in Figure 6.4.

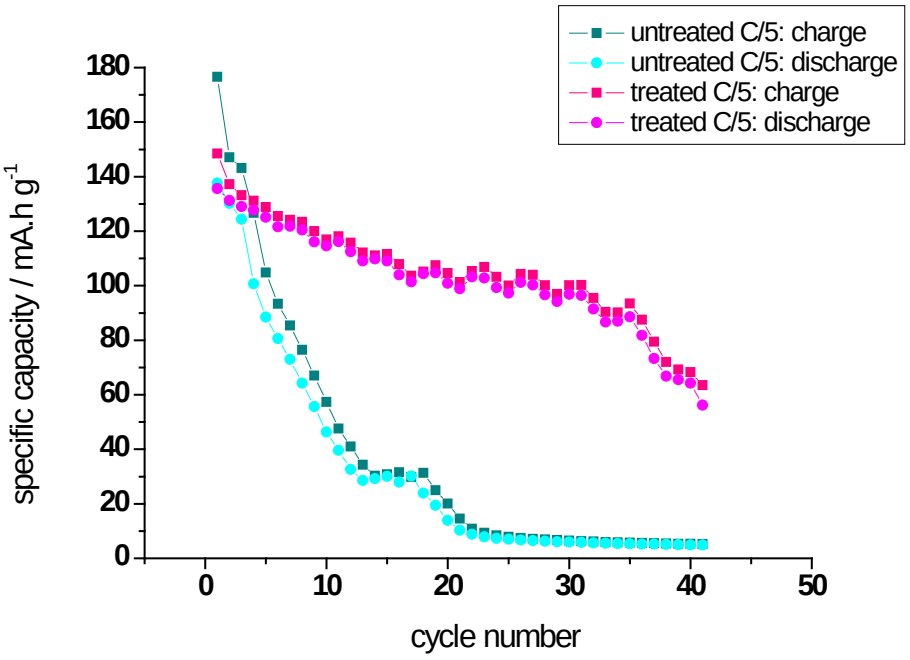

Figure 6.4 Variation of charge and discharge capacities versus cycle number for untreated and treated cells at C/5 for 40 cycles.

From Figure 6.4 it is clear to see the capacity of untreated cell decreased sharply during the first 20 cycles and dropped down below 10 mA h g^{-1}. In the case of treated cell its specific capacity was still quite high (63.55 mA h g^{-1}) retaining 42.81 % of the initial capacity at cycle 40. The poor cycling behavior of the untreated sample is somewhat difficult to explain. The expected result would be that the cell has a stable capacity on cycling which has a significant charge and discharge imbalance. However, one possible explanation is the initial state of the battery. When constructed in the glove box the time between construction and testing is approximately 30 minutes. During this time the cell is exposed to a short circuit condition (even though it has a high resistance). During this time uncontrolled reactions will be occurring on the positive and negative electrodes which could result in the observed performance. The results of the higher rate testing will now be examined.

6.2.3.2.1 Galvanostatic test at C-rate of 2C

Figure 6.5 shows the charge/discharge curves for 1st, 10th, 100th and 200th of the untreated and treated cells cycled at a rate of 2C.

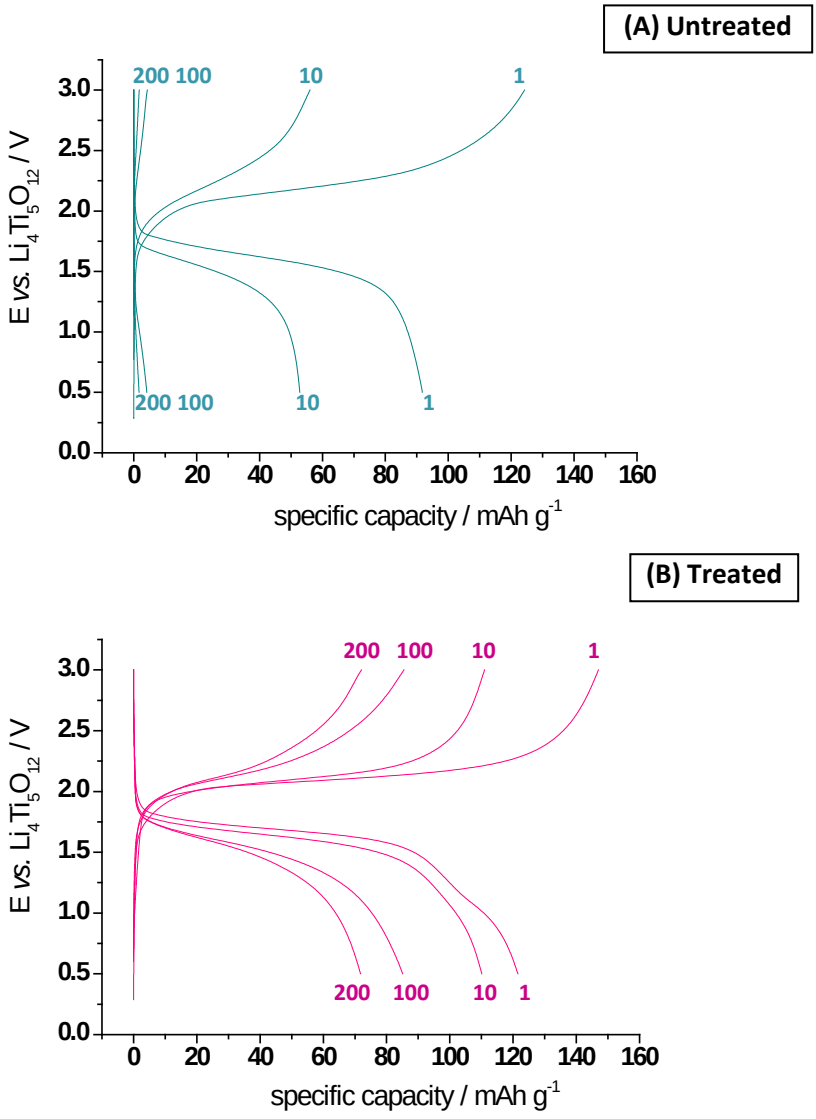

Figure 6.5 Charge/discharge voltage profile of $Li_4T_5O_{12}$/$LiFePO_4$ with the two separator samples (A) untreated and (B) treated at C-rate of 2C for 200 cycles.

Figure 6.5 shows that the treated cell had flat voltage plateaus around 2.0 V during the 1st cycle similar to the performance that seen for the C/5. The untreated cell did not show proper voltage plateaus. The discharge capacity as a percentage of the charge capacity is again examined in Table 6.3.

Table 6.3 Table showing the charge and discharge capacity at first, tenth and fortieth cycles of the battery shown in Figure 6.5. Also indicated is the discharge capacity as a percentage of the charge capacity.

Untreated			
Cycle Number	Charge Capacity (mA h g^{-1})	Discharge Capacity (mA h g^{-1})	Discharge Percentage of Charge (%)
1	124.23	91.76	73.86
10	56.02	52.80	94.25
100	-	-	-
200	-	-	-
Treated			
Cycle Number	Charge Capacity (mA h g^{-1})	Discharge Capacity (mA h g^{-1})	Discharge Percentage of Charge (%)
1	142.18	117.53	82.66
10	107.35	106.52	99.23
100	82.68	82.34	99.59
200	69.54	69.17	99.47

Table 6.3 shows the same charge discharge imbalance at this rate which is indicative of a short circuit as described earlier. The treated sample shows an unusually high charge discharge capacity imbalance on the first cycle however is remarkably balanced thereafter. Again to examine the cyclability of these materials in more detail a plot of capacity *vs.* cycle number is shown in Figure 6.6.

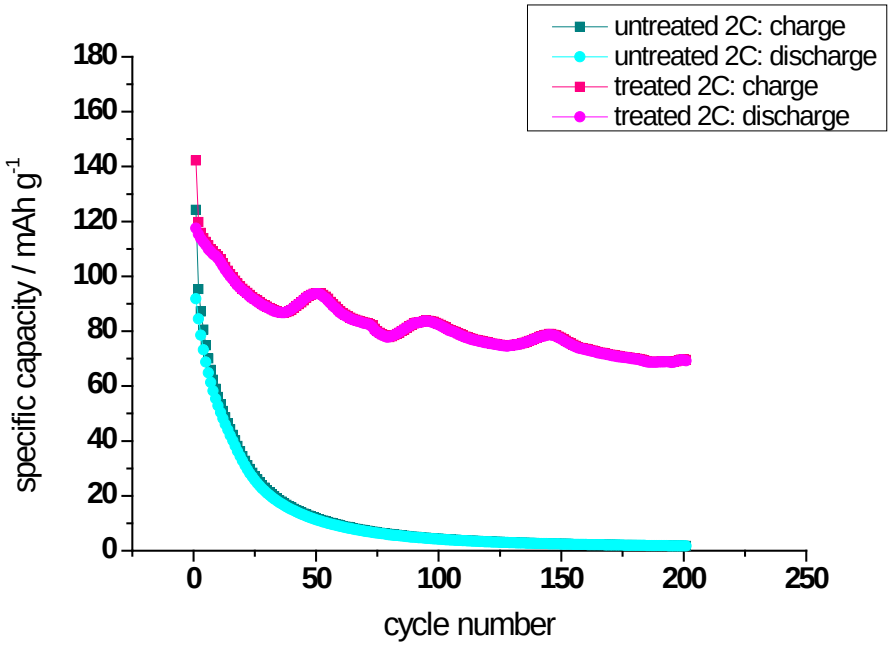

Figure 6.6 Variation of charge and discharge capacities versus cycle number for untreated and treated cell at C-rate of 2C for 200 cycles.

The capacity of the untreated cell decreased sharply during the first 60 cycles where the extractable capacity had dropped down below 10 mA h g^{-1}. This may be explained in the same way as described earlier for the C/5 cell. In the case of treated sample the cell maintained 48.91 % capacity retention for 200 cycles. This performance is reasonably good and shows that at these rates the percentage of initial capacity retention after 200 cycles is actually higher than that of the cell cycled at C/5 after only 40 cycles. The performance of the battery at this increased rate is a good indication that the ionic conductivity of these composite style electrolyte materials is reasonably high as the performance is similar to those reported in the literature with conventional liquid electrolyte soaked separators[5].

The general galvanostatic performance of these batteries prepared with the treated samples is not perfect however it is acceptable if only a low number of cycles was required. Enhanced performance may be achieved by improving the technique used to form the electrolyte pellets as this was not optimised in the experiments presented here and considering improved conditions to destroy the electronic conductivity. However, these

experiments show that the electrolyte can be used effectively to cycle a battery and should be sufficient for use in proof of concept experiments for the construction of a 3D microbattery. This will be shown in the following section.

6.3 Electrodeposited PP2O3 with Application in 3D Batteries

The 3D battery concept is to design cells that comprise of anodes and cathodes which have active surface areas exposed in three dimensions[6]. With 3D structures, making electrodes longer, rather than thicker resulting in increased cell capacity. These structures require three conformal layers to be coated on a current corrector i.e. cathode, electrolyte and anode.

In this work a RVC substrate was used to provide the high aspect ratio. This gave an increase in surface area of 25 times per footprint area. This substrate was then coated with the commercial battery material $LiFePO_4$, this was done using an established coating route developed by co-workers in Southampton. The untreated PP2O3 film was electrodeposited over this substrate and then the overoxidation treatment was applied as explained in Chapter 5. Finally a Li-Hg amalgam was used as an anode material in order to provide soft contact on 3D structure coated in the PP2O3 film.

6.3.1 Chemicals, Materials, Equipment and Procedure

6.3.1.1 Chemicals and materials

P2O3 was synthesised as explained in Chapter 4. ACN, LiTFSI, Li metal and Mercury were obtained from Aldrich. $LiFePO_4$ was received from Hydro Québec. Carbon black was obtained from Hydro Québec super graphite. The 3D reticulated vitreous carbon substrate (RVC) (100 ppi (pores per inch) was purchased from AEG aerospace engineering. The 1 M $LiPF_6$ in EC:DMC electrolyte was received from Novolyte technologies.

An ink of $LiFePO_4$ containing 1.8 g of $LiFePO_4$, 0.3 g PVdF-HFP, 0.3 g of carbon black and 25 g of CP. The mixture was left string overnight. This resulted in a homogeneous $LiFePO_4$ ink.[7].

Li-Hg was prepared by dissolving lithium chunks in Hg. The mixture was left stirring overnight. The excess lithium chunks were removed. The homogeneous Li-Hg was obtained. The Li insertion potential into Li-Hg occurs at potential around 1 V *vs.* lithium[8].

6.3.1.2 Equipment

A schematic of the cell used is shown in Figure 6.7. This was connected to the potentiostat (VMP2) for galvanostatic test. The procedure for assembling this cell is described below.

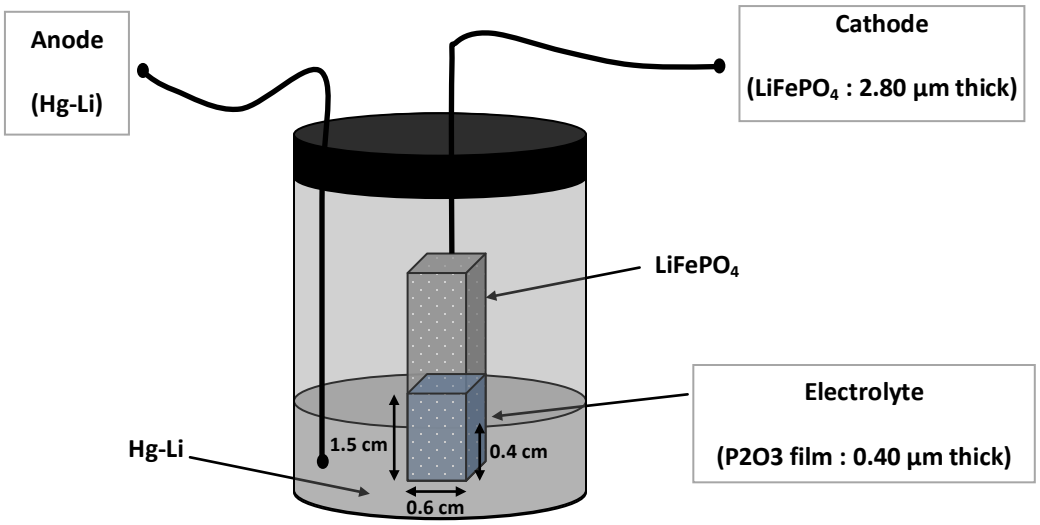

Figure 6.7 The 3D cell construction for galvanostatic test

6.3.1.3 Procedure

To fabricate the complete 3D battery there were five steps as follows.

1) Coating $LiFePO_4$ on 3D RVC using $LiFePO_4$ ink by spin coating technique

- This was done by submerging the 3D RVC in the $LiFePO_4$ ink. The excess ink was removed by spinning the foam. The spinning was performed by clipping the foam

to a crocodile clip which was directly attached to a computer fan. The rotation rate of the fan was around 1200 rpm. The electrode was then left in ambient condition to dry over night.

2) Coating PP2O3 film on $LiFePO_4$ by electrochemical deposition.

- PP2O3 was electrodeposited on $LiFePO_4$ coated 3D RVC from ACN containing 10 mM P2O3 and 50 mM LiTFSI by applying 1.0 V *vs.* Ag/10mM $AgNO_3$ for 4 minutes. Pt gauze and Ag/10 mM $AgNO_3$ were used as counter and reference electrodes respectively. Contact was made to the foam using a crocodile clip connection.

3) Converting the electronic conductive polymer to non electronic conducting material by the overoxidation treatment.

- The same approach for the treatment was used as that described in Chapter 4 and 5. However, contact was made to the foam using a crocodile clip connection.

4) Soaking the sample in 1 M $LiPF_6$ in EC:DMC

5) Finishing the complete battery fabrication by submerging the sample in Li-Hg anode as shown in Figure 6.7. The complete battery could then be examined under galvanostatic test.

6.3.2 Results and discussion

6.3.2.1 Preparation of $LiFePO_4$ coated 3D RVC

The $LiFePO_4$ coated 3D RVC samples were examined using SEM as can be seen from the Figure 6.8.

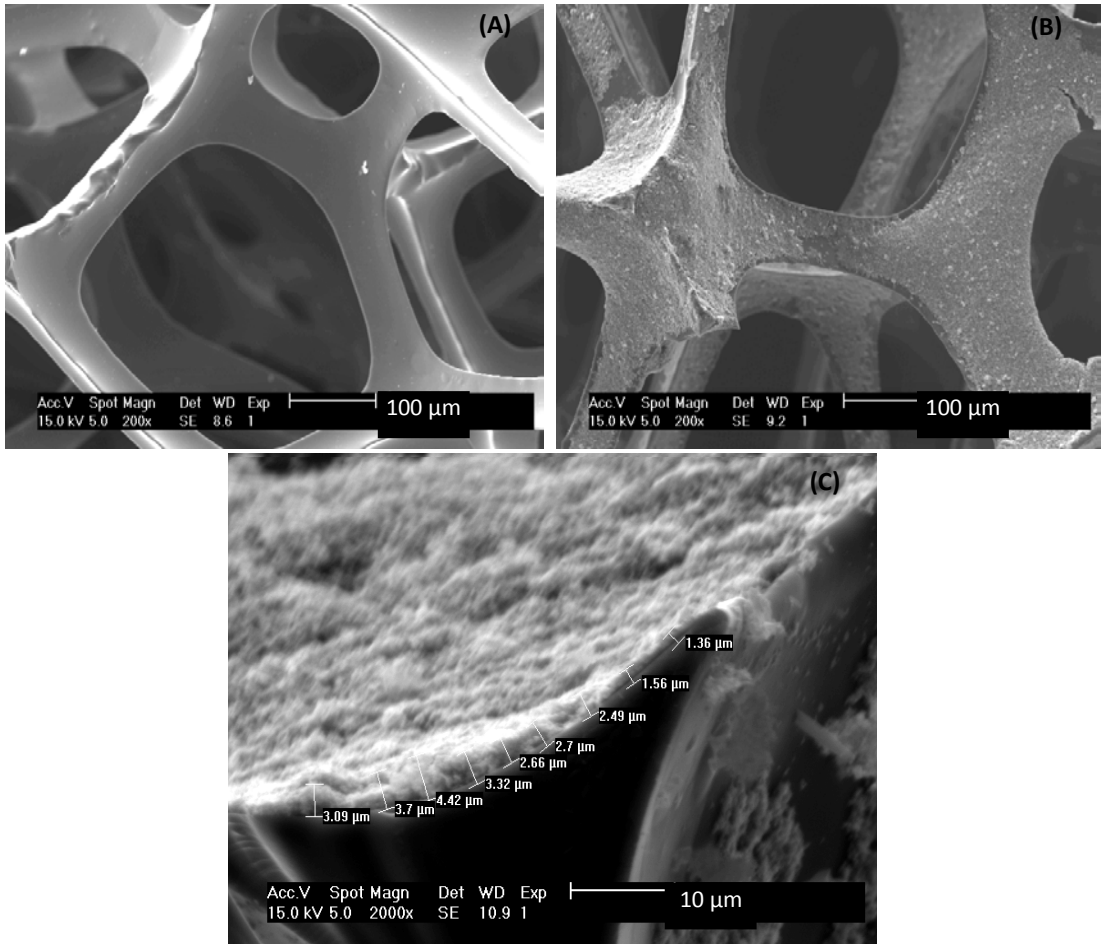

Figure 6.8 The SEM images of $LiFePO_4$ coated 3D RVC (A) bare 3D RVC (B) $LiFePO_4$ coated 3D RVC and (C) cross section of $LiFePO_4$ coated 3D RVC

The $LiFePO_4$ layer was approximately smooth and of reasonably consistent thickness as can be seen from Figure 6.8 (B). The thickness of $LiFePO_4$ layer on 3D RVC was determined by observing the cross sectional area of a piece of fracture foam as shown in Figure 6.8 (C). The average thickness from this evaluation was 2.81 µm.

6.3.2.2 Preparation of PP2O3 film on $LiFePO_4$ coated 3D RVC

The current response recorded during the potential step used to deposit the PP2O3 film on the $LiFePO_4$ coated RVC substrate is shown in Figure 6.9.

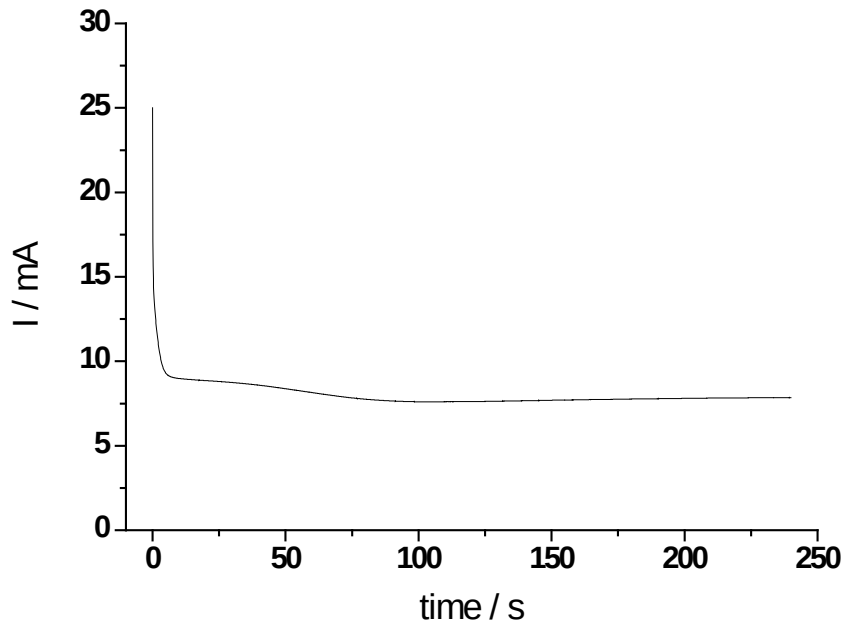

Figure 6.9 Electrodeposition of PP2O3 film in 10 mM P2O3 containing 50 mM LiTFSI in ACN at an applied potential of 1.0 V *vs.* Ag/10 mM $AgNO_3$ for 4 minutes

By assuming the films were conformal as indicated later in Figure 6.11 (B). The estimated film thickness was around 0.40 µm. The polymer was then converted to an electronic insulator using an overoxidation treatment. The cyclic voltammograms recorded during the overoxidation treatment are shown in Figure 6.10.

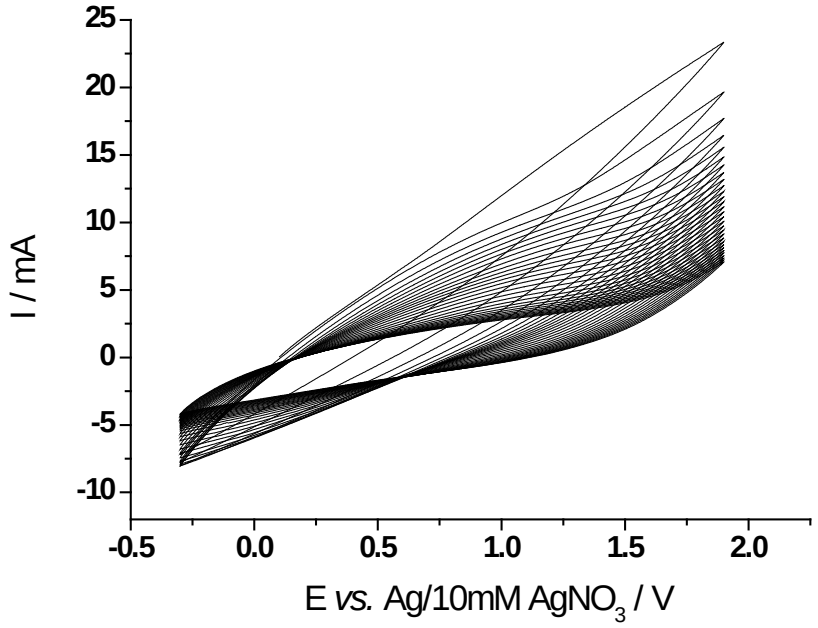

Figure 6.10 Cyclic voltammograms for cycling PP2O3 film at the over oxidation potential range between -0.3 and +1.9 V in 50 mM LiTFSI in ACN at 100 mV/s for preparing treated film.

From Figure 6.10 it can be seen that the maximum currents observed during the cyclic voltammograms decrease slightly from cycle to cycle during the over oxidative treatment. It was determined that after 20 cycles the polymer had become electrochemically inactive. Cyclic voltammograms were stable and only double layer charge was seen. The large current envelope over the whole potential range indicates a high double layer capacitance resulting from the large surface area of PP2O3 on 3D RVC. The SEM images of the untreated and treated PP2O3 films are shown in Figure 6.11 (B) and (C) respectively.

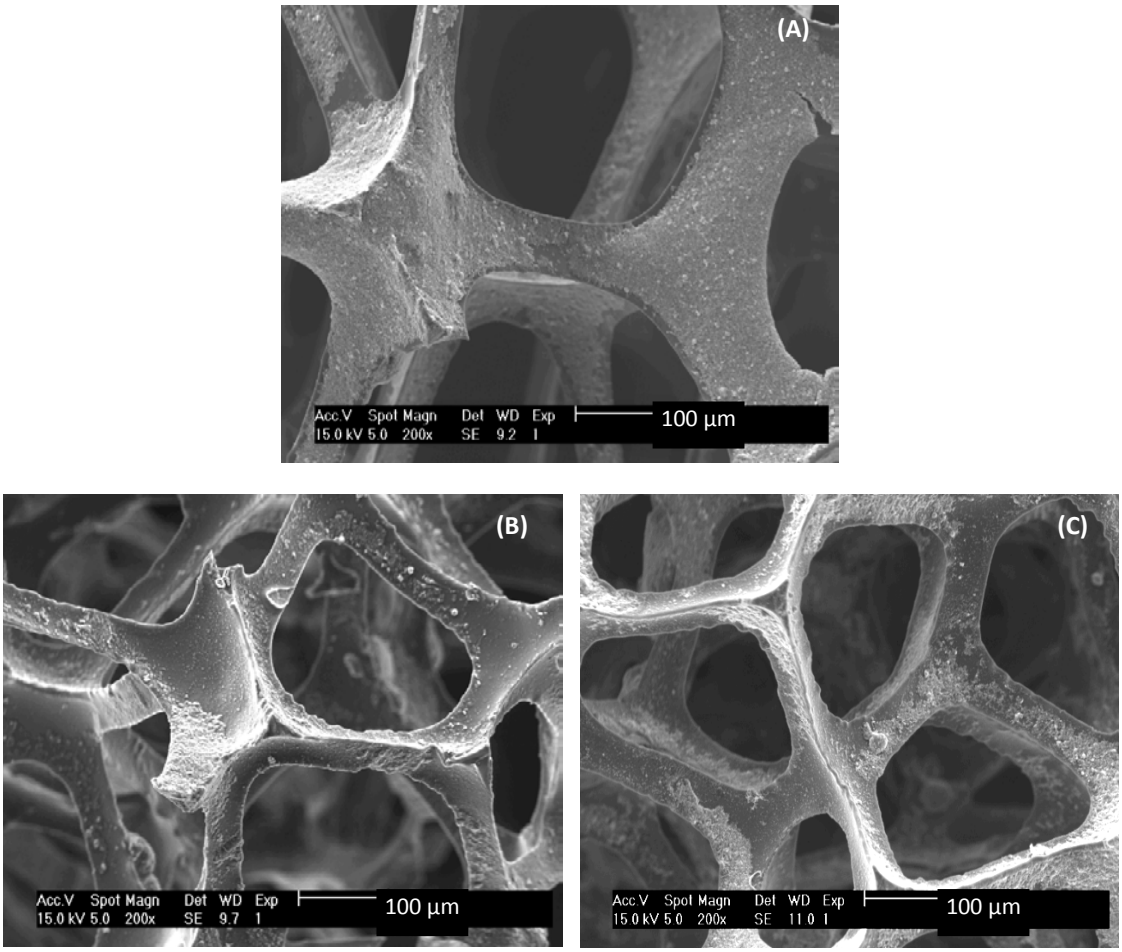

Figure 6.11 The SEM images (A) $LiFePO_4$ coated 3D RVC (B) untreated PP2O3 film coated on $LiFePO_4$ surface and (C) treated PP2O3 film coated on $LiFePO_4$ surface

The first observation to be made when looking at the SEM images shown in Figure 6.11 is the clear difference in the images (A) and (B). The $LiFePO_4$ coating is grainy and obviously containing large amounts of particulate. In the polymer coated sample this has been broadly covered by the smooth polymer layer, however in some areas the some evidence of the particulate under layer can still be seen this may indicate slight thinner regions of polymer coverage. The untreated and treated sample images can be seen in Figure 6.11 (B) and (C) respectively. Both films look similar, conformal and smooth without physical damage. However, from observation of these images it could be suggested that the particulate underlayer is more clearly visible in the treated sample than in the untreated one. This may be some indication that a slight thinning in the layer has occurred during the conductivity

destruction. However, the surface of the coating on the film still looks significantly different from that of the image (A) to confirm that the film is still present.

6.3.2.3 Galvanostatic test

The cell was charged and discharged at 50 µA and - 50 µA respectively i.e. at 10C within the potential ranges of 1.6 to 3.3 V for 11 cycles as shown in Figure 6.12.

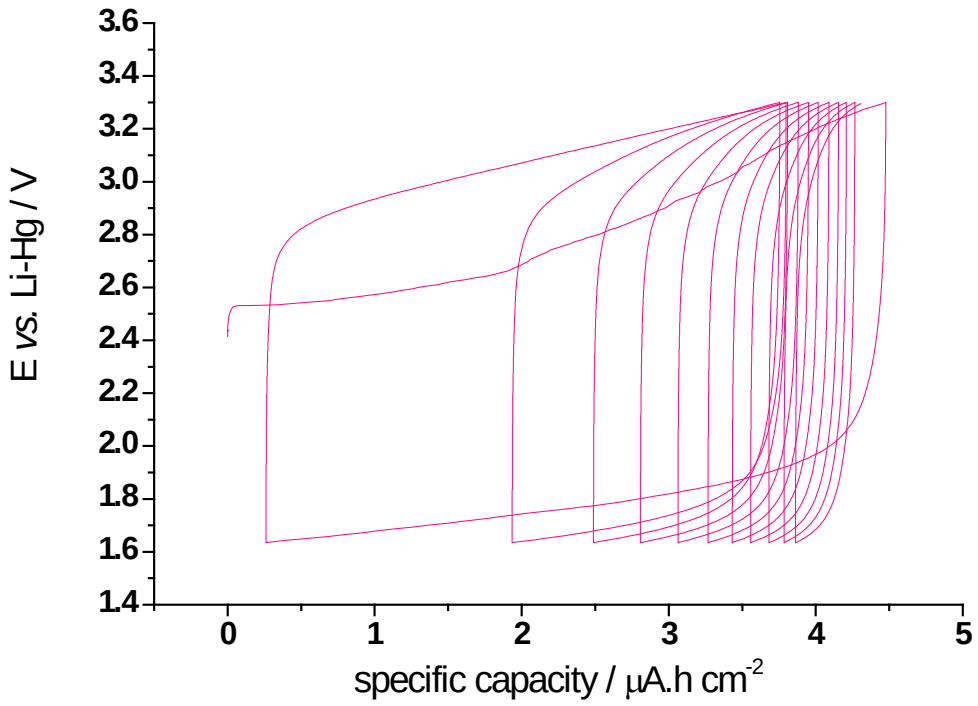

Figure 6.12 Charge/discharge voltage profile of the cell configuration of Li-Hg/treated PP2O3 sample/$LiFePO_4$ at charge/discharge rate of 10C

From the charge/discharge voltage profile in Figure 6.12 the open circuit potential was 2.40 V which is approximately as expected. This is based on previous knowledge that $LiFePO_4$ cells *vs.* Li typically have an open circuit voltage of 3.4 V *vs.* Li and Li-Hg is known to have a potential of around 1 V *vs.* Li. This open circuit potential was stable and observed for 5 minutes with no degradation indicating there was no significant short circuit in the cell. This is further evidence of conformal coating of the polymer over the surface of

$LiFePO_4$ coated foams. On charging the cell an initial curve is seen as a gradual slope between 2.4 and 3.3 V. The $LiFePO_4$ plateau would typically be flat, however, the Li insertion in Hg occurs over a potential range proportional to the Li concentration, explaining the slight charging slope. The behaviour is therefore consistent with Li ions being extracted from the $LiFePO_4$ cathode and inserted into the Li-Hg anode. On discharge the potential of the cell dropped steeply to 2 V and continued dropping gradually to 1.6 V. This plateau is much lower than the discharge would be anticipated to occur which would be around 2.4 V. This is likely during to the build up of some high resistance film between the contact of the Li-Hg amalgam and the polymer layer. This is concluded based on visual observation of the film after removal from the amalgam. However, further experiments would be required to confirm this. The capacity can be seen to drop steeply from cycle to cycle. This is accompanied by an increased in the IR drop seen at the start of each charge or discharge segment. This is more evidence of increased internal resistance possibly resulting from this resistive film. However the charging behavior indicates that no significant short circuit was observed in the cell. Specific capacity and capacity retention were determined and can be seen from Figure 6.13.

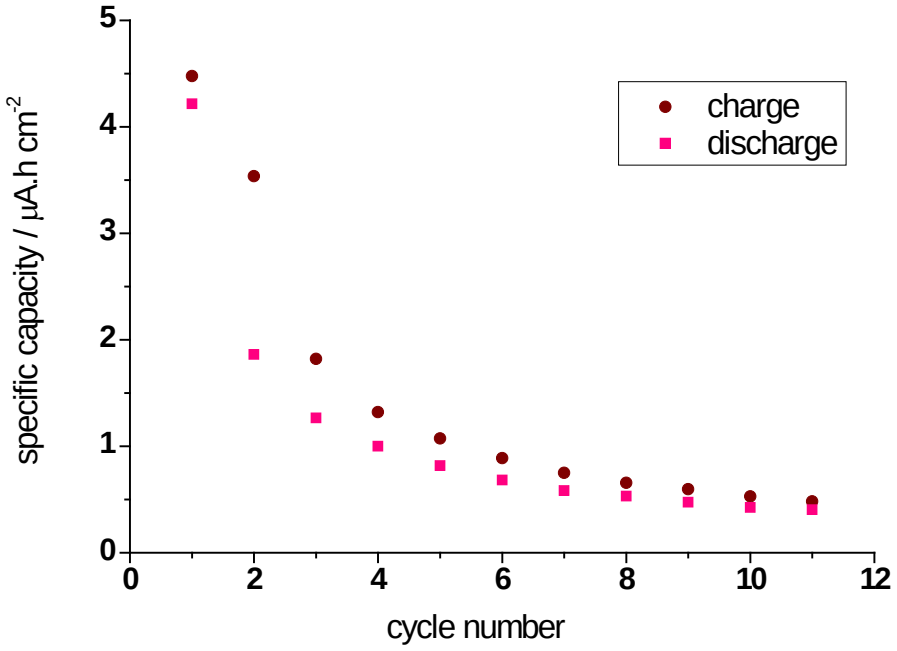

Figure 6.13 Charge and discharge capacities versus cycle number of the cell configuration of Li-Hg/treated PP2O3 sample/$LiFePO_4$ at charge/discharge rate of 10C

The first charge/discharge capacity was about 4.5 μA h/cm^2. The specific capacity decreased continuously down to less than 1 μA h/cm^2 in 6 cycles. The specific capacities anticipated for this deposit is approximately 100 μA h/cm^2 so the observed capacities are only around 5 % of that anticipated. The low specific capacity was possibly due to loss of contact surface between Hg-Li anode and PP2O3 film. This is because the Hg-Li did not perfectly penetrate into 3D structure of the sample as expected meaning that only a fraction of the available capacity could be accessed. It is also not an optimized anode system and is difficult to work handle. It is therefore concluded that the result could be improved by using composite anode inks such as TiO_2 and $Li_4Ti_5O_{12}$ instead. This experiment however confirms that 3D battery worked to some extent and is an operational proof of the concept.

6.4 Chapter 6 Conclusions

In case of the powder samples both untreated and treated were used as electrolytes in a cell configuration of $Li_4Ti_5O_{12}$/electrolyte/$LiFePO_4$. The short circuit resistances of the cells were measured using a self-discharge test and also by following the specific capacities as a function of cycling by galvanostatic test. As expected the untreated cell showed a lower short circuit resistance than that of the treated one due to the higher electronic conduction in the untreated polymer network. Under examination using both C-rates, 2C and C/5, the treated cells had better retention of capacity on cycling than those of the untreated ones.

The 3D battery fabrication using the homogeneous electrodeposited films was successful. The $LiFePO_4$ cathode layer was conformal on 3D RVC current corrector formed using a spin coating technique. The electrolyte layer was prepared by electrodeposition of PP2O3 and then treatment by overoxidation. The treated film was smooth and conformal without cracks or holes. The Li-Hg anode was chosen to provide soft contact on 3D structured polymer layer. There were no short circuits resulting from cracks in the polymer layer. Its specific capacity however was quite low. The first charge/discharge capacity was about 4.5 $\mu A\ h/cm^2$. This was possibly due to a loss of contact surface between Hg-Li anode and 3D PP2O3 film structure. Li-Hg did not penetrate into the 3D structure of the sample. Its specific capacity could possibly be improved by using a composite anode ink instead. This result however did confirm the proof of concept in preparing 3D microbatteries in this way.

6.5 Chapter 6 References

[1] D. Zhang, R. Cai, Y. K. Zhou, Z. P. Shao, X. Z. Liao and Z. F. Ma, *Electrochimica Acta* **2010**, *55*, 2653-2661.
[2] A. Jaiswal, C. R. Horne, O. Chang, W. Zhang, W. Kong, E. Wang, T. Chern and M. M. Doeff, *Journal of the Electrochemical Society* **2009**, *156*, A1041-A1046.
[3] G. Armstrong, A. R. Armstrong, P. G. Bruce, P. Reale and B. Scrosati, *Advanced Materials* **2006**, *18*, 2597-2600.
[4] J. Morales, R. Trocoli, S. Franger and J. Santos-Pena, *Electrochimica Acta* **2010**, *55*, 3075-3082.
[5] C. Koga, S. Wada and M. Nakayama, *Electrochimica Acta 55*, 2561-2566.
[6] R. W. Hart, H. S. White, B. Dunn and D. R. Rolison, *Electrochemistry Communications* **2003**, *5*, 120-123.
[7] M. R. Roberts, G. Vitins and J. R. Owen, *Journal of Power Sources* **2008**, *179*, 754-762.
[8] D. R. C. a. J. N. Butler, *The Journal of electrochemical society* **1967**, *72*, 4.

Chapter 7

Conclusions and Further Work

7.1 Polymer Prepararation by Electrochemical and Chemical Techniques

This work has focused on the use of mixed ionically and electronically conducting polymers for use as electrolytes in batteries. The electronic conductivity is used to allow the deposition of well controlled conformal layers on 3D substrates. The electronic conductivity can then be broken so that the film can act as an insulating separator.

In Chapter 3 conformal layers of electronically conducting PEDOT were deposited on 3D and 2D substrates. This polymer has a conjugated polymer backbone and some ability to absorb solvent and coordinate cations due to the presence of ether oxygens. Conversion of this polymer to an insulator was then attempted. However, its electronic activity could not be completely destroyed by electrochemical means without loss of adhesion to the substrate. This meant that the polymer had limited use as an electrolyte, but provided a conceptual proof of concept as the electronic conductivity was significantly reduced by the electrochemical oxidation treatment.

Chapter 4 describes polymerisation of the polypyrrole derivative P2O3 by both electrochemical and chemical techniques to give a conjugated polymer, PP2O3 with solvating oligoether linkages. Smooth and conformal PP2O3 films were prepared by electrochemical deposition on planar carbon substrates and 3D structured RVC.

Polymer films were cycled in an electrolyte outside the potential stability range with the intention of disrupting the π-bond delocalization and electronic conductivity. EQCM was used to observe mass changes during deposition and the overoxidation treatment of samples. It was found that the deposition mass increased linearly with a constant rate around 1.849 µg/cycle cm^2. During the overoxidation treatment the polymer gained weight due to trapped anions. This resulted in irreversible loss of electronic activity. This treatment may also have caused the polymer to lose some oligoether linkages.

Chemical polymerisation of the monomer was achieved using Iron(III) trichloride oxidant with 83 % yield. To break the electronic conductivity the alkene groups were oxidized

using alkaline $KMnO_4$ solution. The yield was around 106 % wt. The excess mass was probably due to the by-product MnO_2.

7.2 Electronic and Ionic Conductivities of PP2O3

The electronic and ionic conductivities of both the chemically and electrochemically prepared PP2O3 samples were determined by EIS.

For the chemically prepared samples the conductive properties were determined by impedance measurement using two ionically blocking electrodes. The electronic conductivities of the as-prepared and treated samples were quite low, 10^{-7} and 10^{-8} S/cm, whereas the ionic conductivity of both samples was in the range of 10^{-5} - 10^{-6} S/cm. An ionic conductivity slightly higher than that seen from the electrochemically prepared sample was attributed to the presence of PC plasticiser in the chemically prepared sample. However the bulk samples had such poor mechanical properties and binder (PTFE) and plasticiser (PC) needed to be added to the powder polymers in order to form pellet samples.

In the case of the electrodeposited samples, the ionic and electronic conductivities as well as capacitance were determined as a function of the applied doping potential. The electronic conductivity of the as-prepared film largely depended on the doping level of the polymer (influenced by the potential at which the polymer was held during impedance measurement). At the maximum doping potential, around 0.30 V *vs.* Ag/Ag^+, the treated sample had around 50,000 times smaller electronic conductivity than that of untreated one ($1.69x10^{-5}$ and $3.43x10^{-10}$ S/cm for the untreated and treated respectively). The ionic conductivity of both samples had similar values around 10^{-6} S/cm. The electronic conductivity therefore corresponded to only 0.06 % of the total conductivity. The treated sample was technically considered to be sufficiently electronically insulating to act as a battery separator.

7.3 Battery Applications of PP2O3

PP2O3 samples prepared by both techniques were used as electrolytes in batteries. In the case of the chemically prepared polymer, the three components, i.e. $LiFePO_4$ cathode, untreated and treated $PP2O_3$ electrolyte and $Li_4Ti_5O_{12}$ anode were prepared into pellets and then compacted into a cell as in a conventional 2D battery. During a self-discharge test the untreated sample showed a lower short circuit resistance than that of the treated one due to residual electronic conduction in untreated polymer network. This explained the lower specific capacities of the untreated cell observed with the galvanostatic test. The specific capacity of the cell was related to the ability of the electrode material to store charge and the electrolyte sample to act as an electronic insulator to prevent the electrodes from leaking charge due to its residual electronic conductivity. Cells with both the treated and untreated electrolyte were tested at different C-rates, 2C and C/5, cells with the treated electrolyte had higher cyclabilities than those of the untreated ones. This confirms the results of the lower electronic conductivity in the treated sample.

To prepare 3D batteries using the electrodeposited polymer a reticulated vitreous carbon (RVC) was used as a 3D current corrector. A layer of $LiFePO_4$ cathode was prepared as a conformal layer on the 3D RVC using a modified spin coating technique. PP2O3 was then deposited electrochemically and then converted to an electronic insulator by the overoxidation treatment. Finally, Li-Hg was used as the anode to provide a soft contact to the 3D structured cell. The cell worked without short circuit, indicating an absence of cracks in the polymer electrolyte. The specific capacity of the electrode was quite low because Hg-Li did not perfectly penetrate into 3D structure of the sample as expected and only a fraction of the available capacity could be accessed. However, this result was a proof of concept for the 3D battery principle.

7.4 Suggestions for Further Work

The electrodeposited film preparation in 3D batteries is a better option than chemical polymerisation to obtain a uniform thin film with good mechanical properties.

The following properties could be improved by the discovery of new polymers.

- Ionic resisitance; the ionic conductivity could be improved, and the interfacial resistance could be lowered by suitable molecular design.

- an increase in the electronic conductivity over a wider potential range would be useful to allow more scope for the deposition of a second electrode layer on top of the polymer before conversion into an electrolyte. Extending the potential range may be possible by using a different backbone or a combination of conjugated polymers, e.g polythiophenes, phenylenes, anilines.

- alternative techniques for disrupting the electronic conductivity, e.g. using different chemistries, would remove the constraints on electrodeposition of a second electrode as above.

- the cell performance could be improved using cathode and anode materials with a higher capacity [1, 2] and the 3D concept could be further explored. Moreover ionic conductivity of electrodeposited PP2O3 itself could be improved by adding organic solvent as plasticiser[3-5] during film preparation.

- adhesion of the polymer to electrode surfaces could be improved by surface derivatisation before deposition.

7.5 Chapter 7 References

[1] H. W. Lu, W. Zeng, Y. S. Li and Z. W. Fu, *Journal of Power Sources* **2007**, *164*, 874-879.
[2] A. Zhang, Z. M. Zheng, F. Y. Cheng, Z. L. Tao and J. Chen, *Science China-Chemistry* **2011**, *54*, 936-940.
[3] C. W. Walker and M. Salomon, *Plasticisers for solid polymer electrolytes*, Washington **1995**, p. 30.
[4] M. Kumar and S. S. Sekhon, *Ionics* **2002**, *8*, 223-233.
[5] M. Andrei and M. Soprani, *Electrochimica Acta* **1998**, *43*, 1205-1215.

Appendices

Appendix 1

1.1 Study of the PEDOT Film thickness versus deposition charge

PEDOT samples from different preparation conditions could have different densities and therefore thicknesses. This can happen as a result of a more spongy deposit. The effect of electrolyte solutions on PEDOT film thickness was studied. This focused only on the aqueous electrolyte routes. The reason for this is that only limited access to the profilometer used for these measurements could be achieved during this project and unfortunately a comprehensive investigation could not be completed.

1.1.1 Chemicals, Materials and Equipment

EDOT, SDS and TSNa were received from Sigma Aldrich. Two different aqueous solutions were also prepared 10 mM EDOT containing 50 mM SDS (SDS electrolyte) in DI water and the second a 10 mM EDOT containing 10 mM TSNa (TSNa electrolyte) and 5 % of isopropanol in DI.

A gold coated slide working electrode was used as this provided a flat surface reference point which the film thickness could be easily determined from. Pt gauze counter electrode and SCE reference electrode were used. The cell was connected to a potentiostat (VMP2 from Bio Logic instruments)

1.1.2 Procedure

PEDOT films were electrodeposited from the two aqueous electrolyte solutions. Chronoamperometry was used as the deposition method on the gold coated glass slides at applied potentials of 0.9 V *vs.* SCE for SDS solution and 1.0 V *vs.* SCE for TSNa solution (potentials were chosen as 0.1 V above the deposition onset potential as determined from the CV). Polymerisation times of 4, 6 and 8 minutes were used in order to obtain different film thicknesses. The film thicknesses were measured using a profilometer (real thickness) and compared with the polymerisation charge.

1.1.3 Results and Discussion

The plots of polymerisation charge *vs.* film thickness of both films can be seen from Figure 1.

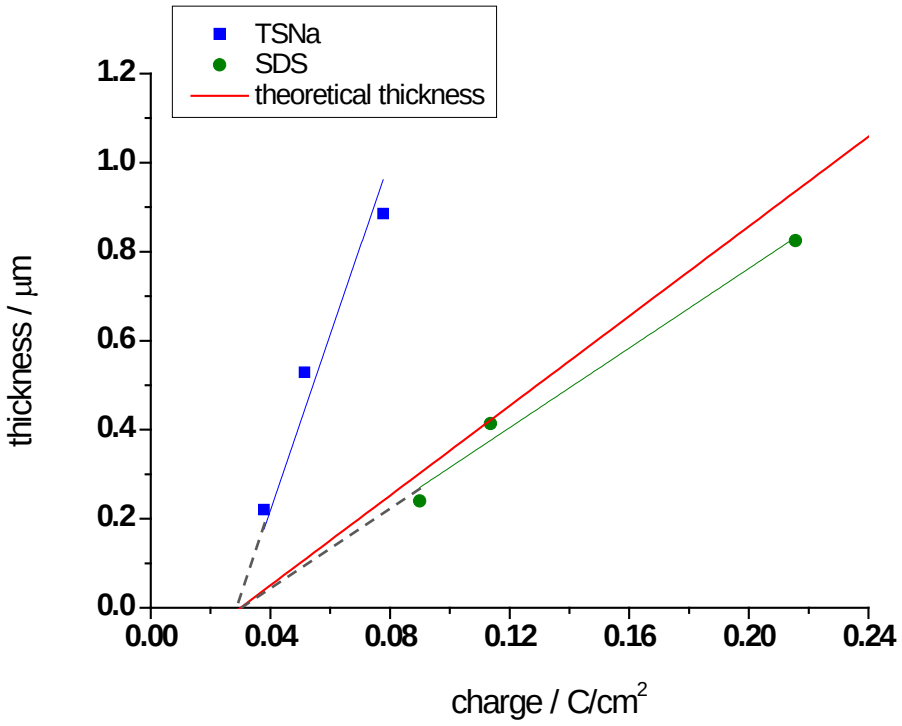

Figure 1 The dependence of film thickness on polymerisation charge. The first, second and last dots in each line represented different polymerization time composed of 4, 6 and 8 minutes respectively. The blue and represented PEDOT film from solution of TSNa, green represented film from solution of SDS and the red line is theoretical thickness.

The results deviate from the theoretical line as follows for the TSNa electrolyte the observed thickness were considerably larger than theoretical. This can be explained by a lower density, incorporation of water or combination of both. In the case of SDS the thickness is slightly lower than theoretical. The deviation may be explained by a higher density, a reduced Faradic efficiency, or both.

Furthermore, it is important to notice that the films from both solutions had a similar charge of onset to the PEDOT deposit at ca. 0.03 C/cm^2 as can be seen from the intercept at x-axis of the two dash lines. This is possibly due to the soluble oligomers. PEDOT could not be deposited on the substrate at the charge below 0.03 C/cm^2.

The morphology of the deposit was investigated using SEM. The images recorded are shown in Figure 2.

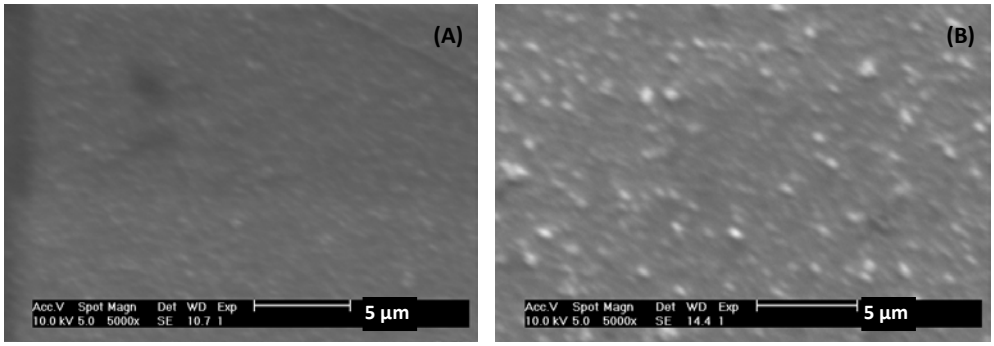

Figure 2 Scanning electron micrographs of PEDOT films. The films were electrodeposited by chronoamperometry at 0.9 V for SDS solution and 1.0 V for TSNa solution for 4 minutes using Au as a working electrode, Pt gauze as a counter electrode and SCE as a reference electrode; (A) the film from SDS solution and (B) the film from TSNa solution.

Figure 2 (A) shows that the polymer film surface from the SDS solution was quite smooth, whereas in Figure 2 (B) the film surface from TSNa solution was quite rough and had some globules on a compact film. It is therefore possible to conclude that the PEDOT film surface from SDS solution was smoother and the film was denser than those of PEDOT film from TSNa solution. This agreed well with the previous results of thickness on electropolymerisation charge. This experiment indicates that calculating the approximate thickness based on the theoretical thickness may not be always valid as the polymers do not deposit as perfect flat compact films.

Appendix 2

2.1 Study of the effect of film growth and adhesion

Due to poor adhesion of PEDOT films on substrates, an investigation of suitable substrates for electrodepositing PEDOT was undertaken.

2.2 Chemicals, Materials, Equipment and Procedure

EDOT was obtained from Sigma. SDS was received from Aldrich.

PEDOT films were electrodeposited in an electrolyte solution consisting of 10 mM EDOT and 10 mM SDS in aqueous solution by cyclic voltammetry at scan rate of 50 mV/s with the potential range of -0.5 to +1.2 V for 50 cycles. Pt gauze and SCE were used as counter and reference electrodes respectively whereas several substrates i.e. ITO glass, stainless steel sheet and Au and Pt coated slides were used as working electrodes in order to investigate suitable substrates for electrodeposition of PEDOT films from aqueous solution.

2.3 Results and Discussion

The cyclic voltammograms of electrodeposition of PEDOT films on the different substrates are shown in Figure 3, 4, 5 and 6.

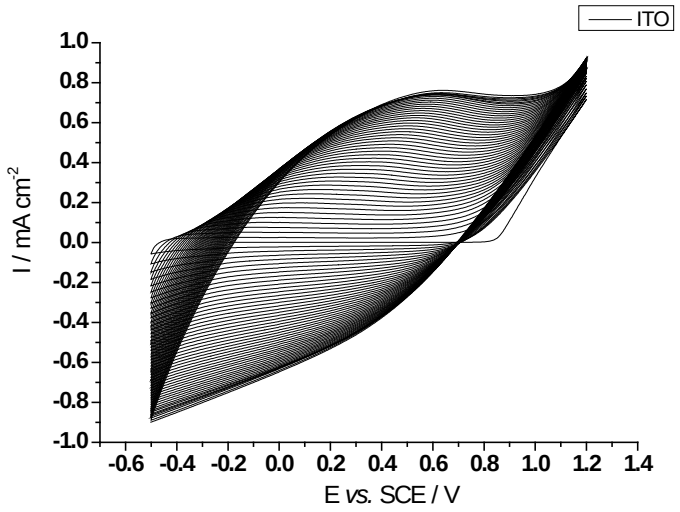

Figure 3 Cyclic voltammograms for the deposition of PEDOT film recorded between -0.5 and +1.2 V at 50 mV/s. The PEDOT film from a solution of 10 mM EDOT and 10 mM SDS was deposited on ITO coated glass electrode.

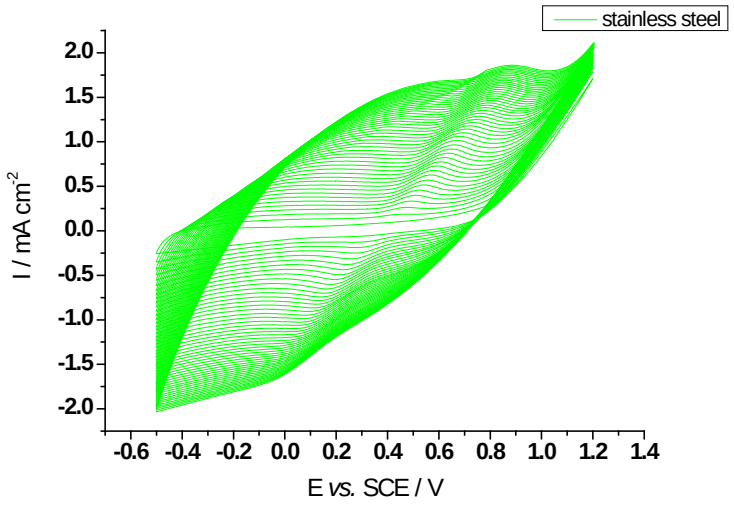

Figure 4 Cyclic voltammograms for the deposition of PEDOT film recorded between -0.5 and +1.2 V at 50 mV/s. The PEDOT film from a solution of 10 mM EDOT and 10 mM SDS was deposited on stainless steel electrode.

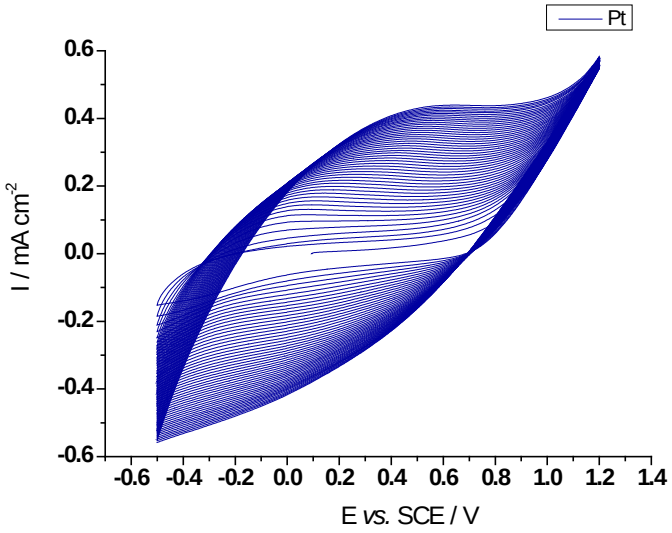

Figure 5 Cyclic voltammograms for the deposition of PEDOT film recorded between -0.5 and +1.2 V at 50 mV/s. The PEDOT film from a solution of 10 mM EDOT and 10 mM SDS was deposited on platinum coated slide.

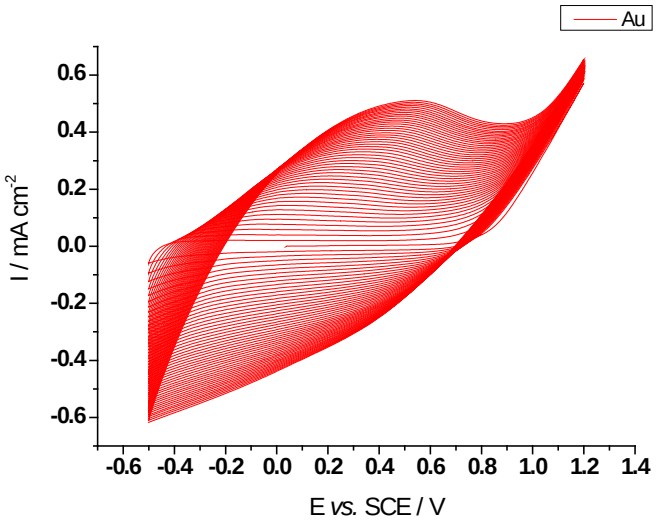

Figure 6 Cyclic voltammograms for the deposition of PEDOT film recorded between -0.5 and +1.2 V at 50 mV/s. The PEDOT film from a solution of 10 mM EDOT and 10 mM SDS was deposited on Au coated slide.

The cyclic voltammograms had a similar shape except the one recorded during the deposition on stainless steel. In this case there was a small peak at around 0.4 V *vs.* SCE shifting gradually to 0.8 V *vs.* SCE with increasing cycle number as can be seen from Figure 4. This was possibly due to substrate corrosion. All CVs had an onset of

polymerisation around 0.8 V *vs.* SCE. Their currents increased from cycle to cycle which indicated continuous deposition of more polymer. The rates of polymerisation however were quite different as noticed from the different currents seen with the different substrates. The polymerisation charges recorded on the various substrates were calculated and are shown in Table 1.

Table 1 The results of polymerisation charge and adhesion of PEDOT film on different substrates.

Working electrode	**Polymerisation charge (mC/cm^2)**	**Observation**
ITO glass	6.89	The film surface was not smooth and the film peeled off easily
Stainless steel	17.54	The film surface was smooth but the film peeled off easily
Pt coated slide	5.33	The film surface was quite smooth and the film had a very good adhesion
Au coated slide	7.08	The film surface was very smooth and the film had a very good adhesion

Electrodeposition of PEDOT films on the different substrates resulted in different rates of electrodeposition. Electrodeposition of PEDOT on stainless steel had the highest charge. This was however due to a side reaction corresponded to corrosion of substrate. The film did not have a good adhesion on the substrate. It came off easily like powder spread over the substrate, not like a film. Its surface morphology was covered with globules as can be seen from Figure 7 (B). On ITO glass the 50 cycle deposition resulted in a much small charge, however this was not very smooth and peeled off easily. Its surface morphology showed curvature as can be seen from Figure 7 (A). For the films on Pt and Au coated slides, both film surfaces were quite smooth and had a

very good adhesion. The film surface on Au coated slide was comprised of a compact film covered by small globules probably due to dendrite growth. Similarly, the film surface on the Pt coated slide was composed of a compact film covered by uneven globules.

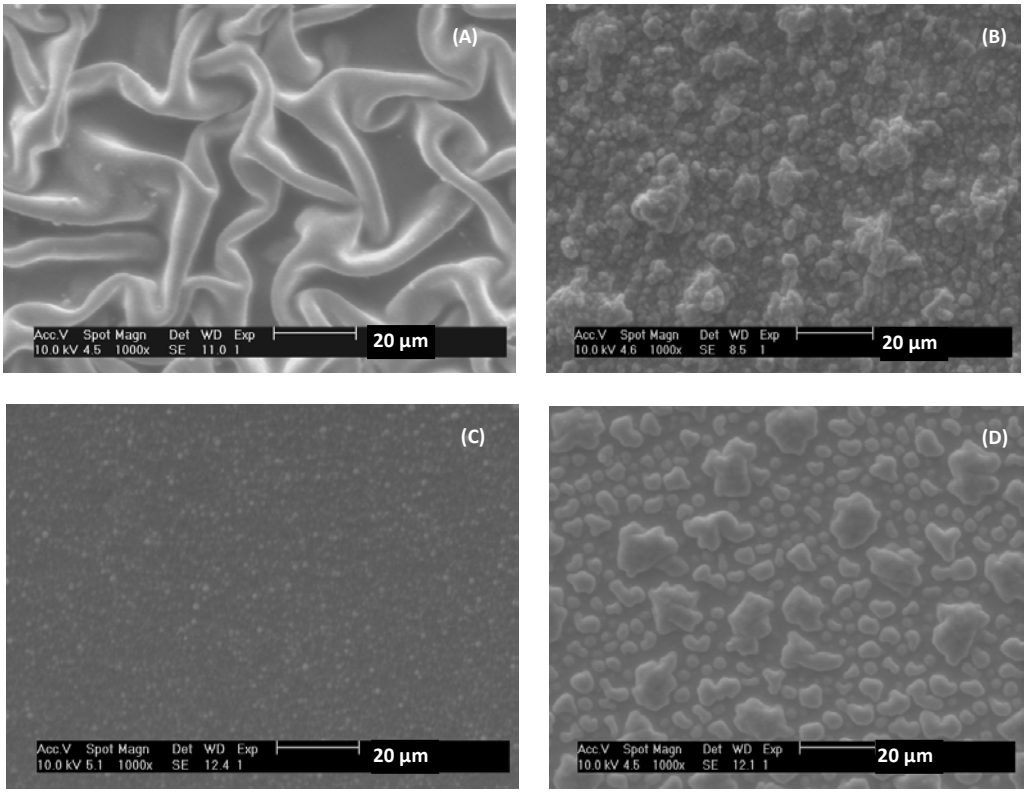

Figure 7 Scanning electron micrographs of PEDOT films on different substrates:
(A) ITO glass (B) Stainless steel (C) Au coated slide and (D) Pt coated slide

It can be concluded that Au and Pt coated slides could be suitable substrates for electrodeposition of PEDOT film in aqueous solution. The films had a very good adhesion and the film surfaces were visibly smooth.

Appendix 3

Fitting the equivalent circuits to impedance of the powder samples i.e. untreated and treated.

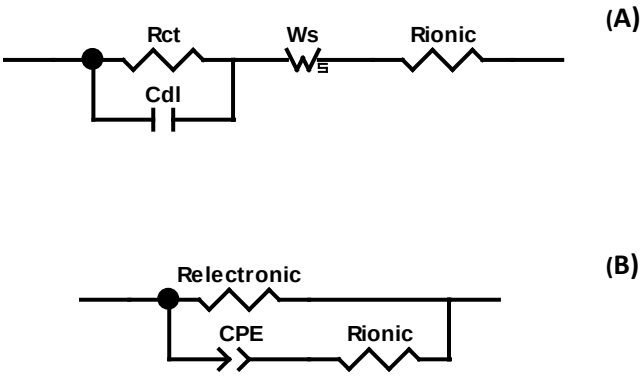

Figure 8 the equivalent circuit of untreated (A) and treated (B) samples

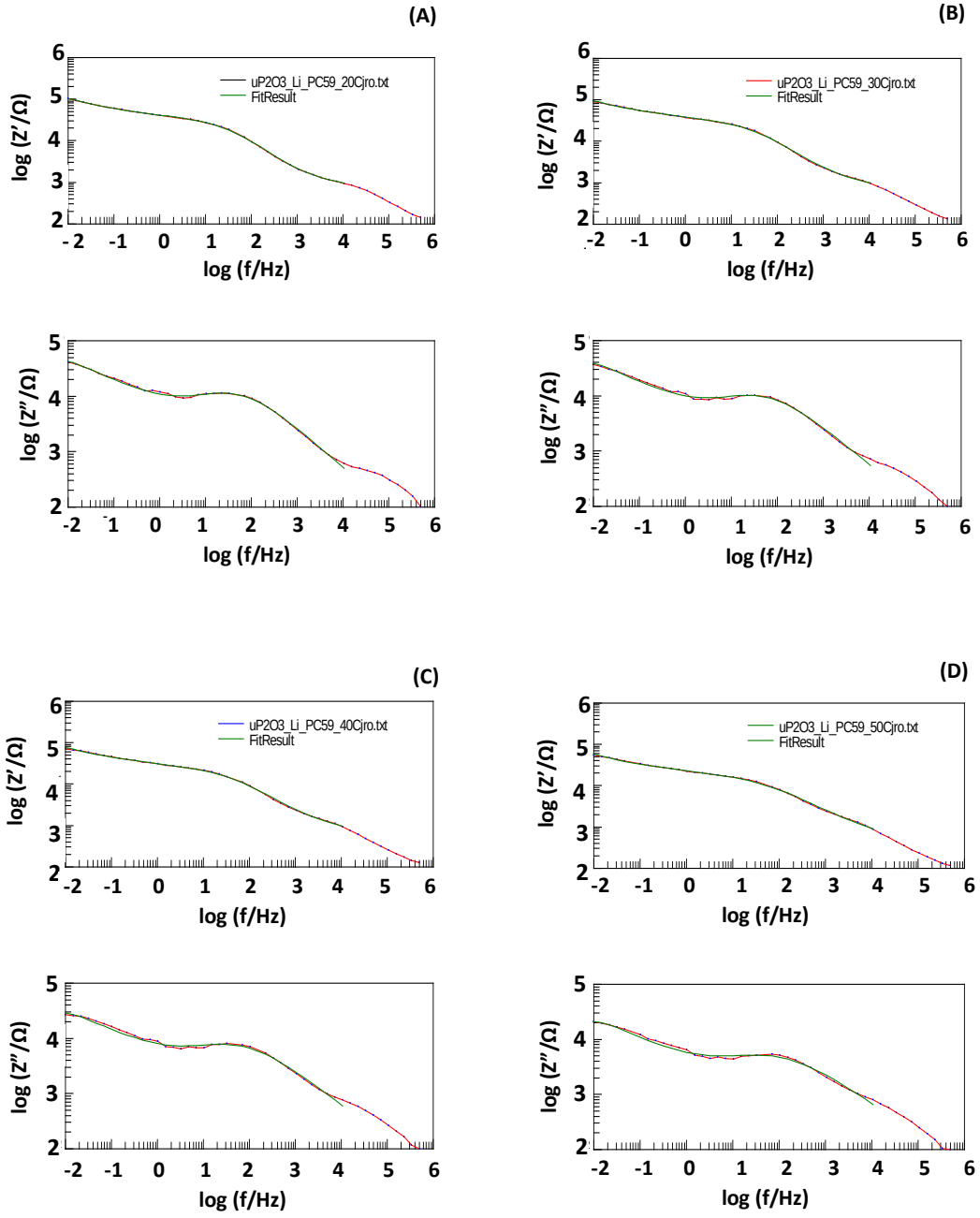

Figure 9 Fitting the equivalent circuits to impedance of the untreated samples at (A) 20 ^{o}C, (B) 30 ^{o}C, (C) 40 ^{o}C and (D) 50 ^{o}C.

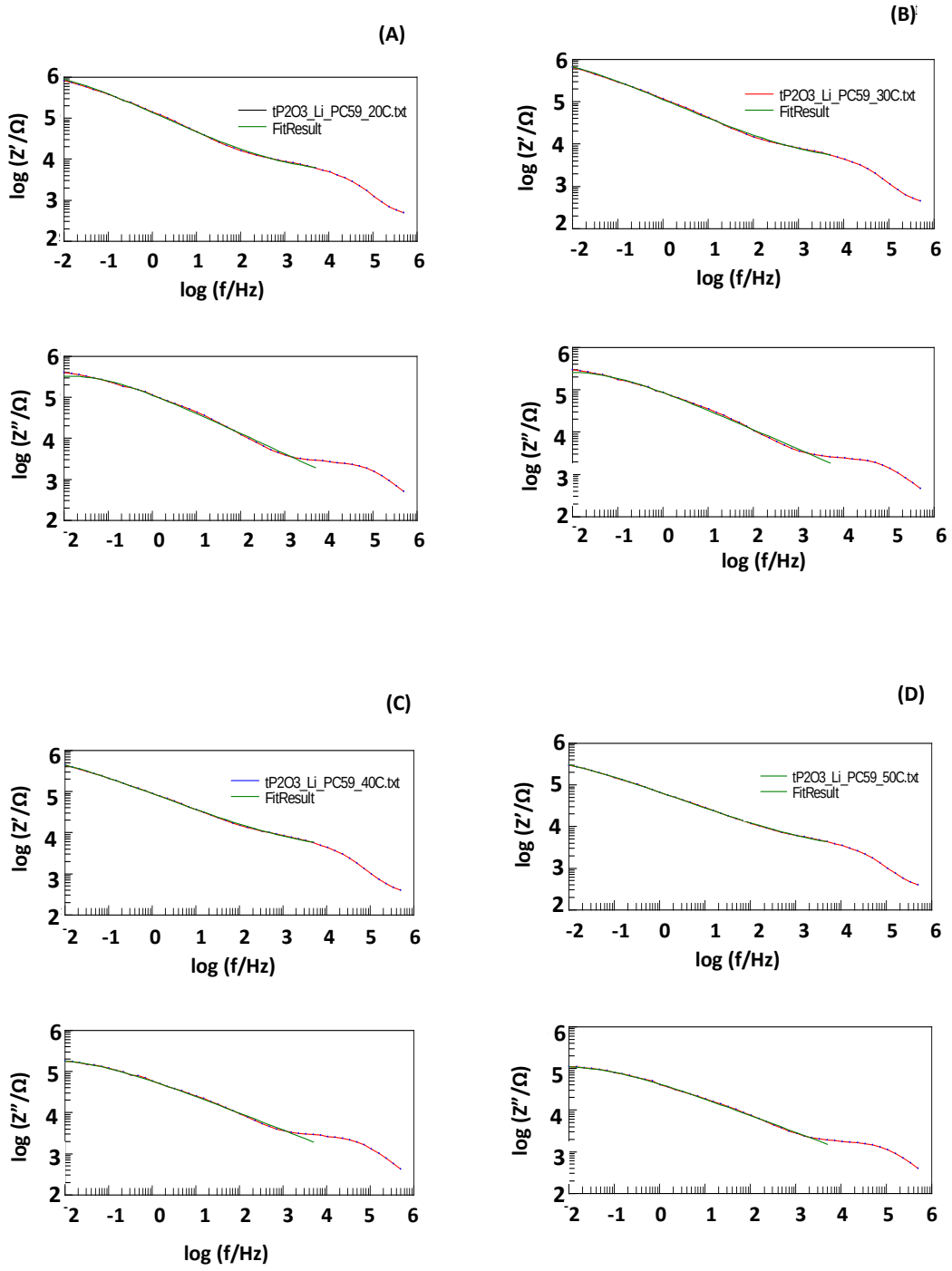

Figure 10 Fitting the equivalent circuits to impedance of the treated samples at (A) 20 ^{o}C, (B) 30 ^{o}C, (C) 40 ^{o}C and (D) 50 ^{o}C.